Managing Uncertainties in Grid-Integration of Distributed Energy Resources: Safety, Stability, and Optimality

by

Sijia Geng

A dissertation submitted in partial fulfillment
of the requirements for the degree of
Doctor of Philosophy
(Electrical and Computer Engineering)
in The University of Michigan
2022

Doctoral Committee:

Professor Ian A. Hiskens, Chair
Professor Anouck Girard
Associate Professor Johanna Mathieu
Associate Professor Peter Seiler

Sijia Geng
sgeng@umich.edu
ORCID iD: 0000-0002-5477-2378

To my parents.

ACKNOWLEDGMENTS

I would like to express my deepest gratitude to my PhD advisor, Professor Ian Hiskens. He showed me how to be a candid researcher, a cordial colleague, and a cheerful friend. He tolerated my stubbornness and guided me with remarkable patience. He and his family constantly supported me and cared for me during the ups and downs.

I have also been extremely lucky to receive kindness from many people during this journey towards my PhD. I would like to thank everyone I interacted with in the past five years. I am deeply in debt to your kindness and support.

Finally, without the love and support of my family and friends, I wouldn't be the person I am today. I am grateful and want to take this opportunity to thank you all.

TABLE OF CONTENTS

LIST OF FIGURES

LIST OF TABLES

LIST OF ABBREVIATIONS

CBF Control Barrier Function
CC Chance-Constrained
CHP Combined Heat and Power
CLF Control Lyapunov Function
DAE Differential-Algebraic Equation
DAIS Differential-Algebraic Impulsive Switched
DER Distributed Energy Resource
LN Logarithmic Norm
LP Linear Program
MPC Model Predictive Control
NPC Net Present Cost
ODE Ordinary Differential Equation
OPF Optimal Power Flow
PC Principal Component
PCA Principal Component Analysis
PCC Point of Common Coupling
PLL Phase-Locked Loop
PV Solar Photovoltaic
ROA Region of Attraction
SG Stochastic Gradient
SMIB Single Machine Infinite Bus
SoC State of Charge
SOS Sum-of-Squares
SVD Singular Value Decomposition
TS Trajectory Sensitivity
VUF Voltage Unbalance Factor

ABSTRACT

Distributed energy resources (DERs), in particular renewable resources, are witnessing substantial technology improvements and cost reductions. Large-scale integration of DERs into electric power systems is therefore becoming technically and economically viable. Various critical challenges must be addressed, however, to achieve a successful transition to a clean energy future. Meanwhile, safety, stability, and optimality are of paramount importance for power systems.

The uncertainties introduced by renewable DERs, such as solar photovoltaic (PV) and wind generation, require careful treatments for achieving safe system operation. In the first part of this dissertation, theoretical results and efficient algorithms are developed to analyze the impacts of uncertainties and external disturbances on system dynamics. First, theoretical results for characterizing the second-order trajectory sensitivities for general nonlinear hybrid systems are established. Then, rigorous bounds are developed to quantify all possible system behaviors for general nonlinear systems, by constructing the second-order trajectory sensitivities and exploiting the mathematical tool of the logarithmic norm. Efficient algorithms are proposed for computing the reach-set, which enables safety verification by checking if the reach-set intersects any unsafe region.

Furthermore, DERs are typically connected to power systems through inverter interfaces, whose dynamics are dominated by the enforced control law. This dissertation proposes a control scheme for inverters that can achieve autonomous switch between grid-connected operation and islanded operation. A detailed dynamic model for inverter-based power systems is presented. Discussions on system behavior at steady state and system stability are provided. It is recognized that the fast dynamics introduced by inverter-based resources add another layer of complexity for ensuring system safety. In this dissertation, a barrier-function-based method is extended to construct distributed control laws for inverters in microgrids, which can explicitly certify safety constraints for the overall system. Algorithmic constructions of these control laws are proposed using sum-of-squares optimization.

With the critical issues of safety and stability handled, the second part of this dissertation explores opportunities offered by renewable DERs. First, the collective reactive power capability of multiple DERs such as solar PVs is exploited to balance voltages across the distribution network. Distributed and decentralized Steinmetz-based controllers are proposed, and the interactions and convergence of the controllers are analyzed. Rigorous convergence guarantees are established for the overall system using the Banach fixed-point theory. The convergence guarantee is essential to ensure robustness of the proposed control algorithms in realistic settings where parameters are uncertain, disturbances are prevalent, and control and measurement signals are prone to delays.

Second, the local energy supply from DERs enables off-grid energy systems, such as renewable-only microgrids and community-based energy hub systems that incorporate multiple energy carriers. Designing the system to achieve a balanced trade-off between economic cost and operational reliability is increasingly important. In this dissertation, the design problem is formulated as a stochastic chance-constrained optimization to explicitly address the uncertainty induced by renewable resources and load. An original cluster-based multi-policy formulation is proposed and incorporated in the chance-constrained formulation, which achieves much more flexible storage dispatches. A novel iterative optimization-validation algorithm is devised to efficiently solve the design problem, where a scalar auxiliary parameter is dynamically adjusted for tuning the robustness level. To achieve reliable and economic real-time operation, a two-level control strategy is proposed, and several energy hubs are interconnected to exploit energy sharing capability through electrical and gas networks.

CHAPTER 1

Introduction

Increasing electricity demand together with the retirement of coal-fired power plants is forcing power systems to operate ever closer to their limits. At the same time, distributed energy resources (DERs), in particular renewable resources, are witnessing substantial technology improvements and cost reductions [6]. Large-scale integration of DERs into power systems is therefore becoming technically and economically viable. This dissertation addresses the critical issues of safety and stability of power systems that integrate substantial renewable DERs. Furthermore, this dissertation also explores opportunities enabled by DERs, such as providing grid services, supplying local clean energy, and forming multi-energy systems. The unifying theme throughout this dissertation is to manage the uncertainties introduced by renewable DERs. Section 1.1 provides the background on the emerging DERs in power systems, which motivates the investigation of challenges arising from integrating DERs to the grid. In Section 1.2, the various technical challenges and research gaps of integrating DERs, in particular in the presence of uncertainties, are discussed. Section 1.3 explains the organization and structure of this dissertation and provides the outline to the remaining chapters.

1.1 Background and Motivation

Conventional power systems are supplied by large centralized power plants, typically utilizing fossil fuels such as coal and natural gas. However, the accompanying impacts on the environment and public health caused by fossil-based generation have drawn growing concerns. Much attention and efforts have been shifted to renewable energy resources [7], including wind power, solar photovoltaics (PVs), solar thermal power, hydropower, and bio-energy. Among these emerging renewable energy resources, wind and solar PV have been proven to be both cost-efficient and accessible. Figure 1.1 shows the significant decline of average installation cost and the increase of deployment of solar PV systems in

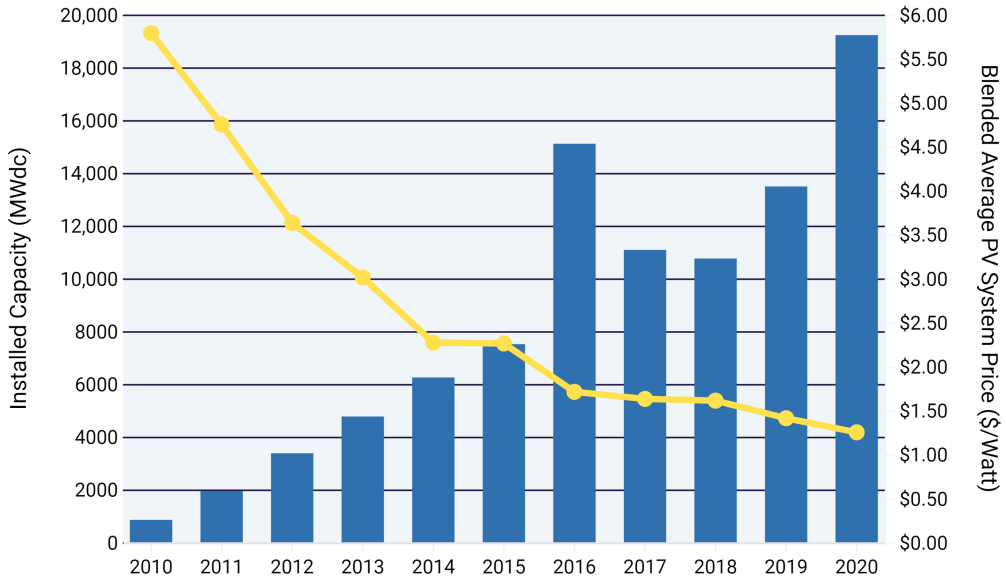

Figure 1.1: Price decline and deployment growth of solar PV systems in the U.S. [1]. The yellow curve shows the price decline, corresponding to the axis on the right. The blue bars demonstrate the deployment growth, corresponding to the axis on the left.

the U.S. in recent years.

The fundamental operation principle of power systems is to balance the generation and load in real time. In conventional power systems, the power output from dispatchable generations is controlled by the power system operators to follow the varying load. The key challenges with wind and solar resources are their intrinsic variability and uncertainty. Variability refers to the nature that the maximum available power from wind turbines or solar PVs is changing from time to time. Uncertainty means that we cannot predict with accuracy of the maximum available power. Figure 1.2 demonstrates the variability and uncertainty of a wind plant and a solar plant over 48 hours. It is clear that such renewable generations are non-dispatchable, meaning that they are not able to adjust their power output according to the request from power system operators. Therefore, the increasing integration of renewable resources at the cost of replacing conventional dispatchable generations leads to critical challenges for real-time power system operation. Furthermore, the uncertainty from renewable resources also has profound impacts on the long-term design of power systems, which demands efficient approaches to explicitly manage uncertainty.

Figure 1.3 demonstrates the variability of solar generation in much higher time resolution. The variation of renewable generation at such timescale would influence power system dynamics. It is important that we carefully analyze and quantify the impacts, and design control schemes to ensure system safety and stability.

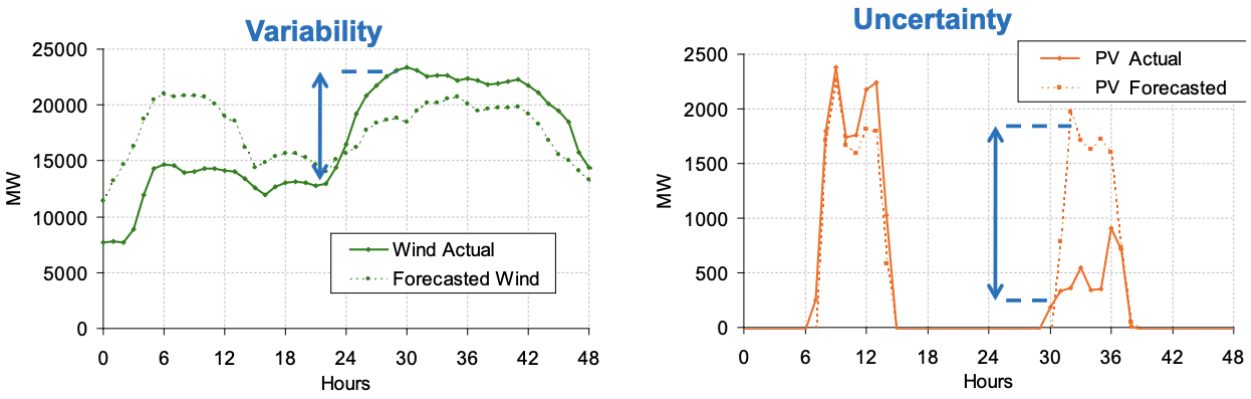

Figure 1.2: Examples of the variability and uncertainty of a wind plant and a solar plant [2].

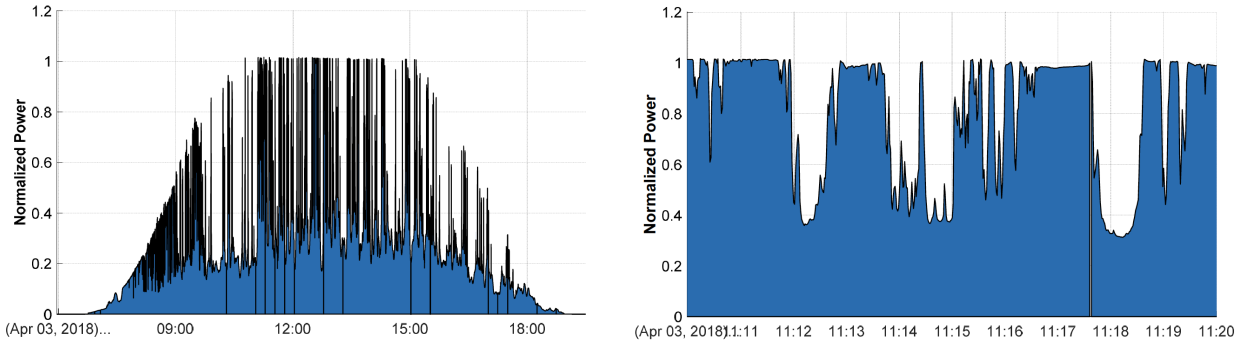

Figure 1.3: Normalized power generation at a 5kW rooftop PV in Florida: Most variable day (left) and 10-min period (right) over 1-year [3].

Traditionally, power systems are dominated by large synchronous generators whose electro-mechanical dynamics are well-understood. In contrast, DERs are usually connected to power systems through power electronics, whose dynamics are dominated by the enforced control law. Representative configurations of wind turbine systems and solar PV systems are displayed in Fig. 1.4 and Fig. 1.5, respectively. As more and more inverter-based DERs replace synchronous generations, the dynamic characteristics of power systems will inevitably change. For example, the convenient timescale separation between frequency and voltage dynamics will vanish. The long-standing assumption of neglecting transmission line dynamics in power system studies may no longer hold for inverter-based systems. It is important to investigate the dynamics and stability characteristics of such inverter-based power systems, to fully appreciate the impacts of DERs on power systems. Moreover, such investigations form a solid basis for constructing appropriate control schemes for DERs that ensure system safety and stability.

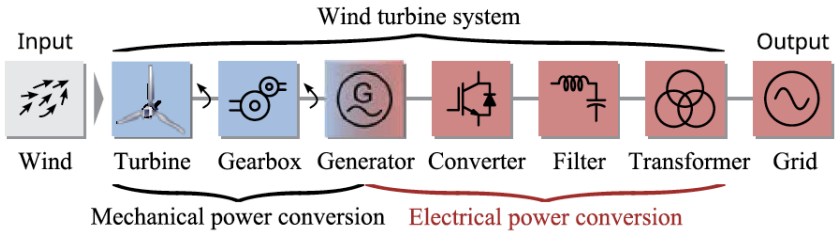

Figure 1.4: Representative configuration of wind generation systems [4].

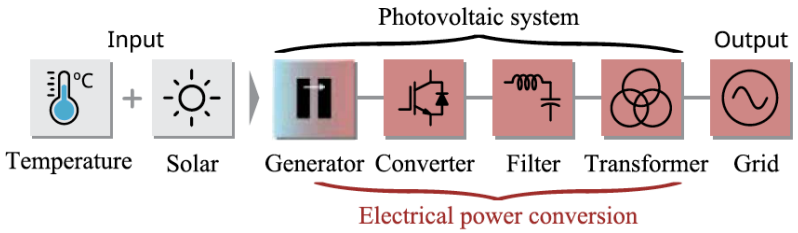

Figure 1.5: Representative configuration of solar PV systems [4].

Unlike large synchronous generators, DERs are typically small in capacity and are usually connected to power systems in a decentralized manner. Figure 1.6 demonstrates the evolution of power generation in Denmark from the centralized generation in 1985 to the decentralized generation in 2015, when more than 50% of the energy is supplied by renewable resources. In future DER-based smart grids, there can easily be hundreds of millions of control and actuation points. The current centralized control schemes are not able to handle and process the data at such scale in real time. In practical scenarios, communication between DERs may be expensive and limited, and subject to time delays. Therefore, innovative distributed control schemes should be designed for coordinating DERs, which utilize communication and information infrastructures wisely. On the other hand, the decentralized deployment of DERs brings about valuable opportunities to provide grid services, offer local clean energy supply, and enable interconnections between multiple energy carriers to supply reliable energy in rural areas.

1.2 Research Gaps and Research Goals

Power systems are complex cyber-physical systems. The physical power system, consisting of electricity generation, transmission system, distribution system, and load, is supported by cyberinfrastructures in the form of energy management systems that provide monitoring and control functionality. Based on the characteristic timescales, analysis of power systems can be categorized into three main types,

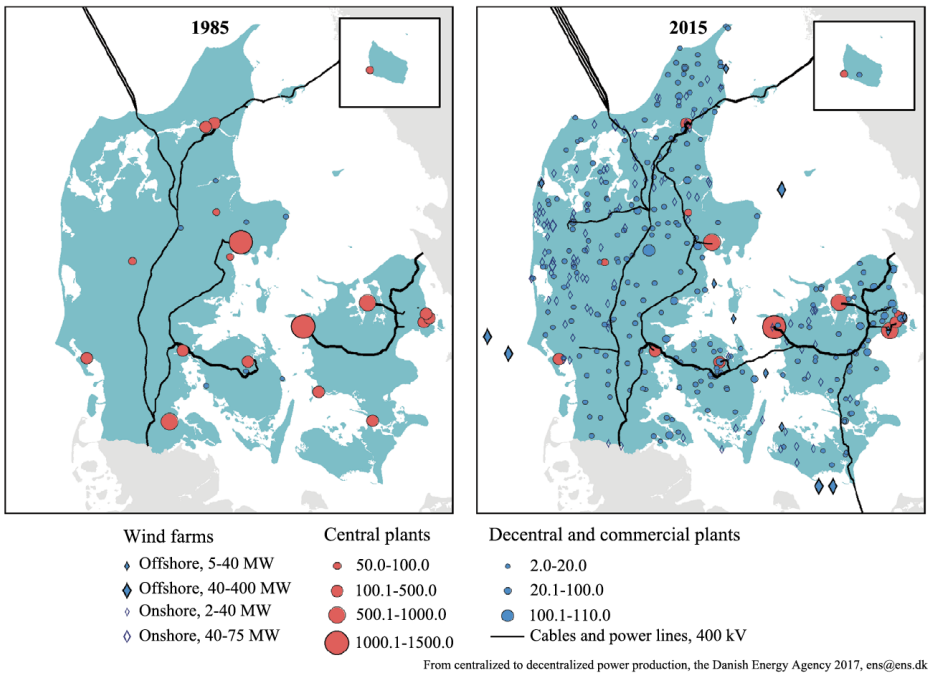

Figure 1.6: Evolution of power generation in Denmark (left: centralized electric power infrastructure in 1985, right: decentralized electric power infrastructure in 2015) [5].

- Dynamic analysis: modeled by ordinary differential equation (ODE), differential-algebraic equation (DAE), or differential-algebraic impulsive switched (DAIS) model.
- Static and quasi-static analysis: modeled by power flow equations.
- Long-term design and planning: modeled by optimization and decision making problems.

The challenges of the grid-integration of DERs need to be approached and addressed from all three timescales to guarantee a comprehensive consideration on ensuring the safety, stability, and optimality of power systems.

1.2.1 Safety Verification and Safety Synthesis

Many physical systems need to abide by a set of safety constraints established by engineers for the purpose of ensuring the safe operation of the system [8,9]. A safety-critical system refers to a system for which the violation of safety constraints will lead to serious economic loss or personal casualty [10]. Power system falls into such category considering the loss resulting from a large-scale blackout and failure to supply critical loads such as hospital and process plant. To assist the discussion that follows, we give the definition of *safety* based on the concept of *reach-set*.

Definition 1. *Reach-set is the union of all states in the state space that can be visited by trajectories of a dynamic system that are:*

- *originating from a set consisting of uncertain initial conditions.*
- *under the influence of admissible parameter uncertainties and external disturbances.*

Definition 2. *A system is safe if there is no intersection of the reach-set and any unsafe region, where the unsafe region is defined by the safety constraints established by system engineers.*

Given the reach-set, system safety can be easily verified by checking set intersection of the reach-set and the unsafe region. However, in general it is difficult, if not impossible, to compute the exact reach-set for a nonlinear system [11]. Much research has been devoted to computing over-approximations of the reach-set. A Taylor flowpipe model is used in [12] to over-approximate the reach-set of hybrid systems for a set of initial conditions. Other approaches to reach-set computation include abstraction-based methods [13], level-set methods [14], and differential inequalities [15]. Reachability analysis of nonlinear differential-algebraic systems is studied in [16] using a conservative linearization method, where zonotopes are used to represent the reach-set. A common issue across all these methods is conservativeness, which is partially because of the accumulation of error over time, i.e., the wrapping effect. Computational burden is another issue when considering high-dimensional applications such as power systems.

In power systems, safety verification is conducted through the so-called dynamic security assessment [17], which involves repeated time-domain simulations of the power system models for a set of uncertain parameters and initial conditions. For the information to be valuable, such assessment needs to be completed in a timely manner at the scale of minutes [18]. However, computational power restricts the number of simulations to be performed therefore limiting the range of scenarios to be analyzed. Formal analysis methods that are computationally efficient are needed to cater to the large scale and nonlinearity of power systems.

In the context of reach-set computation, the safety verification problem boils down to efficiently quantifying the impacts of uncertainties and disturbances on power system dynamics. Trajectory approximation is an efficient approach that can be used to approximate perturbed trajectories associated with uncertain parameters and initial conditions, thus avoiding repeated simulations [19]. However, there is no guarantee that the computed approximation is an enclosure of the true reach-set. In Chapter 3, we analytically quantify the error inherent in trajectory approximation using the second-order trajectory sensitivity as developed in Chapter 2. To quantify the impacts of external disturbances

on the excursion of system trajectories, the mathematical tool of the logarithmic norm is employed to improve and extend an existing result to DAE systems. Efficient algorithms are proposed for computing the reach-set, which enables safety verification by checking if the reach-set intersects any unsafe region.

In addition to verifying system safety by developing efficient and rigorous methods to compute the reach-set, we need to synthesize control schemes to guarantee by-construction the satisfaction of safety constraints. One promising direction is based on the concept of positively invariant set [20], which refers to a set that is forward invariant, i.e., if the initial state is within the set, the system trajectory will remain in the set for all future time. The control community has developed the methods of barrier certificates [21] and control barrier functions [22] to certify safety by guaranteeing the forward invariance of a set via Lyapunov-like conditions. The idea of a barrier certificate is to construct a continuously differentiable barrier function that is non-negative in the safe set, negative in the unsafe set, while ensuring at the zero-level set, the value of the barrier function is increasing along the system trajectories. Control barrier function extends the previous formulation to include control inputs, as inspired by control Lyapunov function. In Chapter 5, a method based on control barrier functions is extended to a distributed scheme to construct distributed control laws for inverters in microgrids.

1.2.2 Dynamics and Stability of Inverter-Based Power Systems

Ensuring stability is vital for power systems in order to avoid massive disruption arising from large-scale blackouts. In 2004, the IEEE/CIGRE Joint Task Force on Stability Terms and Definitions provided a physically motivated definition of power system stability [23], which conforms to the precise system-theoretic mathematical definitions.

Definition 3. *Power system stability is the ability of an electric power system, for a given initial operating condition, to regain a state of operating equilibrium after being subjected to a physical disturbance, with most system variables bounded so that practically the entire system remains intact.*

In particular, to facilitate identifying key contributors to instability and devising countermeasures, power system stability is classified into three main categories which encompass most practical instability scenarios [23, 24].

- Angle Stability: Rotor angle stability refers to the ability of synchronous machines of an interconnected power system to remain in synchronism after being subjected to a disturbance.

- Frequency Stability: Frequency stability refers to the ability of a power system to maintain steady frequency following a severe system upset resulting in a significant imbalance between generation and load.

- Voltage Stability: Voltage stability refers to the ability of a power system to maintain steady voltages at all buses in the system after being subjected to a disturbance from a given initial operating condition.

However, the above classification is originated from conventional power systems that are dominated by large synchronous generators, where under most scenarios the dynamic behaviors show convenient timescale separation for angle, frequency and voltage issues [7]. With the increasing penetration of inverter-based resources replacing synchronous generations, the dynamic characteristics of power systems will inevitably change. To incorporate the effects of fast-response power electronic devices, a Task Force was established in 2016 to revisit and extend the stability classifications. Two new categories were added concerning the faster dynamics introduced by power electronic devices [25].

- Converter-Driven Stability: Slow- and fast-interactions are differentiated based on the frequencies of the observed phenomena.

  - Slow-Interaction (typically, less than 10 Hz): Slow dynamic interactions of the control systems of power electronic-based devices with slow-response components of the power system such as the electro-mechanical dynamics of synchronous generators and some generator controllers.
  - Fast-Interaction (typically, tens to hundreds of Hz, and possibly into kHz): Fast dynamic interactions of the control systems of power electronic-based systems with fast-response components of the power system such as the transmission network, the stator dynamics of synchronous generators, or other power electronic-based devices.

- Resonance stability: The resonance, in general, occurs when energy exchange takes place periodically in an oscillatory manner. These oscillations grow in case of insufficient dissipation of energy in the flow path and are manifested (in electrical power systems) in magnification of voltage/current/torque magnitudes. When these magnitudes exceed specified thresholds, it is said that a resonance instability has occurred.

  - Torsional: Due to a resonance between series compensation and the mechanical torsional frequencies of the turbine-generator shaft.

– Electrical: Due to a resonance between series compensation and the electrical characteristics of the generator.

Investigations, at a fundamental level, of the structural differences between the dynamics of conventional power systems and inverter-dominated power systems are needed. There is an extensive literature in the power electronic community which focuses on the device-level analysis of inverters [26, 27]. At the system level, however, much debating still needs answers regarding how inverter-based resources should interact with the rest of the power system. It is still inconclusive about what kinds and levels of system services inverter-based resources should provide and what control standards should be enforced.

Despite the various terminologies for categorizing control schemes for inverter-based resources, two common modes are the grid-following mode [28] and the grid-forming mode [29]. In the grid-following mode, the inverter aims to supply desired active and reactive power, while tracking the terminal voltage set by the grid. The tracking is typically achieved through a phase-locked loop [30]. Grid-following inverters can be viewed as a current source, that is, the inverter follows network voltage and forms current to supply desired power. Grid-forming inverters, on the other hand, establish terminal voltage according to voltage magnitude and frequency set-points. Various techniques have been proposed for grid-forming control, among which the most widely accepted method is the droop-based control [31]. Grid-forming inverters can be viewed as a voltage source. Grid-following has been the current practice since renewable resources are largely variable and non-dispatchable unless paired with battery devices. However, with the increasing replacement of synchronous generators, it is foreseeable that inverter-based resources will be responsible for providing grid services in the near future.

In Chapter 4, a novel inverter control scheme is proposed which can achieve autonomous mode switching between grid-following and grid-forming. Modeling and analysis of inverter-based power systems are presented.

1.2.3 Opportunities Enabled by Distributed Energy Resources

Traditionally, distribution systems have been passive radial networks where energy flows in a single direction from the substation to the loads. The operation of distribution systems is currently based on centralized control schemes realized through Supervisory Control and Data Acquisition (SCADA) system and Distribution Management System (DMS) [32]. The increasing penetration of DERs, however, is transforming distribution systems into Active Distribution Networks (ADN) [33]. The local supply from DERs should be harnessed and the decentralized deployment of a large number of DERs can be

exploited to collectively provide grid services.

One practical issue faced by distribution systems is the three-phase voltage unbalance, primarily as a consequence of structural and operational factors [34]. Voltage unbalance may cause induction motor overheating, transformer saturation, and increased power losses [35,36]. Much research has been devoted to phase balancing of distribution systems, including system reconfiguration [37], static Var compensation [38], and three-phase optimal power flow algorithms [39]. In Chapter 6, distributed and decentralized Steinmetz-based controllers are proposed to balance voltages across the distribution network, by exploiting the collective capability of multiple DERs. Convergence guarantees are provided by analyzing the interactions between multiple controllers.

The various challenges of integrating renewable DERs are accompanied by great opportunities for revolutionizing power systems. Microgrids, i.e., small-scale power systems, offer a promising opportunity for achieving 100% of renewable generation. As DER-based microgrid systems evolve, they will likely incorporate multiple energy carriers, typically electricity, heat, natural gas, and hydrogen, along with the respective energy conversion processes. We refer to such multi-energy systems as energy hubs [40]. It is clear that energy hubs offer the potential for highly versatile operating strategies, though depending on careful hub composition and component sizing. Sufficient capacity must be available within the off-grid system to supply loads securely, while excessive capacity should be avoided to minimize the overall cost. This implies that in rare cases where renewable generation is extremely limited, loads with low priority are subject to load shedding, as a last resort. Designing microgrids and energy hubs to achieve a balanced trade-off between equipment cost and operational flexibility is becoming increasingly important.

The problems of optimal capacity design and operation of microgrids and energy hubs have been gaining attention due to the potential in hosting a high level of renewable DERs. The key challenge in approaching the design and operation problem lies in the stochasticity of renewable resources. In the design phase, all possible renewable generation scenarios need to be taken into account, in order to achieve a proper trade-off between system reliability and cost efficiency. In the operation phase, appropriate control strategies need to be devised to respond to the stochasticity in renewable generation, in order to achieve reliable and economic operation.

Most literature handles stochastic variables using Monte Carlo simulation and heuristic algorithms, which cannot provide probability guarantees in a tractable way. Recently there has been substantial interest in chance-constrained formulations. Chance-constrained problems are generally difficult to solve analytically, except for rare cases where the un-

certain variables are uniformly or normally distributed [41]. However, under certain light assumptions, randomized optimization methods [42] can solve chance-constrained problems and provide solutions with *a priori* probability guarantees and appealing tractability properties. Chapters 7 and 8 exploit the chance-constrained formulation and explicitly deal with the stochasticity in renewable resources and load.

1.3 Dissertation Outline

The organization style of this dissertation is that each chapter is self-contained and the mathematical notations and definitions are defined in each chapter. The remainder of this dissertation is organized as follows.

Chapters 2 to **5** constitute the first part of this dissertation, which focuses on addressing the critical issues of power system safety and stability with the grid-integration of DERs. Specifically, **Chapters 2** and **3** develop theoretical results and efficient algorithms to analyze the impacts of uncertainties and external disturbances on power system dynamics. The proposed reach-set computation algorithm enables efficient safety verification. **Chapters 4** and **5** investigate the dynamics and stability characteristics of inverter-based power systems. Two control schemes are proposed for inverters. The controller presented in **Chapter 4** can achieve autonomous switch between grid-connected operation and islanded operation. The controller presented in **Chapter 5** can explicitly certify safety constraints on voltage magnitude during transients. Both control schemes are distributed, meaning that no centralized coordination is needed.

With the critical issues of safety and stability handled, the second part of this dissertation consists of **Chapters 6** to **8**, which focuses on exploring opportunities offered by renewable DERs. **Chapter 6** exploits the collective reactive power capability of multiple DERs to balance voltages across the distribution network, while providing rigorous convergence guarantees for the proposed distributed controllers. **Chapters 7** and **8** exploit the local energy supply from DERs to enable the design of renewable-only microgrids and energy hub systems that incorporate multiple energy carriers. Managing the uncertainty from renewable resources is the key consideration of these chapters.

Finally, **Chapter 9** concludes this dissertation by summarizing the key contributions and providing future perspectives.

CHAPTER 2

Theoretical Development of the Second-Order Trajectory Sensitivity for Hybrid Systems

2.1 Chapter Introduction

Hybrid dynamical systems refer to a class of systems where continuous dynamics and discrete events intrinsically interact [43]. Such systems may exhibit complicated and rich forms of behaviors. Examples of hybrid systems include power systems [44], motor drives [45], temperature control systems [46] and robots [47]. Considering the potentially complex nonlinear non-smooth behavior of such systems, opportunities for formal analysis are limited. Although Lyapunov-like methods are available for analyzing stability and boundedness of certain hybrid systems [43, 48, 49], time-domain simulation is widely adopted for evaluating hybrid system behavior [50]. The disadvantage of such a technique is that one time-domain simulation only provides information for a single scenario. Slight perturbations of system parameters or initial conditions require repeated time-domain simulations. For large-scale system such as power systems, repetitive simulations are computationally intensive.

Trajectory sensitivity analysis provides a means of avoiding such computational challenges. Instead of performing multiple simulations, it approximates the numerous perturbed trajectories using trajectory sensitivities that can be obtained through a single simulation of the nominal case. This technique linearizes the system around the nominal trajectory, establishing an (approximate) relationship between variations in the initial conditions and/or system parameters and the corresponding perturbed trajectories. Reference [51] has derived the first-order trajectory sensitivities for general hybrid dynamical systems that are described via a differential-algebraic-discrete model. This provides an important extension to the analysis of continuous models [52–56]. A modification for sensitivity-based trajectory approximation is presented in [57] for improving accuracy in the vicinity of the stability boundary. The computational burden grows linearly with the

number of initial conditions and/or uncertain parameters of interest. Recent work [58] developed a discrete adjoint sensitivity approach which requires a fixed computational effort that is independent of the number of uncertain variables.

First-order trajectory sensitivity analysis offers only limited accuracy in situations where higher-order dynamics become non-negligible. To improve the accuracy of trajectory approximation in such situations, second-order trajectory sensitivities can be considered. Second-order trajectory sensitivities for continuous systems are derived in [59–61]. The objective of this chapter is to fully characterize second-order sensitivities with respect to parameters and initial conditions for general hybrid systems. The chapter builds on the results of [51] and extends the results of [62] by including algebraic variables in the system model. The key contribution of this chapter is the development of the jump conditions describing the evolution of second-order sensitivities at discrete (switching and state reset) events. For completeness, the differential-algebraic equation (DAE) model that describes second-order sensitivities for continuous dynamics is derived and compared with [60]. The jump conditions at discrete events and the DAE model for smooth dynamics together enable second-order trajectory sensitivity analysis of hybrid dynamical systems.

Trajectory sensitivity analysis underpins numerous applications, including quantifying the impact of uncertainty on dynamical systems [19, 60, 63], model predictive control and tracking control [64–67], design optimization [68–70], and power system stability assessment and enhancement [71–77]. The gradient information provided by trajectory sensitivities has been used in parameter estimation and boundary value problems [78–80]. The results presented in this chapter form the basis for extending applications to incorporate second-order trajectory sensitivities.

This chapter is organized as follows: Section 2.2 presents a general hybrid system model. An overview of first-order trajectory sensitivity analysis is given in Section 2.3, along with the calculation of sensitivities for both continuous dynamics and discrete events. Section 2.4 derives the second-order sensitivities away from events and provides a comparison with previous work. The jump conditions describing second-order sensitivities at discrete events are established in Section 2.5. Trajectory approximation is introduced in Section 2.6 and a case study is presented in Section 2.7. Section 2.8 provides conclusions.

2.2 Mathematical Models

Hybrid dynamical systems feature comprehensive interactions between smooth dynamics and discrete events. To fully capture this intrinsic characteristic, a differential-algebraic

impulsive switched (DAIS) model [19] has been adopted:

$$\dot{x} = f(x, y) \tag{2.2.1a}$$

$$0_m = g(x, y) \triangleq \begin{cases} \underline{g}(x, y), & s(x, y) < 0 \\ \overline{g}(x, y), & s(x, y) > 0 \end{cases} \tag{2.2.1b}$$

$$x^+ = h(x^-, y^-), \qquad s(x, y) = 0 \tag{2.2.1c}$$

where $x \in \mathbb{R}^n$ are the dynamic states, $y \in \mathbb{R}^m$ are the algebraic states, $f : \mathbb{R}^{n+m} \to \mathbb{R}^n$, $g : \mathbb{R}^{n+m} \to \mathbb{R}^m$, $h : \mathbb{R}^{n+m} \to \mathbb{R}^n$, $s : \mathbb{R}^{n+m} \to \mathbb{R}$, and 0_m is the m-length vector of zeros.

The differential equations (2.2.1a) govern the continuous behavior of the system, under the influence of the vector field f. The algebraic equations (2.2.1b) capture switching events in the system. In particular, g is composed of the set of equations $\underline{g}$ when the switching function $s(x, y)$ is negative and the equations $\overline{g}$ when $s(x, y)$ is positive. The scalar equation $s(x, y) = 0$ defines the switching hypersurface, which is denoted by $\mathcal{S} \triangleq \{(x, y) : s(x, y) = 0\}$. When $s = 0$, the system trajectory encounters the switching hypersurface and a switching event is triggered. State reset events are described by equations (2.2.1c), where the superscripts "$-$" and "$+$" indicate the time instants just prior to and just after the event triggering time, respectively. Reset events imply a step change in the state variables x. Based on the model (2.2.1b)-(2.2.1c), a switching event and a reset event are triggered simultaneously when $s = 0$. The extension to multiple separate switching and reset events is straightforward [19].

To incorporate parameters λ into trajectory sensitivity analysis, the dynamic states x can be augmented by λ through the introduction of trivial differential equations $\dot{\lambda} = 0$. In this way, parameters of interest can be included in the augmented initial conditions x_0 rather than explicitly introducing them into the DAIS model.

Let τ be the junction time when a discrete event is triggered. Define τ^- and τ^+ to be the instant just prior to and just after τ, respectively. The intersection point $(x(\tau), y(\tau)) \in \mathcal{S}$ is referred to as the junction point. Based on the DAIS model, away from the junction time τ, system dynamics are governed by the differential-algebraic equation (DAE) model:

$$\dot{x} = f(x, y) \tag{2.2.2a}$$

$$0_m = g(x, y), \tag{2.2.2b}$$

where the algebraic equations g are determined by the triggering conditions.

Several important assumptions underpin trajectory sensitivity analysis. From the Implicit Function Theorem [81], if the Jacobian matrix $\partial g/\partial y$ is nonsingular then there

exists a unique (though possibly not explicit) function φ such that $y = \varphi(x)$. Substituting this function into equation (2.2.1a) gives $\dot{x} = f(x, y) = f(x, \varphi(x))$.

Assumption 1. *The algebraic Jacobian matrix $\partial g/\partial y$ is nonsingular along system trajectories.*

Other common assumptions for hybrid system analysis include:

Assumption 2. *System trajectories must be transversal to the triggering hypersurface $\mathcal{S}$.*

Assumption 3. *The triggering function $s(x, y)$ has a unique normal at points that lie on the triggering hypersurface $\mathcal{S}$.*

Assumption 4. *At a junction point $(x(\tau), y(\tau)) \in \mathcal{S}$, $s(x(\tau^-), y(\tau^-)) \times s(x(\tau^+), y(\tau^+)) < 0$.*

Assumption 2 ensures that trajectories cannot be tangential to the hypersurface $\mathcal{S}$ and so avoids situations where the event triggering time τ is infinitely sensitive to perturbations in initial conditions and/or parameters. Assumption 3 eliminates degeneracies in the triggering function. Assumption 4 eliminates switching deadlock [82]. Further details can be found in [51, 83].

Define the system trajectory (also referred to as the flow):

$$x(t) = \phi(x_0, t) \tag{2.2.3a}$$

$$y(t) = \psi(x_0, t). \tag{2.2.3b}$$

The corresponding initial conditions are given by:

$$x(t_0) = \phi(x_0, t_0) = x_0 \tag{2.2.4a}$$

$$y(t_0) = \psi(x_0, t_0) = y_0. \tag{2.2.4b}$$

Note that the system flow does not explicitly depend on y_0. This is because y_0 is implicitly related to x_0 through $g(x_0, y_0) = 0$.

2.3 First-Order Trajectory Sensitivity

This section introduces the concept of first-order trajectory sensitivities and summarizes their behavior during continuous dynamics and at discrete events.

2.3.1 Trajectory Sensitivity Analysis

Trajectory sensitivity analysis quantifies the change in the system flow when initial conditions and/or parameters are perturbed from their nominal values. Since parameters are incorporated into the dynamic states x, analyzing the sensitivity of the flow with respect to the augmented initial conditions x_0 will fully cover both initial conditions and parameters.

Taylor series expansion of the system flow (2.2.3) yields:

$$\phi_i(x_0 + \Delta x_0, t) = \phi_i(x_0, t) + \frac{\partial \phi_i(x_0, t)}{\partial x_0}\Delta x_0 + \frac{1}{2}\Delta x_0^\intercal \frac{\partial^2 \phi_i(x_0, t)}{\partial x_0^2}\Delta x_0 + \varepsilon_i^\phi(x_0, t, \Delta x_0), \tag{2.3.1a}$$

$$\psi_j(x_0 + \Delta x_0, t) = \psi_j(x_0, t) + \frac{\partial \psi_j(x_0, t)}{\partial x_0}\Delta x_0 + \frac{1}{2}\Delta x_0^\intercal \frac{\partial^2 \psi_j(x_0, t)}{\partial x_0^2}\Delta x_0 + \varepsilon_j^\psi(x_0, t, \Delta x_0), \tag{2.3.1b}$$

for $i = 1, ..., n$ and $j = 1, ..., m$. Keeping only the first-order terms of the Taylor series yields:

$$\begin{aligned}\Delta x(t) &= \phi(x_0 + \Delta x_0, t) - \phi(x_0, t) \\ &\approx \frac{\partial \phi(x_0, t)}{\partial x_0}\Delta x_0 = \frac{\partial x(t)}{\partial x_0}\Delta x_0 \triangleq x_{x_0}(t)\Delta x_0 \end{aligned} \tag{2.3.2a}$$

$$\begin{aligned}\Delta y(t) &= \psi(x_0 + \Delta x_0, t) - \psi(x_0, t) \\ &\approx \frac{\partial \psi(x_0, t)}{\partial x_0}\Delta x_0 = \frac{\partial y(t)}{\partial x_0}\Delta x_0 \triangleq y_{x_0}(t)\Delta x_0, \end{aligned} \tag{2.3.2b}$$

where $x_{x_0}(t)$ and $y_{x_0}(t)$ are the first-order trajectory sensitivities. Hence, equation (2.3.2) gives the first-order approximation for the change in the flow resulting from small perturbations Δx_0.

2.3.2 Computation of First-Order Sensitivities

The computation of first-order trajectory sensitivities for hybrid dynamical systems has been fully described in [51]. A summary of the main results is provided for completeness.

Over regions of smooth behavior between events, the system is governed by the DAE model (2.2.2). Taking the derivative of equations (2.2.2a) and (2.2.2b) with respect to x_0 gives the DAE model that describes the corresponding evolution of the first-order sensitivities:

$$\dot{x}_{x_0} = f_x(t)x_{x_0} + f_y(t)y_{x_0} \tag{2.3.3a}$$

$$0_{m\times n} = g_x(t)x_{x_0} + g_y(t)y_{x_0}, \tag{2.3.3b}$$

where $0_{m\times n}$ denotes the $(m\times n)$-matrix of zeros, and f_x, f_y, g_x, g_y denote $\partial f/\partial x$, $\partial f/\partial y$, $\partial g/\partial x$, $\partial g/\partial y$, respectively. This partial derivative notation will be used throughout the chapter. Note that these matrices are evaluated along trajectories and hence are time-varying.

The initial condition for x_{x_0} is given by $x_{x_0}(t_0) = I_n$, where I_n is the n-dimensional identity matrix. The initial condition $y_{x_0}(t_0)$ follows from equation (2.3.3b) and is given by:

$$y_{x_0}(t_0) = -g_y(t_0)^{-1} g_x(t_0). \tag{2.3.4}$$

At the instant when a discrete event is triggered, the jump conditions for first-order trajectory sensitivities are given by [51]:

$$x_{x_0}(\tau^+) = \tilde{h}_x x_{x_0}(\tau^-) - \left(f^+ - \tilde{h}_x f^-\right)\tau_{x_0}, \tag{2.3.5}$$

where $\tilde{h}_x$, τ_{x_0}, f^+, and f^- are given by:

$$\tilde{h}_x = \left(h_x - h_y(g_y)^{-1} g_x\right)\Big|_{\tau^-} \tag{2.3.6}$$

$$\tau_{x_0} = -\frac{\left(s_x - s_y(g_y)^{-1} g_x\right)\Big|_{\tau^-} x_{x_0}(\tau^-)}{\left(s_x - s_y(g_y)^{-1} g_x\right)\Big|_{\tau^-} f^-} \tag{2.3.7}$$

$$f^+ \triangleq f\left(x(\tau^+), y(\tau^+)\right) \tag{2.3.8}$$

$$f^- \triangleq f\left(x(\tau^-), y(\tau^-)\right), \tag{2.3.9}$$

and $\tau_{x_0} \triangleq \frac{\partial \tau}{\partial x_0}$ represents the dependence of the junction time τ on the initial condition x_0. It describes the variation of τ that results from a small perturbation in x_0. A graphical interpretation of equation (2.3.5) is provided in Subsection 2.5.4, where the jump conditions for first- and second-order sensitivities are compared. After $x_{x_0}(\tau^+)$ has been computed, $y_{x_0}(\tau^+)$ is given by:

$$y_{x_0}(\tau^+) = -\left(g_y^{-1} g_x\right)\Big|_{\tau^+} x_{x_0}(\tau^+). \tag{2.3.10}$$

In summary, first-order sensitivities are computed by firstly initializing $x_{x_0}(t_0)$ and $y_{x_0}(t_0)$, then numerically integrating equation (2.3.3) along with the system trajectory. If the trajectory encounters a switching hypersurface, jump conditions (2.3.5), (2.3.10) determine the corresponding change in x_{x_0}, y_{x_0}. The post-event sensitivities $x_{x_0}(\tau^+)$, $y_{x_0}(\tau^+)$ then serve as initial conditions for equation (2.3.3), which is integrated over the subsequent section of smooth behavior.

2.4 Second-Order Sensitivity Away from Events

Like any linearization, first-order trajectory sensitivities may lose accuracy when higher-order nonlinearities become dominant. In such cases, accuracy can be improved by considering the second-order trajectory sensitivities in equation (2.3.1), i.e., the terms,

$$\frac{\partial^2 \phi_i(x_0, t)}{\partial x_0^2} \triangleq \frac{\partial^2 x_i(t)}{\partial x_0^2}, \qquad \forall i = 1, ..., n, \tag{2.4.1a}$$

$$\frac{\partial^2 \psi_j(x_0, t)}{\partial x_0^2} \triangleq \frac{\partial^2 y_j(t)}{\partial x_0^2}, \qquad \forall j = 1, ..., m. \tag{2.4.1b}$$

This section derives the DAE model that governs the evolution of second-order sensitivities when the underlying dynamics are smooth. The behavior of second-order sensitivities at discrete events is derived in Section 2.5.

2.4.1 Second-Order Sensitivities for Smooth Dynamics

Away from events, system dynamics are governed by the DAE model (2.2.2). Differentiating equation (2.2.2a) with respect to x_0 results in equation (2.3.3a) which can be written,

$$\frac{d}{dt}\Big(\frac{\partial x_k}{\partial x_0}\Big) = \sum_{i=1}^{n} \frac{\partial f_k}{\partial x_i}\frac{\partial x_i}{\partial x_0} + \sum_{j=1}^{m} \frac{\partial f_k}{\partial y_j}\frac{\partial y_j}{\partial x_0},$$

for $k = 1, ..., n$. Transposing this equation and taking partial derivatives with respect to x_0 gives,

$$\begin{aligned}
\frac{d}{dt}\Big(\frac{\partial^2 x_k}{\partial x_0^2}\Big) &= \frac{\partial}{\partial x_0}\Big(\sum_{i=1}^{n} \frac{\partial f_k}{\partial x_i}\frac{\partial x_i}{\partial x_0}^{\top} + \sum_{j=1}^{m} \frac{\partial f_k}{\partial y_j}\frac{\partial y_j}{\partial x_0}^{\top}\Big) \\
&= \sum_{i=1}^{n} \frac{\partial}{\partial x_0}\Big(\frac{\partial f_k}{\partial x_i}\frac{\partial x_i}{\partial x_0}^{\top}\Big) + \sum_{j=1}^{m} \frac{\partial}{\partial x_0}\Big(\frac{\partial f_k}{\partial y_j}\frac{\partial y_j}{\partial x_0}^{\top}\Big) \\
&= \sum_{i=1}^{n} \Big(\frac{\partial x_i}{\partial x_0}^{\top}\frac{\partial}{\partial x_0}\Big(\frac{\partial f_k}{\partial x_i}\Big) + \frac{\partial f_k}{\partial x_i}\frac{\partial^2 x_i}{\partial x_0^2}\Big) + \sum_{j=1}^{m} \Big(\frac{\partial y_j}{\partial x_0}^{\top}\frac{\partial}{\partial x_0}\Big(\frac{\partial f_k}{\partial y_j}\Big) + \frac{\partial f_k}{\partial y_j}\frac{\partial^2 y_j}{\partial x_0^2}\Big),
\end{aligned} \tag{2.4.2}$$

for $k = 1, ..., n$. The terms $\frac{\partial}{\partial x_0}\Big(\frac{\partial f_k}{\partial x_i}\Big)$ and $\frac{\partial}{\partial x_0}\Big(\frac{\partial f_k}{\partial y_j}\Big)$ in equation (2.4.2) can be expanded as:

$$\frac{\partial}{\partial x_0}\Big(\frac{\partial f_k}{\partial x_i}\Big) = \frac{\partial^2 f_k}{\partial x_i \partial x}\frac{\partial x}{\partial x_0} + \frac{\partial^2 f_k}{\partial x_i \partial y}\frac{\partial y}{\partial x_0}, \tag{2.4.3a}$$

$$\frac{\partial}{\partial x_0}\Big(\frac{\partial f_k}{\partial y_j}\Big) = \frac{\partial^2 f_k}{\partial y_j \partial x}\frac{\partial x}{\partial x_0} + \frac{\partial^2 f_k}{\partial y_j \partial y}\frac{\partial y}{\partial x_0}. \tag{2.4.3b}$$

Similarly, differentiating equation (2.2.2b) with respect to x_0 results in equation (2.3.3b), which can be written,

$$\sum_{i=1}^{n} \frac{\partial g_l}{\partial x_i}\frac{\partial x_i}{\partial x_0} + \sum_{j=1}^{m} \frac{\partial g_l}{\partial y_j}\frac{\partial y_j}{\partial x_0} = 0_n^\intercal,$$

for $l = 1, ..., m$. Transposing this equation and taking partial derivatives with respect to x_0 gives,

$$\begin{aligned} 0_{n\times n} &= \frac{\partial}{\partial x_0}\Big(\sum_{i=1}^{n} \frac{\partial g_l}{\partial x_i}\frac{\partial x_i}{\partial x_0}^\intercal + \sum_{j=1}^{m} \frac{\partial g_l}{\partial y_j}\frac{\partial y_j}{\partial x_0}^\intercal\Big) \\ &= \sum_{i=1}^{n} \frac{\partial}{\partial x_0}\Big(\frac{\partial g_l}{\partial x_i}\frac{\partial x_i}{\partial x_0}^\intercal\Big) + \sum_{j=1}^{m} \frac{\partial}{\partial x_0}\Big(\frac{\partial g_l}{\partial y_j}\frac{\partial y_j}{\partial x_0}^\intercal\Big) \\ &= \sum_{i=1}^{n} \Big(\frac{\partial x_i}{\partial x_0}^\intercal \frac{\partial}{\partial x_0}\Big(\frac{\partial g_l}{\partial x_i}\Big) + \frac{\partial g_l}{\partial x_i}\frac{\partial^2 x_i}{\partial x_0^2}\Big) + \sum_{j=1}^{m} \Big(\frac{\partial y_j}{\partial x_0}^\intercal \frac{\partial}{\partial x_0}\Big(\frac{\partial g_l}{\partial y_j}\Big) + \frac{\partial g_l}{\partial y_j}\frac{\partial^2 y_j}{\partial x_0^2}\Big), \end{aligned} \tag{2.4.4}$$

for $l = 1, ..., m$. The terms $\frac{\partial}{\partial x_0}\Big(\frac{\partial g_l}{\partial x_i}\Big)$ and $\frac{\partial}{\partial x_0}\Big(\frac{\partial g_l}{\partial y_j}\Big)$ in equation (2.4.4) can be expanded as:

$$\frac{\partial}{\partial x_0}\Big(\frac{\partial g_l}{\partial x_i}\Big) = \frac{\partial^2 g_l}{\partial x_i \partial x}\frac{\partial x}{\partial x_0} + \frac{\partial^2 g_l}{\partial x_i \partial y}\frac{\partial y}{\partial x_0}, \tag{2.4.5a}$$

$$\frac{\partial}{\partial x_0}\Big(\frac{\partial g_l}{\partial y_j}\Big) = \frac{\partial^2 g_l}{\partial y_j \partial x}\frac{\partial x}{\partial x_0} + \frac{\partial^2 g_l}{\partial y_j \partial y}\frac{\partial y}{\partial x_0}. \tag{2.4.5b}$$

Substituting equation (2.4.3) into equation (2.4.2) and equation (2.4.5) into equation (2.4.4) results in the DAE model for the second-order sensitivities,

$$\begin{aligned} \frac{d}{dt}\Big(\frac{\partial^2 x_k}{\partial x_0^2}\Big) = \frac{\partial x}{\partial x_0}^\intercal \Big(\frac{\partial^2 f_k}{\partial x^2}\frac{\partial x}{\partial x_0} + \frac{\partial^2 f_k}{\partial x \partial y}\frac{\partial y}{\partial x_0}\Big) + \frac{\partial y}{\partial x_0}^\intercal \Big(\frac{\partial^2 f_k}{\partial y \partial x}\frac{\partial x}{\partial x_0} + \frac{\partial^2 f_k}{\partial y^2}\frac{\partial y}{\partial x_0}\Big) \\ + \sum_{i=1}^{n} \frac{\partial f_k}{\partial x_i}\frac{\partial^2 x_i}{\partial x_0^2} + \sum_{j=1}^{m} \frac{\partial f_k}{\partial y_j}\frac{\partial^2 y_j}{\partial x_0^2}, \end{aligned} \tag{2.4.6a}$$

for $k = 1, ..., n$ and,

$$0_{n\times n} = \frac{\partial x}{\partial x_0}^\intercal \Big(\frac{\partial^2 g_l}{\partial x^2}\frac{\partial x}{\partial x_0} + \frac{\partial^2 g_l}{\partial x \partial y}\frac{\partial y}{\partial x_0}\Big) + \frac{\partial y}{\partial x_0}^\intercal \Big(\frac{\partial^2 g_l}{\partial y \partial x}\frac{\partial x}{\partial x_0} + \frac{\partial^2 g_l}{\partial y^2}\frac{\partial y}{\partial x_0}\Big)$$

$$+ \sum_{i=1}^{n} \frac{\partial g_l}{\partial x_i} \frac{\partial^2 x_i}{\partial x_0^2} + \sum_{j=1}^{m} \frac{\partial g_l}{\partial y_j} \frac{\partial^2 y_j}{\partial x_0^2}, \tag{2.4.6b}$$

for $l = 1, ..., m$.

This DAE model can be expressed more compactly by defining,

$$\frac{\partial^2 x}{\partial x_0^2} \triangleq \begin{bmatrix} \frac{\partial^2 x_1}{\partial x_0^2} \\ \vdots \\ \frac{\partial^2 x_n}{\partial x_0^2} \end{bmatrix}, \quad \frac{\partial^2 y}{\partial x_0^2} \triangleq \begin{bmatrix} \frac{\partial^2 y_1}{\partial x_0^2} \\ \vdots \\ \frac{\partial^2 y_m}{\partial x_0^2} \end{bmatrix},$$

and arranging n copies of $\frac{\partial x}{\partial x_0}$ according to,

$$\operatorname{diag}_n\Big(\frac{\partial x}{\partial x_0}\Big) \triangleq \begin{bmatrix} \frac{\partial x}{\partial x_0} & & \\ & \ddots & \\ & & \frac{\partial x}{\partial x_0} \end{bmatrix} = I_n \otimes \frac{\partial x}{\partial x_0},$$

$$\operatorname{vec}_n\Big(\frac{\partial x}{\partial x_0}\Big) \triangleq \begin{bmatrix} \frac{\partial x}{\partial x_0} \\ \vdots \\ \frac{\partial x}{\partial x_0} \end{bmatrix} = 1_n \otimes \frac{\partial x}{\partial x_0},$$

where I_n is the n-dimensional identity matrix, 1_n is the n-dimensional vector of 1s, and $\otimes$ denotes the Kronecker product. The matrices $\operatorname{diag}_m\Big(\frac{\partial x}{\partial x_0}\Big)$ and $\operatorname{vec}_m\Big(\frac{\partial x}{\partial x_0}\Big)$ are defined similarly, along with the "diag" and "vec" versions of $\frac{\partial y}{\partial x_0}$. Also define,

$$\frac{\partial^2 f}{\partial x^2} \triangleq \begin{bmatrix} \frac{\partial^2 f_1}{\partial x^2} & & \\ & \ddots & \\ & & \frac{\partial^2 f_n}{\partial x^2} \end{bmatrix}, \quad \frac{\partial^2 f}{\partial x \partial y} \triangleq \begin{bmatrix} \frac{\partial^2 f_1}{\partial x \partial y} & & \\ & \ddots & \\ & & \frac{\partial^2 f_n}{\partial x \partial y} \end{bmatrix},$$

and likewise $\frac{\partial^2 f}{\partial y \partial x}$, $\frac{\partial^2 f}{\partial y^2}$, and the second-order partial derivatives of g. Then the DAE model (2.4.6) can be written compactly as,

$$\begin{aligned} \frac{d}{dt}\Big(\frac{\partial^2 x}{\partial x_0^2}\Big) = {} & \operatorname{diag}_n\Big(\frac{\partial x}{\partial x_0}\Big)^{\mathsf{T}}\Big(\frac{\partial^2 f}{\partial x^2}\operatorname{vec}_n\Big(\frac{\partial x}{\partial x_0}\Big) + \frac{\partial^2 f}{\partial x \partial y}\operatorname{vec}_n\Big(\frac{\partial y}{\partial x_0}\Big)\Big) \\ & + \operatorname{diag}_n\Big(\frac{\partial y}{\partial x_0}\Big)^{\mathsf{T}}\Big(\frac{\partial^2 f}{\partial y \partial x}\operatorname{vec}_n\Big(\frac{\partial x}{\partial x_0}\Big) + \frac{\partial^2 f}{\partial y^2}\operatorname{vec}_n\Big(\frac{\partial y}{\partial x_0}\Big)\Big) \\ & + \Big(\frac{\partial f}{\partial x} \otimes I_n\Big)\frac{\partial^2 x}{\partial x_0^2} + \Big(\frac{\partial f}{\partial y} \otimes I_n\Big)\frac{\partial^2 y}{\partial x_0^2}, \end{aligned} \tag{2.4.7a}$$

and

$$
\begin{aligned}
0_{nm\times n} = \operatorname{diag}_m\Big(\frac{\partial x}{\partial x_0}\Big)^\intercal\Big(\frac{\partial^2 g}{\partial x^2}\operatorname{vec}_m\Big(\frac{\partial x}{\partial x_0}\Big) + \frac{\partial^2 g}{\partial x \partial y}\operatorname{vec}_m\Big(\frac{\partial y}{\partial x_0}\Big)\Big) \\
+ \operatorname{diag}_m\Big(\frac{\partial y}{\partial x_0}\Big)^\intercal\Big(\frac{\partial^2 g}{\partial y \partial x}\operatorname{vec}_m\Big(\frac{\partial x}{\partial x_0}\Big) + \frac{\partial^2 g}{\partial y^2}\operatorname{vec}_m\Big(\frac{\partial y}{\partial x_0}\Big)\Big) \\
+ \Big(\frac{\partial g}{\partial x}\otimes I_n\Big)\frac{\partial^2 x}{\partial x_0^2} + \Big(\frac{\partial g}{\partial y}\otimes I_n\Big)\frac{\partial^2 y}{\partial x_0^2},
\end{aligned} \tag{2.4.7b}
$$

where $0_{nm\times n}$ refers to the $(nm \times n)$-matrix of zeros. Initialization is given by $\frac{\partial^2 x}{\partial x_0^2}(t_0) = 0_{n^2\times n}$ and solving equation (2.4.7b) at t_0 for $\frac{\partial^2 y}{\partial x_0^2}(t_0)$. By Assumption 1, $\frac{\partial g}{\partial y}$ is nonsingular, therefore $\frac{\partial g}{\partial y}\otimes I_n$ is also nonsingular. Hence, equation (2.4.7b) is solvable.

2.4.2 Computation

The DAE model (2.4.7) consists of n^3 differential equations governing the n matrix variables $\frac{\partial^2 x_i}{\partial x_0^2}$ together with $n^2 m$ algebraic equations that couple the m matrix variables $\frac{\partial^2 y_j}{\partial x_0^2}$. Fortunately, the computational cost of evaluating this model along trajectories can be reduced significantly by exploiting the problem structure. If trapezoidal integration is used to simulate equation (2.4.7) then stepping from time-step t to time-step $t+1$, with time-step length h, involves solving the linear matrix equation,

$$
\begin{bmatrix}
\frac{h}{2}\Big(\frac{\partial f}{\partial x}\otimes I_n\Big) - I_{n^2} & \frac{h}{2}\Big(\frac{\partial f}{\partial y}\otimes I_n\Big) \\
\frac{\partial g}{\partial x}\otimes I_n & \frac{\partial g}{\partial y}\otimes I_n
\end{bmatrix}
\begin{bmatrix}
\frac{\partial^2 x}{\partial x_0^2}(t+1) \\
\frac{\partial^2 y}{\partial x_0^2}(t+1)
\end{bmatrix} =
$$

$$
\begin{bmatrix}
F_1\Big(x(t+1), y(t+1), x_{x_0}(t+1), y_{x_0}(t+1), \\
\quad x(t), y(t), x_{x_0}(t), y_{x_0}(t), \frac{\partial^2 x}{\partial x_0^2}(t), \frac{\partial^2 y}{\partial x_0^2}(t)\Big) \\
F_2\Big(x(t+1), y(t+1), x_{x_0}(t+1), y_{x_0}(t+1)\Big)
\end{bmatrix}, \tag{2.4.8}
$$

where the matrix on the left is evaluated at $t+1$, and F_1, F_2 follow directly from the trapezoidal rule. Solution for the unknowns $\frac{\partial^2 x}{\partial x_0^2}(t+1)$, $\frac{\partial^2 y}{\partial x_0^2}(t+1)$ can be achieved by decomposing the matrix on the left into its LU factors and performing forward and backward substitution. Notice though that,

$$
\begin{bmatrix}
\frac{h}{2}\Big(\frac{\partial f}{\partial x}\otimes I_n\Big) - I_{n^2} & \frac{h}{2}\Big(\frac{\partial f}{\partial y}\otimes I_n\Big) \\
\frac{\partial g}{\partial x}\otimes I_n & \frac{\partial g}{\partial y}\otimes I_n
\end{bmatrix} =
\begin{bmatrix}
\Big(\frac{h}{2}\frac{\partial f}{\partial x} - I_n\Big)\otimes I_n & \Big(\frac{h}{2}\frac{\partial f}{\partial y}\Big)\otimes I_n \\
\frac{\partial g}{\partial x}\otimes I_n & \frac{\partial g}{\partial y}\otimes I_n
\end{bmatrix} =
\begin{bmatrix}
\frac{h}{2}\frac{\partial f}{\partial x} - I_n & \frac{h}{2}\frac{\partial f}{\partial y} \\
\frac{\partial g}{\partial x} & \frac{\partial g}{\partial y}
\end{bmatrix}\otimes I_n. \tag{2.4.9}
$$

As shown in [51], the LU factors of the matrix on the left of the Kronecker product in equation (2.4.9) are already available as a by-product of computing the nominal trajectory, and are also used in computing the first-order sensitivities. Hence, the LU factors required for solving equation (2.4.8) can be built very efficiently. The computational cost of solving for the second-order sensitivities is therefore effectively reduced to the cost of forward and backward substitution of this very sparse problem.

2.4.3 Comparison with Prior Work

A DAE model for second-order sensitivities of continuous systems was derived in [60]. A comparison with the model developed in Subsection 2.4.1 is quite informative.

A slightly different formulation was adopted in [60]. Instead of capturing all initial conditions and parameters in x_0, that work defined a new variable u which includes all the parameters and inputs of the system. It should be noted that although the structure of the results in [60] is correct, there are two missing x–y cross-terms in the resulting DAE models (17),(19) of [60]. This can be seen from (37),(38),(40),(41) in Appendix A of [60]. Considering (37) for example, the two missing terms are $\sum_{m=1}^{D}\sum_{j=1}^{A}\frac{\partial^2 g_k}{\partial x_m \partial y_j}\frac{\partial y_j}{\partial u_i}\frac{\partial x_m}{\partial u_i}$ and $\sum_{m=1}^{A}\sum_{j=1}^{D}\frac{\partial^2 g_k}{\partial y_m \partial x_j}\frac{\partial x_j}{\partial u_i}\frac{\partial y_m}{\partial u_i}$.

The formulation developed in Subsection 2.4.1 will be compared with the corrected version of [60]. To do so, the results from [60] are translated by taking $u = x_0$ and adopting the notation of Subsection 2.4.1. The corrected DAE model given by [60] for second-order sensitivities can then be expressed as,

$$\begin{aligned}\frac{d}{dt}\left(\frac{\partial^2 x_k}{\partial x_{0p}^2}\right) = &\sum_{i=1}^{n}\left(\sum_{j=1}^{n}\frac{\partial^2 f_k}{\partial x_i \partial x_j}\frac{\partial x_j}{\partial x_{0p}}\frac{\partial x_i}{\partial x_{0p}} + \sum_{j=1}^{m}\frac{\partial^2 f_k}{\partial x_i \partial y_j}\frac{\partial y_j}{\partial x_{0p}}\frac{\partial x_i}{\partial x_{0p}} + \frac{\partial f_k}{\partial x_i}\frac{\partial^2 x_i}{\partial x_{0p}^2}\right)\\ &+\sum_{i=1}^{m}\left(\sum_{j=1}^{n}\frac{\partial^2 f_k}{\partial y_i \partial x_j}\frac{\partial x_j}{\partial x_{0p}}\frac{\partial y_i}{\partial x_{0p}} + \sum_{j=1}^{m}\frac{\partial^2 f_k}{\partial y_i \partial y_j}\frac{\partial y_j}{\partial x_{0p}}\frac{\partial y_i}{\partial x_{0p}} + \frac{\partial f_k}{\partial y_i}\frac{\partial^2 y_i}{\partial x_{0p}^2}\right),\end{aligned} \tag{2.4.10a}$$

for $k = 1, ..., n$ and $p = 1, ..., n$;

$$\begin{aligned}\frac{d}{dt}\left(\frac{\partial^2 x_k}{\partial x_{0p}\partial x_{0q}}\right) = &\sum_{i=1}^{n}\left(\sum_{j=1}^{n}\frac{\partial^2 f_k}{\partial x_i \partial x_j}\frac{\partial x_j}{\partial x_{0q}}\frac{\partial x_i}{\partial x_{0p}} + \sum_{j=1}^{m}\frac{\partial^2 f_k}{\partial x_i \partial y_j}\frac{\partial y_j}{\partial x_{0q}}\frac{\partial x_i}{\partial x_{0p}} + \frac{\partial f_k}{\partial x_i}\frac{\partial^2 x_i}{\partial x_{0p}\partial x_{0q}}\right)\\ &+\sum_{i=1}^{m}\left(\sum_{j=1}^{n}\frac{\partial^2 f_k}{\partial y_i \partial x_j}\frac{\partial x_j}{\partial x_{0q}}\frac{\partial y_i}{\partial x_{0p}} + \sum_{j=1}^{m}\frac{\partial^2 f_k}{\partial y_i \partial y_j}\frac{\partial y_j}{\partial x_{0q}}\frac{\partial y_i}{\partial x_{0p}} + \frac{\partial f_k}{\partial y_i}\frac{\partial^2 y_i}{\partial x_{0p}\partial x_{0q}}\right),\end{aligned} \tag{2.4.10b}$$

for $k = 1, ..., n$, $p = 1, ..., n$ and $q = 1, ..., n$;

$$0 = \sum_{i=1}^{n}\Big(\sum_{j=1}^{n}\frac{\partial^2 g_l}{\partial x_i \partial x_j}\frac{\partial x_j}{\partial x_{0p}}\frac{\partial x_i}{\partial x_{0p}} + \sum_{j=1}^{m}\frac{\partial^2 g_l}{\partial x_i \partial y_j}\frac{\partial y_j}{\partial x_{0p}}\frac{\partial x_i}{\partial x_{0p}} + \frac{\partial g_l}{\partial x_i}\frac{\partial^2 x_i}{\partial x_{0p}^2}\Big)$$
$$+ \sum_{i=1}^{m}\Big(\sum_{j=1}^{n}\frac{\partial^2 g_l}{\partial y_i \partial x_j}\frac{\partial x_j}{\partial x_{0p}}\frac{\partial y_i}{\partial x_{0p}} + \sum_{j=1}^{m}\frac{\partial^2 g_l}{\partial y_i \partial y_j}\frac{\partial y_j}{\partial x_{0p}}\frac{\partial y_i}{\partial x_{0p}} + \frac{\partial g_l}{\partial y_i}\frac{\partial^2 y_i}{\partial x_{0p}^2}\Big), \tag{2.4.10c}$$

for $l = 1, ..., m$ and $p = 1, ..., n$;

$$0 = \sum_{i=1}^{n}\Big(\sum_{j=1}^{n}\frac{\partial^2 g_l}{\partial x_i \partial x_j}\frac{\partial x_j}{\partial x_{0q}}\frac{\partial x_i}{\partial x_{0p}} + \sum_{j=1}^{m}\frac{\partial^2 g_l}{\partial x_i \partial y_j}\frac{\partial y_j}{\partial x_{0q}}\frac{\partial x_i}{\partial x_{0p}} + \frac{\partial g_l}{\partial x_i}\frac{\partial^2 x_i}{\partial x_{0p}\partial x_{0q}}\Big)$$
$$+ \sum_{i=1}^{m}\Big(\sum_{j=1}^{n}\frac{\partial^2 g_l}{\partial y_i \partial x_j}\frac{\partial x_j}{\partial x_{0q}}\frac{\partial y_i}{\partial x_{0p}} + \sum_{j=1}^{m}\frac{\partial^2 g_l}{\partial y_i \partial y_j}\frac{\partial y_j}{\partial x_{0q}}\frac{\partial y_i}{\partial x_{0p}} + \frac{\partial g_l}{\partial y_i}\frac{\partial^2 y_i}{\partial x_{0p}\partial x_{0q}}\Big), \tag{2.4.10d}$$

for $l = 1, ..., m$, $p = 1, ..., n$, and $q = 1, ..., n$.

A comparison of equation (2.4.6) and equation (2.4.10) indicates that they are equivalent, with the only difference being that equation (2.4.6) is expressed in matrix form.

2.5 Second-Order Sensitivity at Discrete Events

To fully characterize the evolution of second-order sensitivities in hybrid dynamical systems, jump conditions governing their step change at a discrete event must be established. This derivation is more involved than that of the smooth DAE model developed in Section 2.4.

2.5.1 Second-Order Dependence of Switching Time

The time at which a discrete event is triggered, i.e., when the trajectory encounters the switching hypersurface, is given by the switching time τ. Generally, if x_0 is perturbed slightly then τ will change accordingly. The first step in deriving the jump conditions for the second-order sensitivities is to determine the (second-order) dependence of τ on x_0, denoted $\frac{\partial^2 \tau}{\partial x_0^2}$.

Consider the time instant $\tau^- < \tau$ incrementally prior to event triggering, where:

$$x^- \triangleq x(\tau^-) = \phi(x_0, \tau^-) \tag{2.5.1a}$$
$$y^- \triangleq y(\tau^-) = \psi(x_0, \tau^-) \tag{2.5.1b}$$

$$g(x^-, y^-) = 0_m, \tag{2.5.1c}$$

and the triggering condition is satisfied in the limit:

$$s(x^-, y^-) = 0. \tag{2.5.2}$$

Assumption 1 guarantees that $\partial g/\partial y$ is nonsingular along system trajectories, so the Implicit Function Theorem ensures the existence of a unique function φ such that $y = \varphi(x)$. Substituting this function into equation (2.5.2) gives,

$$\tilde{s}(x^-) \triangleq s\Big(x^-, \varphi(x^-)\Big), \tag{2.5.3}$$

allowing the triggering condition (2.5.2) to be expressed as,

$$\tilde{s}(x^-) = 0. \tag{2.5.4}$$

The reduced function $\tilde{s}(\cdot)$ will be used in the following analysis to simplify notation. The connection back to $s(\cdot,\cdot)$ is established in Subsection 2.5.3.

Differentiating equation (2.5.1a) gives,

$$\frac{dx^-}{dx_0} = \Big(\frac{\partial x}{\partial x_0} + \frac{\partial x}{\partial \tau}\frac{\partial \tau}{\partial x_0}\Big)\Big|_{\tau^-}, \tag{2.5.5}$$

where from equation (2.3.2a), $\frac{\partial x}{\partial x_0} \triangleq x_{x_0}$ is the first-order trajectory sensitivity matrix. The perturbation dx^- should be interpreted as the change in the state x along the triggering hypersurface $\mathcal{S}$ when x_0 is perturbed. A graphical interpretation of the difference between $\frac{dx^-}{dx_0}$ and $\frac{\partial x^-}{\partial x_0}$ is provided in Fig. 2.1.

From equation (2.2.1a),

$$\frac{\partial x}{\partial \tau}\Big|_{\tau^-} = \dot{x}(\tau^-) = f\Big(x(\tau^-), y(\tau^-)\Big) = f(x^-, y^-) \triangleq f^-.$$

Substituting into equation (2.5.5) gives,

$$\frac{dx^-}{dx_0} = \frac{\partial x^-}{\partial x_0} + f^-\frac{\partial \tau}{\partial x_0}\Big|_{\tau^-}. \tag{2.5.6}$$

Differentiating equation (2.5.4) with respect to x_0 gives,

$$\frac{d\tilde{s}}{dx_0}\Big|_{\tau^-} = \Big(\frac{\partial \tilde{s}}{\partial x}\frac{dx}{dx_0}\Big)\Big|_{\tau^-} = 0_n^\intercal. \tag{2.5.7}$$

The switching-time sensitivity $\frac{\partial \tau}{\partial x_0}$ given by equation (2.3.7) follows by substituting equation (2.5.6) into equation (2.5.7).

The second-order sensitivity $\frac{d^2\tilde{s}}{dx_0^2}$ can be obtained by taking the derivative of the transpose of equation (2.5.7) with respect to x_0. In doing so, all quantities refer to time τ^-, though for notational convenience this dependence is not explicitly shown. Consequently,

$$
\begin{aligned}
0_{n\times n} &= \frac{d^2\tilde{s}}{dx_0^2}\Big|_{\tau^-} = \frac{d}{dx_0}\Big(\Big(\frac{\partial \tilde{s}}{\partial x}\frac{dx}{dx_0}\Big)^\intercal\Big)\Big|_{\tau^-} = \frac{d}{dx_0}\Big(\sum_{i=1}^{n}\frac{\partial \tilde{s}}{\partial x_i}\frac{dx_i^-}{dx_0}^\intercal\Big) = \sum_{i=1}^{n}\frac{d}{dx_0}\Big(\frac{\partial \tilde{s}}{\partial x_i}\frac{dx_i^-}{dx_0}^\intercal\Big) \\
&= \sum_{i=1}^{n}\frac{dx_i^-}{dx_0}^\intercal\frac{d}{dx_0}\Big(\frac{\partial \tilde{s}}{\partial x_i}\Big) + \sum_{i=1}^{n}\frac{\partial \tilde{s}}{\partial x_i}\frac{d}{dx_0}\Big(\frac{dx_i^-}{dx_0}^\intercal\Big) \\
&= \sum_{i=1}^{n}\frac{dx_i^-}{dx_0}^\intercal\frac{\partial^2 \tilde{s}}{\partial x_i \partial x}\frac{dx^-}{dx_0} + \sum_{i=1}^{n}\frac{\partial \tilde{s}}{\partial x_i}\frac{d}{dx_0}\Big(\frac{\partial x_i^-}{\partial x_0}^\intercal + f_i^-\frac{\partial \tau}{\partial x_0}^\intercal\Big) \\
&= \frac{dx^-}{dx_0}^\intercal\frac{\partial^2 \tilde{s}}{\partial x^2}\frac{dx^-}{dx_0} + \sum_{i=1}^{n}\frac{\partial \tilde{s}}{\partial x_i}\frac{\partial}{\partial x_0}\Big(\frac{\partial x_i^-}{\partial x_0}^\intercal + f_i^-\frac{\partial \tau}{\partial x_0}^\intercal\Big) + \sum_{i=1}^{n}\frac{\partial \tilde{s}}{\partial x_i}\frac{\partial}{\partial \tau}\Big(\frac{\partial x_i^-}{\partial x_0}^\intercal + f_i^-\frac{\partial \tau}{\partial x_0}^\intercal\Big)\frac{\partial \tau}{\partial x_0} \\
&= \frac{dx^-}{dx_0}^\intercal\frac{\partial^2 \tilde{s}}{\partial x^2}\frac{dx^-}{dx_0} + \sum_{i=1}^{n}\frac{\partial \tilde{s}}{\partial x_i}\Big(\frac{\partial^2 x_i^-}{\partial x_0^2} + \frac{\partial \tau}{\partial x_0}^\intercal\frac{\partial f_i^-}{\partial x_0} + f_i^-\frac{\partial^2 \tau}{\partial x_0^2}\Big) \\
&\quad + \sum_{i=1}^{n}\frac{\partial \tilde{s}}{\partial x_i}\Big(\frac{\partial}{\partial \tau}\Big(\frac{\partial x_i^-}{\partial x_0}\Big)^\intercal + \frac{\partial \tau}{\partial x_0}^\intercal\frac{\partial f_i^-}{\partial \tau} + f_i^-\frac{\partial}{\partial \tau}\Big(\frac{\partial \tau}{\partial x_0}\Big)^\intercal\Big)\frac{\partial \tau}{\partial x_0},
\end{aligned}
\tag{2.5.8}
$$

where

$$
\frac{\partial f^-}{\partial x_0} = \frac{\partial f^-}{\partial x}\frac{\partial x^-}{\partial x_0} + \frac{\partial f^-}{\partial y}\frac{\partial y^-}{\partial x_0} \tag{2.5.9}
$$

and

$$
\frac{\partial f^-}{\partial \tau} = \frac{\partial f^-}{\partial x}\frac{\partial x^-}{\partial \tau} + \frac{\partial f^-}{\partial y}\frac{\partial y^-}{\partial \tau}. \tag{2.5.10}
$$

Referring to equation (2.5.9), note that $\frac{\partial x^-}{\partial x_0} \triangleq x_{x_0}^-$ and $\frac{\partial y^-}{\partial x_0} \triangleq y_{x_0}^-$ are the trajectory sensitivities evaluated at time τ^-, so equation (2.3.3a) gives,

$$
\frac{\partial f^-}{\partial x_0} = \dot{x}_{x_0}(\tau^-) = \frac{\partial}{\partial \tau}\Big(\frac{\partial x^-}{\partial x_0}\Big). \tag{2.5.11}
$$

Equation (2.5.10) can be expressed in a form that eliminates $\frac{\partial y^-}{\partial \tau}$ by differentiating equation (2.5.1c) with respect to τ, rearranging and substituting to give,

$$
\frac{\partial f^-}{\partial \tau} = \Big(\frac{\partial f^-}{\partial x} - \frac{\partial f^-}{\partial y}\Big(\frac{\partial g^-}{\partial y}\Big)^{-1}\frac{\partial g^-}{\partial x}\Big)f^-, \tag{2.5.12}
$$

where by definition $\frac{\partial x^-}{\partial \tau} = f^-$. Lastly, equation (2.5.4) can be written $\tilde{s}\Big(\phi(x_0, \tau^-)\Big) = 0$, so by the Implicit Function Theorem, τ^- is a function only of x_0. Hence, $\frac{\partial}{\partial \tau}\Big(\frac{\partial \tau^-}{\partial x_0}\Big) = 0_n^\intercal$.

Therefore equation (2.5.8) can be written,

$$\frac{dx^-}{dx_0}^\intercal \frac{\partial^2 \tilde{s}}{\partial x^2} \frac{dx^-}{dx_0} + \sum_{i=1}^{n} \frac{\partial \tilde{s}}{\partial x_i} \frac{d^2 x_i^-}{dx_0^2} = 0_{n \times n}, \tag{2.5.13}$$

where,

$$\frac{d^2 x_i^-}{dx_0^2} = \frac{\partial^2 x_i^-}{\partial x_0^2} + \frac{\partial \tau}{\partial x_0}^\intercal \frac{\partial f_i^-}{\partial x_0} + \frac{\partial f_i^-}{\partial x_0}^\intercal \frac{\partial \tau}{\partial x_0} + \frac{\partial \tau}{\partial x_0}^\intercal \frac{\partial f_i^-}{\partial \tau} \frac{\partial \tau}{\partial x_0} + f_i^- \frac{\partial^2 \tau}{\partial x_0^2}. \tag{2.5.14}$$

Note that equation (2.5.13) can also be obtained by substituting,

$$\Delta_2 x_i^- = \frac{dx_i^-}{dx_0} \Delta x_0 + \frac{1}{2} \Delta x_0^\intercal \frac{d^2 x_i^-}{dx_0^2} \Delta x_0,$$

into

$$\Delta \tilde{s} = \frac{\partial \tilde{s}}{\partial x} \Delta_2 x^- + \frac{1}{2} \Delta_2 x^-{}^\intercal \frac{\partial^2 \tilde{s}}{\partial x^2} \Delta_2 x^- = 0,$$

and ignoring terms where the order of Δx_0 is higher than two.

Rearranging equations (2.5.13), (2.5.14) gives:

$$\frac{\partial^2 \tau}{\partial x_0^2}(\tau^-) = -\frac{\text{num}}{\frac{\partial \tilde{s}}{\partial x} f^-} \tag{2.5.15}$$

where

$$\text{num} = \frac{dx^-}{dx_0}^\intercal \frac{\partial^2 \tilde{s}}{\partial x^2} \frac{dx^-}{dx_0} + \sum_{i=1}^{n} \frac{\partial \tilde{s}}{\partial x_i} \Big(\frac{\partial^2 x_i^-}{\partial x_0^2} + \frac{\partial \tau}{\partial x_0}^\intercal \frac{\partial f_i^-}{\partial x_0} + \frac{\partial f_i^-}{\partial x_0}^\intercal \frac{\partial \tau}{\partial x_0} + \frac{\partial \tau}{\partial x_0}^\intercal \frac{\partial f_i^-}{\partial \tau} \frac{\partial \tau}{\partial x_0} \Big), \tag{2.5.16}$$

and all terms are evaluated at τ^-. This second-order dependence of the junction time τ on x_0 is used in the following subsection to establish the desired second-order jump conditions. The remaining two undefined terms in equations (2.5.15), (2.5.16), $\frac{\partial \tilde{s}}{\partial x}$ and $\frac{\partial^2 \tilde{s}}{\partial x^2}$, are derived in Subsection 2.5.3.

2.5.2 Jump Conditions for Second-Order Sensitivities

Analysis proceeds by deriving the jump conditions that govern the step change in second-order sensitivities at discrete events. This derivation is based on a comparison of equation (2.5.14), which corresponds to time instant $\tau^- < \tau$ just prior to event triggering, with

the equivalent term $\frac{d^2x_i^+}{dx_0^2}$ at time instant $\tau^+ > \tau$ immediately following event triggering. In this latter case,

$$x^+ \triangleq x(\tau^+) = \phi(x_0, \tau^+) \tag{2.5.17a}$$

$$y^+ \triangleq y(\tau^+) = \psi(x_0, \tau^+), \tag{2.5.17b}$$

and,

$$\frac{\partial x}{\partial \tau}\Big|_{\tau^+} = \dot{x}(\tau^+) = f\Big(x(\tau^+), y(\tau^+)\Big) = f(x^+, y^+) \triangleq f^+, \tag{2.5.18}$$

with similar analysis to equation (2.5.8) giving,

$$\frac{d^2x_i^+}{dx_0^2} = \frac{\partial^2 x_i^+}{\partial x_0^2} + \frac{\partial \tau}{\partial x_0}^\intercal \frac{\partial f_i^+}{\partial x_0} + \frac{\partial f_i^+}{\partial x_0}^\intercal \frac{\partial \tau}{\partial x_0} + \frac{\partial \tau}{\partial x_0}^\intercal \frac{\partial f_i^+}{\partial \tau} \frac{\partial \tau}{\partial x_0} + f_i^+ \frac{\partial^2 \tau}{\partial x_0^2}. \tag{2.5.19}$$

The state reset equation $h(\cdot, \cdot)$ in equation (2.2.1c) governs the pre- to post-event transition. Using the Implicit Function Theorem, $h(\cdot, \cdot)$ can be expressed as,

$$\tilde{h}(x^-) \triangleq h(x^-, \varphi(x^-)), \tag{2.5.20}$$

and can therefore be written,

$$x^+ = \tilde{h}(x^-). \tag{2.5.21}$$

The first-order jump condition (2.3.5) derived in [51] follows from differentiating equation (2.5.21),

$$\frac{dx^+}{dx_0} = \frac{\partial \tilde{h}}{\partial x} \frac{dx^-}{dx_0}, \tag{2.5.22}$$

where $\frac{\partial \tilde{h}}{\partial x} \triangleq \tilde{h}_x$ is given by equation (2.3.6). This can be seen by substituting equation (2.5.6) and the equivalent expression for $\frac{dx^+}{dx_0}$ into equation (2.5.22). For each element x_i of the dynamic state x, differentiating the transpose of equation (2.5.22) with respect to x_0 gives:

$$\begin{aligned}
\frac{d^2x_i^+}{dx_0^2} &= \frac{d}{dx_0}\Big(\frac{dx_i^+}{dx_0}^\intercal\Big) = \frac{d}{dx_0}\Big(\Big(\frac{\partial \tilde{h}_i}{\partial x}\frac{dx^-}{dx_0}\Big)^\intercal\Big) = \frac{d}{dx_0}\Big(\sum_{j=1}^n \frac{\partial \tilde{h}_i}{\partial x_j}\frac{dx_j^-}{dx_0}^\intercal\Big) = \sum_{j=1}^n \frac{d}{dx_0}\Big(\frac{\partial \tilde{h}_i}{\partial x_j}\frac{dx_j^-}{dx_0}^\intercal\Big) \\
&= \sum_{j=1}^n \frac{dx_j^-}{dx_0}^\intercal \frac{d}{dx_0}\Big(\frac{\partial \tilde{h}_i}{\partial x_j}\Big) + \sum_{j=1}^n \frac{\partial \tilde{h}_i}{\partial x_j}\frac{d}{dx_0}\Big(\frac{dx_j^-}{dx_0}^\intercal\Big) \\
&= \frac{dx^-}{dx_0}^\intercal \frac{\partial^2 \tilde{h}_i}{\partial x^2}\frac{dx^-}{dx_0} + \sum_{j=1}^n \frac{\partial \tilde{h}_i}{\partial x_j}\frac{d^2x_j^-}{dx_0^2}.
\end{aligned} \tag{2.5.23}$$

Subtracting equation (2.5.14) from equation (2.5.19) and substituting equation (2.5.23)

gives,

$$\begin{aligned}\frac{\partial^2 x_i^+}{\partial x_0^2} = \frac{\partial^2 x_i^-}{\partial x_0^2} + \frac{dx^-}{dx_0}^\intercal \frac{\partial^2 \tilde{h}_i}{\partial x^2} \frac{dx^-}{dx_0} + \sum_{j=1, j\neq i}^{n} \frac{\partial \tilde{h}_i}{\partial x_j} \frac{d^2 x_j^-}{dx_0^2} + \Big(\frac{\partial \tilde{h}_i}{\partial x_i} - 1\Big) \frac{d^2 x_i^-}{dx_0^2} \\ - \frac{\partial \tau}{\partial x_0}^\intercal \Big(\frac{\partial f_i^+}{\partial x_0} - \frac{\partial f_i^-}{\partial x_0}\Big) - \Big(\frac{\partial f_i^+}{\partial x_0} - \frac{\partial f_i^-}{\partial x_0}\Big)^\intercal \frac{\partial \tau}{\partial x_0} \\ - (f_i^+ - f_i^-) \frac{\partial^2 \tau}{\partial x_0^2} - \frac{\partial \tau}{\partial x_0}^\intercal \Big(\frac{\partial f_i^+}{\partial \tau} - \frac{\partial f_i^-}{\partial \tau}\Big) \frac{\partial \tau}{\partial x_0}, \end{aligned} \tag{2.5.24}$$

where $\frac{dx^-}{dx_0}$ is given by equation (2.5.5), $\frac{\partial \tilde{h}}{\partial x}$ is given by equation (2.3.6), $\frac{d^2 x_i^-}{dx_0^2}$ is given by equation (2.5.14), $\frac{\partial \tau}{\partial x_0}$ is given by equation (2.3.7), $\frac{\partial^2 \tau}{\partial x_0^2}$ is given by equations (2.5.15), (2.5.16), $\frac{\partial f^-}{\partial x_0}$ is given by equation (2.5.9), and $\frac{\partial f^-}{\partial \tau}$ is given by equation (2.5.12). The terms $\frac{\partial f^+}{\partial x_0}$ and $\frac{\partial f^+}{\partial \tau}$ take the same form as their τ^- counterparts. The remaining term $\frac{\partial^2 \tilde{h}}{\partial x^2}$ is derived in Subsection 2.5.3.

Equation (2.5.24) gives the post-event second-order sensitivities $\frac{\partial^2 x^+}{\partial x_0^2}$. The corresponding value for $\frac{\partial^2 y^+}{\partial x_0^2}$ can be obtained by evaluating equation (2.4.7b) at τ^+. Hence, equation (2.5.24) and equation (2.4.7b) together provide the jump conditions describing second-order sensitivities at switching and reset events.

2.5.3 Deriving the Remaining Terms

Differentiating equation (2.5.1c) with respect to x gives,

$$\frac{\partial g^-}{\partial x} + \frac{\partial g^-}{\partial y} \frac{\partial y^-}{\partial x} = 0_{m \times n}, \tag{2.5.25}$$

which can be rearranged as,

$$\frac{\partial y^-}{\partial x} = -\Big(\frac{\partial g^-}{\partial y}\Big)^{-1} \frac{\partial g^-}{\partial x}. \tag{2.5.26}$$

Hence, the term $\frac{\partial \tilde{s}}{\partial x}$ can be expressed as:

$$\frac{\partial \tilde{s}}{\partial x} = \frac{\partial s}{\partial x} + \frac{\partial s}{\partial y} \frac{\partial y^-}{\partial x} \tag{2.5.27a}$$

$$= \frac{\partial s}{\partial x} - \frac{\partial s}{\partial y} \Big(\frac{\partial g^-}{\partial y}\Big)^{-1} \frac{\partial g^-}{\partial x}. \tag{2.5.27b}$$

Differentiating the transpose of equation (2.5.27a) with respect to x gives,

$$\begin{aligned}\frac{\partial^2 \tilde{s}}{\partial x^2} &= \frac{\partial}{\partial x}\Big(\Big(\frac{\partial s}{\partial x} + \frac{\partial s}{\partial y}\frac{\partial y^-}{\partial x}\Big)^\intercal\Big) + \frac{\partial}{\partial y}\Big(\Big(\frac{\partial s}{\partial x} + \frac{\partial s}{\partial y}\frac{\partial y^-}{\partial x}\Big)^\intercal\Big)\frac{\partial y^-}{\partial x} \\ &= \frac{\partial^2 s}{\partial x^2} + \frac{\partial y^-}{\partial x}^\intercal \frac{\partial^2 s}{\partial y \partial x} + \sum_{j=1}^{m} \frac{\partial s}{\partial y_j}\frac{\partial^2 y_j^-}{\partial x^2} + \frac{\partial^2 s}{\partial x \partial y}\frac{\partial y^-}{\partial x} + \frac{\partial y^-}{\partial x}^\intercal \frac{\partial^2 s}{\partial y^2}\frac{\partial y^-}{\partial x}, \end{aligned} \tag{2.5.28}$$

where $\frac{\partial}{\partial y}\Big(\frac{\partial y^-}{\partial x}\Big) = 0$ because y is an implicit function of x only. The terms $\frac{\partial^2 y_j^-}{\partial x^2}$ in equation (2.5.28) can be derived by expanding equation (2.5.25),

$$\frac{\partial g_k^-}{\partial x} + \sum_{j=1}^{m} \frac{\partial g_k^-}{\partial y_j}\frac{\partial y_j^-}{\partial x} = 0_n^\intercal,$$

for $k = 1, ..., m$, and taking the derivative of the transpose with respect to x,

$$\begin{aligned} 0_{n\times n} &= \frac{\partial}{\partial x}\Big(\Big(\frac{\partial g_k^-}{\partial x} + \frac{\partial g_k^-}{\partial y}\frac{\partial y^-}{\partial x}\Big)^\intercal\Big) + \frac{\partial}{\partial y}\Big(\Big(\frac{\partial g_k^-}{\partial x} + \frac{\partial g_k^-}{\partial y}\frac{\partial y^-}{\partial x}\Big)^\intercal\Big)\frac{\partial y^-}{\partial x} \\ &= \frac{\partial^2 g_k^-}{\partial x^2} + \frac{\partial y^-}{\partial x}^\intercal \frac{\partial^2 g_k^-}{\partial y \partial x} + \sum_{j=1}^{m} \frac{\partial g_k^-}{\partial y_j}\frac{\partial^2 y_j^-}{\partial x^2} + \frac{\partial^2 g_k^-}{\partial x \partial y}\frac{\partial y^-}{\partial x} + \frac{\partial y^-}{\partial x}^\intercal \frac{\partial^2 g_k^-}{\partial y^2}\frac{\partial y^-}{\partial x}. \end{aligned} \tag{2.5.29}$$

Rearranging gives,

$$\sum_{j=1}^{m} \frac{\partial g_k^-}{\partial y_j}\frac{\partial^2 y_j^-}{\partial x^2} = -\frac{\partial^2 g_k^-}{\partial x^2} - \frac{\partial y^-}{\partial x}^\intercal \frac{\partial^2 g_k^-}{\partial y \partial x} - \frac{\partial^2 g_k^-}{\partial x \partial y}\frac{\partial y^-}{\partial x} - \frac{\partial y^-}{\partial x}^\intercal \frac{\partial^2 g_k^-}{\partial y^2}\frac{\partial y^-}{\partial x}, \tag{2.5.30}$$

for $k = 1, ..., m$. This problem has m matrix variables and m matrix equations (or $n^2 m$ scalar variables and $n^2 m$ scalar equations). It can be written in matrix form and solved for $\frac{\partial^2 y_j^-}{\partial x^2}$ for $j = 1, ..., m$.

Similarly, $\frac{\partial \tilde{h}}{\partial x}$ can be computed as,

$$\frac{\partial \tilde{h}}{\partial x} = \frac{\partial h}{\partial x} + \frac{\partial h}{\partial y}\frac{\partial y^-}{\partial x} \tag{2.5.31a}$$

$$= \frac{\partial h}{\partial x} - \frac{\partial h}{\partial y}\Big(\frac{\partial g^-}{\partial y}\Big)^{-1}\frac{\partial g^-}{\partial x}. \tag{2.5.31b}$$

Differentiating $\frac{\partial \tilde{h}_i}{\partial x}^\intercal$ from equation (2.5.31a), for $i = 1, ..., n$, results in,

$$\frac{\partial^2 \tilde{h}_i}{\partial x^2} = \frac{\partial}{\partial x}\Big(\Big(\frac{\partial h_i}{\partial x} + \frac{\partial h_i}{\partial y}\frac{\partial y^-}{\partial x}\Big)^\intercal\Big) + \frac{\partial}{\partial y}\Big(\Big(\frac{\partial h_i}{\partial x} + \frac{\partial h_i}{\partial y}\frac{\partial y^-}{\partial x}\Big)^\intercal\Big)\frac{\partial y^-}{\partial x}$$

$$= \frac{\partial^2 h_i}{\partial x^2} + \frac{\partial y^-}{\partial x}^\intercal \frac{\partial^2 h_i}{\partial y \partial x} + \sum_{j=1}^{m} \frac{\partial h_i}{\partial y_j} \frac{\partial^2 y_j^-}{\partial x^2} + \frac{\partial^2 h_i}{\partial x \partial y} \frac{\partial y^-}{\partial x} + \frac{\partial y^-}{\partial x}^\intercal \frac{\partial^2 h_i}{\partial y^2} \frac{\partial y^-}{\partial x}, \tag{2.5.32}$$

where the $\frac{\partial^2 y_j^-}{\partial x^2}$ are given by equation (2.5.30).

2.5.4 Visual Interpretation of the Jump Conditions

To simplify visualization of the jump conditions, consider the case where the state reset is simply $x^+ = x^-$, i.e., only a switching event occurs at the junction time τ. That corresponds to $\tilde{h}(x) = x$, so $\tilde{h}_x \triangleq \frac{\partial \tilde{h}}{\partial x} = I_n$ and $\frac{\partial^2 \tilde{h}_i}{\partial x^2} = 0_{n \times n}$ for $i = 1, ..., n$. The first-order jump condition equation (2.3.5) is reduced to,

$$x_{x_0}(\tau^+) = x_{x_0}(\tau^-) - \left(f^+ - f^-\right)\tau_{x_0}. \tag{2.5.33}$$

Likewise, the second-order jump condition (2.5.24) reduces to,

$$\begin{aligned} \frac{\partial^2 x_i^+}{\partial x_0^2} = \frac{\partial^2 x_i^-}{\partial x_0^2} &- \frac{\partial \tau}{\partial x_0}^\intercal \left(\frac{\partial f_i^+}{\partial x_0} - \frac{\partial f_i^-}{\partial x_0}\right) - \left(\frac{\partial f_i^+}{\partial x_0} - \frac{\partial f_i^-}{\partial x_0}\right)^\intercal \frac{\partial \tau}{\partial x_0} \\ &- (f_i^+ - f_i^-)\frac{\partial^2 \tau}{\partial x_0^2} - \frac{\partial \tau}{\partial x_0}^\intercal \left(\frac{\partial f_i^+}{\partial \tau} - \frac{\partial f_i^-}{\partial \tau}\right)\frac{\partial \tau}{\partial x_0}. \end{aligned} \tag{2.5.34}$$

Fig. 2.1 illustrates the behavior of system trajectories at a switching event and enables a visual interpretation of the first- and second-order jump conditions.

2.5.4.1 Interpretation for First-Order Sensitivity

The nominal trajectory is denoted by x in Fig. 2.1. Assume Δx_0 is a perturbation in initial conditions x_0 which results in a perturbed trajectory. Denote the first-order trajectory approximation by $\tilde{x}$, and the first-order approximation of the switching surface by $\mathcal{S}_1$. Under the perturbation Δx_0, the junction point where the perturbed trajectory encounters $\mathcal{S}_1$ will change, with the variation along the first-order switching hypersurface denoted by $\Delta x \triangleq \frac{dx}{dx_0}\Delta x_0$. The perturbation Δx_0 will also result in a change in the junction time τ, which is denoted by $\Delta\tau \triangleq \frac{\partial \tau}{\partial x_0}\Delta x_0$.

Post-multiplying equation (2.5.6) by Δx_0 gives,

$$\Delta x^- \triangleq \frac{dx^-}{dx_0}\Delta x_0 = x_{x_0}^- \Delta x_0 + f^- \Delta\tau, \tag{2.5.35a}$$

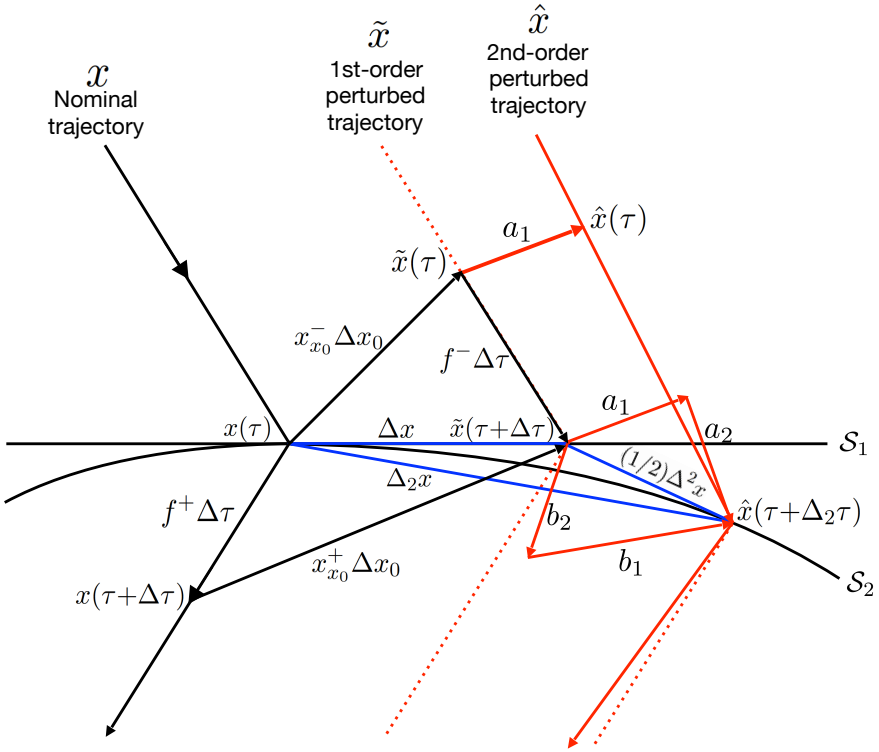

Figure 2.1: Interpretation of jump conditions for first- and second-order sensitivity.

and likewise at time τ^+,

$$\Delta x^+ \triangleq \frac{dx^+}{dx_0}\Delta x_0 = x^+_{x_0}\Delta x_0 + f^+\Delta\tau. \tag{2.5.35b}$$

With no reset event, $\frac{dx^-}{dx_0} = \frac{dx^+}{dx_0}$, so that,

$$\Delta x = x^-_{x_0}\Delta x_0 + f^-\Delta\tau = x^+_{x_0}\Delta x_0 + f^+\Delta\tau. \tag{2.5.36}$$

This relationship is illustrated in Fig. 2.1. At time τ, the nominal trajectory encounters the triggering hypersurface $\mathcal{S}_1$ at the point $x(\tau)$. However, the perturbed trajectory $\tilde{x}$ has not yet arrived at the hypersurface. It takes an extra $\Delta\tau$ time to arrive at the new junction point $\tilde{x}(\tau+\Delta\tau) = x(\tau) + \Delta x$. During the time interval $\Delta\tau$, the nominal trajectory evolves to the new point $x(\tau+\Delta\tau) = x(\tau) + f^+\Delta\tau$. The post-event sensitivity $x^+_{x_0}\Delta x_0$ must therefore compensate for the distance between the new point $x(\tau+\Delta\tau)$ and the new junction point $x(\tau) + \Delta x$.

2.5.4.2 Interpretation for Second-Order Sensitivity

Now consider the second-order trajectory approximation which is denoted by $\hat{x}$. In this second-order case the linear approximation $\mathcal{S}_1$ of the switching hypersurface is amended to the hypersurface $\mathcal{S}_2$ which captures the second-order curvature. Under the same perturbation Δx_0, there is a new junction point where the perturbed trajectory $\hat{x}$ encounters the adjusted switching hypersurface $\mathcal{S}_2$. The change in x lying on the switching hypersurface $\mathcal{S}_2$ is denoted by $\Delta_2 x = \Delta x + \frac{1}{2}\Delta^2 x$ where,

$$\Delta_2 x_i = \frac{dx_i}{dx_0}\Delta x_0 + \frac{1}{2}\Delta x_0^\intercal \frac{d^2 x_i}{dx_0^2}\Delta x_0,$$

i.e., Δx represents the first-order perturbation, $\frac{1}{2}\Delta^2 x$ is the second-order perturbation, and $\Delta_2 x$ is the total perturbation due to first- and second-order effects. The change in the junction time is denoted by,

$$\Delta_2 \tau = \Delta\tau + \frac{1}{2}\Delta^2\tau \triangleq \frac{\partial \tau}{\partial x_0}\Delta x_0 + \frac{1}{2}\Delta x_0^\intercal \frac{\partial^2 \tau}{\partial x_0^2}\Delta x_0. \tag{2.5.37}$$

The second-order approximate trajectory $\hat{x}$ encounters the hypersurface $\mathcal{S}_2$ at the time $\tau + \Delta_2\tau$, where the new junction point is,

$$\hat{x}(\tau + \Delta_2\tau) = x(\tau) + \Delta_2 x = \tilde{x}(\tau + \Delta\tau) + \frac{1}{2}\Delta^2 x.$$

The distance between the first-order junction point $\tilde{x}(\tau+\Delta\tau)$ and the second-order junction point $\hat{x}(\tau + \Delta_2\tau)$ is $\frac{1}{2}\Delta^2 x = \Delta_2 x - \Delta x$, which can be considered a correction to the first-order approximation.

The correction term $\frac{1}{2}\Delta^2 x$ is composed of multiple sections for both the pre- and post-event cases. Pre-multiplying equation (2.5.14) and equation (2.5.19) by $\frac{1}{2}\Delta x_0^\intercal$ and post-multiplying by Δx_0 results in,

$$\begin{aligned}
\frac{1}{2}\Delta^2 x_i^- &\triangleq \frac{1}{2}\Delta x_0^\intercal \frac{d^2 x_i^-}{dx_0^2}\Delta x_0 \\
&= \frac{1}{2}\Delta x_0^\intercal \frac{\partial^2 x_i^-}{\partial x_0^2}\Delta x_0 + \Delta\tau\Delta f_i^- + \frac{1}{2}\Delta\tau\frac{\partial f_i^-}{\partial \tau}\Delta\tau + \frac{1}{2}f_i^-\Delta^2\tau, && \text{(2.5.38a)} \\
\frac{1}{2}\Delta^2 x_i^+ &\triangleq \frac{1}{2}\Delta x_0^\intercal \frac{d^2 x_i^+}{dx_0^2}\Delta x_0 \\
&= \frac{1}{2}\Delta x_0^\intercal \frac{\partial^2 x_i^+}{\partial x_0^2}\Delta x_0 + \Delta\tau\Delta f_i^+ + \frac{1}{2}\Delta\tau\frac{\partial f_i^+}{\partial \tau}\Delta\tau + \frac{1}{2}f_i^+\Delta^2\tau. && \text{(2.5.38b)}
\end{aligned}$$

With no reset event, $\frac{d^2x_i^-}{dx_0^2} = \frac{d^2x_i^+}{dx_0^2}$, so equation (2.5.38a) and equation (2.5.38b) are equal. The symmetry of this relationship can be seen in Fig. 2.1, where the terms for the pre-event case are labeled:

$$(a_1) : \frac{1}{2}\Delta x_0^\intercal \frac{\partial^2 x_i^-}{\partial x_0^2}\Delta x_0,$$
$$(a_2) : \Delta\tau\Delta f_i^- + \frac{1}{2}\Delta\tau\frac{\partial f_i^-}{\partial\tau}\Delta\tau + \frac{1}{2}f_i^-\Delta^2\tau,$$

and for the post-event case:

$$(b_1) : \frac{1}{2}\Delta x_0^\intercal \frac{\partial^2 x_i^+}{\partial x_0^2}\Delta x_0,$$
$$(b_2) : \Delta\tau\Delta f_i^+ + \frac{1}{2}\Delta\tau\frac{\partial f_i^+}{\partial\tau}\Delta\tau + \frac{1}{2}f_i^+\Delta^2\tau.$$

2.6 Second-Order Trajectory Approximation

Trajectory approximation is an important and very useful application of trajectory sensitivities. Time-domain simulation for large-scale hybrid systems, such as power system, is computationally intensive. Trajectory approximation is applicable when there are small changes in initial condition and/or uncertain parameters. In such circumstances, trajectory sensitivities can be used to approximate the perturbed trajectories instead of performing repetitive full time-domain simulation. Having fully characterized the evolution of second-order sensitivities, second-order trajectory approximation is now possible for hybrid systems. The inclusion of second-order sensitivity information improves the accuracy of trajectory approximation.

Trajectory approximation requires the simulation of the nominal case together with calculation of the first-order and second-order sensitivities along the nominal trajectories. Approximate perturbed trajectories follow directly from the Taylor series expansion (2.3.1). Ignoring the remainder terms with order higher than two gives the second-order trajectory approximation:

$$\phi_i(x_0 + \Delta x_0, t) \approx \phi_i(x_0, t) + \frac{\partial\phi_i(x_0,t)}{\partial x_0}\Delta x_0 + \frac{1}{2}\Delta x_0^\intercal \frac{\partial^2\phi_i(x_0,t)}{\partial x_0^2}\Delta x_0, \tag{2.6.1a}$$

$$\psi_j(x_0 + \Delta x_0, t) \approx \psi_j(x_0, t) + \frac{\partial\psi_j(x_0,t)}{\partial x_0}\Delta x_0 + \frac{1}{2}\Delta x_0^\intercal \frac{\partial^2\psi_j(x_0,t)}{\partial x_0^2}\Delta x_0, \tag{2.6.1b}$$

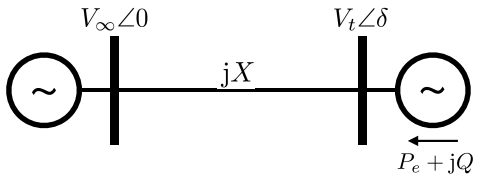

Figure 2.2: Single machine infinite bus system with Q limit.

for $i = 1, ..., n$ and $j = 1, ..., m$, and where $\frac{\partial \phi_i(x_0,t)}{\partial x_0} \triangleq \frac{\partial x_i}{\partial x_0}(t)$ and $\frac{\partial \psi_j(x_0,t)}{\partial x_0} \triangleq \frac{\partial y_j}{\partial x_0}(t)$ are the first-order sensitivities, and $\frac{\partial^2 \phi_i(x_0,t)}{\partial x_0^2} \triangleq \frac{\partial^2 x_i}{\partial x_0^2}(t)$ and $\frac{\partial^2 \psi_j(x_0,t)}{\partial x_0^2} \triangleq \frac{\partial^2 y_j}{\partial x_0^2}(t)$ are the second-order sensitivities.

The foregoing trajectory approximation is applicable for smooth sections of the trajectory. At discrete events, however, certain refinements should be made over the $\Delta_2\tau$ time interval defined in equation (2.5.37). This refinement for first-order trajectory approximation is developed in [19].

2.7 Case Study

To illustrate the jump conditions for second-order sensitivities, and demonstrate the improvement in trajectory approximation, a single machine infinite bus (SMIB) system, as shown in Fig. 2.2, is considered. The infinite bus provides a constant voltage magnitude and angle. The generator is represented by a classical second-order model, though an upper limit Q_{max} has been imposed on the generated reactive power Q to introduce switching events. When Q is smaller than Q_{max}, the generator bus is modeled as a PV bus, where voltage magnitude V_t is constant and equal to V_{set}, while Q is allowed to vary. If Q increases to its upper limit Q_{max}, the generator switches to a PQ bus, where Q is fixed at Q_{max} and the voltage magnitude V_t reduces. As V_t returns to the set-point V_{set} due to swinging of the rotor angle δ and angular velocity ω, the bus switches back to a PV bus.

The dynamic behavior of the SMIB system is described by:

$$\dot{\delta} = \omega \tag{2.7.1a}$$

$$\dot{\omega} = \frac{1}{M}(P_m - P_e - D\omega), \tag{2.7.1b}$$

where δ is the rotor angle, ω is the angular velocity, M is the inertia constant, P_m is mechanical power, P_e is electrical power, and D is the damping. The electrical power in equation (2.7.1b) is given by,

$$P_e = \frac{V_\infty V_t}{X} \sin(\delta), \tag{2.7.2}$$

where V_∞ is the constant voltage magnitude of the infinite bus, V_t is the voltage magnitude

of the generator bus, and X is the line reactance. Imposing an upper limit on reactive power requires the relationship between injected electrical power $P_e + jQ$ and the bus voltage magnitude,

$$\frac{V_\infty^2 V_t^2}{X^2} = P_e^2 + \Big(\frac{V_t^2}{X} - Q\Big)^2. \tag{2.7.3}$$

The dynamic states are denoted by $x = [x_1, x_2]^\intercal = [\delta, \omega]^\intercal$, and the algebraic states by $y = [y_1, y_2]^\intercal = [V_t, Q]^\intercal$. In the PV bus mode, Q varies while V_t is fixed at V_{set}, whereas in the PQ bus mode, V_t varies with Q fixed at Q_{max}. A switching event is triggered when Q encounters the switching surface $Q = Q_{max}$ or V encounters the switching surface $V = V_{set}$.

The differential-algebraic impulsive switched (DAIS) model can be represented by:

$$\frac{d}{dt}\begin{bmatrix}\delta\\ \omega\end{bmatrix} = \begin{cases}\omega\\ \dfrac{1}{M}\Big(P_m - \dfrac{V_\infty V_t}{X}\sin(\delta) - D\omega\Big)\end{cases} \tag{2.7.4a}$$

$$0 = \Big(\frac{V_\infty V_t}{X}\sin(\delta)\Big)^2 + \Big(\frac{V_t^2}{X} - Q\Big)^2 - \frac{V_\infty^2 V_t^2}{X^2} \tag{2.7.4b}$$

$$0 = \begin{cases}V_t - V_{set}, & Q - Q_{max} < 0\\ Q - Q_{max}, & V_{set} - V_t > 0.\end{cases} \tag{2.7.4c}$$

To be consistent with the DAIS model of Section 2.2, a new algebraic variable y_3 is introduced and the switched equation (2.7.4c) is reformulated as:

$$0 = \begin{cases}V_t - V_{set}\\ y_3 - (Q - Q_{max}),\end{cases} \qquad y_3 < 0 \tag{2.7.5a}$$

$$0 = \begin{cases}Q - Q_{max}\\ y_3 - (V_{set} - V_t),\end{cases} \qquad y_3 > 0. \tag{2.7.5b}$$

The implicit trapezoidal method was used to numerically integrate the DAE models describing states, first- and second-order sensitivities. At junction times when events are triggered, reset equations and jump conditions determine the post-event values for states and sensitivities, respectively. The post-event values serve as initial conditions for the DAE models over the subsequent smooth section.

The system parameters were set to $M = 7.3784$, $P_m = 3.1831$ pu, $V_\infty = 1$ pu, $X = 1/6$ pu, $D = 1$, $V_{set} = 1$ pu, and $Q_{max} = 0.8$ pu. For the nominal case, initial conditions $x_0 = [0.4, 0.2]^\intercal$ were chosen. This gave $y_0 = [1, 0.4736, -0.3264]^\intercal$.

In Fig. 2.3, the solid black line shows the nominal trajectory of x_1 (rotor angle), the blue dash-dot line shows the first-order sensitivity of x_1 with respect to $x_{0,1}$ (the initial

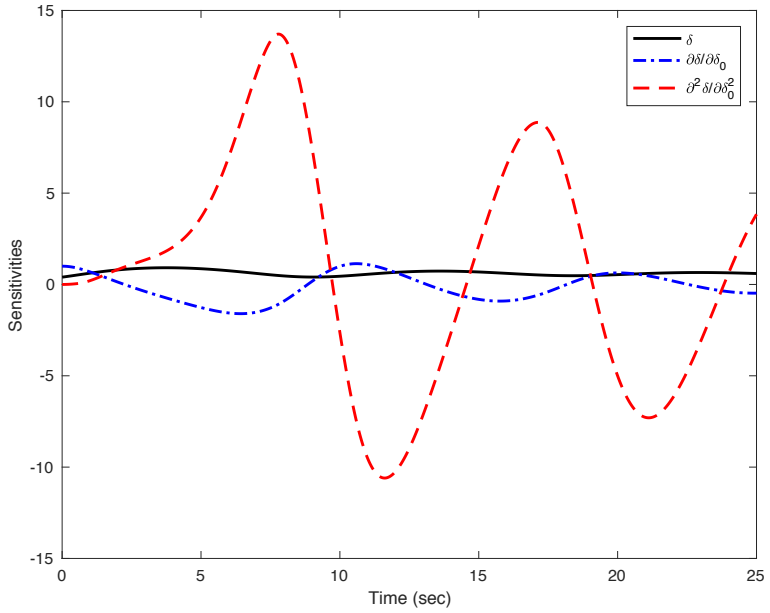

Figure 2.3: First- and second-order sensitivities for rotor angle.

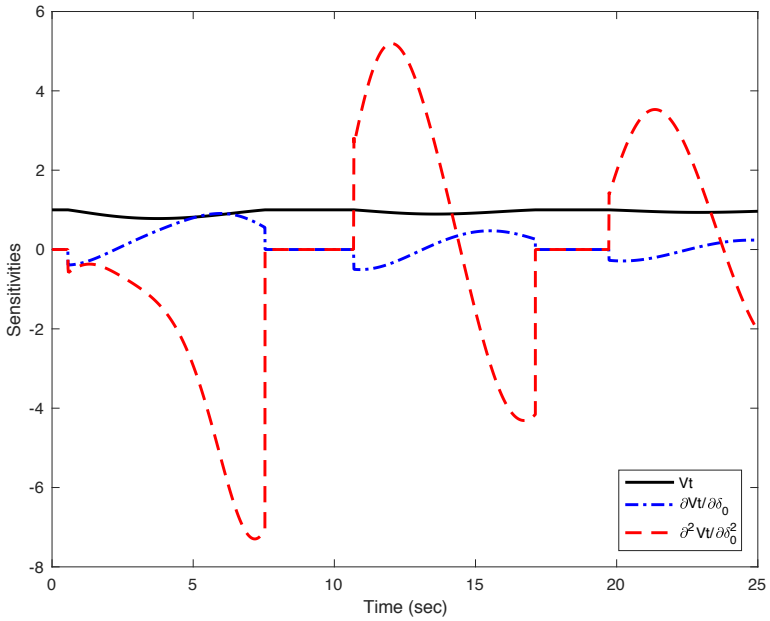

Figure 2.4: First- and second-order sensitivities for voltage magnitude.

condition for the first dynamic state x_1), and the red dashed line shows the second-order sensitivity of x_1 with respect to $x_{0,1}$, i.e., $\partial^2 x_1/\partial x_{0,1}^2$. The relative magnitudes of the first- and second-order sensitivities for this test case are clearly exhibited.

Similarly, the nominal trajectory of y_1 (voltage magnitude) is shown as the solid black line in Fig. 2.4. The first-order sensitivity of y_1 with respect to $x_{0,1}$ is shown as the blue dash-dot line, and the second-order sensitivity of y_1 with respect to $x_{0,1}$, i.e., $\partial^2 y_1/\partial x_{0,1}^2$, is shown as the red dashed line. It can be seen that five events occur at times 0.5661s, 7.5459s, 10.6938s, 17.1205s and 19.7325s. The complementary nature of the first- and second-order sensitivities for this case is also reflected in Fig. 2.4.

To demonstrate the application of sensitivities for approximating perturbed trajectories, initial conditions were altered to $x_0 = [0.47, 0.2]^\intercal$. Note that the initial conditions for algebraic variables have to change accordingly to $y_0 = [1, 0.6506, -0.1494]^\intercal$ to guarantee the algebraic equations are satisfied. The sensitivities resulting from the nominal trajectory were utilized to synthesize approximations of the perturbed trajectory[1]. For comparison, another time-domain simulation was run to generate the actual perturbed trajectory resulting from the altered initial condition.

Figure 2.5 shows the nominal trajectory, the perturbed trajectory, the first-order approximation (using only first-order sensitivities), and the second-order approximation (including both first- and second-order sensitivities) for rotor angle. It can be concluded that the second-order approximation outperforms the first-order approximation especially when the curvature of the perturbed trajectory is large. The l^2-norm of the residual of the first-order approximation is 0.2842 whereas it is 0.1528 for the second-order approximation. The error reduction is around 46%.

Similarly, Fig. 2.6 shows the nominal trajectory, the perturbed trajectory, and the first- and second-order approximations for voltage magnitude. From Figs. 2.4 and 2.6 it can be seen that step changes occur in the sensitivities, and hence the trajectory approximations, at the event triggering times. The l^2-norm of the residual of the first-order approximation is 0.4631 whereas it is 0.1666 for the second-order approximation. The error reduction is around 64%.

The angle-frequency phase portrait view of the trajectory approximations are shown in Fig. 2.7. The blue line emanating from the initial point $x_0 = [0.4, 0.2]^\intercal$ represents the nominal trajectory. The first- and second-order approximations are shown as the dashed magenta line and the red dotted line, respectively. For comparison, the actual perturbed trajectory is shown as the solid green line. It can be observed that the first-order approximation is initially rather accurate but breaks away from the actual perturbed

[1]The refinement over the delay interval described in [51] was not considered in this case.

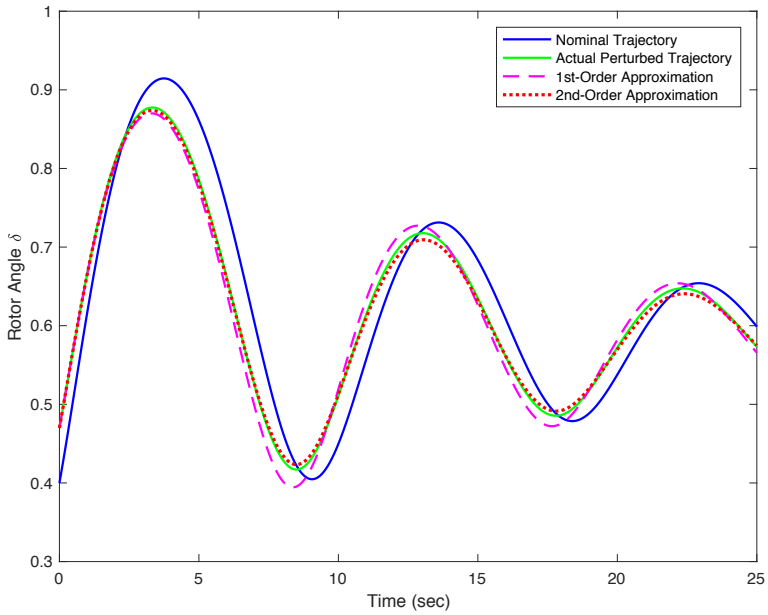

Figure 2.5: First- and second-order trajectory approximations for rotor angle.

trajectory for a large portion of the trajectory. The second-order approximation, however, constantly tracks the true perturbed trajectory with satisfactory accuracy.

2.8 Chapter Conclusion

Hybrid dynamical systems are characterized by coupling between continuous and discrete dynamics. A general differential-algebraic impulsive switched (DAIS) model is adopted in this chapter to represent such phenomena. Due to the intrinsic complexity of hybrid system dynamics, analysis is usually based on time-domain simulation. Exploring behavior over a range of parameter values and initial conditions usually involves repeated simulation. To overcome the associated computational burden, trajectory sensitivity analysis enables approximation of numerous perturbed trajectories using only the information obtained from the nominal trajectory. This technique linearizes the system around the nominal (nonlinear, non-smooth) trajectory and provides an approximate relationship between variations in initial conditions and/or system parameters and the resulting perturbed trajectories. Derivation of first-order trajectory sensitivities was undertaken in [51].

It follows from the Taylor series expansion that first-order trajectory sensitivities lack higher-order information that may be important in certain situations. This motivates the development of second-order sensitivities to recover some of the higher-order information and so improve the accuracy of trajectory approximation.

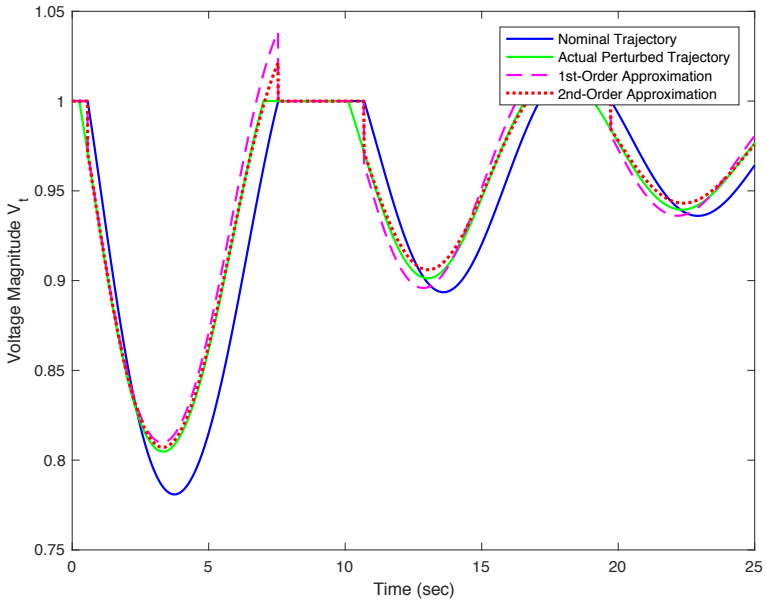

Figure 2.6: First- and second-order trajectory approximations for voltage magnitude.

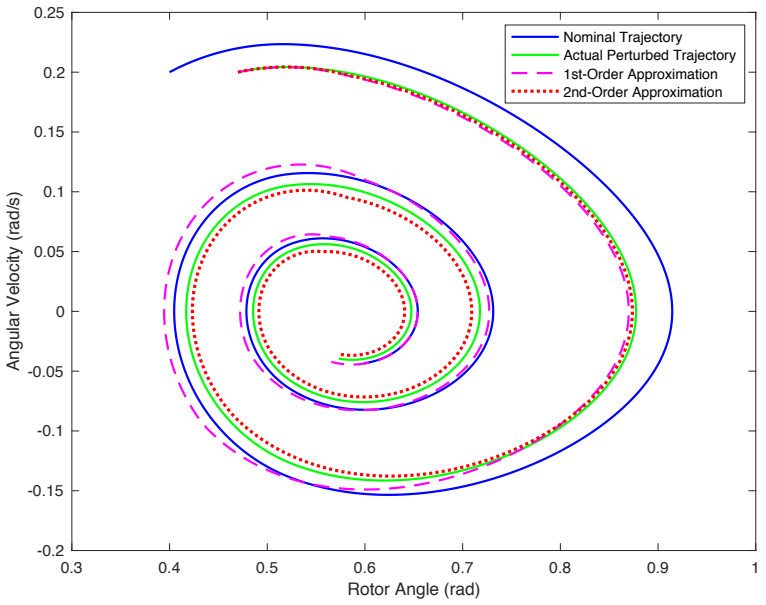

Figure 2.7: Phase portrait showing trajectory approximations.

This chapter formulates the differential-algebraic equation (DAE) model that governs second-order sensitivities over regions where dynamics are smooth, i.e., away from events. The jump conditions describing the step change of second-order sensitivities at discrete (switching and state reset) events are also derived. The DAE model together with the jump conditions fully characterize second-order sensitivities with respect to initial conditions and/or uncertain parameters for general hybrid dynamical systems. This work forms the basis for incorporating higher-order information into applications of first-order trajectory sensitivity analysis.

CHAPTER 3

Analysis and Quantification of Impacts of Uncertainties on System Dynamics

3.1 Chapter Introduction

The concept of reach-set refers to the union of all possible states that can be visited by system trajectories originating from a set of uncertain initial conditions, under the influence of admissible parameter uncertainties and external disturbances. Given the reach-set, safety specifications can be checked by verifying there is no intersection of the reach-set and any unsafe region. This is important for safety-critical applications such as power systems [84]. However, in general it is hard to compute the exact reach-set for a nonlinear system.

Much research has been devoted to computing over-approximations of the reach-set. A Taylor flowpipe model is used in [12] to over-approximate the reach-set of hybrid systems for a set of initial conditions. Other approaches to reach-set computation include abstraction-based methods [13], level-set methods [14], and differential inequalities [15]. Reachability analysis of nonlinear differential-algebraic systems is studied in [16] using a conservative linearization method, where zonotopes are used to represent the reach-set. A common issue across all these methods is conservativeness, which is partially because of the accumulation of error over time, i.e., the wrapping effect. Computational burden is another issue when considering high-dimensional applications.

This chapter explores reach-set approximation in the context of trajectory sensitivity analysis. Trajectory sensitivities can be used to approximate perturbed trajectories associated with uncertain initial conditions and/or parameter sets, thus avoiding repeated simulations [51, 62, 85]. It is shown in [86] that with sign-stable sensitivity matrices, only a small subset of the boundary of the initial set is required to be evaluated. However, sign-stability is a strong requirement. Reference [87] provide an extension that only requires bounded sensitivity. However, the bound itself needs to be estimated through

sampling and falsification. In [63], sensitivity analysis has been used for verification through simulation of continuous and hybrid systems. However, there is no guarantee that the computed approximation is an enclosure of the true reach-set, since there is no explicit theoretical guarantee for the accuracy of such approximations. The same applies for [60], where a semidefinite program is solved to search for the outermost trajectories.

In this chapter, we analytically quantify the error inherent in trajectory approximation using the second-order trajectory sensitivity [85]. We exploit results on multivariate Taylor's theorem and higher-order remainders to give a theoretical error bound for the first-order trajectory approximation. Sampled-data approaches [87] can be used to estimate the bound. To ease computational effort, we also provide practical solutions for computing an error bound estimate. With an explicit numerical error bound available, we can provide a sufficiently accurate estimation of the reach-set by locating worst-case vertices of the uncertainty set [19].

The effect of external disturbances on differential-algebraic equation (DAE) systems is also investigated in this chapter. We first extend to DAE systems a Lipschitz-based result from nonlinear systems theory that quantifies the effects of initial conditions and bounded external disturbances. Then we improve the result by exploiting properties of the logarithmic norm. The logarithmic norm, or matrix measure, is a useful tool for quantifying bounds on the divergence of adjacent trajectories, hence is useful for providing error bounds on linear approximation of nonlinear systems [88], and for analyzing contractive systems [89]. In [90], the logarithmic norm has been used to compute over-approximation of the reach-set for switched nonlinear systems with uncertain initial conditions. In this chapter, we also quantify the effects of external disturbances on system dynamics.

The contributions of this chapter are as follows. Firstly, we provide an explicit theoretical error bound for trajectory sensitivity analysis, using second-order trajectory sensitivities. This theoretical bound is then estimated using efficient trajectory-based approach. Secondly, a theoretical result on quantifying the effects of external disturbances on nonlinear DAE systems is derived, using the mathematical tool of logarithmic norm. Thirdly, we provide an efficient approach to compute an accurate estimation of the reach-set of nonlinear DAE systems, under uncertain initial conditions and/or parameters, and external disturbances. This is achieved by combining the results on error bound for trajectory sensitivity analysis and the results on bounding the effects of external disturbances.

This chapter is organized as follows: Section 3.2 presents system model and provides an overview of trajectory sensitivity analysis and logarithmic norm. The error bounds for trajectory approximation are derived in Section 3.3. Section 3.4 establishes theoretical results on quantifying the propagation of external disturbances. Reach-set computation

with Minkowski sum formulation is described in Section 3.5. Simulation results are given in Section 3.6 and conclusions are drawn in Section 3.7.

3.2 Preliminaries

In this chapter, we adopt a DAE model to describe the dynamic behavior of the system,

$$\dot{x}(t) = f(x(t), y(t)) + w(t), \tag{3.2.1a}$$

$$0 = g(x(t), y(t)), \tag{3.2.1b}$$

where $x(t) \in \mathcal{D}_x \subset \mathbb{R}^n$ are the dynamic states at time t, $y(t) \in \mathcal{D}_y \subset \mathbb{R}^m$ are the algebraic states at time t, $f : \mathcal{D}_x \times \mathcal{D}_y \to \mathbb{R}^n$ is the vector field, and $g : \mathcal{D}_x \times \mathcal{D}_y \to \mathbb{R}^m$ describes the algebraic manifold. Nonlinear functions f and g are assumed to be Lipschitz in their arguments and of class C^2. A bounded time-varying unknown external disturbance $w(t)$ is added to the differential equation. This disturbance term will not be considered until Section 3.4. Several technical assumptions are required for subsequent analysis:

Assumption 5. *The solution of equation (3.2.1) exists for initial conditions and disturbances of interest, and is unique.*

Assumption 6. *The Jacobian $\partial g/\partial y$ is nonsingular along system trajectories.*

For given initial conditions $x(t_0) = x_0$, $y(t_0) = y_0$, where $g(x_0, y_0) = 0$, the corresponding system trajectory (or flow) can be expressed as,

$$x(t) = \phi(x_0, t), \tag{3.2.2a}$$

$$y(t) = \psi(x_0, t). \tag{3.2.2b}$$

Uncertainty in initial conditions x_0 will be considered, with y_0 implicitly dependent upon x_0. To take into account uncertain parameters λ, the dynamic states x can be augmented with λ and trivial differential equations $\dot{\lambda} = 0$ added. This way, uncertain parameters are incorporated into the expanded initial conditions x_0.

3.2.1 Trajectory Sensitivity and Trajectory Approximation

Trajectory sensitivities describe the change in the system flow resulting from a change in initial conditions x_0. Forming the Taylor series expansion of the flow (3.2.2) with respect

to x_0 along the nominal trajectory yields,

$$\phi_i(x_0 + \Delta x_0, t) = \phi_i(x_0, t) + \frac{\partial \phi_i(x_0, t)}{\partial x_0}\Delta x_0 + \frac{1}{2}\Delta x_0^\intercal \frac{\partial^2 \phi_i(x_0, t)}{\partial x_0^2}\Delta x_0 + \varepsilon_2^{\phi_i}(x_0, \Delta x_0, t), \tag{3.2.3a}$$

$$\psi_j(x_0 + \Delta x_0, t) = \psi_j(x_0, t) + \frac{\partial \psi_j(x_0, t)}{\partial x_0}\Delta x_0 + \frac{1}{2}\Delta x_0^\intercal \frac{\partial^2 \psi_j(x_0, t)}{\partial x_0^2}\Delta x_0 + \varepsilon_2^{\psi_j}(x_0, \Delta x_0, t), \tag{3.2.3b}$$

$$\forall i = 1, ...n, \ \forall j = 1, ...m,$$

where the terms $\frac{\partial \phi_i(x_0,t)}{\partial x_0} \in \mathbb{R}^{1\times n}$ and $\frac{\partial \psi_j(x_0,t)}{\partial x_0} \in \mathbb{R}^{1\times n}$ are first-order trajectory sensitivities and $\frac{\partial^2 \phi_i(x_0,t)}{\partial x_0^2} \in \mathbb{R}^{n\times n}$ and $\frac{\partial^2 \psi_j(x_0,t)}{\partial x_0^2} \in \mathbb{R}^{n\times n}$ are second-order trajectory sensitivities. The terms $\varepsilon_2^{\phi_i}(x_0, \Delta x_0, t)$ and $\varepsilon_2^{\psi_j}(x_0, \Delta x_0, t)$ capture the higher-order terms beyond the second.

The DAE variational equations describing first- and second-order trajectory sensitivities are given in [51] and [85], respectively. We only summarize the DAE model for the first-order trajectory sensitivity here. Taking the derivatives of equation (3.2.1) with respect to x_0 yields,

$$\dot{x}_{x_0} = f_x(t)x_{x_0} + f_y(t)y_{x_0}, \tag{3.2.4a}$$

$$0 = g_x(t)x_{x_0} + g_y(t)y_{x_0}, \tag{3.2.4b}$$

where x_{x_0} and y_{x_0} denote the first-order trajectory sensitivities. We use f_x, f_y, g_x, g_y to denote $\partial f/\partial x, \partial f/\partial y, \partial g/\partial x, \partial g/\partial y$ respectively, which are time-varying matrices evaluated along the nominal trajectory. Initial conditions are given by $x_{x_0}(t_0) = I$, the identity matrix, and $y_{x_0}(t_0) = -(g_y(t_0))^{-1}g_x(t_0)$.

From equation (3.2.3), we have the first-order approximation,

$$\hat{\phi}(x_0 + \Delta x_0, t) = \phi(x_0, t) + \frac{\partial \phi(x_0, t)}{\partial x_0}\Delta x_0, \tag{3.2.5a}$$

$$\hat{\psi}(x_0 + \Delta x_0, t) = \psi(x_0, t) + \frac{\partial \psi(x_0, t)}{\partial x_0}\Delta x_0. \tag{3.2.5b}$$

Since higher-order terms are neglected, there are discrepancies between the approximated trajectory (3.2.5) and the true perturbed trajectory (3.2.3). Define the error in the first-order approximation by,

$$\varepsilon_1^{\phi}(x_0, \Delta x_0, t) \triangleq \phi(x_0 + \Delta x_0, t) - \hat{\phi}(x_0 + \Delta x_0, t), \tag{3.2.6a}$$

$$\varepsilon_1^{\psi}(x_0, \Delta x_0, t) \triangleq \psi(x_0 + \Delta x_0, t) - \hat{\psi}(x_0 + \Delta x_0, t). \tag{3.2.6b}$$

From classic perturbation theory [55], we know that the first-order approximation errors are of order $O(\|\Delta x_0\|^2)$. That is, there exists positive constants k^ϕ, k^ψ and c, such that $\|\varepsilon_1^\phi(x_0, \Delta x_0, t)\| \leq k^\phi \|\Delta x_0\|^2$ and $\|\varepsilon_1^\psi(x_0, \Delta x_0, t)\| \leq k^\psi \|\Delta x_0\|^2$, for all $\|\Delta x_0\| < c$. However, the magnitudes of k^ϕ and k^ψ are not known. Therefore, the big-O notation cannot be translated into a useful numerical error bound. This problem is investigated further in Section 3.3.

3.2.2 Logarithmic Norm

For any vector norm $\|\cdot\|$ on $\mathbb{R}^n$, and its induced matrix norm $\|\cdot\|$ on $\mathbb{R}^{n\times n}$, the logarithmic norm of a matrix $A \in \mathbb{R}^{n\times n}$ is a real-valued functional $\mu : \mathbb{R}^{n\times n} \to \mathbb{R}$, defined by [88],

$$\mu(A) = \lim_{s\to 0^+} \frac{\|I + sA\| - 1}{s}. \tag{3.2.7}$$

Explicit expressions exist for common vector norms such as the l_1, l_2 and l_∞-norms [91]. The logarithmic norm has a number of important properties [90],

1 For any eigenvalue $\lambda_i(A)$ of A, we know,
$-\|A\| \leq -\mu(-A) \leq \mathrm{Re}(\lambda_i(A)) \leq \mu(A) \leq \|A\|$.

2 $\mu(cA) = c\mu(A), \forall c \geq 0$.

3 $\mu(A + B) \leq \mu(A) + \mu(B)$.

Fundamental results that connect the logarithmic norm to dynamical systems are summarized in [92] for linear systems and [89] for nonlinear systems.

3.3 Error Bound for Trajectory Approximation

We are interested in deriving an explicit numerical bound for the error in the first-order trajectory approximation. Such an error bound provides theoretical guarantees for the accuracy of trajectory approximations and justifies their application to safety-critical scenarios such as dynamic security assessment [93]. In this section, we exploit multivariate Taylor's theorem and Lagrange's remainder, and derive an error bound for trajectory approximation by formulating an optimization problem. To ease the computational effort of solving the global optimization, we then propose an efficient approach to practically estimating the error bound.

3.3.1 Multivariate Taylor's Theorem and Remainder

Multi-index notation [94] is adopted to simplify the presentation of the following results.

Theorem 3.3.1. *[95] Suppose $f : \mathbb{R}^n \to \mathbb{R}$ is of class $C^{\kappa+1}$ on an open convex set $\mathcal{S}$. If $\boldsymbol{a} \in \mathcal{S}$ and $\boldsymbol{a} + \boldsymbol{h} \in \mathcal{S}$ then,*

$$f(\boldsymbol{a} + \boldsymbol{h}) = \sum_{|\alpha| \leq \kappa} \partial^\alpha f(\boldsymbol{a}) \frac{\boldsymbol{h}^\alpha}{\alpha!} + R_\kappa(\boldsymbol{a}, \boldsymbol{h}), \tag{3.3.1}$$

where the remainder is given in Lagrange's form by,

$$R_\kappa(\boldsymbol{a}, \boldsymbol{h}) = \sum_{|\alpha| = \kappa+1} \partial^\alpha f(\boldsymbol{a} + c\boldsymbol{h}) \frac{\boldsymbol{h}^\alpha}{\alpha!}, \text{ for some } c \in (0, 1). \tag{3.3.2}$$

Based on equation (3.3.2), an estimate for the remainder term is given by the following corollary.

Corollary 3.3.1. *If f is of class $C^{\kappa+1}$ on $\mathcal{S}$ and $|\partial^\alpha f(\boldsymbol{x})| \leq M$ for $\boldsymbol{x} \in \mathcal{S}$ and $|\alpha| = \kappa + 1$, then*

$$|R_\kappa(\boldsymbol{a}, \boldsymbol{h})| \leq \frac{M}{(\kappa+1)!} \|\boldsymbol{h}\|_1^{\kappa+1}, \tag{3.3.3}$$

where $\|\boldsymbol{h}\|_1 = |h_1| + |h_2| + \ldots + |h_n|$.

3.3.2 Error Bound by Second-Order Trajectory Sensitivity

Assigning time t to be any fixed time instant τ in equation (3.2.3), we obtain a regular Taylor expansion of $\phi_i(\tilde{x}_0, \tau)$ and $\psi_j(\tilde{x}_0, \tau)$, where $x_0 - \Delta x_0 \leq \tilde{x}_0 \leq x_0 + \Delta x_0$ with the vector inequality interpreted element-wise. Truncating all higher-order terms and applying Taylor's Inequality (3.3.3) gives remainders of the first-order approximations bounded as,

$$|R_1^{\phi_i}(x_0, \Delta x_0, \tau)| \leq \frac{M^{\phi_i}(x_0, \Delta x_0, \tau)}{2} \|\Delta x_0\|_1^2, \tag{3.3.4a}$$

$$|R_1^{\psi_j}(x_0, \Delta x_0, \tau)| \leq \frac{M^{\psi_j}(x_0, \Delta x_0, \tau)}{2} \|\Delta x_0\|_1^2, \tag{3.3.4b}$$

$\forall i = 1, \ldots, n$ and $\forall j = 1, \ldots, m$, where,

$$M^{\phi_i}(x_0, \Delta x_0, \tau) \geq \max_{\substack{x_0 - \Delta x_0 \leq \tilde{x}_0 \leq x_0 + \Delta x_0 \\ 1 \leq k \leq l \leq n}} \left| \left\{ \frac{\partial^2 \phi_i(\tilde{x}_0, \tau)}{\partial x_0^2} \right\}_{k,l} \right| \tag{3.3.5a}$$

$$M^{\psi_j}(x_0, \Delta x_0, \tau) \geq \max_{\substack{x_0 - \Delta x_0 \leq \tilde{x}_0 \leq x_0 + \Delta x_0 \\ 1 \leq k \leq l \leq n}} \left| \left\{ \frac{\partial^2 \psi_j(\tilde{x}_0, \tau)}{\partial x_0^2} \right\}_{k,l} \right| \tag{3.3.5b}$$

where the scalars k, l are indices for the entries of the symmetric second-order trajectory sensitivity matrices $\frac{\partial^2 \phi_i(\tilde{x}_0,\tau)}{\partial x_0^2}$, $\frac{\partial^2 \psi_j(\tilde{x}_0,\tau)}{\partial x_0^2}$ whose expressions are given in [85].

Allowing τ to vary is equivalent to replacing τ with t in equations (3.3.4) and (3.3.5). Also, larger Δx_0 implies larger $M^{\phi_i}(x_0, \Delta x_0, t)$ and $M^{\psi_j}(x_0, \Delta x_0, t)$, since the maximum is taken over a larger set.

3.3.3 Optimization Problem for the Error Bound

The question of finding a numerical error bound for the first-order trajectory approximation (relative to the true perturbed trajectory), or equivalently of quantifying the higher-order remainder of the first-order approximation, reduces to finding the entry-wise maximum absolute value for second-order trajectory sensitivities (at each time instant) corresponding to all possible trajectories originating from the initial condition set $\mathcal{X}_0 := \{\tilde{x}_0 \in \mathbb{R}^n \big| x_0 - \Delta x_0 \leq \tilde{x}_0 \leq x_0 + \Delta x_0\}$. This problem can be written explicitly as the following optimization,

$$
\begin{aligned}
(\mathcal{P}1) \quad M^{\phi_i}(t) &= \max_{\substack{\tilde{x}_0 \in \mathcal{X}_0 \\ 1 \leq k \leq l \leq n}} \left| \left\{ \frac{\partial^2 \phi_i(\tilde{x}_0, t)}{\partial x_0^2} \right\}_{k,l} \right| \\
M^{\psi_j}(t) &= \max_{\substack{\tilde{x}_0 \in \mathcal{X}_0 \\ 1 \leq k \leq l \leq n}} \left| \left\{ \frac{\partial^2 \psi_j(\tilde{x}_0, t)}{\partial x_0^2} \right\}_{k,l} \right| \\
&\forall i = 1, \ldots, n, \ \forall j = 1, \ldots, m.
\end{aligned}
$$

Although this establishes a theoretical form for the error bound, the global optimal solution to $(\mathcal{P}1)$ is hard to obtain. Firstly, the second-order trajectory sensitivity information is obtained by numerically integrating a DAE model, as given in [85]. Hence, no analytical form of the function is available. Secondly, at each time instant t, for each of the n dynamic states and each of the m algebraic states, we need to solve $n(n+1)/2$ global optimization problems. Such computational difficulty is to be expected, since in general it is hard to quantify the error resulting from a linear approximation of its nonlinear counterpart. Existing methods in [96] and the recent development of [97] for formally solving this problem involve enforcing global conditions on a Lipschitz constant of the vector field or on the logarithmic norm of the Jacobian matrix, and finding the global maximum of a non-convex optimization problem. The resulting error bounds from such methods also tend to be overly conservative.

To solve the non-convex problem $(\mathcal{P}1)$, we can use sampling-falsification methods such as described in [87]. Firstly, we can select a few samples in the space of initial conditions,

and evaluate their second-order trajectory sensitivities, resulting in an initial estimate for the bound. Secondly, the previously estimated bounds are iteratively enlarged by searching for other initial conditions to falsify the prior bounds. However, numerical test cases show that computing only the nominal trajectory together with the trajectories for the extreme vertices (which can be viewed as the coarsest grid for the uncertain set $\mathcal{X}_0$) suffices to provide an accurate estimate for the error bound. In practice, if k out of n states have uncertain initial conditions, we can simply evaluate $2^k + 1$ trajectories (2^k vertex cases and one nominal case) and find the maximum second-order trajectory sensitivities at each time instant. This serves as an efficiently estimated error bound for the first-order trajectory approximation. Following this idea, the optimization program ($\mathcal{P}1$) is reduced to the tractable problem,

$$
\begin{aligned}
(\mathcal{P}2) \quad \hat{M}^{\phi_i}(t) &= \max_{\substack{\tilde{x}_0 \in (\mathrm{Vert}(\mathcal{X}_0) \cup x_0) \\ 1 \le k \le l \le n}} \left| \left\{ \frac{\partial^2 \phi_i(\tilde{x}_0, t)}{\partial x_0^2} \right\}_{k,l} \right| \\
\hat{M}^{\psi_j}(t) &= \max_{\substack{\tilde{x}_0 \in (\mathrm{Vert}(\mathcal{X}_0) \cup x_0) \\ 1 \le k \le l \le n}} \left| \left\{ \frac{\partial^2 \psi_j(\tilde{x}_0, t)}{\partial x_0^2} \right\}_{k,l} \right| \\
&\qquad \forall i = 1, \ldots n, \ \forall j = 1, \ldots m,
\end{aligned}
$$

where the notation $\mathrm{Vert}(\mathcal{X}_0)$ denotes the operation of extracting the finite set of vertices of the polytope $\mathcal{X}_0$.

3.4 Quantify External Disturbances

We wish to quantify the flow excursion caused by a bounded time-varying disturbance, relative to the noise-free nominal trajectory. A well-known result for ordinary differential equation (ODE) systems is based on knowledge of the Lipschitz constant of the vector field, see for example, Theorem 3.4 in [55]. We first generalize this result to DAE systems and then establish an improved result based on the logarithmic norm.

Referring to equation (3.2.1), by the Implicit Function Theorem and Assumption 6, there exists (locally) a unique function φ such that $y = \varphi(x)$. Furthermore, we make the following assumption.

Assumption 7. *There exists a function $\varphi : \mathcal{D}_x \to \mathcal{D}_y$, where $\mathcal{D}_x \subset \mathbb{R}^n$ and $\mathcal{D}_y \subset \mathbb{R}^m$, such that $g(x, \varphi(x)) = 0$, and φ is Lipschitz with constant L_φ.*

The existence of such a "global" implicit function holds under various conditions [98, 99], for example, if $\mathcal{D}_x$ is simply connected together with some technical conditions

as discussed in Theorem 4.2 of [99]. Inserting this implicit function into equation (3.2.1a) yields $\dot{x} = f(x, y) = f(x, \varphi(x)) \triangleq h(x)$.

We derive the following Corollary for DAE systems.

Corollary 3.4.1. *Let $f(x, y)$ be Lipschitz in x and y on $\mathcal{D}_x \times \mathcal{D}_y$ with Lipschitz constants L_x and L_y, where $\mathcal{D}_x \times \mathcal{D}_y \subset \mathbb{R}^n \times \mathbb{R}^m$ is an open connected set. Let $(x(t), y^x(t))$ be the solution of $\dot{x} = f(x, y)$, $0 = g(x, y)$, $x(t_0) = x_0$, and $(z(t), y^z(t))$ be the solution of $\dot{z} = f(z, y) + w(t)$, $0 = g(z, y)$, $z(t_0) = z_0$, such that $(x(t),\ y^x(t)) \in \mathcal{D}_x \times \mathcal{D}_y$, $(z(t),\ y^z(t)) \in \mathcal{D}_x \times \mathcal{D}_y$ for all $t \in [t_0, t_1]$. Suppose that $\|w(t)\| \leq \mathrm{w}$, $\forall t \in [t_0, t_1]$ for some $\mathrm{w} > 0$. Based on Assumption 7, we further assume that $y^x = \varphi(x)$, and $y^z = \varphi(z)$. Let $L_h = L_x + L_y L_\varphi$, where L_φ is the Lipschitz constant of the implicit function φ. Then, $\|x(t) - z(t)\| \leq \|x_0 - z_0\| \exp[L_h(t - t_0)] + \frac{\mathrm{w}}{L_h}\Big(\exp[L_h(t - t_0)] - 1\Big)$ and $\Big\|y^x(t) - y^z(t)\Big\| \leq L_\varphi \|x_0 - z_0\| \exp[L_h(t - t_0)] + L_\varphi \frac{\mathrm{w}}{L_h}\Big(\exp[L_h(t - t_0)] - 1\Big)$.*

Proof. Using the implicit function φ in the differential equations gives $\dot{x} = f(x, y) = f(x, \varphi(x)) \triangleq h(x)$, $\dot{z} = f(z, y) + w(t) = f(z, \varphi(z)) + w(t) \triangleq h(z) + w(t)$. Since the implicit function φ and the vector field $f(\cdot, \cdot)$ are Lipschitz, the composite function h is also Lipschitz. For any two points $x_1, x_2 \in \mathcal{D}_x$,

$$\begin{aligned}
\frac{h(x_1) - h(x_2)}{x_1 - x_2} &= \frac{f(x_1, \varphi(x_1)) - f(x_2, \varphi(x_2))}{x_1 - x_2} \\
&= \frac{\Big(f(x_1, \varphi(x_1)) - f(x_2, \varphi(x_1))\Big) + \Big(f(x_2, \varphi(x_1)) - f(x_2, \varphi(x_2))\Big)}{x_1 - x_2} \\
&\leq L_x + \frac{f(x_2, \varphi(x_1)) - f(x_2, \varphi(x_2))}{\varphi(x_1) - \varphi(x_2)} \cdot \frac{\varphi(x_1) - \varphi(x_2)}{x_1 - x_2} \\
&\leq L_x + L_y L_\varphi. \qquad (3.4.1)
\end{aligned}$$

Therefore, the Lipschitz constant L_h for the composite function h is upper bounded by $L_x + L_y L_\varphi$. Apply Theorem 3.4 in [55] and the results follow. Furthermore, we have $\Big\|y^x(t) - y^z(t)\Big\| = \Big\|\varphi(x(t)) - \varphi(z(t))\Big\| \leq L_\varphi \|x(t) - z(t)\|$. □

Next, we improve Theorem 3.4 in [55] and Corollary 3.4.1 by deriving a tighter bound, using the logarithmic norm instead of Lipschitz constants. Property 1 in Section 3.2.2 indicates that the logarithmic norm of the Jacobian matrix is guaranteed to be upper-bounded by the Lipschitz constant of the vector field. Consequently, we obtain the following improved result.

Theorem 3.4.1. *Let the Jacobian matrix f_x satisfy $\mu(f_x(x)) \leq c$, $\forall x \in \mathcal{D}$, where $\mathcal{D} \subset \mathbb{R}^n$ is an open convex set. Let $x(t)$ be the solution of $\dot{x} = f(x)$, $x(t_0) = x_0$, and $z(t)$ be the solution of $\dot{z} = f(z) + w(t)$, $z(t_0) = z_0$, such that $x(t), z(t) \in \mathcal{D}$ for all $t \in [t_0, t_1]$. Suppose that $\|w(t)\| \leq \mathrm{w}$, $\forall t \in [t_0, t_1]$ for some $\mathrm{w} > 0$. Then, $\|x(t) - z(t)\| \leq \|x_0 - z_0\| \exp[c(t - t_0)] + \frac{\mathrm{w}}{c}\Big(\exp[c(t - t_0)] - 1\Big)$.*

Proof. Based on the fundamental theorem of calculus,

$$\begin{aligned}\dot{x} - \dot{z} &= f(x) - f(z) - w(t) \\ &= \int_0^1 f_x(z + s(x-z))(x-z)ds - w(t) \\ &= \int_0^1 f_x(z + s(x-z))ds \cdot (x-z) - w(t). \end{aligned} \tag{3.4.2}$$

Let $x - z = e$ so that $\dot{e} = \int_0^1 f_x(z + se)ds \cdot e - w(t)$. By convexity of $\mathcal{D}$ and $s \in [0,1]$, we have $(z + s(x-z)) \in \mathcal{D}, \forall t \in [t_0, t_1]$. Since $\mu(f_x(x)) \leq c$, $\forall x \in \mathcal{D}$, apply Proposition 1 of [97] and the subadditivity property of the logarithmic norm to give $D_t^+\|e\| \leq c\|e\| + \|w\| \leq c\|e\| + \mathrm{w}$. The notation D_t^+ is the upper right-hand Dini derivative with respect to time t. Based on Duhamel's formula and comparison lemma, we obtain,

$$\begin{aligned}\|e(t)\| &\leq \|e(t_0)\| \exp[c(t-t_0)] + \int_{t_0}^t \exp[c(t-\tau)] \cdot \mathrm{w} d\tau \\ &= \|e(t_0)\| \exp[c(t-t_0)] + \frac{\mathrm{w}}{c}\Big(\exp[c(t-t_0)] - 1\Big), \end{aligned} \tag{3.4.3}$$

where $e(t_0) = x_0 - z_0$. □

Theorem 3.4.1 can be generalized to DAE systems.

Corollary 3.4.2. *Let the Jacobian matrix $\frac{\partial h}{\partial x}(x,y) = \frac{\partial f}{\partial x} + \frac{\partial f}{\partial y}\frac{\partial y}{\partial x}$ satisfy $\mu(\frac{\partial h}{\partial x}(x,y)) \leq c_h$, $\forall (x,y) \in \mathcal{D}_x \times \mathcal{D}_y$, where $\mathcal{D}_x \times \mathcal{D}_y \subset \mathbb{R}^n \times \mathbb{R}^m$ is an open convex set. Let $(x(t), y^x(t))$ be the solution of $\dot{x} = f(x,y)$, $0 = g(x,y)$, $x(t_0) = x_0$, and $(z(t), y^z(t))$ be the solution of $\dot{z} = f(z,y) + w(t)$, $0 = g(z,y)$, $z(t_0) = z_0$, such that $(x(t),\ y^x(t)) \in \mathcal{D}_x \times \mathcal{D}_y$, $(z(t),\ y^z(y)) \in \mathcal{D}_x \times \mathcal{D}_y$ for all $t \in [t_0, t_1]$. Suppose that $\|w(t)\| \leq \mathrm{w}$, $\forall (t) \in [t_0, t_1]$ for some $\mathrm{w} > 0$. Based on Assumption 7, we further assume that $y^x = \varphi(x)$, and $y^z = \varphi(z)$. Let $L_h = L_x + L_y L_\varphi$, where L_φ is the Lipschitz constant of the implicit function φ. Then, $\|x(t) - z(t)\| \leq \|x_0 - z_0\| \exp[c_h(t-t_0)] + \frac{\mathrm{w}}{c_h}\Big(\exp[c_h(t-t_0)] - 1\Big)$ and $\Big\|y^x(t) - y^z(t)\Big\| \leq L_\varphi \|x_0 - z_0\| \exp[c_h(t-t_0)] + L_\varphi \frac{\mathrm{w}}{c_h}\Big(\exp[c_h(t-t_0)] - 1\Big)$.*

Proof. Use similar techniques as in the proof for Corollary 3.4.1 and Theorem 3.4.1. □

Note that in using these results, we require the global information L_x, L_y, L_φ (Corollary 3.4.1), c (Theorem 3.4.1), and c_h(Corollary 3.4.2). Furthermore, the terms L_φ and c_h require special treatment because they involve the implicit function φ. Differentiating the algebraic equation (3.2.1b) with respect to x yields $\frac{\partial g}{\partial x} + \frac{\partial g}{\partial y}\frac{\partial y}{\partial x} = 0$, which gives,

$$\frac{\partial y}{\partial x} = -\Big(\frac{\partial g}{\partial y}\Big)^{-1}\frac{\partial g}{\partial x}. \tag{3.4.4}$$

For implementation, these terms can be computed off-line and stored for later use. However, global optimizations need to be solved. For example, computing c_h requires solving the non-convex problem,

$$(\mathcal{P}3) \quad c_h = \max_{(x,y)\in\mathcal{D}_x\times\mathcal{D}_y} \mu\Big(\frac{\partial h}{\partial x}(x,y)\Big).$$

We can either resort to global optimization solvers or estimate the value by sample-based methods.

3.5 Reach-Set Computation

Designing tractable algorithms for computing reach-sets for nonlinear systems is a challenging problem. In this section, we use results from Sections 3.3 and 3.4 to propose an efficient method for computing a sufficiently accurate reach-set estimate for nonlinear DAE systems with uncertain initial conditions and external disturbances.

3.5.1 Reach-Set with Uncertain Initial Conditions

The orthotope $\mathcal{X}_0 = \{\tilde{x}_0 \in \mathbb{R}^n \big| x_0 - \Delta x_0 \leq \tilde{x}_0 \leq x_0 + \Delta x_0\}$ of all possible initial conditions can be equivalently characterized as $\mathcal{X}_0 := x_0 \oplus \mathcal{B}$, where x_0 is the nominal initial point and $\mathcal{B} := \{\Delta\tilde{x}_0 \in R^n : -\Delta x_0 \leq \Delta\tilde{x}_0 \leq \Delta x_0\}$. In [19], it is shown that trajectory sensitivities can be used to approximate the reach-set efficiently, by locating worst-case vertices of the uncertainty set. Under the affine transformations (3.2.5), the orthotope $\mathcal{B}$ is shifted and distorted to form time-dependent parallelotopes:

$$\mathcal{P}^{\phi}(t) = \phi(x_0,t) + \frac{\partial\phi(x_0,t)}{\partial x_0}\mathcal{B}, \tag{3.5.1a}$$

$$\mathcal{P}^{\psi}(t) = \psi(x_0,t) + \frac{\partial\psi(x_0,t)}{\partial x_0}\mathcal{B}. \tag{3.5.1b}$$

Since the orthotope $\mathcal{B}$ is convex, the affine transformation (3.2.5) maintains its convexity. Moreover, the vertices of $\mathcal{B}$ are mapped to the vertices of $\mathcal{P}^{\phi}(t)$ and $\mathcal{P}^{\psi}(t)$, which define the approximated boundaries of the reach-set. However, there is no guarantee that such approximated boundaries will cover the true reach-set since the first-order trajectory approximations possess error. By taking advantage of the established error bounds, we can compute an over-approximation of the reach-set. In practice, the error bound is estimated from the simplified problem ($\mathcal{P}2$), which increases the confidence of covering

the true reach-set.

It follows that we only need to bound approximation error for the extreme vertex cases of $\mathcal{P}^{\phi}(t), \mathcal{P}^{\psi}(t)$. Define the time-dependent error bound tubes as,

$$\mathcal{E}^{\phi}(t) \triangleq \{\tilde{e}(t) \in \mathbb{R}^n \Big| |\tilde{e}_i(t)| \leq \frac{M^{\phi_i}(t)}{2} ||\Delta x_0||_1^2\}, \tag{3.5.2a}$$

$$\mathcal{E}^{\psi}(t) \triangleq \{\tilde{e}(t) \in \mathbb{R}^m \Big| |\tilde{e}_j(t)| \leq \frac{M^{\psi_j}(t)}{2} ||\Delta x_0||_1^2\}, \tag{3.5.2b}$$

$$\forall i = 1, \ldots, n, \ \forall j = 1, \ldots, m,$$

where Δx_0 denotes the maximum deviations from the nominal initial point x_0, i.e. the vertices of $\mathcal{X}_0$. Theoretically, the terms M^{ϕ_i} and M^{ψ_i} are computed from ($\mathcal{P}$1). In practice, we instead use the $\hat{M}^{\phi_i}$ and $\hat{M}^{\psi_i}$ from ($\mathcal{P}$2).

Consider uncertain initial conditions $\tilde{x}_0$ within the set $\mathcal{X}_0$, and define the reach-set of all perturbed trajectories $x(t) = \phi(\tilde{x}_0, t)$, $y(t) = \psi(\tilde{x}_0, t)$ originating from $\mathcal{X}_0$ to be,

$$\begin{bmatrix} \mathcal{X}(t) \\ \mathcal{Y}^x(t) \end{bmatrix} = \begin{bmatrix} \phi(\mathcal{X}_0, t) \\ \psi(\mathcal{X}_0, t) \end{bmatrix} \triangleq \left\{ \begin{array}{l|c} x(t) \in \mathbb{R}^n & \dot{x}(t) = f(x(t), y(t)) \\ y(t) \in \mathbb{R}^m & 0 = g(x(t), y(t)), \ x(t_0) \in \mathcal{X}_0 \end{array} \right\}. \tag{3.5.3}$$

Based on the previous reasoning, we have the following over-approximation of the reach-set $\mathcal{X}(t)$, $\mathcal{Y}^x(t)$,

$$\mathcal{X}(t) \subset \mathcal{P}^{\phi}(t) \oplus \mathcal{E}^{\phi}(t), \tag{3.5.4a}$$

$$\mathcal{Y}^x(t) \subset \mathcal{P}^{\psi}(t) \oplus \mathcal{E}^{\psi}(t), \tag{3.5.4b}$$

where $\oplus$ denotes Minkowski sum. Since $\mathcal{P}^{\phi}(t)$, $\mathcal{P}^{\psi}(t)$, $\mathcal{E}^{\phi}(t)$, and $\mathcal{E}^{\psi}(t)$ are polytopes represented by vertices, their Minkowski sum can be converted to taking combinations of vertices and computing their convex hull, which is relatively tractable.

3.5.2 Reach-Set with External Disturbances

By using results from Section 3.4, we are also able to quantify the effects of external disturbances. By Corollary 3.4.2, we know that for every initial point $x_0 \in \mathcal{X}_0$, the trajectory $(x(t), y^x(t)),\ x(t_0) = x_0$ and $(z(t), y^z(t)),\ z(t_0) = x_0$ have the relationship,

$$\|x(t) - z(t)\| \leq \frac{\mathrm{w}}{c_h}\Big(\exp[c_h(t - t_0)] - 1\Big), \tag{3.5.5a}$$

$$\Big\|y^x(t) - y^z(t)\Big\| \leq L_{\varphi}\frac{\mathrm{w}}{c_h}\Big(\exp[c_h(t - t_0)] - 1\Big), \tag{3.5.5b}$$

which implies the trajectories $z(t)$, $y^z(t)$ must lie within the tubes of time-varying radius $\frac{\mathrm{w}}{c_h}\Big(\exp[c_h(t-t_0)]-1\Big)$, $L_\varphi\frac{\mathrm{w}}{c_h}\Big(\exp[c_h(t-t_0)]-1\Big)$ around the disturbance-free trajectories $x(t)$, $y^x(t)$, respectively. Define the tubes as:

$$\mathcal{T}^\phi(t) \triangleq \Big\{\tilde{\xi}(t)\in\mathbb{R}^n \Big| \big\|\tilde{\xi}(t)\big\| \le \frac{\mathrm{w}}{c_h}\Big(\exp[c_h(t-t_0)]-1\Big)\Big\}, \tag{3.5.6a}$$

$$\mathcal{T}^\psi(t) \triangleq \Big\{\tilde{\xi}(t)\in\mathbb{R}^m \Big| \big\|\tilde{\xi}(t)\big\| \le L_\varphi\frac{\mathrm{w}}{c_h}\Big(\exp[c_h(t-t_0)]-1\Big)\Big\}, \tag{3.5.6b}$$

where the vector norm is the same as the one used for defining the logarithmic norm.

Next consider all initial points in the set $\mathcal{X}_0$. In equation (3.5.3) we have defined the reach-set of all disturbance-free trajectories originating from $\mathcal{X}_0$ to be $\mathcal{X}(t)$, $\mathcal{Y}^x(t)$. Similarly, define $\mathcal{Z}(t)$, $\mathcal{Y}^z(t)$ to be the reach-set for system with disturbances,

$$\begin{bmatrix}\mathcal{Z}(t)\\ \mathcal{Y}^z(t)\end{bmatrix} \triangleq \left\{ \begin{matrix} z(t)\in\mathbb{R}^n \\ y(t)\in\mathbb{R}^m \end{matrix} \middle| \begin{matrix} \dot{z}(t) = f(z(t),y(t)) + w(t) \\ 0 = g(z(t),y(t)),\ z(t_0)\in\mathcal{X}_0 \end{matrix} \right\}. \tag{3.5.7}$$

From equation (3.5.5), we know that the set of noisy trajectories $\mathcal{Z}(t)$, $\mathcal{Y}^z(t)$ is over-bounded by the Minkowski sum,

$$\mathcal{Z}(t) \subset \mathcal{X}(t) \oplus \mathcal{T}^\phi(t), \tag{3.5.8a}$$

$$\mathcal{Y}^z(t) \subset \mathcal{Y}^x(t) \oplus \mathcal{T}^\psi(t). \tag{3.5.8b}$$

Together with equation (3.5.4), we obtain the final expression for an estimated over-approximation of the reach-set,

$$\mathcal{Z}(t) \subset \mathcal{P}^\phi(t) \oplus \mathcal{E}^\phi(t) \oplus \mathcal{T}^\phi(t), \tag{3.5.9a}$$

$$\mathcal{Y}^z(t) \subset \mathcal{P}^\psi(t) \oplus \mathcal{E}^\psi(t) \oplus \mathcal{T}^\psi(t), \tag{3.5.9b}$$

where $\mathcal{P}^\phi(t)$, $\mathcal{P}^\psi(t)$ are defined in equation (3.5.1), $\mathcal{E}^\phi(t)$, $\mathcal{E}^\psi(t)$ are defined in equation (3.5.2), and $\mathcal{T}^\phi(t)$, $\mathcal{T}^\psi(t)$ are defined in equation (3.5.6).

3.6 Simulation Results

We demonstrate the proposed reach-set computation approach through a single machine infinite bus (SMIB) power system, as shown in Fig. 3.1. The DAE model for the SMIB

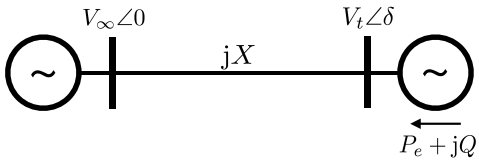

Figure 3.1: Single machine infinite bus power system.

system is given by:

$$\frac{d}{dt}\begin{bmatrix} x_1 \\ x_2 \end{bmatrix} = \begin{cases} x_2 \\ \frac{1}{M}\Big(P_m - \frac{V_\infty V_t}{X}\sin(x_1) - Dx_2\Big) + w(t) \end{cases} \tag{3.6.1a}$$

$$0 = \Big(\frac{V_\infty V_t}{X}\sin(x_1)\Big)^2 + \Big(\frac{V_t^2}{X} - y\Big)^2 - \frac{V_\infty^2 V_t^2}{X^2}. \tag{3.6.1b}$$

The dynamic states are $x = [x_1, x_2]^\intercal = [\delta, \omega]^\intercal$, where δ is the rotor angle and ω is the angular velocity. The algebraic state is $y = Q$, the reactive power generation. V_∞ is the constant voltage magnitude of the infinite bus, V_t is the voltage magnitude of the generator bus, M is the inertia constant, P_m is the mechanical power, X is the line reactance, and D is the damping. An unknown external disturbance term $w(t)$ is added to the second differential equation. It is modeled as a uniformly distributed random variable, with a bound of $\|w(t)\| \leq \mathrm{w} = 0.005$. The vector norm is defined as $\|\cdot\| = \sqrt{(\cdot)^\intercal P(\cdot)}$, where P solves the Lyapunov equation $A^\intercal P + PA + Q = 0$, where $Q = I$, and A is the Jacobian matrix evaluated at the stable equilibrium. With this vector norm, the logarithmic norm is defined accordingly as, $\mu(J) = \lambda_{max}\Big(\frac{(P^{1/2}JP^{-1/2}) + (P^{1/2}JP^{-1/2})^\intercal}{2}\Big)$, where λ_{max} represents the largest eigenvalue.

The system parameters are set to $V_\infty = 1$ pu, $V_t = 1$ pu, $M = 7.3784$ pu, $P_m = 3.1831$ pu, $X = 1/6$ pu, and $D = 1$ pu. For the nominal case, initial conditions are $x_0 = [0.55, 0.15]^\intercal$, giving $y_0 = 0.8849$. The implicit trapezoidal method was adopted to numerically integrate the DAE models describing the dynamics of states, the first- and second-order sensitivities. When including the stochastic disturbance, the trapezoidal integration method was modified as described in [100] to approximate the integration of the stochastic differential equation. We assume that the initial condition for rotor angle δ is uncertain and lies within the range $[0.5, 0.6]$. The logarithmic norm is estimated off-line as $\mu(J(x, y)) \leq c_h = -0.0104$, over the operating range.

Figure 3.2 shows the reach-set when there are only initial condition uncertainties but no external disturbance. The red solid lines indicate the reach-set estimated using the trajectory sensitivity (TS) method. The blue dash-dot lines give the theoretical bound de-

rived using the logarithmic norm (LN). The green dashed lines are eleven true trajectories with their initial conditions uniformly distributed over the initial condition set. It can be observed that all trajectories are contained within the estimated and theoretical bounds. Moreover, the reach-set estimation given by the trajectory sensitivity method is much tighter than the theoretical bound, while still encompassing all the true trajectories.

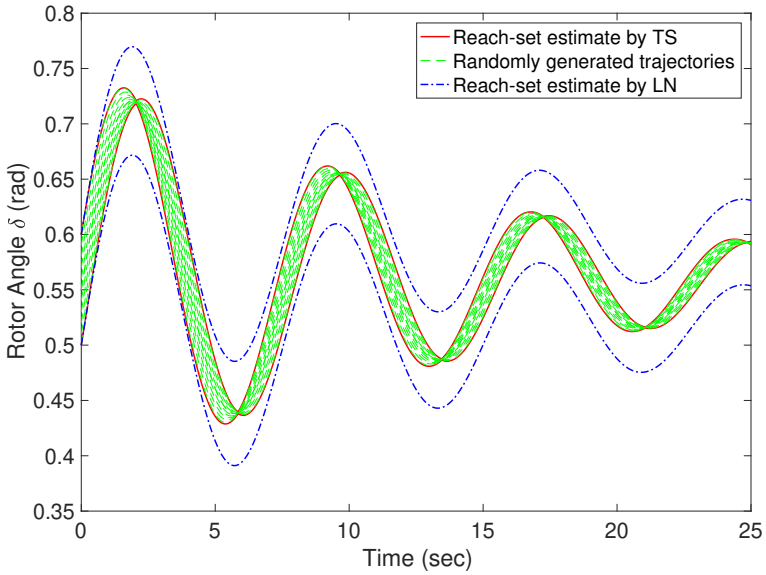

Figure 3.2: Reach-set estimates based on the trajectory sensitivity and logarithmic norm methods for uncertain initial conditions.

Figure 3.3 presents the case when there are only external disturbances but no initial condition uncertainty. The bound provided by the logarithmic norm is shown by blue lines. The green dashed lines are 30 randomly generated trajectories.

Finally, we consider the case when there are both uncertain initial conditions and external disturbances. The reach-set estimated by the trajectory sensitivity plus logarithmic norm (TS+LN) method and by the logarithmic norm only are presented in Fig. 3.4. The red solid lines refer to the bound given by the TS+LN method and the blue dash-dot lines refer to the bound given by the logarithmic norm. The green dashed lines are 55 randomly generated true trajectories emanating from the initial condition set and subjected to external disturbances. It can be observed that the reach-set estimation given by the TS+LN method is able to cover all realizations without being overly conservative, especially when the simulation horizon was quite short. The theoretical bound provided by the logarithmic norm is guaranteed to enclose all the realizations but is more conservative.

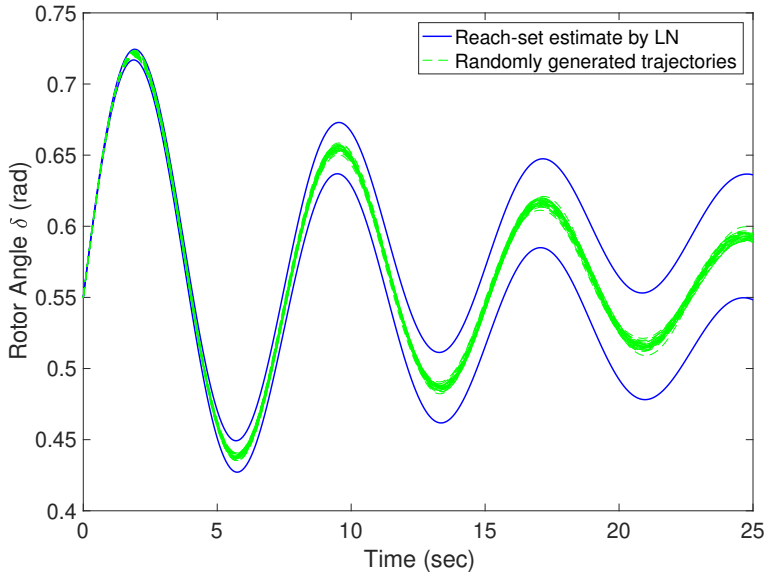

Figure 3.3: Reach-set estimate based on the logarithmic norm method under external disturbances.

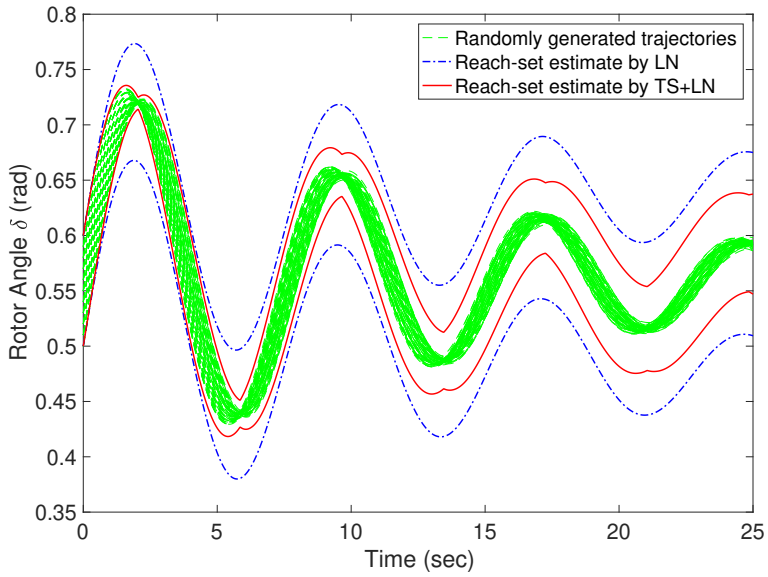

Figure 3.4: Reach-set estimates based on the TS+LN and logarithmic norm methods for uncertain initial conditions and external disturbances.

3.7 Chapter Conclusion

This chapter proposed an efficient approach to constructing a sufficiently accurate estimation of the reach-set of nonlinear DAE systems, under uncertain initial conditions and/or parameters, and external disturbances. This approach is based on establishing

an error bound for the trajectory sensitivity method, as well as characterizing the effects of external disturbances using the logarithmic norm. Although the bound derived from the logarithmic norm is guaranteed to enclose the true reach-set, the trajectory sensitivity method provides a much less conservative reach-set estimation.

CHAPTER 4

Modeling and Control of Inverter-Based Resources for Autonomous Grid-Interconnection

4.1 Chapter Introduction

Due to environmental and sustainability considerations, power systems are currently embracing a significant transition from fossil-fuel-based synchronous generation to renewable and distributed energy resources (DERs) [7]. It is well-known that the physics of conventional synchronous machines guarantee an instantaneous inertial response to power imbalance, which is a favorable feature for power systems. DERs such as fuel cells, solar photovoltaics (PVs), and wind turbines, however, are typically connected to power systems through power electronics, which possess drastically different dynamic characteristics compared to synchronous machines. Careful control and coordination of inverters are necessary to ensure a successful transition to future inverter-based smart grids.

Microgrids offer a promising direction to provide coordinated control of DERs with higher flexibility and efficiency, thereby increasing the penetration level of renewables in power systems [101]. Microgrids, defined as small-scale power systems which aggregate local DERs and loads, are interfaced with the main grid through a single point of common coupling (PCC). The structure of a generic inverter-based microgrid is shown in Fig. 4.1. From the point of view of the main grid, the microgrid can be treated as a single controllable entity, which can operate either in grid-connected mode or in islanded mode, i.e., as a stand-alone system. In grid-connected mode, the main grid dominates the system-level dynamics, and any microgrid generation/load imbalance is satisfied by the main grid. In islanded mode, the microgrid is responsible for establishing the voltage and frequency, and generates the power needed to supply the local loads and losses.

Microgrids are expected to have the capability to switch between grid-connected and islanded operation, upon the opening and reclosing of the circuit breaker at the PCC.

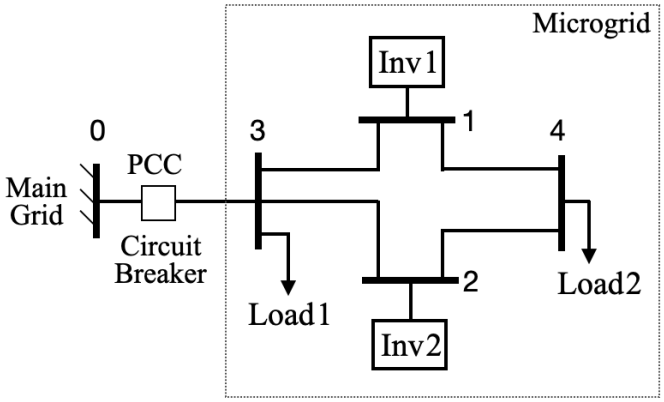

Figure 4.1: Structure of a generic inverter-based network.

Such mode switching is typically achieved through a reconfiguration within the inverter control scheme [102, 103]. In grid-connected operation, the inverter is controlled using a grid-following scheme [28], where the inverter supplies pre-determined active and reactive power, while tracking the terminal voltage set by the main grid. In islanded operation, the inverter is controlled using a grid-forming scheme [29, 31], which establishes terminal voltage according to voltage magnitude and frequency set-points. Other inverter control techniques exist in the literature [104, 105] that avoid switching of inverter control schemes. However, they rely on complex control architectures and are difficult to implement in practice. In [105], a modified voltage-based droop control is developed in order to achieve smooth switching between grid-connected and islanded operation, which requires communication and selecting one particular inverter as the synchronization unit.

In this chapter, we present a novel inverter control scheme that can be used in microgrids to achieve autonomous mode switching between grid-connected and islanded operations. The idea of the proposed controller is motivated by a previous control scheme in [106]. The controller aims to regulate voltage magnitude at the inverter terminal bus and the active power generation. A phase-locked loop (PLL) [30] is used for tracking grid frequency and angle in grid-connected mode and for achieving synchronization in islanded mode. Droop characteristics are enforced to achieve power sharing between inverters. We design lower-level cascaded voltage and current controllers, and include the fast dynamics of the output filter and the line dynamics when modeling the inverter-based network. The proposed controller achieves islanding (i.e., the transition from grid-connected to islanded mode) smoothly due to the voltage forming and power-sharing capability. Reconnection (i.e., the transition from islanded to grid-connected mode) is achieved due to the fact that the voltage in the microgrid is controlled close to the nominal value and the PLL re-synchronizes the microgrid to the main grid.

The chapter is organized as follows: Sections 4.2 presents preliminaries on rotational reference frames and modeling considerations. The proposed inverter model and control scheme are given in Section 4.3. Section 4.4 provides the model of the inverter-based network. The steady-state characteristics of the inverter-based network in both grid-connected and islanded modes are analyzed in Section 4.5. Small-signal stability and simulation results are given in Section 4.6. Conclusions are provided in Section 4.7.

4.2 Preliminaries

Preliminaries on rotational reference frames and the transformations between representations with respect to different frames are introduced in this section.

4.2.1 Rotational Reference Frames

For ease of modeling and control, rotational reference frames, referred to as dq-frames, are adopted for inverters to transform three-phase sinusoidal quantities into dq-quantities [26]. Each inverter adopts a local rotational dq-frame that rotates at a frequency defined locally. All physical and control variables internal to the inverter are represented with respect to its local dq-frame. The rotational speed of the dq-frame for inverter i is denoted by $(\omega_{\text{pll},i} + \omega_0)\omega_\text{b}$ rad/s, where ω_b is the base frequency, $\omega_0 = 1$ p.u. is the nominal frequency, and $\omega_{\text{pll},i}$ will be determined by the corresponding phase-locked loop (PLL) block as further explained in Section 4.3. A pictorial explanation of the rotational reference frames is given in Fig. 4.2.

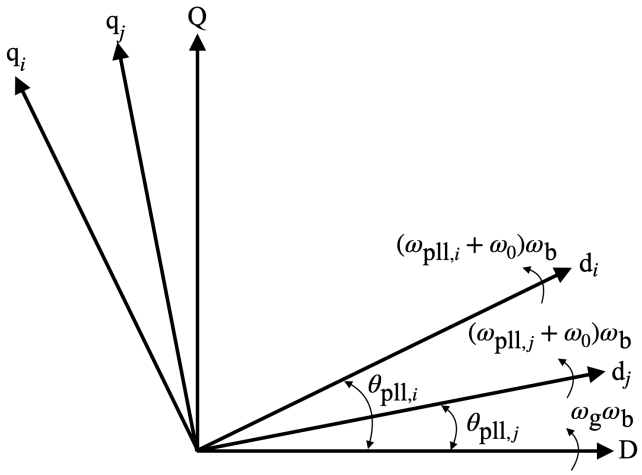

Figure 4.2: Diagram of local and global rotational reference frames.

The modeling of the interconnected network demands a global rotational reference

frame, denoted by the DQ-frame. At the interface of the inverter terminal to the network, the local variables are transformed to the global reference frame. We denote the rotational speed of the DQ-frame to be $\omega_g\omega_b$ rad/s. In theory, the value of ω_g can be selected arbitrarily. However, there are two frequencies that are most useful, i.e., the nominal frequency ω_0 and the steady-state frequency $\omega_{pll}^{ss} + \omega_0$ at which the system operates in steady state.

In normal power system operation, the system frequency at steady state should be quite close to the nominal frequency. Therefore, the nominal case where the system operates at the nominal frequency is an important case to be analyzed. In the nominal case, the rotational speed of the global reference frame should be chosen as the nominal frequency $\omega_0\omega_b$ rad/s, and we refer to this specific reference frame as the $\overline{\text{DQ}}$-frame.

In general case, the actual system frequency at steady state may not be the nominal frequency, that is, $\omega_{pll}^{ss} \neq 0$. The angles of the system will never settle to a steady state relative to the $\overline{\text{DQ}}$-frame, but rather will continually vary over time by $\omega_{pll}^{ss}\omega_b t$ rad relative to the $\overline{\text{DQ}}$-frame. Note though that all angle differences will achieve steady state. It is desirable to express converged conditions as an equilibrium point. This can be achieved by considering a reference frame, denoted by the D'Q'-frame, that is rotating at the constant frequency $(\omega_{pll}^{ss} + \omega_0)\omega_b$ rad/s. The D'Q'-frame is rotating at $\omega_{pll}^{ss}\omega_b$ rad/s relative to the $\overline{\text{DQ}}$-frame. Then angles in the $\overline{\text{DQ}}$-frame and D'Q'-frame are related by,

$$\theta^{\overline{\text{DQ}}} = \theta^{\text{D'Q'}} + \omega_{pll}^{ss}\omega_b t. \tag{4.2.1}$$

The formulation based on the D'Q'-frame requires the knowledge of the steady-state frequency ω_{pll}^{ss}, which can be obtained from performing dynamic simulation and observing the steady-state frequency, or by solving a set of nonlinear equations describing the equilibrium condition. The model is useful since it is normal in power system simulation to start from equilibrium (i.e., the power flow solution) and introduce a disturbance. The steady-state frequency ω_{pll}^{ss} is obtained as part of that equilibrium solution. Other formulations exist that are based on choosing one of the local dq-frame of a specific inverter as the global reference frame [29]. Since we prefer a "plug-and-play" scheme where the inverters serve equal roles, such formulations are not considered. The remaining results of this chapter are firstly presented based on the general global DQ-frame that rotates at the speed $\omega_g\omega_b$ rad/s. The special cases when $\omega_g = \omega_0$ and $\omega_g = \omega_{pll}^{ss} + \omega_0$ will also be discussed.

4.2.2 Transformation of Variables in Local and Global Reference Frames

Define the rotation matrix $\mathcal{R}(\theta)$ parameterized by the angle θ,

$$\mathcal{R}(\theta) = \begin{bmatrix} \cos\theta & -\sin\theta \\ \sin\theta & \cos\theta \end{bmatrix}, \tag{4.2.2}$$

where θ denotes the angle of a local dq-frame with respect to the global DQ-frame, as depicted in Fig. 4.2. We have that,

$$\mathcal{R}(\theta)^{-1} = \mathcal{R}(-\theta). \tag{4.2.3}$$

For a variable y, let $y^{\mathrm{DQ}} = [y^{\mathrm{D}}, y^{\mathrm{Q}}]^\intercal$ and $y^{\mathrm{dq}} = [y^{\mathrm{d}}, y^{\mathrm{q}}]^\intercal$ denote the representation of y with respect to the global DQ-frame and the local dq-frame, respectively. Then the transformation between y^{DQ} and y^{dq} is expressed as,

$$\begin{bmatrix} y^{\mathrm{D}} \\ y^{\mathrm{Q}} \end{bmatrix} = \mathcal{R}(\theta) \begin{bmatrix} y^{\mathrm{d}} \\ y^{\mathrm{q}} \end{bmatrix}, \tag{4.2.4}$$

$$\begin{bmatrix} y^{\mathrm{d}} \\ y^{\mathrm{q}} \end{bmatrix} = \mathcal{R}(-\theta) \begin{bmatrix} y^{\mathrm{D}} \\ y^{\mathrm{Q}} \end{bmatrix}. \tag{4.2.5}$$

4.3 Inverter Model and Control Scheme

This section describes the proposed inverter model and inverter control scheme. The inverter control scheme is demonstrated in Fig. 4.3. This controller aims to establish the voltage magnitude at the inverter terminal and the active power delivered by the inverter. It consists of the power calculation and filtering block (not shown in Fig. 4.3), the PLL, the P-ω droop and Q-V droop, the active power controller, and the cascaded voltage and current controllers.

4.3.1 Power Calculation and Filtering

The active and reactive power are computed based on dq-frame voltage and current. The computed active and reactive power are filtered through a low-pass filter to remove high-frequency components of the electrical quantities. The equations are given by,

$$p = v_{\mathrm{t}}^{\mathrm{d}} i_{\mathrm{t}}^{\mathrm{d}} + v_{\mathrm{t}}^{\mathrm{q}} i_{\mathrm{t}}^{\mathrm{q}} \tag{4.3.1}$$

$$q = v_{\mathrm{t}}^{\mathrm{q}} i_{\mathrm{t}}^{\mathrm{d}} - v_{\mathrm{t}}^{\mathrm{d}} i_{\mathrm{t}}^{\mathrm{q}} \tag{4.3.2}$$

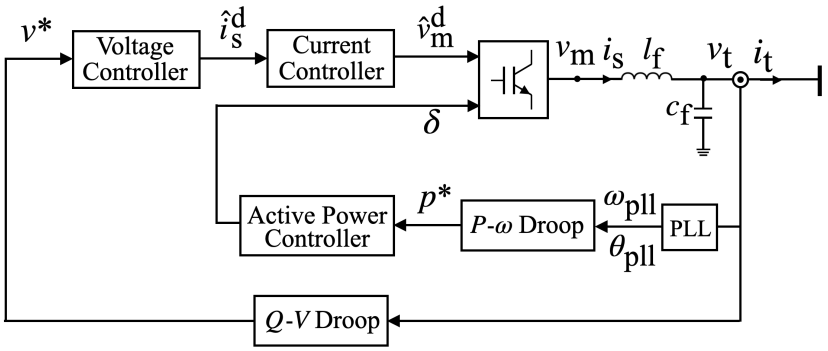

Figure 4.3: Schematic of the inverter model and control blocks.

$$\dot{\tilde{p}} = \omega_c(p - \tilde{p}) \tag{4.3.3}$$

$$\dot{\tilde{q}} = \omega_c(q - \tilde{q}), \tag{4.3.4}$$

where p and q are the instantaneous active and reactive power measured at the inverter terminal bus, i.e., where the inverter is connected to the grid, $\tilde{p}$ and $\tilde{q}$ are the filtered version of the active and reactive power, v_t^d and v_t^q are the d- and q-components of the voltage at the inverter terminal bus, and i_t^d and i_t^q are the d- and q-components of the current at inverter terminal bus. The parameter ω_c is the cut-off frequency of the low-pass filter.

4.3.2 Phase-Locked Loop

In order to connect the inverter to the grid, it is necessary to establish a local AC waveform that tracks the terminal bus voltage. This is typically achieved using a PLL, where a modulated signal θ_{pll}, i.e., the PLL angle, serves as an estimate of the terminal voltage angle θ_t. Note that θ_t is unknown to the inverter while θ_{pll} is accessible to the inverter for control purpose. Also, the PLL frequency ω_{pll} is a filtered version of the terminal bus frequency and is also available for inverter control. The frequency variables are in per unit, and represent deviations of the actual frequency from the nominal frequency $\omega_0 = 1\,\text{p.u.}$.

The PLL dynamics can be written in the form,

$$\dot{\xi} = \theta_t - \theta_{pll} \tag{4.3.5}$$

$$\omega_{pll} = K_{p,pll}(\theta_t - \theta_{pll}) + K_{i,pll}\xi \tag{4.3.6}$$

$$\dot{\theta}_{pll} = (\omega_{pll} + \omega_0 - \omega_g)\omega_b \tag{4.3.7}$$

$$0 = v_t^D \sin(\theta_t) - v_t^Q \cos(\theta_t), \tag{4.3.8}$$

where ξ is the integral state, ω_{pll} is the PLL frequency, and θ_{pll} is the PLL angle. As shown in Fig. 4.4, θ_{pll} establishes the angle of the local dq-frame with respect to the global DQ-frame rotating at speed $\omega_g\omega_b$ rad/s. Fig. 4.4 also shows the real and imaginary parts of v_t which are denoted by v_t^D and v_t^Q, respectively, in the global DQ-frame. Their counterparts in the local dq-frame are denoted by v_t^d and v_t^q, respectively. The angle θ_t is related to v_t^D and v_t^Q by equation (4.3.8). The parameters $K_{i,\text{pll}}$ and $K_{p,\text{pll}}$ are the integral and proportional gains.

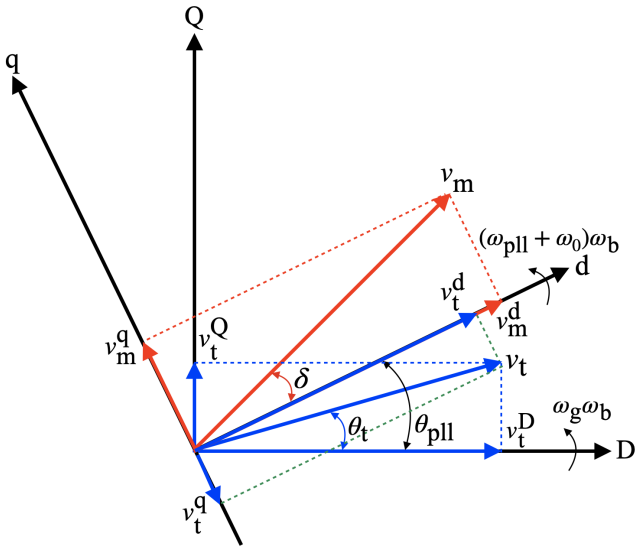

Figure 4.4: Diagram showing different vectors in the inverter model.

The PLL dynamics seek to drive $\theta_t - \theta_{\text{pll}}$ to zero. As can be seen from Fig. 4.4, that is equivalent to aligning the d-axis of the local dq-frame with the terminal voltage. Therefore, at steady state, $v_t^q = 0$ and $v_t^d = |v_t|$, the magnitude of v_t.

Typically, fast PLL dynamic response means fast phase locking. However, the fast response also makes the PLL susceptible to noise. Therefore, a careful trade-off is required to achieve a balance between fast response and suppression of noise.

4.3.3 Active Power Control and P-ω Droop

The P-ω droop characteristic is implemented where the term "droop" is standard in the power systems community and refers to proportional control. We enforce,

$$p^* = p^0 - m_p\omega_{\text{pll}}, \tag{4.3.9}$$

where p^0 is the external reference value for active power, ω_{pll} is the PLL frequency, the parameter m_p is the P-ω droop constant, and p^* is the resulting set-point for active power,

based on the droop characteristic. By properly choosing the droop constants for the inverters, for example, based on the inverter capacity, we can achieve load sharing when there is a power imbalance in the power system, just as in the case with conventional synchronous machines.

We then use an integral controller to drive the filtered active power $\tilde{p}$ to its set-point p^*. This is achieved through,

$$\dot{\delta} = K_{\mathrm{i},p}(p^* - \tilde{p}), \tag{4.3.10}$$

where $K_{\mathrm{i},p}$ is the integral gain, and δ is the angle between the d-axis of the dq-frame and the inverter internal bus voltage v_m. Because the angle difference δ strongly influences the generated power p, it can be used to drive the active power to its set-point value.

4.3.4 Q-V Droop

A droop characteristic is also implemented between reactive power and voltage magnitude,

$$v^* = v^0 - m_q(q^0 - \tilde{q}), \tag{4.3.11}$$

where v^0 is the external reference value for the voltage magnitude of the inverter terminal bus, q^0 is the external reference value for reactive power, $\tilde{q}$ is the filtered reactive power, m_q is the reactive power droop constant, and v^* is the resulting set-point for the terminal voltage magnitude.

4.3.5 Inner-Loop Cascaded Voltage and Current Controllers

Faster inner-loop cascaded voltage and current controllers are widely used in inverter control. They are designed to suppress high-frequency disturbances and damp the output LC filter [29]. In the proposed inverter control scheme, we design a voltage and a current controller, for controlling the d-component quantities.

The voltage controller is described by,

$$\dot{\phi}_{\mathrm{d}} = v^* - v_{\mathrm{t}}^{\mathrm{d}} \tag{4.3.12}$$

$$\hat{i}_{\mathrm{s}}^{\mathrm{d}} = k_{\mathrm{p}}^v(v^* - v_{\mathrm{t}}^{\mathrm{d}}) + k_{\mathrm{i}}^v\phi_{\mathrm{d}} + k_{\mathrm{f}}^v i_{\mathrm{t}}^{\mathrm{d}} - (\omega_{\mathrm{pll}} + \omega_0)c_{\mathrm{f}}v_{\mathrm{t}}^{\mathrm{q}}, \tag{4.3.13}$$

where ϕ_{d} is the integral state, k_{p}^v, k_{i}^v, k_{f}^v are the proportional gain, integral gain, and feedforward gain, respectively. The parameter c_{f} denotes filter capacitance in per unit.

The current controller is described by,

$$\dot{\gamma}_{\mathrm{d}} = \hat{i}_{\mathrm{s}}^{\mathrm{d}} - i_{\mathrm{s}}^{\mathrm{d}} \tag{4.3.14}$$

$$\hat{v}_{\mathrm{m}}^{\mathrm{d}} = k_{\mathrm{p}}^{i}(\hat{i}_{\mathrm{s}}^{\mathrm{d}} - i_{\mathrm{s}}^{\mathrm{d}}) + k_{\mathrm{i}}^{i}\gamma_{\mathrm{d}} + k_{\mathrm{f}}^{i}v_{\mathrm{t}}^{\mathrm{d}} - (\omega_{\mathrm{pll}} + \omega_0)l_{\mathrm{f}}i_{\mathrm{s}}^{\mathrm{q}}, \tag{4.3.15}$$

where γ_{d} is the integral state, k_{p}^{i}, k_{i}^{i}, k_{f}^{i} are the proportional gain, integral gain, and feedforward gain, respectively. The parameter l_{f} denotes filter inductance in per unit.

Compared to standard cascaded voltage and current controllers in the literature, we only control the d-component variables. This reflects the novel structure of our control scheme, which exploits angle difference δ for active power control and manipulates $\hat{v}_{\mathrm{m}}^{\mathrm{d}}$ for voltage control.

4.3.6 Inverter Modulation

The current controller provides the set-point $\hat{v}_{\mathrm{m}}^{\mathrm{d}}$ for the d-component of the inverter internal bus voltage. The active power controller provides the set-point for the inverter internal bus angle δ (relative to the d-axis). These set-points are fed into a PWM block to provide a modulation signal for the inverter. For simplicity, we assume that the inverter internal bus voltage can be perfectly controlled to the set-point, so $v_{\mathrm{m}}^{\mathrm{d}} = \hat{v}_{\mathrm{m}}^{\mathrm{d}}$. Then, we can solve the following algebraic equations to compute $|v_{\mathrm{m}}|$ and $v_{\mathrm{m}}^{\mathrm{q}}$,

$$|v_{\mathrm{m}}|\cos(\delta) = v_{\mathrm{m}}^{\mathrm{d}} \tag{4.3.16}$$

$$|v_{\mathrm{m}}|\sin(\delta) = v_{\mathrm{m}}^{\mathrm{q}}, \tag{4.3.17}$$

where $|v_{\mathrm{m}}|$ is the magnitude of the inverter internal bus voltage v_{m}, and $v_{\mathrm{m}}^{\mathrm{q}}$ is the q-component of v_{m}.

4.3.7 Output LC Filter

An output LC filter is augmented to remove undesired switching-frequency components from the output current spectrum [107]. The inductor is designed to limit the inductor current ripple, while the capacitor and inductor work together to filter high-frequency harmonics.

The dynamics of the output LC filter is given as follows,

$$\dot{i}_{\mathrm{s}}^{\mathrm{d}} = \frac{\omega_{\mathrm{b}}}{l_{\mathrm{f}}}(v_{\mathrm{m}}^{\mathrm{d}} - v_{\mathrm{t}}^{\mathrm{d}}) + \omega_{\mathrm{b}}(\omega_{\mathrm{pll}} + \omega_0)i_{\mathrm{s}}^{\mathrm{q}} \tag{4.3.18}$$

$$\dot{i}_{\mathrm{s}}^{\mathrm{q}} = \frac{\omega_{\mathrm{b}}}{l_{\mathrm{f}}}(v_{\mathrm{m}}^{\mathrm{q}} - v_{\mathrm{t}}^{\mathrm{q}}) - \omega_{\mathrm{b}}(\omega_{\mathrm{pll}} + \omega_0) i_{\mathrm{s}}^{\mathrm{d}} \tag{4.3.19}$$

$$\dot{v}_{\mathrm{t}}^{\mathrm{d}} = \frac{\omega_{\mathrm{b}}}{c_{\mathrm{f}}}(i_{\mathrm{s}}^{\mathrm{d}} - i_{\mathrm{t}}^{\mathrm{d}}) + \omega_{\mathrm{b}}(\omega_{\mathrm{pll}} + \omega_0) v_{\mathrm{t}}^{\mathrm{q}} \tag{4.3.20}$$

$$\dot{v}_{\mathrm{t}}^{\mathrm{q}} = \frac{\omega_{\mathrm{b}}}{c_{\mathrm{f}}}(i_{\mathrm{s}}^{\mathrm{q}} - i_{\mathrm{t}}^{\mathrm{q}}) - \omega_{\mathrm{b}}(\omega_{\mathrm{pll}} + \omega_0) v_{\mathrm{t}}^{\mathrm{d}}, \tag{4.3.21}$$

where $i_{\mathrm{s}}^{\mathrm{dq}}$ is the current flowing through the inductor and $i_{\mathrm{t}}^{\mathrm{dq}}$ is the current flowing to the grid, as shown in Fig. 4.3. Again, $v_{\mathrm{m}}^{\mathrm{dq}}$ and $v_{\mathrm{t}}^{\mathrm{dq}}$ are the internal and terminal voltages of the inverter, respectively. l_{f} denotes filter inductance and c_{f} denotes filter capacitance. Note that the equations are written using per unit variables.

At steady state, the left-hand-sides of equations (4.3.18) to (4.3.21) are zero, and the dynamic model of the output filter reverts to the algebraic equations,

$$v_{\mathrm{m}}^{\mathrm{d}} - v_{\mathrm{t}}^{\mathrm{d}} = -(\omega_{\mathrm{pll}} + \omega_0) l_{\mathrm{f}} i_{\mathrm{s}}^{\mathrm{q}} \tag{4.3.22}$$

$$v_{\mathrm{m}}^{\mathrm{q}} - v_{\mathrm{t}}^{\mathrm{q}} = (\omega_{\mathrm{pll}} + \omega_0) l_{\mathrm{f}} i_{\mathrm{s}}^{\mathrm{d}} \tag{4.3.23}$$

$$i_{\mathrm{s}}^{\mathrm{d}} = i_{\mathrm{t}}^{\mathrm{d}} - (\omega_{\mathrm{pll}} + \omega_0) c_{\mathrm{f}} v_{\mathrm{t}}^{\mathrm{q}} \tag{4.3.24}$$

$$i_{\mathrm{s}}^{\mathrm{q}} = i_{\mathrm{t}}^{\mathrm{q}} + (\omega_{\mathrm{pll}} + \omega_0) c_{\mathrm{f}} v_{\mathrm{t}}^{\mathrm{d}}. \tag{4.3.25}$$

4.3.8 Compact Inverter Model

For analysis of the inverter-based network, the model of an individual inverter developed in previous subsections is rewritten compactly as,

$$\dot{x} = f(x) + g(x) i_{\mathrm{t}}^{\mathrm{dq}} + F u^0, \tag{4.3.26}$$

where $i_{\mathrm{t}}^{\mathrm{dq}}$ denotes the current flowing out of the inverter, $u^0 = (p^0, q^0, v^0)^\intercal$ collects the external reference inputs. The vector x collects all the dynamic states in an individual inverter, that is, $x = (\tilde{p}, \tilde{q}, \xi, \theta_{\mathrm{pll}}, \delta, \phi_{\mathrm{d}}, \gamma_{\mathrm{d}}, i_{\mathrm{s}}^{\mathrm{dq}}, v_{\mathrm{t}}^{\mathrm{dq}}) \in \mathbb{R}^{11}$. The functions $f(x)$, $g(x)$, and the matrix F are derived from the inverter model.

4.4 Network Model

In this section, we present the model for the inverter-based network, including the line model and load model. The network topology is modeled by a weighted graph $\mathcal{G}$, consisting of node (bus) set $\mathcal{N}$, and edge (branch) set $\mathcal{E} \subseteq \mathcal{N} \times \mathcal{N}$. To model the inverter-based network, we consider three types of nodes. The infinite bus is indexed number 0, which represents the interface with the main grid and is viewed as a stiff voltage source

with voltage $v_\infty^{\mathrm{DQ}} = [1, 0]^\intercal$ [1]. There are $n \geq 1$ inverter buses collected in the index set $\mathcal{N}_\mathrm{I} = \{1, \dots n\}$. We consider l load buses in the network, which belong to the index set $\mathcal{N}_\mathrm{L} = \{n+1, \dots, n+l\}$. Overall, the index set can be written as $\mathcal{N} = \{0\} \cup \mathcal{N}_\mathrm{I} \cup \mathcal{N}_\mathrm{L}$ with cardinality $|\mathcal{N}| = 1 + l + n \triangleq N$. We assume that there are in total $|\mathcal{E}| = m$ branches in the network.

4.4.1 Phasor-Based Line Model

In the analysis of conventional power systems with synchronous machines, phasor-based representation is typically adopted for the network model, where fast line dynamics are omitted and the system frequency is assumed to be the nominal frequency. We first give the phasor-based representation of the network using line admittances. For each branch $(i, j) \in \mathcal{E}$ that connects node i and node j, the complex weight is given by the line admittance [2] $y_{ij} = y_{ji} = 1/(r_{ij} + j\omega_0 l_{ij})$, where r_{ij} is the line resistance and l_{ij} is the line inductance. Let $Y \in \mathbb{C}^{N \times N}$ denotes the complex admittance matrix of the network [3],

$$Y_{ij} = \begin{cases} \sum_{k \in \mathcal{N}_i} y_{ik}, & \text{if } i = j \\ -y_{ij}, & \text{if } (i, j) \in \mathcal{E} \\ 0, & \text{otherwise} \end{cases}$$

where the index set $\mathcal{N}_i$ represents the neighboring nodes connected to bus i.

Denote the nodal current injection at all buses by $\mathbf{i} = (i_\infty, \mathbf{i}_\mathrm{I}^\intercal, \mathbf{i}_\mathrm{L}^\intercal)^\intercal \in \mathbb{C}^N$, where i_∞, $\mathbf{i}_\mathrm{I}$, and $\mathbf{i}_\mathrm{L}$ denote the nodal current injections from the infinite bus, the inverter buses, and the load buses, respectively. Similarly, denote the nodal voltage at all buses by $\mathbf{v} = (v_\infty, \mathbf{v}_\mathrm{I}^\intercal, \mathbf{v}_\mathrm{L}^\intercal)^\intercal \in \mathbb{C}^N$, where v_∞, $\mathbf{v}_\mathrm{I}$, and $\mathbf{v}_\mathrm{L}$ denote the nodal voltage at the infinite bus, the inverter buses, and the load buses, respectively. Note that quantities in the phasor-based network model are represented as a complex number in the global DQ-frame. For example, $v_\infty = v_\infty^\mathrm{D} + j v_\infty^\mathrm{Q}$.

The phasor-based line model assumes that the network satisfies the nodal representation of the circuit equations,

$$\mathbf{i} = Y\mathbf{v}. \tag{4.4.1}$$

[1] This is under the assumption that the infinite bus has the same frequency as the rotational speed of the global DQ-frame. If, however, the infinite bus has a frequency $\omega_1 \neq \omega_\mathrm{g}$, the voltage $v_\infty^{\mathrm{DQ}} = [1, 0]^\intercal$ would be assumed at the initial time $t = 0$ s and would rotate at a frequency $(\omega_1 - \omega_\mathrm{g})\omega_\mathrm{b}$ rad/s.

[2] Note that typically the nominal frequency is assumed when computing the line admittances. The true system frequency at steady state, however, may not be the nominal frequency but should be quite close.

[3] The shunt components are neglected for simplicity of the line model.

4.4.2 Dynamic Line Model and the Steady State

With the existence of inverter-based resources, it may be important to include the fast line dynamics to fully investigate the dynamic interactions of inverters with the network. The line branch $\epsilon \in \mathcal{E}$ connecting bus i and bus j is modeled by series resistance r_ϵ and inductance l_ϵ, with dynamic equations given by,

$$\dot{i}_\epsilon^{\mathrm{D}} = \frac{\omega_{\mathrm{b}}}{l_\epsilon}(v_i^{\mathrm{D}} - v_j^{\mathrm{D}}) - \Big(\frac{r_\epsilon}{l_\epsilon}\omega_{\mathrm{b}} i_\epsilon^{\mathrm{D}} - \omega_{\mathrm{b}}\omega_{\mathrm{g}} i_\epsilon^{\mathrm{Q}}\Big) \tag{4.4.2}$$

$$\dot{i}_\epsilon^{\mathrm{Q}} = \frac{\omega_{\mathrm{b}}}{l_\epsilon}(v_i^{\mathrm{Q}} - v_j^{\mathrm{Q}}) - \Big(\frac{r_\epsilon}{l_\epsilon}\omega_{\mathrm{b}} i_\epsilon^{\mathrm{Q}} + \omega_{\mathrm{b}}\omega_{\mathrm{g}} i_\epsilon^{\mathrm{D}}\Big), \tag{4.4.3}$$

where i_ϵ^{DQ} is the current flowing through the line branch from bus i to bus j, represented in the global DQ-frame that rotates at speed $\omega_{\mathrm{g}}\omega_{\mathrm{b}}$ rad/s.

To obtain the steady-state representation that relates to the phasor-based line model, we first discuss the nominal case, where the system operates at the nominal frequency ω_0 at steady state. In this case, we choose $\omega_{\mathrm{g}} = \omega_0$, that is, selecting the $\overline{\mathrm{DQ}}$-frame as the global reference frame. This choice leads to constant $\overline{\mathrm{DQ}}$-quantities at steady state. Therefore, the left-hand-sides of equations (4.4.2) and (4.4.3) are set to zero and we revert to the algebraic line model,

$$v_i^{\overline{\mathrm{D}}} - v_j^{\overline{\mathrm{D}}} = r_\epsilon i_\epsilon^{\overline{\mathrm{D}}} - \omega_0 l_\epsilon i_\epsilon^{\overline{\mathrm{Q}}} \tag{4.4.4}$$

$$v_i^{\overline{\mathrm{Q}}} - v_j^{\overline{\mathrm{Q}}} = r_\epsilon i_\epsilon^{\overline{\mathrm{Q}}} + \omega_0 l_\epsilon i_\epsilon^{\overline{\mathrm{D}}}. \tag{4.4.5}$$

Note that stating equations (4.4.4), (4.4.5) are satisfied for every line branch is equivalent to stating equation (4.4.1) is satisfied in the phasor-based line model.

In general case, the system at steady state may operate at an off-nominal frequency $\omega_1 = \omega_{\mathrm{pll}}^{\mathrm{ss}} + \omega_0 \neq \omega_0$. In this case, the electrical quantities represented in the $\overline{\mathrm{DQ}}$-frame are sinusoidal signals with frequency $\omega_1 - \omega_0 = \omega_{\mathrm{pll}}^{\mathrm{ss}}$. Their time derivatives are also sinusoidal signals with the same frequency. In fact, recalling the definition of the $\overline{\mathrm{DQ}}$-quantities (i.e., the projections to the $\overline{\mathrm{DQ}}$-axes), we know that, $\dot{i}_\epsilon^{\overline{\mathrm{D}}} = -(\omega_1 - \omega_0)\omega_{\mathrm{b}} i_\epsilon^{\overline{\mathrm{Q}}}$ and $\dot{i}_\epsilon^{\overline{\mathrm{Q}}} = (\omega_1 - \omega_0)\omega_{\mathrm{b}} i_\epsilon^{\overline{\mathrm{D}}}$. Implementing these into the left-hand-sides of equations (4.4.2) and (4.4.3) respectively, we obtain,

$$-(\omega_1 - \omega_0)\omega_{\mathrm{b}} i_\epsilon^{\overline{\mathrm{Q}}} = \frac{\omega_{\mathrm{b}}}{l_\epsilon}(v_i^{\overline{\mathrm{D}}} - v_j^{\overline{\mathrm{D}}}) - \Big(\frac{r_\epsilon}{l_\epsilon}\omega_{\mathrm{b}} i_\epsilon^{\overline{\mathrm{D}}} - \omega_{\mathrm{b}}\omega_0 i_\epsilon^{\overline{\mathrm{Q}}}\Big)$$

$$(\omega_1 - \omega_0)\omega_{\mathrm{b}} i_\epsilon^{\overline{\mathrm{D}}} = \frac{\omega_{\mathrm{b}}}{l_\epsilon}(v_i^{\overline{\mathrm{Q}}} - v_j^{\overline{\mathrm{Q}}}) - \Big(\frac{r_\epsilon}{l_\epsilon}\omega_{\mathrm{b}} i_\epsilon^{\overline{\mathrm{Q}}} + \omega_{\mathrm{b}}\omega_0 i_\epsilon^{\overline{\mathrm{D}}}\Big)$$

Cancelling out the same terms on both sides of the equations and rearranging gives,

$$0 = \frac{\omega_{\mathrm{b}}}{l_\epsilon}(v_i^{\overline{\mathrm{D}}} - v_j^{\overline{\mathrm{D}}}) - \left(\frac{r_\epsilon}{l_\epsilon}\omega_{\mathrm{b}} i_\epsilon^{\overline{\mathrm{D}}} - \omega_{\mathrm{b}}\omega_1 i_\epsilon^{\overline{\mathrm{Q}}}\right) \tag{4.4.6}$$

$$0 = \frac{\omega_{\mathrm{b}}}{l_\epsilon}(v_i^{\overline{\mathrm{Q}}} - v_j^{\overline{\mathrm{Q}}}) - \left(\frac{r_\epsilon}{l_\epsilon}\omega_{\mathrm{b}} i_\epsilon^{\overline{\mathrm{Q}}} + \omega_{\mathrm{b}}\omega_1 i_\epsilon^{\overline{\mathrm{D}}}\right) \tag{4.4.7}$$

Further rearranging gives,

$$(v_i^{\overline{\mathrm{D}}} - v_j^{\overline{\mathrm{D}}}) = \left(r_\epsilon i_\epsilon^{\overline{\mathrm{D}}} - \omega_1 l_\epsilon i_\epsilon^{\overline{\mathrm{Q}}}\right) \tag{4.4.8}$$

$$(v_i^{\overline{\mathrm{Q}}} - v_j^{\overline{\mathrm{Q}}}) = \left(r_\epsilon i_\epsilon^{\overline{\mathrm{Q}}} + \omega_1 l_\epsilon i_\epsilon^{\overline{\mathrm{D}}}\right). \tag{4.4.9}$$

Comparing equations (4.4.8), (4.4.9) back to equations (4.4.4), (4.4.5), it is clear that the same relationships hold except that the frequency terms are changed from ω_0 to ω_1.

For this general case, we can select the rotational speed of the global reference frame to be $\omega_1 = \omega_{\mathrm{pll}}^{\mathrm{ss}} + \omega_0$, that is, selecting the D'Q'-frame. At steady state, $i_\epsilon^{\mathrm{D}'}$ and $i_\epsilon^{\mathrm{Q}'}$ are constants, and equations (4.4.2), (4.4.3) become,

$$v_i^{\mathrm{D}'} - v_j^{\mathrm{D}'} = r_\epsilon i_\epsilon^{\mathrm{D}'} - \omega_1 l_\epsilon i_\epsilon^{\mathrm{Q}'} \tag{4.4.10}$$

$$v_i^{\mathrm{Q}'} - v_j^{\mathrm{Q}'} = r_\epsilon i_\epsilon^{\mathrm{Q}'} + \omega_1 l_\epsilon i_\epsilon^{\mathrm{D}'}. \tag{4.4.11}$$

where $\omega_1 = \omega_{\mathrm{pll}}^{\mathrm{ss}} + \omega_0$.

4.4.3 Load Model

For simplicity, constant resistive loads are considered, which gives,

$$\mathbf{v}_{\mathrm{L}} = -\mathrm{diag}(\mathbf{r}_{\mathrm{L}})\mathbf{i}_{\mathrm{L}}, \tag{4.4.12}$$

where $\mathbf{r}_{\mathrm{L}}$ is a vector collecting the value of resistive loads in per unit, and the operator "diag" turns a vector into a diagonal matrix.

4.5 Steady-State Behavior of the Inverter-Based Network

In this section, we study the steady-state behavior of the inverter-based network. As in the discussion in Subsection 4.4.2, two cases are considered, i.e., the nominal condition and off-nominal condition. For illustration purposes, we assume that in the grid-connected mode, the system operates in the nominal condition. In the islanded mode, the system is

perturbed to an off-nominal condition.

4.5.1 Grid-Connected Operation Mode

In grid-connected mode, an infinite bus indexed by bus 0 exists in the network, representing the stiff voltage source provided by the main grid. We assume that the infinite bus sets the nominal frequency for the network, that is, $\omega_0 = 1$ p.u.. The $\overline{\text{DQ}}$-frame is adopted as the global reference frame. We study the equilibrium of the grid-connected system.

To begin with, we set the reactive power droop constant of all inverters to zero, that is, $R_\text{q} = 0$. In the nominal operating point, the inverter output power is $p = p^0$, and the terminal bus voltage magnitude is $|v_\text{t}| = v^0$.

Partition the admittance matrix Y as,

$$Y = \begin{bmatrix} Y_{00} & Y_{0\text{I}} & Y_{0\text{L}} \\ Y_{\text{I}0} & Y_{\text{II}} & Y_{\text{IL}} \\ Y_{\text{L}0} & Y_{\text{LI}} & Y_{\text{LL}} \end{bmatrix}.$$

Using relationship (4.4.12), we obtain from equation (4.4.1) that,

$$\mathbf{i}_\text{I} = Y_\text{red}\mathbf{v}_\text{I} + Y_\infty v_\infty, \tag{4.5.1}$$

where,

$$\begin{aligned} Y_\text{red} &\triangleq Y_{\text{II}} - Y_{\text{IL}}\Big(Y_{\text{LL}} + (\text{diag}(\mathbf{r}_\text{L}))^{-1}\Big)^{-1}Y_{\text{LI}} \\ Y_\infty &\triangleq Y_{\text{I}0} - Y_{\text{IL}}\Big(Y_{\text{LL}} + (\text{diag}(\mathbf{r}_\text{L}))^{-1}\Big)^{-1}Y_{\text{L}0}. \end{aligned}$$

In addition, we have the constraints at inverter terminals,

$$|\mathbf{v}_\text{I}| = \mathbf{v}^0 \tag{4.5.2}$$

$$\mathbf{Re}(\text{diag}(\mathbf{v}_\text{I})\overline{\mathbf{i}_\text{I}}) = \mathbf{p}^0, \tag{4.5.3}$$

where the operator $|\cdot| : \mathbb{C}^n \to \mathbb{R}^n$ returns the magnitude of the entries of a complex vector, the operator $\mathbf{Re}(\cdot) : \mathbb{C}^n \to \mathbb{R}^n$ takes the real part of the entries of a complex vector, and the operator $\overline{(\cdot)}$ takes entry-wise complex conjugate of a complex vector. The vectors $\mathbf{v}^0$ and $\mathbf{p}^0$ collect the external reference inputs for terminal voltage magnitude and output active power of all inverters. Equations (4.5.2), (4.5.3) coupled with equation (4.5.1) form the power flow equations, and we denote the power flow solution by $\mathbf{v}_\text{I}^\text{nom}$ and $\mathbf{i}_\text{I}^\text{nom}$,

represented in the $\overline{\text{DQ}}$-frame. For each individual inverter, the solution is denoted by the complex numbers $v_{\text{t}}^{\text{nom}}$ and $i_{\text{t}}^{\text{nom}}$, i.e., $v_{\text{t}}^{\text{nom}} = v_{\text{t}}^{\overline{\text{D}},\text{nom}} + jv_{\text{t}}^{\overline{\text{Q}},\text{nom}}$ and $i_{\text{t}}^{\text{nom}} = i_{\text{t}}^{\overline{\text{D}},\text{nom}} + ji_{\text{t}}^{\overline{\text{Q}},\text{nom}}$. This solution corresponds to the equilibrium of the inverter-based network in the nominal operating point in the grid-connected mode. At steady state, the PLL angle satisfies,

$$\theta_{\text{pll}}^{\text{nom}} = \angle v_{\text{t}}^{\text{nom}}, \ (\overline{\text{DQ}}\text{-frame}),$$

Therefore, we have,

$$\begin{bmatrix} v_{\text{t}}^{\text{d,nom}} \\ v_{\text{t}}^{\text{q,nom}} \end{bmatrix} = \mathcal{R}(-\theta_{\text{pll}}^{\text{nom}}) \begin{bmatrix} v_{\text{t}}^{\overline{\text{D}},\text{nom}} \\ v_{\text{t}}^{\overline{\text{Q}},\text{nom}} \end{bmatrix}, \tag{4.5.4}$$

$$\begin{bmatrix} i_{\text{t}}^{\text{d,nom}} \\ i_{\text{t}}^{\text{q,nom}} \end{bmatrix} = \mathcal{R}(-\theta_{\text{pll}}^{\text{nom}}) \begin{bmatrix} i_{\text{t}}^{\overline{\text{D}},\text{nom}} \\ i_{\text{t}}^{\overline{\text{Q}},\text{nom}} \end{bmatrix}. \tag{4.5.5}$$

It follows from equation (4.5.4) that $v_{\text{t}}^{\text{q,nom}} = 0$.

The equilibrium of other dynamic states in an inverter is given by the constants,

$$\begin{aligned}
\tilde{p}^{\text{nom}} &= p^0, \\
\tilde{q}^{\text{nom}} &= \mathbf{Im}(v_{\text{t}}^{\text{nom}} \overline{i_{\text{t}}^{\text{nom}}}), \\
\xi^{\text{nom}} &= 0, \\
\phi_{\text{d}}^{\text{nom}} &= \frac{1 - k_{\text{f}}^v}{k_{\text{i}}^v} i_{\text{t}}^{\text{d,nom}}, \\
\gamma_{\text{d}}^{\text{nom}} &= \frac{1 - k_{\text{f}}^i}{k_{\text{i}}^i} v^0, \\
i_{\text{s}}^{\text{d,nom}} &= i_{\text{t}}^{\text{d,nom}} - \omega_0 c_{\text{f}} v_{\text{t}}^{\text{q,nom}}, \\
i_{\text{s}}^{\text{q,nom}} &= i_{\text{t}}^{\text{q,nom}} + \omega_0 c_{\text{f}} v_{\text{t}}^{\text{d,nom}}, \\
\delta^{\text{nom}} &= \angle v_{\text{m}}^{\text{nom}}, \ (v_{\text{m}}^{\text{nom}} = v_{\text{m}}^{\text{d,nom}} + jv_{\text{m}}^{\text{q,nom}} \text{ in dq-frame}), \text{ where} \\
&\quad v_{\text{m}}^{\text{d,nom}} = v_{\text{t}}^{\text{d,nom}} - \omega_0 l_{\text{f}} i_{\text{s}}^{\text{q,nom}}, \\
&\quad v_{\text{m}}^{\text{q,nom}} = v_{\text{t}}^{\text{q,nom}} + \omega_0 l_{\text{f}} i_{\text{s}}^{\text{d,nom}}.
\end{aligned}$$

4.5.2 Islanded Operation Mode

We then analyze the general case where the steady-state frequency differs from the nominal frequency. The islanded inverter-based network is used as an example to illustrate the idea, since in this mode the operating point is typically perturbed away from the nominal frequency. In particular, the PLL frequency of inverters could converge to $\omega_{\text{pll}}^{\text{ss}} \neq 0$. In the

$\overline{\text{DQ}}$-frame, the converged inverter terminal voltage and current are time-varying. The PLL angle is also time-varying. Since it is desirable to obtain the equilibrium at convergence, the D'Q'-frame is adopted, leading to constant quantities at steady state. We denoted the converged inverter terminal voltage and current, with respect to the D'Q'-frame, by v_{t}^{ss} and i_{t}^{ss}. These quantities are constant, along with the converged PLL angle $\theta_{\text{pll}}^{\text{ss}} = \angle v_{\text{t}}^{\text{ss}}$. We have,

$$\begin{bmatrix} v_{\text{t}}^{\text{d,ss}} \\ v_{\text{t}}^{\text{q,ss}} \end{bmatrix} = \mathcal{R}(-\theta_{\text{pll}}^{\text{ss}}) \begin{bmatrix} v_{\text{t}}^{\text{D',ss}} \\ v_{\text{t}}^{\text{Q',ss}} \end{bmatrix}, \tag{4.5.6}$$

$$\begin{bmatrix} i_{\text{t}}^{\text{d,ss}} \\ i_{\text{t}}^{\text{q,ss}} \end{bmatrix} = \mathcal{R}(-\theta_{\text{pll}}^{\text{ss}}) \begin{bmatrix} i_{\text{t}}^{\text{D',ss}} \\ i_{\text{t}}^{\text{Q',ss}} \end{bmatrix}. \tag{4.5.7}$$

which gives constant values $v_{\text{t}}^{\text{dq,ss}}$, $i_{\text{t}}^{\text{dq,ss}}$. Note that the local variables represented in the local dq-frame are constant at steady state regardless of which global reference frame is chosen.

The equilibrium of other dynamic states in an inverter is given by the constants,

$$\begin{aligned}
\tilde{p}^{\text{ss}} &= p^0 - m_p \omega_{\text{pll}}^{\text{ss}}, \\
\tilde{q}^{\text{ss}} &= \mathbf{Im}(v_{\text{t}}^{\text{ss}} \overline{i_{\text{t}}^{\text{ss}}}), \\
\xi^{\text{ss}} &= \omega_{\text{pll}}^{\text{ss}} / K_{\text{i,pll}}, \\
\phi_{\text{d}}^{\text{ss}} &= \frac{1 - k_{\text{f}}^v}{k_{\text{i}}^v} i_{\text{t}}^{\text{d,ss}}, \\
\gamma_{\text{d}}^{\text{ss}} &= \frac{1 - k_{\text{f}}^i}{k_{\text{i}}^i} v^0, \\
i_{\text{s}}^{\text{d,ss}} &= i_{\text{t}}^{\text{d,ss}} - (\omega_{\text{pll}}^{\text{ss}} + \omega_0) c_{\text{f}} v_{\text{t}}^{\text{q,ss}}, \\
i_{\text{s}}^{\text{q,ss}} &= i_{\text{t}}^{\text{q,ss}} + (\omega_{\text{pll}}^{\text{ss}} + \omega_0) c_{\text{f}} v_{\text{t}}^{\text{d,ss}}, \\
\delta^{\text{ss}} &= \angle v_{\text{m}}^{\text{ss}}, \ \ (v_{\text{m}}^{\text{ss}} = v_{\text{m}}^{\text{d,ss}} + j v_{\text{m}}^{\text{q,ss}} \text{ in dq-frame}), \text{ where,} \\
v_{\text{m}}^{\text{d,ss}} &= v_{\text{t}}^{\text{d,ss}} - (\omega_{\text{pll}}^{\text{ss}} + \omega_0) l_{\text{f}} i_{\text{s}}^{\text{q,ss}}, \\
v_{\text{m}}^{\text{q,ss}} &= v_{\text{t}}^{\text{q,ss}} + (\omega_{\text{pll}}^{\text{ss}} + \omega_0) l_{\text{f}} i_{\text{s}}^{\text{d,ss}}.
\end{aligned}$$

4.6 Simulation Results

We demonstrate the proposed controller using the five-bus inverter-based network as shown in Fig. 4.1. This system is comprised of a four-bus microgrid and an infinite bus

Table 4.1: Parameters of the Inverter.

Parameter	Symbol	Value	Unit
Active power control integral gain	$K_{\mathrm{i},p}$	0.2	p.u.
PLL integral gain	$K_{\mathrm{i,pll}}$	0.2	p.u.
PLL proportional gain	$K_{\mathrm{p,pll}}$	0.2	p.u.
Reference input for active power	p^0	0.5	p.u.
Reference input for voltage	v^0	1	p.u.
Reference input for reactive power	q^0	0.1	p.u.
Droop gain for active power	m_p	500	-
Droop gain for reactive power	m_q	0.05	-
Base value of frequency	ω_{b}	$2\pi 60$	rad/s
Voltage control proportional gain	k_{p}^v	1	-
Voltage control integral gain	k_{i}^v	2	-
Voltage control feedforward gain	k_{f}^v	1	-
Current control proportional gain	k_{p}^i	1	-
Current control integral gain	k_{i}^i	2	-
Current control feedforward gain	k_{f}^i	0	-
Output filter capacitance	c_f	0.074	p.u.
Output filter inductance	l_f	0.08	p.u.

representing the main grid. In the microgrid, two inverters are connected to buses 1 and 2, and two constant resistive loads are connected to buses 3 and 4. The microgrid is connected to the main-grid through a circuit breaker at the PCC. In the nominal operating condition, the circuit breaker is closed and the microgrid is operated in grid-connected mode. During an event (planned or unplanned) in the main grid, the circuit breaker is open and the microgrid is isolated from the main grid and operates in islanded mode. When the event in the main grid is cleared, the circuit breaker will be closed, re-connecting the microgrid to the main grid. The small-signal stability of the inverter-based network under nominal condition is analyzed. We discuss the dynamic behavior of the inverter-based network, especially focusing on the transients during islanding and re-connection.

The system is modeled using per unit quantities. The two inverters have the same parameters, as given in Table 4.1. The active power droop constants of the two inverters were set to be the same, in order to equally share the active power load. The parameters

Table 4.2: Parameters of the Network.

Parameter	Symbol	Value	Unit
Nominal value of frequency	ω_0	1	p.u.
Line resistance	r_ϵ	0.2	p.u.
Line impedance	l_ϵ	0.2	p.u.
Load active power consumption	p_{L}^0	0.6	p.u.
Load reactive power consumption	q_{L}^0	0	p.u.
Infinite bus voltage	$v_\infty^{\mathrm{D}} + jv_\infty^{\mathrm{Q}}$	$1 + j0$	p.u.

Table 4.3: Nominal Operating Condition.

Variable	Value	Variable	Value
$\tilde{p}$	$[0.50, 0.50]$	$\tilde{q}$	$[-0.22, -0.22]$
ξ	$[0, 0]$	θ_{pll}	$[0.085, 0.085]$
δ	$[0.042, 0.042]$		
ϕ_{d}	$[0, 0]$	γ_{d}	$[0.49, 0.49]$
$i_{\mathrm{s}}^{\mathrm{d}}$	$[0.51, 0.51]$	$i_{\mathrm{s}}^{\mathrm{q}}$	$[0.29, 0.29]$
$v_{\mathrm{t}}^{\mathrm{d}}$	$[0.98, 0.98]$	$v_{\mathrm{t}}^{\mathrm{q}}$	$[0, 0]$
i_ϵ^{d}	$[0.16, 0.33, 0.16, 0.33]$	i_ϵ^{q}	$[0.26, 6e\text{-}3, 0.26, 6e\text{-}3]$

of the network, including the line parameters and the load values are given in Table 4.2. The network has a high R/X ratio which is typical in low voltage distribution systems. The two resistive loads have the same value, each consuming 0.6 p.u. active power under nominal voltage.

The network was initially set to be in the nominal condition, with the circuit breaker closed and the devices operating in the specified conditions. The nominal condition is computed by solving the power flow solution and is reported in Table 4.3. The entries for inverter states collect the values for inverter 1 and inverter 2, respectively. The entries for i_ϵ^{d} and i_ϵ^{q} collect the values of the states of line 1-3, 1-4, 2-3, 2-4, respectively. All quantities are expressed in per unit values, except for the angles, which are expressed in radians.

4.6.1 Small-Signal Stability

The eigenvalues of the inverter-based network for the nominal condition are shown in Fig. 4.5. The values of the eigenvalues and the major participation factors are listed

in Table. 4.4. The first 16 eigenvalues are largely dominated by the line dynamics and inverter output filter dynamics, which correspond to the fast dynamics in the system and are relatively well-separated from the other slower modes (i.e., clustered around the origin in Fig. 4.5). The slower modes are dominated by the power filters, the active power control, the voltage and current controls, and the PLL. The slower modes are well-damped for the selected control parameters.

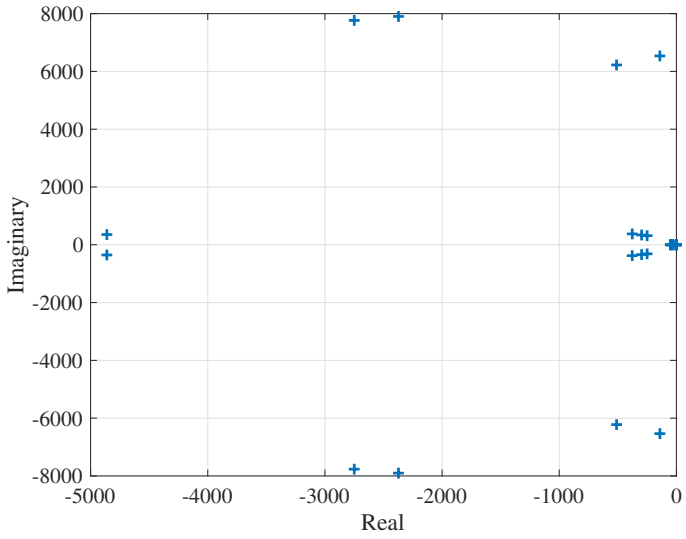

Figure 4.5: Eigenvalues of the inverter-based network for the nominal condition.

4.6.2 Dynamic Behavior During Islanding and Re-Connection

The dynamic behavior of the inverter-based network is analyzed in this subsection. We adopt the $\overline{\text{DQ}}$-frame as the global reference frame to demonstrate the dynamic results. We assume that an event occurs in the main grid and the circuit breaker is opened at time $T = 1$ s. The event lasted for 2 s and the circuit breaker is signaled to close at $T = 3$ s. Note that due to the symmetry of the test system, the same dynamic behavior of inverter 1 also applies to the states of inverter 2. The dynamics of active power generated by inverter 1 or 2, consumed by load 1, consumed by load 2, and supplied by the infinite bus is shown in Fig. 4.6 (a)-(d). The dynamics of voltage magnitude at the terminal bus of inverter 1 or 2, the load 1 bus, the load 2 bus, and the infinite bus are shown in Fig. 4.7 (a)-(d), respectively.

Before the circuit breaker opens, the inverter-based network operates in the nominal condition. Referring to Fig. 4.6, both inverters each supplies active power of 0.5 p.u. to the system, and both loads each consumes 0.6 p.u. of active power, while 0.28 p.u. of active

Table 4.4: Eigenvalues and Participation Factors of the Inverter-Based Network.

Index	Eigenvalues	Major participants
1, 2	$-2.75e{+}3 \pm 7.77e{+}3$	i_{s1}^{d}, v_{t1}^{d}, i_{s2}^{d}, v_{t2}^{d}
3, 4	$-2.37e{+}3 \pm 7.90e{+}3$	i_{s1}^{d}, v_{t1}^{d}, i_{s2}^{d}, v_{t2}^{d}
5, 6	$-1.41e{+}2 \pm 6.54e{+}3$	i_{s1}^{q}, v_{t1}^{q}, i_{s2}^{q}, v_{t2}^{q}
7, 8	$-5.11e{+}2 \pm 6.22e{+}3$	i_{s1}^{q}, v_{t1}^{q}, i_{s2}^{q}, v_{t2}^{q}
9, 10	$-4.86e{+}3 \pm 3.53e{+}2$	$i_{1\text{-}4}^{DQ}$, $i_{2\text{-}4}^{DQ}$
11, 12	$-2.97e{+}2 \pm 3.40e{+}2$	$i_{1\text{-}3}^{DQ}$, $i_{2\text{-}3}^{DQ}$
13, 14	$-2.50e{+}2 \pm 3.14e{+}2$	i_{s1}^{dq}, i_{s2}^{dq}, $i_{1\text{-}3}^{DQ}$, $i_{1\text{-}4}^{DQ}$, $i_{2\text{-}3}^{DQ}$, $i_{2\text{-}4}^{DQ}$
15, 16	$-3.77e{+}2 \pm 3.77e{+}2$	$i_{1\text{-}3}^{DQ}$, $i_{1\text{-}4}^{DQ}$, $i_{2\text{-}3}^{DQ}$, $i_{2\text{-}4}^{DQ}$
17	-52.18	$\tilde{p}_1$, $\tilde{p}_2$
18	-51.01	$\tilde{p}_1$, $\tilde{p}_2$, $\tilde{q}_1$, $\tilde{q}_2$
19	-46.82	$\tilde{p}_1$, $\tilde{p}_2$, $\tilde{q}_1$, $\tilde{q}_2$
20	-44.80	$\tilde{p}_1$, $\tilde{p}_2$, $\tilde{q}_1$, $\tilde{q}_2$
21	-30.13	δ_1, θ_{pll1}, δ_2, θ_{pll2},
22	-26.98	δ_1, θ_{pll1}, δ_2, θ_{pll2},
23, 24	-0.91 ± 0.93	ϕ_{d1}, γ_{d1}, ϕ_{d2}, γ_{d2}
25, 26	-0.75 ± 0.85	ϕ_{d1}, γ_{d1}, ϕ_{d2}, γ_{d2}
27	-1.57	δ_1, δ_2
28	-1.24	ξ_1, ξ_2
29	-0.89	ξ_1, ξ_2
30	-0.98	ξ_1, ξ_2

power is drawn from the main grid with the 0.08 p.u. surplus compensating for the loss in distribution lines. Referring to Fig. 4.7, the voltage magnitude at inverter terminal bus is 0.98 p.u. which is slightly different from the reference input of $v^0 = 1$ p.u., due to the reactive power droop characteristic. The voltage magnitude at load 1 bus is 1 p.u. and the voltage magnitude at load 2 bus is 0.92 p.u. in the nominal condition.

When the circuit breaker opens at $T = 1$ s, the connection between bus 3 (the load 1 bus) and the infinite bus is lost. The infinite bus remains the original voltage $1\angle 0$, but has zero current flow, therefore providing zero power to the system. Referring to Fig. 4.7, the voltage magnitude at the load 1 bus and load 2 bus drop instantaneously due to the loss of connection to the infinite bus. The voltage magnitude at the inverter terminal bus also

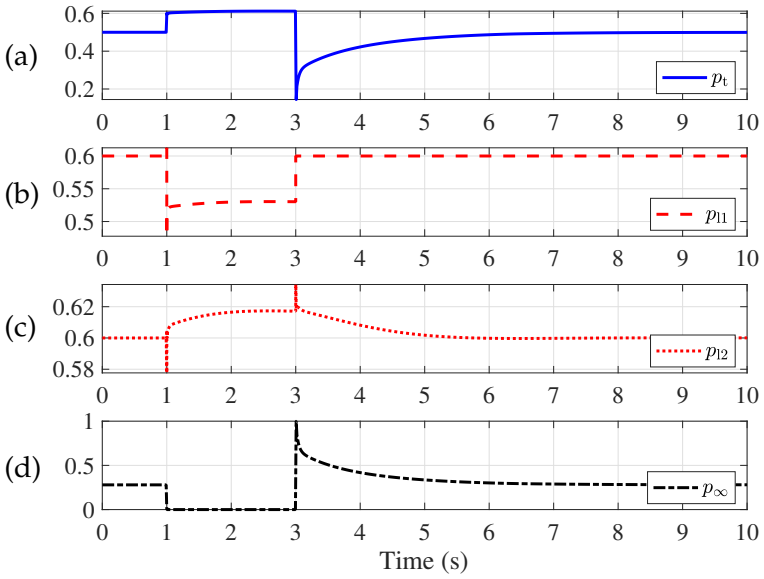

Figure 4.6: Dynamics of active power: (a) generated by inverter 1 or 2; (b) consumed by load 1; (c) consumed by load 2; and (d) supplied by the infinite bus.

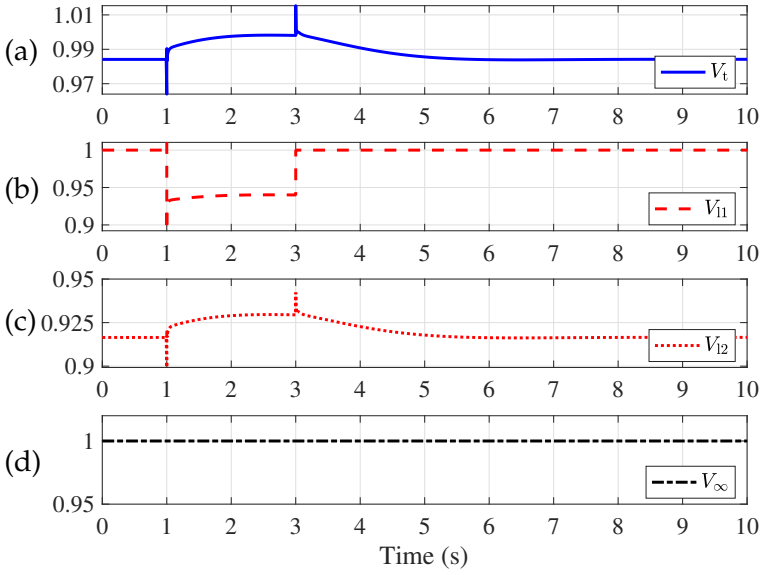

Figure 4.7: Dynamics of voltage magnitude at: (a) terminal bus of inverter 1 or 2; (b) load 1 bus; (c) load 2 bus; and (d) the infinite bus.

drops immediately. The microgrid begins to operate in islanded mode. Due to the voltage regulation capability of the proposed inverter control scheme, the voltage magnitude at the inverter terminal bus is restored to 0.998 p.u. after transients. The voltage at the load 1 bus and load 2 bus are also restored to 0.94 p.u. and 0.93 p.u., respectively. This

test case demonstrates the capability of the proposed inverter control scheme to form microgrid voltage autonomously upon loss of grid connection. Referring to Fig. 4.6, it can be observed that when the circuit breaker is opened, the instantaneous drop of voltage leads to the instantaneous drop of active power consumption of the loads. The active power output of inverters, however, increase immediately to compensate for the loss of power supply from the infinite bus. As can be observed, during the 2 s of islanded operation, the system is perturbed away from the nominal condition and converges to a different steady state, where the active power generation from the inverter is 0.61 p.u., the active power consumption by load 1 and load 2 are 0.53 p.u. and 0.62 p.u., respectively.

At the instant of circuit breaker reclosing at time $T = 3$ s, the voltage at the infinite bus is higher than the load 1 bus. Therefore, the load 1 bus voltage increases instantaneously when the circuit breaker recloses[4], leading to an instant increase of power consumption by the loads. There is a surge of active power flow from the infinite bus, and thereby a large dip of active power generation from the inverters.

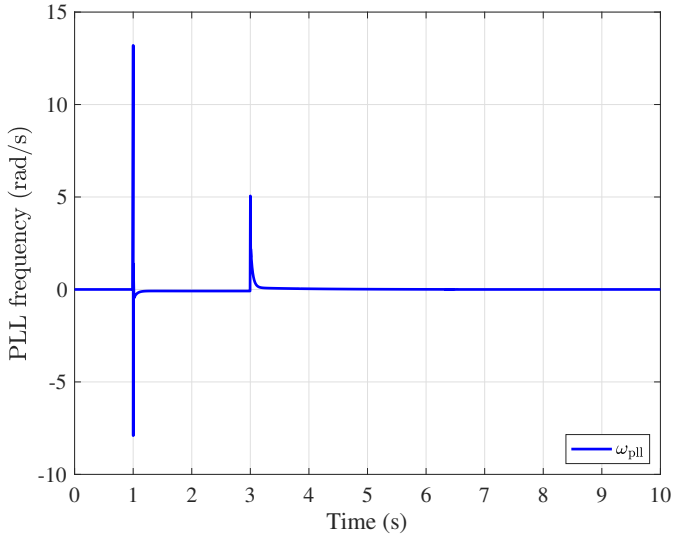

Figure 4.8: Dynamics of phase-locked loop frequency.

The dynamics of PLL frequency ω_{pll} and PLL angle θ_{pll} are shown in Fig. 4.8 and Fig. 4.9. It is shown that initially the PLL frequency is zero in the nominal condition during the grid-connected mode, and the PLL angle stays at 0.085 rad, relative to the global DQ-frame. When the circuit breaker opens at time $T = 1$ s, the operating point is perturbed away from the nominal condition, and the PLL frequency converges to $\omega_{\text{pll}}^{\text{ss}} = -0.085$ rad/s,

[4]The circuit breaker is designed such that, after receiving the reclosing signal, the closing will not take place until the voltage difference appearing across the circuit breaker has a magnitude that is less than a certain threshold.

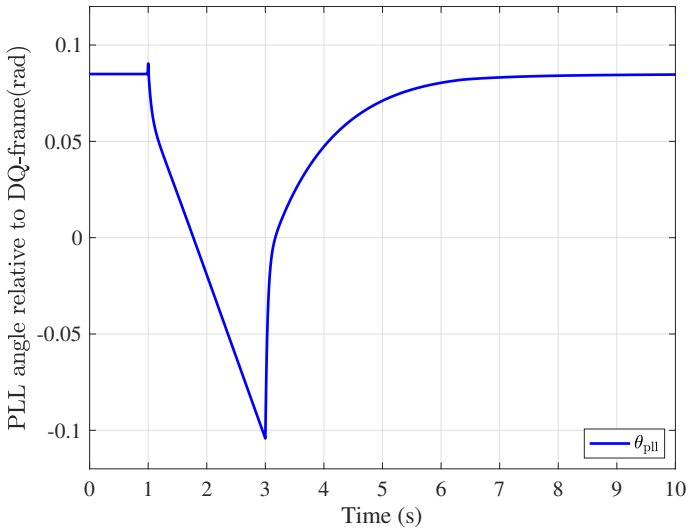

Figure 4.9: Dynamics of phase-locked loop angle.

based on the active power droop characteristic. Accordingly, the PLL angle continues to vary, until the circuit breaker is closed at time $T = 3\,\text{s}$. At that point, the microgrid is reconnected to the main grid, and the PLL dictates the inverter frequency and angle to track the voltage angle established by the main grid.

4.7 Chapter Conclusion

This chapter introduces a novel inverter control scheme that can achieve autonomous mode switching between grid-connected operation and islanded operation, and vice-versa. In grid-connected operation, where a frequency reference exists, a phase-locked loop estimates the grid frequency and grid bus voltage angle for the inverter to follow and therefore achieves synchronization to the grid. In islanded operation, the inverters themselves establish a frequency for the microgrid based on active power droop characteristics and continue to supply the loads. Note that unlike existing control schemes in the literature, such switching between grid-connected and islanded modes is achieved autonomously, that is, there is no need to reconfigure the controller for the inverter. The proposed control scheme can also achieve autonomous operation when multiple inverters exist in the network, with no need for communication and central coordination. Small-signal analysis of the inverter-based network shows that the proposed controller achieves well-damped performance. The dynamics of the proposed controller have been extensively tested and discussed. The interactions between the inverters and the network are considered.

CHAPTER 5

Synthesis of Safety-Certifying Distributed Control Laws for Inverter-Based Resources

5.1 Chapter Introduction

Safety-critical system refers to a system for which the violation of safety constraints will lead to serious economic loss or personal casualty. Power system falls into such category considering the loss resulting from large-scale blackout and critical loads such as hospital and process plant. Modern power system has been evolving towards distributed operation. With the increasing integration of distributed energy resources (DERs), especially renewable resources, challenges have arisen in safely operating power systems as well as guaranteeing stability. Microgrid is a promising direction to tackle the intermittency and uncertainty characteristics that are intrinsic in renewable resources such as wind and solar. An islanded microgrid is a standalone small-scale power system that groups a variety of DERs, especially renewables, together with energy storages and loads to provide better control and operation, higher efficiency and reliability [29]. It is a viable solution for power supply to rural area. Microgrid also provides a new perspective to increase the penetration level of renewables in modern power system. Unlike traditional power system that has large inertia from conventional synchronous generators, DERs in a microgrid are connected to the network through power electronic interface. Considering the stochasticity in renewables and the negligible physical inertia, control of voltage and frequency for microgrids is challenging [108]. While stability analysis and control of inverter-based microgrids have received a lot of attention in the literature [106, 109–112], safety of the microgrids has largely been ignored. For microgrids, the safe region can be defined for voltage magnitudes at every node in the network. The transient voltage in a microgrid can fluctuate by a large amount, causing serious power quality and safety issues, even causing damages to the electrical equipment [113, 114]. Flexible power injections at the droop-controlled inverter nodes can be utilized to stabilize the phase angle, frequency

and voltage magnitude, as well as ensuring the voltage magnitudes at all nodes within the safe region.

Control Lyapunov function (CLFs) have long been used to synthesize stabilizing controllers for nonlinear systems [115]. On the other hand, barrier functions are used to certify safety by guaranteeing the forward invariance of a set via Lyapunov-like conditions. Although barrier function originated in the field of optimization as a penalty function to replace constraints, it prospers in the field of control design too. For example, [116] considers the safety verification problem in both worst-case and stochastic settings by constructing barrier certificates. The ideas of the barrier functions and the CLF were combined to construct the control barrier functions (CBFs) [22] which have since been used in designing safety controllers. Reference [117] applied CBF method to automotive systems to achieve lane keeping and adaptive cruise control simultaneously with safety constraints. Application of CBF method to establish set invariance with the existence of disturbance and uncertainty is considered in [118]. Simultaneous satisfaction of safety and performance objectives via design is not a trivial task. The stabilization objective expressed by a CLF and the safety constraints established by a CBF can be potentially in conflict. In [119], the authors proposed a quadratic program formulation that unifies CLF and CBF to synthesize a controller that enforces the safety constraints but relaxes the stability (performance) requirement when these two objectives are in conflict. Reference [120] proposed an iterative algorithm using sum-of-squares (SOS) technique to search for the most permissive barrier function that gives maximum volume for the certified region, therefore maximize the estimate for safe stabilization region. All trajectories that start within the safe stabilization region can be made to converge to the (equilibrium of interest at the) origin as well as constrained in the safe region.

The main contribution of this chapter is in applying barrier functions based method to certify safety of an inverter-based microgrid considering transient voltage limits. We propose a distributed safety certification method and present computational algorithms to compute safety-ensuring decentralized and distributed control policies. To treat the control design problem in a decentralized perspective, the microgrid is firstly decomposed into several subsystems. Barrier functions are generated for each subsystem by firstly ignoring the interactions from neighboring subsystems. The interaction terms are considered as disturbances with upper limits in the control design phase, resulting in robust local state feedback control strategies. The rest of the chapter is organized as follows: Section 5.2 presents the necessary background; Section 5.3 explains the microgrid model; the main computational and algorithmic developments are described in Section 5.4, with numerical results presented in Section 5.5. We conclude the chapter in Section 5.6. Throughout the

text, we will use $|\cdot|$ to denote both the Euclidean norm of a vector and the absolute value of a scalar; and use $\mathbb{R}[x]$ to denote the ring of all polynomials in $x \in \mathbb{R}^n$.

5.2 Preliminaries

5.2.1 Stability Certificates: Lyapunov Functions

Consider a nonlinear dynamical system of the form

$$\dot{x}(t) = f(x(t)), \quad \forall t \geq 0\,,\ x \in \mathbb{R}^n\,, \tag{5.2.1}$$

with an equilibrium at the origin (i.e., $f(0) = 0$), where $f : \mathbb{R}^n \to \mathbb{R}^n$ is locally Lipschitz. For brevity, we would drop the argument t from the state variables, whenever obvious. The equilibrium point at the origin of (5.2.1) is Lyapunov stable if, for every $\varepsilon > 0$ there is a $\delta > 0$ such that $|x(t)| < \varepsilon,\ \forall t \geq 0$ whenever $|x(0)| < \delta$. Moreover, it is asymptotically stable in a domain $\mathcal{X} \subseteq \mathbb{R}^n$, $0 \in \mathcal{X}$, if it is Lyapunov stable and $\lim_{t\to\infty} |x(t)| = 0$ for every $x(0) \in \mathcal{X}$.

Theorem 5.2.1. *[55, 121] If there is a continuously differentiable radially unbounded positive definite function $V : \mathcal{X} \to \mathbb{R}_{\geq 0}$ such that $\nabla_x V^T f(x)$ is negative definite in $\mathcal{X}$, then the origin of (5.2.1) is asymptotically stable and $V(x)$ is a Lyapunov function.*

Here ∇_x denotes the partial differentiation with respect to x. Using an appropriately scaled Lyapunov function $V(x)$, the region of attraction (ROA) of the origin of (5.2.1) can be estimated by $\{x \in \mathcal{X} \,|\, V(x) \leq 1\}$ [122, 123].

5.2.2 Safety Certificates: Barrier Functions

In contrast to asymptotic stability which concerns with the convergence of the state variables to the stable equilibrium, the notion of "safety" comes from engineering design specifications. From the design perspective, the system trajectories are not supposed to cross into the certain regions in the state-space marked as "unsafe". Let us assume that the "unsafe" region of operation for the system (5.2.1) is given by the domain

$$\mathcal{X}_u := \{x \in \mathbb{R}^n \,|\, w_i(x) > 0\,,\ i = 1, 2, \ldots, l\}, \tag{5.2.2}$$

where $w_i : \mathbb{R}^n \mapsto \mathbb{R}$ are a set of l (≥ 1) polynomials. These are usually engineering constraints that ensure that the system is always operated (controlled) to avoid going into "unsafe" modes of operation. Safety of such systems can be verified through the

existence (or, construction) of continuously differentiable barrier functions $B : \mathbb{R}^n \mapsto \mathbb{R}$ of the form [22, 116, 119, 120]:

$$B(x) \geq 0, \quad \forall x \in \mathbb{R}^n \backslash \mathcal{X}_u \tag{5.2.3a}$$

$$B(x) < 0, \quad \forall x \in \mathcal{X}_u \tag{5.2.3b}$$

$$(\nabla_x B)^T f(x) + \alpha\left(B(x)\right) \geq 0, \quad \forall x \in \mathbb{R}^n \tag{5.2.3c}$$

where $\alpha(\cdot)$ is an extended class-$\mathcal{K}$ function[1]. The third condition ensures that at the level-set $B = 0$ the value of the barrier function is increasing along the system trajectories. Safety is guaranteed for all trajectories starting inside the domain $\{x \,|\, B(x) \geq 0\}$ which is *invariant* under the dynamics (5.2.1).

5.2.3 Sum-of-Squares Optimization

Relatively recent studies have explored how SOS-based methods can be utilized to find Lyapunov functions by restricting the search space to SOS polynomials [123–126]. Let us denote by $\mathbb{R}[x]$ the ring of all polynomials in $x \in \mathbb{R}^n$. A multivariate polynomial $p \in \mathbb{R}[x]$, $x \in \mathbb{R}^n$, is an SOS if there exist some polynomial functions $h_i(x), i = 1 \ldots s$ such that $p(x) = \sum_{i=1}^{s} h_i^2(x)$. We denote the ring of all SOS polynomials in x by $\Sigma[x]$. Whether or not a given polynomial is an SOS is a semi-definite problem which can be solved with SOSTOOLS, a MATLAB® toolbox [127], along with a semi-definite programming solver such as SeDuMi [128]. An important result from algebraic geometry, called Putinar's Positivstellensatz theorem [129, 130], helps in translating conditions such as in (5.2.3) into SOS feasibility problems.

Theorem 5.2.2. *Let $\mathcal{K} = \{x \in \mathbb{R}^n \,|\, k_1(x) \geq 0, \ldots, k_m(x) \geq 0\}$ be a compact set, where k_j are polynomials. Define $k_0 = 1$. Suppose there exists a $\mu \in \left\{\sum_{j=0}^{m} \sigma_j k_j \,\middle|\, \sigma_j \in \Sigma[x], \forall j\right\}$ such that $\{x \in \mathbb{R}^n \,|\, \mu(x) \geq 0\}$ is compact. Then,*

$$p(x) > 0, \ \forall x \in \mathcal{K} \implies p \in \left\{\sum_{j=0}^{m} \sigma_j k_j \,\middle|\, \sigma_j \in \Sigma, \ \forall j\right\}.$$

Remark 1. *Using Theorem 5.2.2, one can translate the problem of checking that $p > 0$ on $\mathcal{K}$ into an SOS feasibility problem where we seek the SOS polynomials σ_0, σ_j, $\forall j$ such that $p - \sum_j \sigma_j k_j$ is SOS. Note that any equality constraint $k_i(x) = 0$ can be expressed as two inequalities $k_i(x) \geq 0$ and $k_i(x) \leq 0$. In many cases, especially for the k_i used throughout this work, a μ satisfying the conditions in Theorem 5.2.2 is guaranteed to exist (see [130]), and need not be searched for.*

[1] A continuous function $\alpha : (-a, b) \mapsto (-\infty, \infty)$, for some $a, b > 0$, is *extended class-$\mathcal{K}$* if it is strictly increasing and $\alpha(0) = 0$ [55].

5.3 Microgrid Model

We consider the following droop-based grid-forming inverter model [110, 131]:

$$\dot{\theta}_i = \omega_i \,, \tag{5.3.1a}$$

$$\tau_i \dot{\omega}_i = -\omega_i + \lambda_i^p \left(P_i^{\text{set}} - P_i\right) \tag{5.3.1b}$$

$$\tau_i \dot{v}_i = v_i^0 - v_i + \lambda_i^q \left(Q_i^{\text{set}} - Q_i\right), \tag{5.3.1c}$$

where $\lambda_i^p > 0$ and $\lambda_i^q > 0$ are the droop constants associated with the active power vs. frequency and the reactive power vs. voltage droop curves, respectively; τ_i is the time-constant of a low-pass filter used for the active and reactive power measurements; θ_i, ω_i and v_i are, respectively, the phase angle, speed and voltage magnitude; v_i^0 is the desired (nominal) voltage magnitude; P_i^{set} and Q_i^{set} are the active power and reactive power set-points, respectively. Finally, P_i and Q_i are, respectively, the active and reactive power injected into the network which relate to the neighboring bus voltage phase angle and magnitudes as:

$$P_i = v_i \sum\nolimits_{k \in \mathcal{N}_i} v_k \left(G_{i,k} \cos\theta_{i,k} + B_{i,k} \sin\theta_{i,k}\right) \tag{5.3.2a}$$

$$Q_i = v_i \sum\nolimits_{k \in \mathcal{N}_i} v_k \left(G_{i,k} \sin\theta_{i,k} - B_{i,k} \cos\theta_{i,k}\right), \tag{5.3.2b}$$

where $\theta_{i,k} = \theta_i - \theta_k$, and $\mathcal{N}_i$ is the set of neighbor nodes. $G_{i,k}$ and $B_{i,k}$ are respectively the transfer conductance and susceptance values of the line connecting the nodes i and k.

At the equilibrium (steady-state) operation:

$$\forall i: \quad P_i = P_i^{\text{set}},\ Q_i = Q_i^{\text{set}},\ \omega_i = 0,\ v_i = v_i^0 \,.$$

As the conditions on the network change (such as changes in load or generation), inverters have the capability to change the control set-points of the active and reactive power output to adjust to the new operating conditions. This is modeled as:

$$P_i^{\text{set}} = P_i^0 + u_i^p \,,\ Q_i^{\text{set}} = Q_i^0 + u_i^q \,, \tag{5.3.3}$$

where P_i^0 and Q_i^0 are the set-points for the unperturbed (or nominal) operating condition; and u_i^p and u_i^q are some feedback control inputs.

Due to the low-inertia of the microgrids, large voltage and frequency fluctuations are quite common during transients [114]. While designing stabilizing control policies, it is therefore important to keep track of the transient voltage and frequency magnitudes to

ensure that those are within the "safety" limits determined via engineering design. In this work, we will restrict ourselves to the consideration of transient voltage limits which are usually higher than the steady-state operational limits [113]. Fluctuations of transient voltage beyond the tolerable ("safe") region cause power quality issues, including the risk of damaging the electrical equipment. In this chapter, we will define the "safe" operational region as:

$$\underline{v_i} \leq v_i(t) \leq \overline{v_i}\,.$$

Typical values for the limits during transients operation could be $\underline{v_i} = 0.6\,\text{p.u.}$ and $\overline{v_i} = 1.2\,\text{p.u.}$.

5.4 Distributed Safety Certificates

The dynamical model of the interconnected microgrid with m droop-controlled inverters is expressed compactly as:

$$\dot{x}_i = f_i(x_i) + g_i(x_i)u_i + \sum\nolimits_{j\in\mathcal{N}_i} h_{ij}(x_i, x_j)\,, \tag{5.4.1a}$$

$$\mathcal{X}_{u,i} := \{x_i \,|\, w_j(x_i) \geq 0\,,\ j = 1, 2, \ldots, l_i\} \tag{5.4.1b}$$

where each $i \in \{1, 2, \ldots, m\}$ identifies an inverter. $x_i \in \mathbb{R}^{n_i}$ is the n_i-dimensional state vector associated with the i-th inverter, while u_i are some control inputs. We assume that the origin is an equilibrium point of interest of the networked system, and that the control input vanishes at the equilibrium point (i.e. $u_i = 0$, $\forall i$ at the origin). Moreover f_i, g_i and h_{ij} are locally Lipschitz functions. The problem we are interested in is:

Problem 1. *Identify continuous functions $B_i(x_i)$, feedback control policies u_i and non-negative scalars c_i such that*

$$\forall i:\ B_i(0) > c_i \tag{5.4.2a}$$

$$B_i(x_i) < 0, \quad \forall x_i \in \mathcal{X}_{u,i} \tag{5.4.2b}$$

$$\dot{B}_i \geq 0, \quad \forall x_i \in \partial\mathcal{D}_i[c_i],\ \forall x_j \in \mathcal{D}_j[c_j], \forall j \in \mathcal{N}_i \tag{5.4.2c}$$

$$\dot{B}_i = \nabla_{x_i} B_i^T \Big(f_i(x_i) + g_i(x_i)u_i + \sum\nolimits_{j\in\mathcal{N}_i} h_{ij}(x_i, x_j) \Big)\,,$$

where we define $\mathcal{D}_i[c_i] := \{x_i \,|\, B_i(x_i) \geq c_i\}, \forall i$ and $\partial\mathcal{D}_i[c_i] := \{x_i \,|\, B_i(x_i) = c_i\}$ as the boundary set of the domain $\mathcal{D}_i[c_i]$.

Theorem 5.4.1. *If there exist continuous functions $B_i(x_i)$, feedback control policies u_i and non-negative scalars c_i satisfying (5.4.2), then the safety of the interconnected system (5.4.1) is guaranteed for all $t \geq 0$ whenever $B_i(x_i(0)) \geq c_i$, $\forall i$, i.e.*

$$x_i(0) \in \mathcal{D}_i[c_i],\ \forall i \implies x_i(t) \in \mathbb{R}^{n_i} \backslash \mathcal{X}_{u,i},\ \forall i,\ \forall t \geq 0\,.$$

Moreover, there is a neighborhood $\mathcal{X}_i$ around origin (i.e., $0 \in \mathcal{X}_i, \forall i$) such that $\mathcal{X}_i \subseteq \mathcal{D}_i[c_i]$.

Proof. Note that because of the condition (5.4.2c), B_i is non-decreasing on the boundary of the domain $\mathcal{D}_i[c_i]$ whenever $x_j \in \mathcal{D}_j[c_j]$ for every neighbor j. Extending this argument to all the subsystems, we conclude that

$$\mathcal{D}_1[c_1] \times \mathcal{D}_2[c_2] \times \cdots \times \mathcal{D}_m[c_m]$$

is an invariant domain. Since $B_i(x_i) < 0$ for every $x_i \in \mathcal{X}_{u,i}$, we conclude the safety of the system is guaranteed for all $t \geq 0$ whenever $x_i(0) \in \mathcal{D}_i[c_i], \forall i$. Finally, since $B_i(0) > c_i$ and B_i is a continuous function, there exists a neighborhood $\mathcal{X}_i$ around origin such that for all $x_i \in \mathcal{X}_i$, $B_i(x_i) \geq c_i$. □

Computation of such barrier functions is not trivial. Recent works have explored the use of sum-of-square optimization methods to compute the barrier certificates for polynomials networks [116, 120]. Note that the power-flows as described in equation (5.3.2) are non-polynomial. Using the polynomial recasting technique proposed in [123], the power systems dynamics can be expressed in a higher-dimensional space as a polynomial differential-algebraic system. In this work, however, we resort to Taylor series expansion (up to the third order) to approximate the dynamics into a polynomial form.

In the rest of this section, we describe a three-step procedure to obtain the distributed barrier certificates. In the first two steps, we consider the isolated and autonomous subsystem model of the form (which we assume to be locally asymptotically stable around the origin):

$$\text{(isolated)} \quad \dot{x}_i = f_i(x_i)\,,$$

and compute the Lyapunov function which is then used to compute a barrier function for the isolated subsystem using the method similar to [120].

5.4.1 Computation of Lyapunov Functions

SOS-based expanding interior algorithm [123, 124] has been used to construct Lyapunov functions and ROA in an iterative search process. In this work, we use a variant of the process, which does not require the bisection search process and hence speeds up the computation at each iteration stage. The algorithmic steps used to implement the modified expanding interior algorithm can be summarized as follows (for notational convenience, we have dropped the subscript i from the subsystem variables to explain the algorithm):

1 Step 0: Compute a Lyapunov function V^0 such that $V^0 \leq 1$ is an estimate of the ROA. The following two steps are then repeated until convergence, such that (hopefully) the final estimate of the ROA is much larger than initial one. Define a positive definite and radially unbounded function $p(x)$ (e.g. $p = \varepsilon|x|^2$ for some small $\varepsilon > 0$).

2 Step k-1: Starting from a Lyapunov function $\hat{V}$ with ROA estimated by $\hat{V} \leq 1$, compute the largest level-set β^k of a positive definite function $p(x)$ contained within $\hat{V} \leq 1$. This is done by solving the following SOS problem:

$$\max_{s_2^k, s_3^k, s_4^k} \quad \beta^k \tag{5.4.3a}$$

$$\hat{s}_1(p - \beta^k) - s_2^k(\hat{V} - 1) \in \Sigma[x] \tag{5.4.3b}$$

$$-s_3^k(1 - \hat{V}) - s_4^k\dot{\hat{V}} - \varepsilon_2|x|^2 \in \Sigma[x] \tag{5.4.3c}$$

where s are SOS polynomials. The $\hat{\cdot}$ implies it is borrowed from the previous step, while k denotes the variables being currently computed. At the first instance of the problem (5.4.3), we initialize $\hat{s}_1 = 1$.

3 Step k-2: In this sub-step at the k-th iteration, a new Lyapunov function V^k is found such that the level-set $V^k = 1$ is an estimate of the ROA, while trying to expand the estimated ROA by maximizing δ such that $p \leq \hat{\beta}$ is contained within the level-set $V^k \leq 1 - \delta^k$, i.e.,

$$\max_{V^k, s_1^k} \quad \delta^k \tag{5.4.4a}$$

$$V^k - \varepsilon_1|x|^2 \in \Sigma[x] \tag{5.4.4b}$$

$$s_1^k(p - \hat{\beta}) - \hat{s}_2(V^k - 1 + \delta^k) \in \Sigma[x] \tag{5.4.4c}$$

$$-\hat{s}_3(1 - V^k) - \hat{s}_4\dot{V}^k - \varepsilon_2|x|^2 \in \Sigma[x] \tag{5.4.4d}$$

The algorithm stops when δ^k is sufficiently small. Set $V = V^k$ as the Lyapunov function

with $V \leq 1$ providing the largest estimate of the ROA .

5.4.2 Computation of Barrier Functions

For the barrier functions computation we adopt a similar approach as in the Algorithm 2 in [120], except that we use the algorithm to compute only the barrier functions, while the original algorithm was used to also search for a "safe" and stabilizing control policy. For completeness we present the algorithm here (once more, for notational convenience, we have dropped the subscript i from the subsystem variables to explain the algorithm):

1 Step 0: As the first step of the iterative process, we compute the maximum level-set of V contained completely inside the *safe region*. This is done by solving the following SOS problem:

$$\max_{s_0^k} \; z\,, \;\; \text{subject to } V - z - \sum_{i=1}^{l} s_{0,i}^k w_i \in \Sigma[x]\,.$$

Set $B^0 = z^{\max} - V$, where $z^{\max}$ is the solution of the above problem, i.e. the maximal level-set of V wholly contained inside the safe region. Note that B^0 is a barrier function by construction. Choose a small scalar $\gamma > 0$.

2 Step k-1: Using the barrier function $\hat{B}$ computed in the previous step, find the largest $\varepsilon > 0$ such that $\dot{\hat{B}} \geq -\gamma \hat{B} + \varepsilon$ whenever $\hat{B} \geq 0$, i.e. solve the SOS problem

$$\max_{s_1^k} \; \varepsilon^k, \;\; \text{subject to } \dot{\hat{B}} + \gamma\, \hat{B} - \varepsilon^k - s_1^k\, \hat{B} \in \Sigma[x]\,.$$

3 Step k-2: In this sub-step we search for a new barrier function of the form $B^k(x) = z(x)^T Q^k z(x)$ where $z(x)$ is a vector of monomials in x , and Q^k is a symmetric matrix, such that $B^k(0) > 0$. The barrier function satisfies $B^k(x) < 0$ on the unsafe set $\{x \,|\, w_i(x) > 0\,,\; i = 1, 2, \ldots, l\}$, along with the constraint on its time-derivative. The following problem is solved:

$$\begin{aligned} \max_{s_{2,i}^k} \quad & \text{trace}\,(Q^k) \\ \dot{B}^k + \gamma\, B^k - \eta - \hat{s}_1\, B^k &\in \Sigma[x] \\ -B^k - \sum\nolimits_{i=1}^{l} s_{2,i}^k w_i &\in \Sigma[x] \end{aligned}$$

where η is a small positive number chosen to avoid the trivial zero solution. The objective function is a proxy for maximizing the volume of the safety region [120].

The algorithm stops when trace(Q^k) converges within some tolerance. Set $B = B^k$ as the barrier function with $B \geq 0$ providing the largest estimate of the certified safety region for the isolated subsystems.

5.4.3 Safety-Certifying Control Policies

In this subsection, we describe an SOS problem to compute control policies u_i such that (5.4.2c) is satisfied for some $c_i \in [0, B_i(0))$. Without any loss of generality, we will assume that the barrier functions satisfy $B_i(0) = 1$ (which is always achievable through scaling), such that we are interested in $c_i \in [0, 1)$. Moreover, we will assume, for simplicity, uniform $c_i = c, \forall i$, while the more generic case can be easily extended. Then we are seeking the existence of control laws u_i such that for some chosen $c \in [0, 1)$,

$$\forall i: \ \forall x_i \in \partial\mathcal{D}_i[c], \ \forall x_j \in \mathcal{D}_j[c], \ j \in \mathcal{N}_i \tag{5.4.5a}$$

$$\nabla_{x_i} B_i^T (f_i + g_i u_i + \sum\nolimits_{j\in\mathcal{N}_i} h_{ij}) \geq 0 \,. \tag{5.4.5b}$$

In this chapter, we will focus on state-feedback control policies. Two alternatives will be considered: 1) a decentralized state-feedback policy of the form $u_i(x_i)$, and 2) a distributed state-feedback policy of the form $u_i = u_{ii}(x_i) + \sum_{j\in\mathcal{N}_i} u_{ij}(x_j)$.

The following problem concerns the design of an optimal decentralized state-feedback control policy $u_i(x_i)$:

$$\min_{u_i(x_i)} \quad U_i \tag{5.4.6a}$$

$$\text{subject to} \quad (5.4.5) \text{ and } \ \|u_i(x_i)\|_\infty \leq U_i, \ \ \forall x_i \in \mathcal{D}_i[c] \,. \tag{5.4.6b}$$

Note that the controller is only used on or near the boundary of the domain $\mathcal{D}_i[c]$ since it is only needed to guarantee that the trajectories never cross the boundary. This can be solved using an equivalent SOS problem, noting that the constraint $\|u_i(x_i)\|_\infty \leq U_i$ translates to polynomial constraints. Similar problem can be formulated for the distributed controller design, with the constraint $\|u_i(x_i)\|_\infty \leq U_i$ needed to be satisfied on $x_j \in \mathcal{D}_j[c]$, $\forall j \in \mathcal{N}_i$ as well as $x_i \in \mathcal{D}_i[c]$.

Remark 2. *Note that the constraint (5.4.5) is satisfied whenever (i.e., sufficient condition) we*

choose a u_i such that

$$\nabla B_i^T g_i u_i \geq \mu := \max_{x_i \in \partial D_i[c], x_j \in \mathcal{D}_j[c]} \left| \sum_{j \in \mathcal{N}_i} \nabla B_i^T h_{ij} \right|$$

If for every $x_i \in \partial D_i[c]$ there always exists a k such that $\left| \left[\nabla B_i^T \right]_k [u_i]_k \right| > 0$ then we can always find a u_i satisfying the above condition.

5.5 Numerical Results

For illustration purpose, we consider the 6-bus (bus 0 to bus 5) microgrid network described in [132]. Disconnecting the utility, we replace the substation (bus 0) by a droop-controlled inverter, with three other inverters placed on buses 1, 4 and 5. The inverter dynamics were modeled in the form of (5.3.1). Bus 0 was considered as the reference bus for the phase angle. The droop constants λ_i^p and λ_i^q were chosen to be 2.43 rad/s/p.u. and 0.2 p.u./p.u., while the filter time-constant τ_i was set to 0.5 s [110]. Nominal values of voltage and frequency, as well as the active and reactive power set-points were obtained by solving the steady-state power flow equations (5.3.2), which were then used to shift the equilibrium point to the origin. The loads were modeled as constant power loads, and Kron reduced network with only the inverter nodes were used for analysis. The unsafe set was defined in terms of the shifted (around the 1 p.u.) nodal voltage magnitudes as follows:

$$\text{(unsafe)} \quad v_i < -0.4\,\text{p.u.} \;\text{ or }\; v_i > 0.2\,\text{p.u.}$$

In Fig. 5.1, we illustrate how the iterative search algorithm presented in Section 5.4 obtains an expanded certified region of safety (marked by the boundary of the outermost green ellipse) starting from the initial estimate given by a level-set of the Lyapunov function (marked by the smaller black dashed ellipse boundary). The plot shows the projections of the ROA and the barrier certified regions on the frequency-voltage space obtained by setting the phase angle differences to 0. The black dashed boundary of the larger ellipse is the estimate of the ROA, while the red dashed lines denote the unsafe region boundary (in voltage magnitudes). Note that the certified invariant region of safe stability is much smaller than the estimated ROA of the isolated inverter. Next we investigate the control efforts needed to guarantee safety of the network over some domain defined using the subsystem barrier function level-sets. Fig. 5.2(a) shows the results of the optimal decentralized control design problem (5.4.6), for a range of different values of the barrier

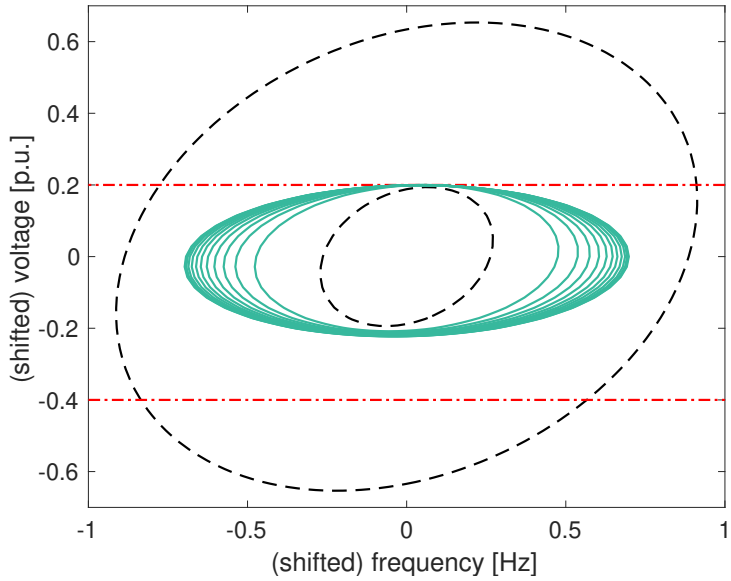

Figure 5.1: Illustration of the iterative search for a barrier certified region of an isolated inverter subsystem. The red dashed lines mark the boundary of the unsafe region. The outer black dashed line marks the estimated ROA, while the inner black dashed line marks the largest Lyapunov functions level-set contained within the safe region. Green lines mark the iterative (growing) estimates of the certified safe region using barrier function.

level-set $c \in [0, 1)$ such that $B_i \geq c, \forall i$ gives a distributed certificate of safety. As expected, the control effort increases (monotonically, in this case) as the value of c decreases, or the certified region of safety increases. Figs. 5.2(b)-5.2(c) show the results when the states of neighboring subsystems are used in the control design in addition to the subsystem's local states, for which we refer as the "distributed control" design. Clearly, distributed control policies require lower minimum control efforts as compared to the decentralized control policy. This observation aligns with the conclusion in [133] regarding the value of communication in distribution network voltage regulation problem. In particular, two different choices of distributed controllers are explored - one in which all of the neighboring subsystems' states are used in the feedback (Fig. 5.2(b)) and another in which the only neighboring subsystem states used in feedback are the voltage magnitudes (Fig. 5.2(c)). In this example, additional measurements from the neighboring subsystems help decrease the minimum control effort needed.

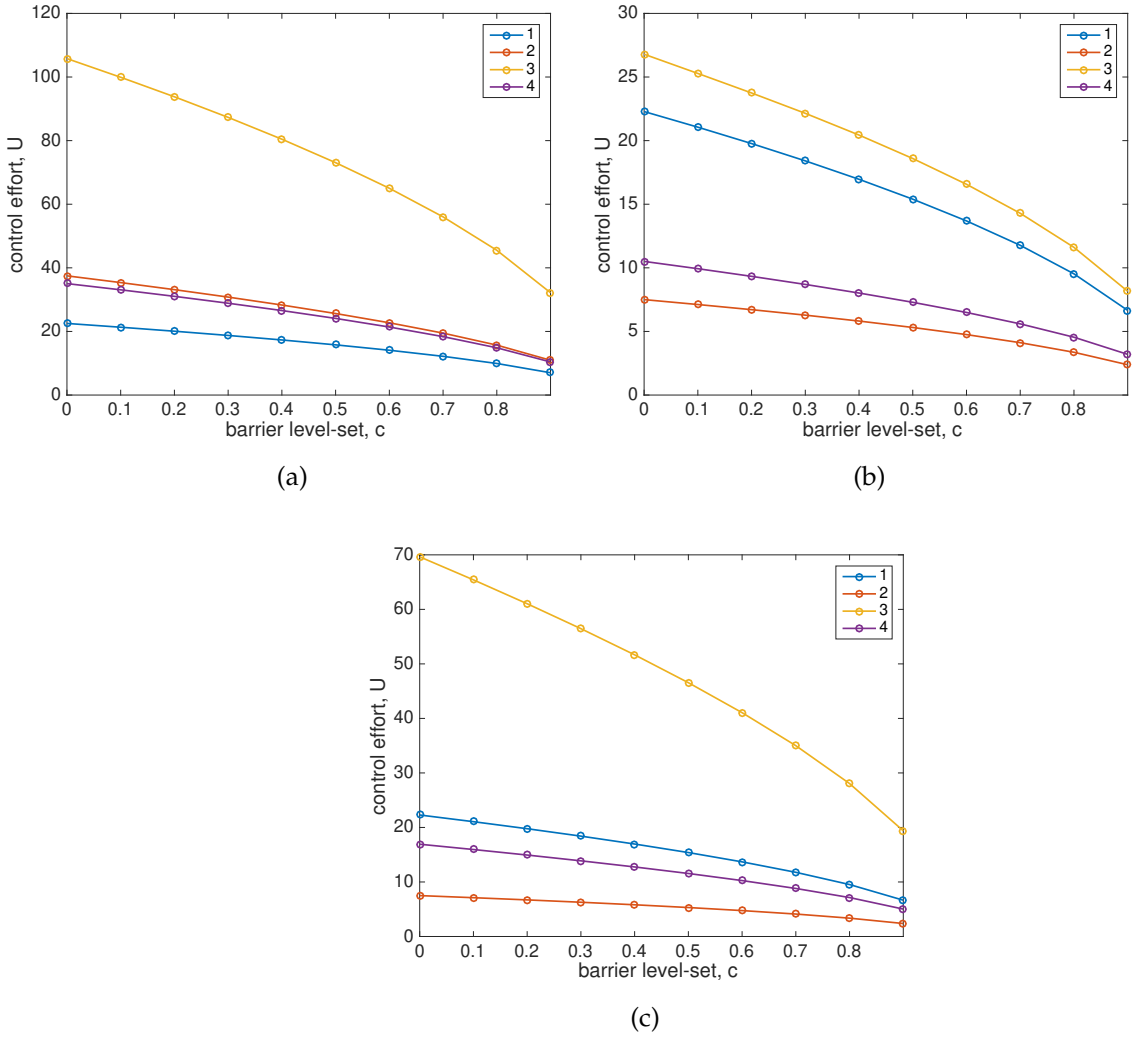

Figure 5.2: Computation of the minimum control effort (U_i) needed to certify safety of the network via subsystem barrier functions, for varying values of $c \in [0, 1)$, using: (a) a decentralized control policy, $u_i(x_i)$, that uses only the subsystem's states; (b) a distributed control policy that uses all the neighbor states into the feedback, in addition to the subsystem's states; and (c) a distributed control policy that uses the neighbor voltage magnitudes into the feedback, in addition to the subsystem's states.

5.6 Chapter Conclusion

In this chapter we consider the problem of safety in inverter-based microgrids. Using the barrier functions based methods, we propose a distributed safety certification of the microgrid network. Sum-of-squares based algorithm is used to present a computational approach to obtain these safety certificates in a distributed manner. Moreover, using a microgrid example, we show how decentralized vs. distributed control policies could pose different requirements on the control effort.

CHAPTER 6

Establishing Convergence Guarantees for Distributed Voltage Balancing Controllers

6.1 Chapter Introduction

Distribution networks are subject to three-phase unbalance, primarily as a consequence of structural and operational factors [34]. Structural factors refer to the inherently unbalanced nature of distribution networks, for example poorly transposed distribution lines and missing phase laterals. The impact of structural unbalance is usually small [134] and is assumed to be the utility's concern. In contrast, operational unbalance caused by single-phase and two-phase loads, unbalanced three-phase loads, and increasing integration of single-phase distributed energy resources (DERs), can be considerable [135]. This chapter seeks to exploit the collective reactive power capability of multiple unbalanced DERs such as solar photovoltaic (PV) to balance voltages in the distribution network.

Symmetrical components are commonly used to assess unbalance, with negative and zero sequence quantities indicative of undesirable conditions. For example, negative sequence voltages can cause induction motor overheating and transformer saturation while zero sequence currents increase power losses [35, 36]. Much research has been devoted to phase balancing of distribution systems, including system reconfiguration [37], static Var compensation [38], and three-phase optimal power flow algorithms [39]. Steinmetz circuit design [136] was applied in [137] to mitigate voltage unbalance at particular nodes in a distribution network.

This chapter considers distribution-network nodes, referred to as *critical nodes*, at which failure to maintain a relatively balanced voltage may have detrimental effects on the connected devices. We are interested in strategies for balancing multiple critical nodes simultaneously across a distribution network. Initially the Steinmetz-based controller of [137] is applied at multiple critical nodes, resulting in a decentralized control structure

that requires no communications. However, it relies on local DERs connected at the critical nodes that are to be balanced. Therefore, we also consider a more flexible distributed control structure that relies on partitioning the radial distribution network based on the locations of the critical nodes. Further details of both control strategies are provided in Section 6.2.

It is important to note that the control actions arising from balancing each critical node will interact with the controllers associated with all the other critical nodes in the network. Such interactions could potentially be destabilizing. Therefore, the chapter undertakes rigorous analysis to establish conditions that guarantee convergence. The derivation of this convergence result is based on Banach fixed-point theory [138].

The analysis begins by adopting a linear multi-phase power flow model [139] derived from a fixed-point form of the power flow equations. An efficient optimization program is formulated to compute an accurate approximation for the final converged point. This results in a high-quality linear power flow model. The Steinmetz-based control scheme can be modeled as an iterative process and expressed explicitly as a quadratic mapping of the reactive power injections from one step to the next. This allows the use of Banach fixed-point theory to prove stability of the control scheme.

This chapter is organized as follows: Section 6.2 provides an introduction to the concepts of voltage unbalance and Steinmetz-based balancing, and presents the proposed decentralized and distributed control structures. Problem formulation, convergence analysis and the main results are given in Section 6.3. Section 6.4 extends the formulation to incorporate time delays. Case studies are discussed in Section 6.5 and conclusions are provided in Section 6.6.

6.2 Steinmetz-Based Control Structure

In a perfectly balanced three-phase system, phasor quantities of all three phases have equal magnitude and angle differences of 120 degrees. Unlike transmission systems, which are approximately balanced and can be represented by their single-line equivalent, distribution systems are usually unbalanced. Various definitions of voltage unbalance exist in the power system community, among which the standards defined by IEC, NEMA and IEEE are most common. The relationships between these definitions were studied in [140]. Since the voltage unbalance factor (VUF) definition from the IEC standard captures unbalance in both voltage magnitude and phase angle, we adopt VUF to characterize

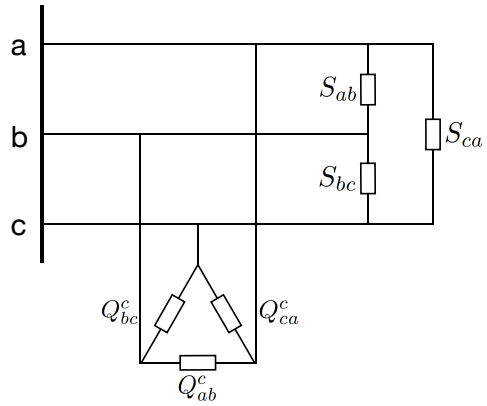

Figure 6.1: Steinmetz circuit design: equivalent load (local plus downstream) and reactive power compensation.

voltage unbalance,

$$\text{VUF } \% = \frac{V_-}{V_+} \times 100, \tag{6.2.1}$$

where the positive sequence voltage V_+, negative sequence voltage V_- and zero-sequence voltage V_0 are the so-called symmetrical components [141] given by,

$$\begin{bmatrix} V_0 \\ V_+ \\ V_- \end{bmatrix} = \frac{1}{3} \begin{bmatrix} 1 & 1 & 1 \\ 1 & a & a^2 \\ 1 & a^2 & a \end{bmatrix} \begin{bmatrix} V_a \\ V_b \\ V_c \end{bmatrix}, \tag{6.2.2}$$

with $a = -\frac{1}{2} + j\frac{\sqrt{3}}{2}$, and V_a, V_b, and V_c form the set of (possibly unbalanced) three-phase voltages.

6.2.1 Steinmetz-Based Controller

Steinmetz circuit design [36] can be used to compute the delta-connected reactances that are required to make a delta-connected impedance load appear balanced, thus balancing the voltage. Such a Steinmetz-based method was developed in [137] to compute the delta reactive power injections that balance the total local plus downstream load, i.e., the total load seen at the balancing point. For a three-phase feeder as shown in Fig. 6.1, the required compensation can be expressed as:

$$Q^c_{LL} = E \cdot P_{LL} + F \cdot Q_{LL}, \tag{6.2.3}$$

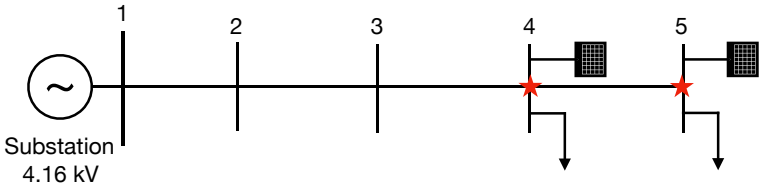

Figure 6.2: Decentralized Steinmetz control scheme.

where $Q^c_{LL} = [Q^c_{ab}, Q^c_{bc}, Q^c_{ca}]^\intercal$ is the required line-to-line reactive power compensation, $P_{LL} = [P_{ab}, P_{bc}, P_{ca}]^\intercal$ and $Q_{LL} = [Q_{ab}, Q_{bc}, Q_{ca}]^\intercal$ are the delta-connected active and reactive power loads, respectively, and,

$$E = \frac{1}{\sqrt{3}} \begin{bmatrix} 0 & 1 & -1 \\ -1 & 0 & 1 \\ 1 & -1 & 0 \end{bmatrix}, \quad F = \frac{1}{3} \begin{bmatrix} -2 & 1 & 1 \\ 1 & -2 & 1 \\ 1 & 1 & -2 \end{bmatrix}. \tag{6.2.4}$$

In order to maintain the voltage profile, the matrix F incorporates an additional constraint that ensures the sum of the reactive power compensation is zero. To implement this strategy, P_{LL} and Q_{LL} are computed from measurements of phase-to-neutral voltages and line currents at the critical node.

A feedback control strategy was proposed in [137] that was based on successively implementing Steinmetz design equation (6.2.3). However, no convergence guarantee was provided for the closed-loop system.

6.2.2 Decentralized Control

The Steinmetz controller can be generalized to simultaneously balance multiple critical nodes along a radial distribution network. Fig. 6.2 provides an example (which will be considered in Section 6.5) where multiple critical nodes, marked by red stars, are to be balanced. Assume initially that three-phase delta-connected solar PV systems are available at each critical node, allowing Steinmetz controllers to be deployed at each location. Note that in this decentralized scenario, control decisions are made locally and no communication is required.

Because decentralized controllers affect the voltages and currents across the network, they interact, with each acting as a disturbance that affects all the others. Such mutual couplings must be analyzed to ensure the stability of the overall system.

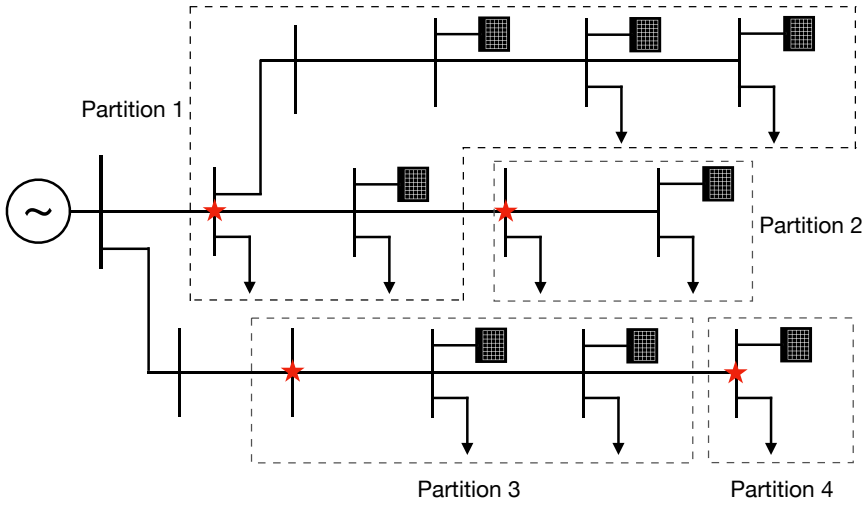

Figure 6.3: Distributed Steinmetz control scheme.

6.2.3 Distributed Control

Since DERs, especially those with three-phase connections, are not necessarily available at all critical nodes, a more general distributed control structure is required. To achieve a distributed scheme, the radial distribution network is subdivided[1] into disjoint partitions that are determined by the locations of the critical nodes, as depicted in Fig. 6.3. Controllable DERs within each partition, potentially open-delta connected, are clustered together and coordinated to balance the single critical node assigned to that partition. In this distributed scenario, each partition is controlled by a single Steinmetz-based controller, with communication only required within each partition. Similarly to the decentralized control case, however, stability guarantees are essential to avoid undesirable interactions between partitions and between DERs within each partition.

6.3 Convergence Analysis

To analyze convergence of the decentralized and distributed control strategies, we first represent the distribution network using a linear multi-phase power flow model. This enables the closed-loop control system to be formulated as an explicit quadratic mapping. The Banach fixed-point theorem [138] is then used to prove existence and uniqueness of the fixed-point of the quadratic mapping.

[1]Since we assume radial structure for the distribution network, it is straightforward to develop an automated procedure for uniquely partitioning the network into disjoint sections.

6.3.1 Problem Formulation

6.3.1.1 Linear Multi-Phase Power Flow Model

Analysis builds on a linear multi-phase power flow model derived from a fixed-point formulation of the power flow equations [139]. This model is suitable for generic multi-phase distribution networks. Assume there is a slack bus and N three-phase PQ buses in the radial distribution network.[2] As shown in [139], the voltage profile $\mathbf{v}$ is given by the fixed-point equation,

$$\mathbf{v} = \mathbf{G}(\mathbf{v}) = \mathbf{w} + \mathbf{Y}_{LL}^{-1}\Big(\text{diag}(\overline{\mathbf{v}})^{-1}\overline{\mathbf{s}}^{Y} + \mathbf{H}^{\intercal}\text{diag}(\mathbf{H}\overline{\mathbf{v}})^{-1}\overline{\mathbf{s}}^{\Delta}\Big), \tag{6.3.1}$$

where $\mathbf{v} \in \mathbb{C}^{3N}$ collects the three-phase line-to-neutral voltages at all PQ buses, $\mathbf{s}^{Y}, \mathbf{s}^{\Delta} \in \mathbb{C}^{3N}$ are the grounded wye-connected and delta-connected complex power injections at all PQ buses, and the overline denotes the conjugate of the complex quantity. The term $\mathbf{w} = -\mathbf{Y}_{LL}^{-1}\mathbf{Y}_{L0}\mathbf{v_0}$ denotes the zero-load voltage profile, where $\mathbf{v_0} \in \mathbb{C}^3$ is the voltage at the slack bus and $\mathbf{Y}_{LL}, \mathbf{Y}_{L0}$ are submatrices of the three-phase admittance matrix. The matrix $\mathbf{H}$ is $3N \times 3N$ block diagonal, with the block $\Gamma = [1, -1, 0; 0, 1, -1; -1, 0, 1]$ down the diagonal and zeros elsewhere[3]. The existence, uniqueness and non-singularity properties of the power flow model (6.3.1) are established in [139].

A linear model is obtained by taking only the first iteration of the fixed-point equation (6.3.1), initialized at a given operating point $\hat{\mathbf{v}}$. The fixed-point linearization model has the form,

$$\tilde{\mathbf{v}} = \mathbf{M}^{Y}\mathbf{x}^{Y} + \mathbf{M}^{\Delta}\mathbf{x}^{\Delta} + \mathbf{w} \tag{6.3.2}$$

$$\tilde{\mathbf{i}} = \mathbf{Y}_{L0}\mathbf{v}_0 + \mathbf{Y}_{LL}\tilde{\mathbf{v}}, \tag{6.3.3}$$

where $\tilde{\mathbf{v}} \in \mathbb{C}^{3N}$ collects the line-to-neutral voltages at all PQ buses, $\tilde{\mathbf{i}} \in \mathbb{C}^{3N}$ collects the net phase current injections at all PQ buses, $\mathbf{x}^{Y} := \left[(\mathbf{p}^{Y})^{\intercal}, (\mathbf{q}^{Y})^{\intercal}\right]^{\intercal} \in \mathbb{R}^{6N}$ stacks the vectors of wye active and reactive power injections, and $\mathbf{x}^{\Delta} := \left[(\mathbf{p}^{\Delta})^{\intercal}, (\mathbf{q}^{\Delta})^{\intercal}\right]^{\intercal} \in \mathbb{R}^{6N}$ stacks the vectors of delta injections. The expressions for $\mathbf{M}^{Y}$ and $\mathbf{M}^{\Delta}$ are given by,

$$\mathbf{M}^{Y} := \begin{bmatrix}\mathbf{Y}_{LL}^{-1}\text{diag}(\overline{\hat{\mathbf{v}}})^{-1} & -j\mathbf{Y}_{LL}^{-1}\text{diag}(\overline{\hat{\mathbf{v}}})^{-1}\end{bmatrix} \tag{6.3.4}$$

$$\mathbf{M}^{\Delta} := \begin{bmatrix}\mathbf{Y}_{LL}^{-1}\mathbf{H}^{\intercal}\text{diag}(\mathbf{H}\overline{\hat{\mathbf{v}}})^{-1} & -j\mathbf{Y}_{LL}^{-1}\mathbf{H}^{\intercal}\text{diag}(\mathbf{H}\overline{\hat{\mathbf{v}}})^{-1}\end{bmatrix}. \tag{6.3.5}$$

We are interested in the changes in voltages and currents at critical nodes that result

[2] The assumption of three-phase buses is purely for ease of exposition.
[3] The corresponding rows in $\mathbf{H}$ are removed when there are missing phases.

from reactive power compensation at injection nodes. We number the nodes in the distribution network from the substation to the feeder end as $i = 1, \cdots, N$, as shown in Fig. 6.2. The critical nodes that are to be balanced, where measurements of voltages and currents are available, are indexed $j = 1, \cdots, m$, with the corresponding bus number given by c_j. Injection nodes, where DERs with reactive power capability are located, may be distributed within a partition, as in Fig. 6.3. However, for notational simplicity, we initially focus on three-phase reactive power injections. These three-phase injection nodes are indexed by $k = 1, \cdots, m$, with corresponding bus numbers i_k. We define the selection matrix for the k-th injection node by $\mathbf{T}_{i_k} = \left[\mathbf{0}|\mathbf{I}_{i_k}|\mathbf{0}\right] \in \mathbb{R}^{3\times 3N}$, which has a 3×3 identity matrix at the $(3i_k - 2) \leftrightarrow 3i_k$ columns and zeros elsewhere.

Let $Q_k = \left[Q_k^{ab}, Q_k^{bc}, Q_k^{ca}\right]^\intercal$, for $k = 1, \cdots, m$, denote the delta-connected reactive power compensation at the k-th injection node. The line-to-neutral voltage profile can be expressed as,

$$\tilde{\mathbf{v}} := \tilde{\mathbf{M}}_1^\Delta Q_1 + \tilde{\mathbf{M}}_2^\Delta Q_2 + \cdots + \tilde{\mathbf{M}}_m^\Delta Q_m + \mathbf{u}, \tag{6.3.6}$$

where $\mathbf{u} := \mathbf{M}^Y \mathbf{x}^Y + \mathbf{M}^\Delta \mathbf{x}^\Delta + \mathbf{w}$. The coefficients $\tilde{\mathbf{M}}_k^\Delta \in \mathbb{C}^{3N\times 3}$ correspond to the k-th compensation node and are the $(3i_k - 2) \leftrightarrow 3i_k$ columns of the second block of $\mathbf{M}^\Delta$ given by (6.3.5). Denoting that second block by $\mathbf{M}_2^\Delta$, we can write $\tilde{\mathbf{M}}_k^\Delta = \mathbf{M}_2^\Delta \mathbf{T}_{i_k}^\intercal$, where $\mathbf{T}_{i_k}$ is the previously defined selection matrix for the k-th injection node.

Even though equation (6.3.6) considered three-phase reactive power injections, catering for single-phase injections at multiple locations within a partition, as in Fig. 6.3, is straightforward. To do so, the single-phase injections, which act together as the k-th injection node, are grouped into $Q_k \in \mathbb{R}^3$ and the selection matrix $\mathbf{T}_{i_k}$ uses indices corresponding to the applicable injection locations.

Line-to-neutral voltages $V_j = [V_j^a, V_j^b, V_j^c]^\intercal$ at the j-th critical node are recovered from the voltage profile $\tilde{\mathbf{v}}$ using the extraction matrix $\mathbf{T}_{c_j} = [\mathbf{0}|\mathbf{I}_{c_j}|\mathbf{0}] \in \mathbb{R}^{3\times 3N}$, which has a 3×3 identity matrix at the $(3c_j - 2) \leftrightarrow 3c_j$ columns and zeros elsewhere. For $j = 1, \cdots, m$,

$$\begin{aligned} V_j &= \mathbf{T}_{c_j}\tilde{\mathbf{v}} \\ &= \mathbf{T}_{c_j}\left(\tilde{\mathbf{M}}_1^\Delta Q_1 + \tilde{\mathbf{M}}_2^\Delta Q_2 + \cdots + \tilde{\mathbf{M}}_m^\Delta Q_m + \mathbf{u}\right) \\ &= \mathbf{T}_{c_j}\tilde{\mathbf{M}}_1^\Delta Q_1 + \cdots + \mathbf{T}_{c_j}\tilde{\mathbf{M}}_m^\Delta Q_m + \mathbf{T}_{c_j}\mathbf{u} \\ &:= A_{j1}Q_1 + A_{j2}Q_2 + \cdots + A_{jm}Q_m + \mu_j \\ &:= \mathbf{A}_j\mathbf{Q} + \mu_j, \end{aligned} \tag{6.3.7}$$

where $\mathbf{Q} = [Q_1^\intercal, \cdots, Q_m^\intercal]^\intercal \in \mathbb{R}^{3m}$ collects all reactive power compensation, $\mathbf{A}_j := \left[A_{j1} \cdots A_{jm}\right]$

and $\mu_j := \mathbf{T}_{c_j}\mathbf{u}$.

Line currents at the j-th critical node (with bus number c_j) are equal to the phase summation of net current injections at that node together with the current flow to downstream nodes. Let d_j denote the last node downstream from the j-th critical node. Then,

$$\begin{aligned} I_j &= \sum_{l=c_j}^{d_j} \begin{bmatrix} i_l^a \\ i_l^b \\ i_l^c \end{bmatrix} \\ &= \Big(\mathbf{T}_{c_j} + \mathbf{T}_{c_j+1} + ... + \mathbf{T}_{d_j}\Big)\tilde{\mathbf{i}} \\ &= \tilde{\mathbf{T}}_j\tilde{\mathbf{i}}, \end{aligned} \tag{6.3.8}$$

where the summation matrix $\tilde{\mathbf{T}}_j$ is of the form $[\mathbf{0}|\mathbf{I}_{c_j}|...|\mathbf{I}_{d_j}|\mathbf{0}]$. Thus, we have line currents at the j-th critical node given by,

$$\begin{aligned} I_j &= \tilde{\mathbf{T}}_j\tilde{\mathbf{i}} = \tilde{\mathbf{T}}_j\Big(\mathbf{Y}_{L0}\mathbf{v}_0 + \mathbf{Y}_{LL}\tilde{\mathbf{v}}\Big) \\ &= \tilde{\mathbf{T}}_j\mathbf{Y}_{L0}\mathbf{v}_0 + \tilde{\mathbf{T}}_j\mathbf{Y}_{LL}\Big(\tilde{\mathbf{M}}_1^{\Delta}Q_1 + \cdots + \tilde{\mathbf{M}}_m^{\Delta}Q_m + \mathbf{u}\Big) \\ &= \tilde{\mathbf{T}}_j\mathbf{Y}_{LL}\tilde{\mathbf{M}}_1^{\Delta}Q_1 + \cdots + \tilde{\mathbf{T}}_j\mathbf{Y}_{LL}\tilde{\mathbf{M}}_m^{\Delta}Q_m + \tilde{\mathbf{T}}_j\mathbf{Y}_{L0}\mathbf{v}_0 + \tilde{\mathbf{T}}_j\mathbf{Y}_{LL}\mathbf{u} \\ &:= B_{j1}Q_1 + B_{j2}Q_2 + \cdots + B_{jm}Q_m + \eta_j \\ &:= \mathbf{B}_j\mathbf{Q} + \eta_j, \end{aligned} \tag{6.3.9}$$

where $\mathbf{B}_j := [B_{j1}\cdots B_{jm}]$ and $\eta_j := \tilde{\mathbf{T}}_j\mathbf{Y}_{L0}\mathbf{v}_0 + \tilde{\mathbf{T}}_j\mathbf{Y}_{LL}\mathbf{u}$.

6.3.1.2 Mapping Expression for Steinmetz Control Schemes

The iterative process of decentralized and distributed Steinmetz-based control proceeds as follows:

1 Measure line-to-neutral voltages V_j and line currents I_j at critical nodes that are to be balanced.

2 Compute VUF at critical nodes.

3 Use the Steinmetz equation (6.2.3) to compute the required compensations Q_k for $k = 1, \cdots, m$.

4 Apply Q_k at injection nodes where DERs are available.

5 Return to Step 1.

In an on-line setting, this control algorithm would run continuously. From an off-line analysis perspective, the algorithm repeats until convergence is achieved.

To analyze convergence characteristics, this iterative procedure can be expressed as a mapping. For every injection node $k \in \{1, \cdots, m\}$, the compensation Q_k is updated according to,

$$Q_k^+ = \mathcal{S}_t\Big\{\Big(D(\mathbf{A}_k\mathbf{Q}^- + \mu_k)\Big) \times \Big(W_I(\mathbf{B}_k\mathbf{Q}^- + \eta_k)\Big)^* - jQ_k^-\Big\}, \tag{6.3.10}$$

where the operator $\mathcal{S}_t\{\cdot\}$ denotes the Steinmetz equation (6.2.3), $\mathcal{S}_t\{\cdot\} = E \cdot \mathbf{Re}(\cdot) + F \cdot \mathbf{Im}(\cdot)$, $D = \Big[1, -1, 0; 0, 1, -1; -1, 0, 1\Big]$ converts line-to-neutral voltages to line-to-line voltages, $W_I = \Big[1, -1, 0; 1, 2, 0; -2, -1, 0\Big]/3$ converts line currents to equivalent delta currents, and the operator "$\times$" denotes element-wise multiplication. Therefore, the term inside the curly braces is the equivalent local plus downstream delta-connected load.[4]

6.3.1.3 Quadratic Mapping

The expression (6.3.10) can be expanded and reorganized into a quadratic mapping,

$$\mathbf{Q}^+ := [(Q_1^+)^\intercal, \cdots, (Q_m^+)^\intercal]^\intercal = f(\mathbf{Q}^-), \tag{6.3.11a}$$

where for $k = 1, \cdots, m$,

$$Q_k^+ = \begin{bmatrix} Q_{k1}^+ \\ Q_{k2}^+ \\ Q_{k3}^+ \end{bmatrix} = \begin{bmatrix} (\mathbf{Q}^-)^\intercal[\alpha_{k1}]\mathbf{Q}^- + \beta_{k1}^\intercal\mathbf{Q}^- + \gamma_{k1} \\ (\mathbf{Q}^-)^\intercal[\alpha_{k2}]\mathbf{Q}^- + \beta_{k2}^\intercal\mathbf{Q}^- + \gamma_{k2} \\ (\mathbf{Q}^-)^\intercal[\alpha_{k3}]\mathbf{Q}^- + \beta_{k3}^\intercal\mathbf{Q}^- + \gamma_{k3} \end{bmatrix}, \tag{6.3.11b}$$

and $Q_{k1} = Q_k^{ab}$, $Q_{k2} = Q_k^{bc}$, and $Q_{k3} = Q_k^{ca}$ are the three phase-to-phase reactive power compensations. Quadratic coefficients $[\alpha_{k\phi}] \in \mathbb{R}^{3m\times 3m}$, linear coefficients $\beta_{k\phi} \in \mathbb{R}^{3m}$, and constant coefficients $\gamma_{k\phi} \in \mathbb{R}$, $\forall k \in \{1, \cdots, m\}$, $\phi \in \{1, 2, 3\}$ collect system parameters such as line impedances, nominal loading conditions, and transformer tap ratios. It is clear from equation (6.3.11) that the Q_k of all the controllers are coupled and thereby influence each other. In fact, certain patterns exist in these coefficients due to the radial structure of distribution systems. This is considered further in the case studies of Section 6.5.

[4]This formulation does not cater for unbalance arising from zero-sequence voltages. Accordingly, we do not consider unbalanced wye-connected load.

6.3.2 Estimate for the Fixed-Point

Since linear multi-phase power flow equation (6.3.2), (6.3.3) is adopted for analyzing convergence properties, we desire an initialization point $\hat{\mathbf{v}}$ that is sufficiently close to the converged voltage profile to ensure an acceptable approximation to the nonlinear power flow. This requires a good estimate for the converged fixed-point. This value also affects the stability region estimate provided by the contraction proof of Subsection 6.3.3.

The special radial structure of distribution networks motivates a heuristic for estimating the fixed-point. This heuristic seeks to minimize certain dominant terms that appear in the self-mapping relationship (6.3.12) that is presented in the following convergence proof. This results in the simple linear program,

$$
\begin{aligned}
(\mathcal{P}1) \quad \min_{\mathbf{Q}^0} \quad & \sum_{k=1}^{m} \sum_{\phi=1}^{3} \sum_{j=1}^{m} v_{k\phi}^{j} + \epsilon \left\| \mathbf{Q}^0 \right\|_1 \\
\text{subject to} \quad & \left\| 2\alpha_{k\phi}(1:3,:) \cdot \mathbf{Q}^0 + \beta_{k\phi}(1:3) \right\|_1 \leq v_{k\phi}^{1} \\
& \left\| 2\alpha_{k\phi}(4:6,:) \cdot \mathbf{Q}^0 + \beta_{k\phi}(4:6) \right\|_1 \leq v_{k\phi}^{2} \\
& \qquad \cdots \\
& \left\| 2\alpha_{k\phi}(3m-2:3m,:) \cdot \mathbf{Q}^0 + \beta_{k\phi}(3m-2:3m) \right\|_1 \leq v_{k\phi}^{m} \\
& \qquad \forall k \in \{1, \cdots, m\}, \ \phi \in \{1,2,3\},
\end{aligned}
$$

where $\epsilon > 0$ is a small constant to penalize the norm of the fixed point $\mathbf{Q}^0$, $\alpha_{k\phi}(1:3,:)$ represents the first three rows of matrix $[\alpha_{k\phi}]$, $\beta_{k\phi}(1:3)$ represents the first three entries of vector $\beta_{k\phi}$, and so on.

The optimizer $\mathbf{Q}^0$ serves as a sufficiently accurate approximation for the final fixed-point $\mathbf{Q}^*$ of the mapping (6.3.11). Substituting $\mathbf{Q}^0$ into equation (6.3.6), we obtain a good initialization $\hat{\mathbf{v}}$ that results in an accurate linear power flow model.

6.3.3 Convergence Proof

The Banach fixed-point theorem [138] can be used to prove contraction of the quadratic mapping (6.3.11), and provide conditions that certify convergence of the decentralized and distributed Steinmetz-based control schemes. The existence and uniqueness of the fixed-point are guaranteed provided those conditions are satisfied. We proceed by establishing two characteristics, 1) the mapping is a self-mapping, and 2) the mapping is a contraction.

6.3.3.1 Self-Mapping

For a certain $r \in \mathbb{R}^m_+$, define the set,

$$\mathcal{S}(r) = \Big\{\mathbf{Q} \in \mathbb{R}^{3m} \Big| \|Q_k - Q_k^0\|_\infty \leq r_k, \forall k \in \{1, \cdots, m\}\Big\},$$

where $\mathbf{Q}^0 = [Q_1^{0\intercal}, \cdots, Q_m^{0\intercal}]^\intercal$ are computed from the linear program $\mathcal{P}1$, and keeping in mind that $Q_k \in \mathbb{R}^3$. We need to show that the mapping (6.3.11) maps from $\mathcal{S}(r)$ to $\mathcal{S}(r)$, i.e., $\mathbf{Q}^+ := f(\mathbf{Q}^-)$, where $f : \mathcal{S}(r) \to \mathcal{S}(r)$. Hence, we need to show that $\Big\{\|Q_k - Q_k^0\|_\infty \leq r_k, \forall k \in \{1, \cdots, m\}\Big\}$ leads to $\Big\{\|Q_k^+ - Q_k^0\|_\infty \leq r_k, \forall k \in \{1, \cdots, m\}\Big\}$. Equivalently, we can instead show that $\Big\{\|Q_k - Q_k^0\|_\infty \leq r_k, \forall k \in \{1, \cdots, m\}\Big\}$ leads to $\Big\{|Q_{k\phi}^+ - Q_{k\phi}^0| \leq r_k, \forall k \in \{1, \cdots, m\}, \forall \phi \in \{1, 2, 3\}\Big\}$. Accordingly,

$$\begin{aligned}
|Q_{k\phi}^+ - Q_{k\phi}^0| &= |\mathbf{Q}^\intercal[\alpha_{k\phi}]\mathbf{Q} + (\beta_{k\phi})^\intercal\mathbf{Q} + \gamma_{k\phi} - Q_{k\phi}^0| \\
&= |(\mathbf{Q} - \mathbf{Q}^0)^\intercal[\alpha_{k\phi}](\mathbf{Q} - \mathbf{Q}^0) + \Big((\beta_{k\phi})^\intercal + 2(\mathbf{Q}^0)^\intercal[\alpha_{k\phi}]\Big) \cdot (\mathbf{Q} - \mathbf{Q}^0) \\
&\qquad + (\mathbf{Q}^0)^\intercal[\alpha_{k\phi}]\mathbf{Q}^0 + (\beta_{k\phi})^\intercal\mathbf{Q}^0 + \gamma_{k\phi} - Q_{k\phi}^0| \\
&\leq \|\mathbf{Q} - \mathbf{Q}^0\|_1 \cdot \|[\alpha_{k\phi}]\|_\infty \cdot \|\mathbf{Q} - \mathbf{Q}^0\|_\infty + \sum_{l=1}^{m} \Big(\|\Big((\beta_{k\phi})^\intercal + 2(\mathbf{Q}^0)^\intercal[\alpha_{k\phi}]\Big)_{[l]}\|_1 \cdot \|Q_l - Q_l^0\|_\infty\Big) \\
&\qquad + |(\mathbf{Q}^0)^\intercal[\alpha_{k\phi}]\mathbf{Q}^0 + (\beta_{k\phi})^\intercal\mathbf{Q}^0 + \gamma_{k\phi} - Q_{k\phi}^0| \\
&\leq 3(r_1 + \cdots + r_m)\max(r_1, \cdots, r_m) \cdot \|[\alpha_{k\phi}]\|_\infty + \sum_{l=1}^{m} \Big(r_l \cdot \|\Big((\beta_{k\phi})^\intercal + 2(\mathbf{Q}^0)^\intercal[\alpha_{k\phi}]\Big)_{[l]}\|_1\Big) \\
&\qquad + |(\mathbf{Q}^0)^\intercal[\alpha_{k\phi}]\mathbf{Q}^0 + (\beta_{k\phi})^\intercal\mathbf{Q}^0 + \gamma_{k\phi} - Q_{k\phi}^0|, \qquad (6.3.12)
\end{aligned}$$

where the subscript $[l]$ denotes the $(3l-2) \leftrightarrow 3l$ rows of the matrix. To ensure $\mathcal{S}(r)$ maps to $\mathcal{S}(r)$, we require equation (6.3.12) $\leq r_k$ for all $k \in \{1, \cdots, m\}$ and $\phi \in \{1, 2, 3\}$.

Define sets

$$\begin{aligned}
\mathcal{M}_{k\phi} = \Big\{&[\alpha_{k\phi}] \in \mathbb{R}^{3m\times 3m}, \beta_{k\phi} \in \mathbb{R}^{3m}, \gamma_{k\phi} \in \mathbb{R}\Big| \\
&3(r_1 + \cdots + r_m) \cdot \hat{r} \cdot \|[\alpha_{k\phi}]\|_\infty + \sum_{l=1}^{m} \Big(r_l \cdot \|\Big((\beta_{k\phi})^\intercal + 2(\mathbf{Q}^0)^\intercal[\alpha_{k\phi}]\Big)_{[l]}\|_1\Big) \\
&+ |(\mathbf{Q}^0)^\intercal[\alpha_{k\phi}]\mathbf{Q}^0 + (\beta_{k\phi})^\intercal\mathbf{Q}^0 + \gamma_{k\phi} - Q_{k\phi}^0| \leq r_k\Big\}, \qquad (6.3.13)
\end{aligned}$$

$\forall k \in \{1, \cdots, m\}$ and $\forall \phi \in \{1, 2, 3\}$, where $\hat{r} = \max(r_1, \cdots, r_m)$. For given fixed $r_k, k = 1, \cdots, m$, we require the intersection of the $3m$ sets $\mathcal{M}_{k\phi}$ given by (6.3.13) to be non-empty for $\mathcal{S}(r)$ to be a self-mapping set.

Alternatively, for a given system with fixed parameters $[\alpha_{k\phi}], \beta_{k\phi}, \gamma_{k\phi}, \forall k \in \{1, \cdots, m\}$, $\phi \in \{1, 2, 3\}$, define the sets,

$$\tilde{\mathcal{M}}_{k\phi} = \Big\{ r \in \mathbb{R}_+^m \Big| 3(r_1 + \cdots + r_m)\, \hat{r} \cdot \|[\alpha_{k\phi}]\|_\infty + \sum_{l=1}^{m} \Big(r_l \cdot \|\Big((\beta_{k\phi})^\intercal + 2(\mathbf{Q}^0)^\intercal [\alpha_{k\phi}] \Big)_{[l]} \|_1 \Big) \\ + |(\mathbf{Q}^0)^\intercal [\alpha_{k\phi}] \mathbf{Q}^0 + (\beta_{k\phi})^\intercal \mathbf{Q}^0 + \gamma_{k\phi} - Q_{k\phi}^0| \leq r_k \Big\}, \tag{6.3.14}$$

$\forall k \in \{1, \cdots, m\}$ and $\forall \phi \in \{1, 2, 3\}$. In this case, the mapping (6.3.11) is a self-mapping on $\mathcal{S}(r)$ when $r \in \cap_{k=1}^m \cap_{\phi=1}^3 \tilde{\mathcal{M}}_{k\phi} \neq \emptyset$.

6.3.3.2 Contraction

Next, we establish conditions under which the mapping (6.3.11) is a contraction on $\mathcal{S}(r)$. Define a norm $\|\mathbf{Q}\|_\delta := a_1 \|Q_1\|_\infty + \cdots + a_m \|Q_m\|_\infty$, where $a_1 = 1, a_k \geq 1, \forall k = 2, \cdots, m$. We need to show that for any two points $\mathbf{Q}^x$ and $\mathbf{Q}^y$ in $\mathcal{S}(r)$, $\|\mathbf{Q}^{x+} - \mathbf{Q}^{y+}\|_\delta \leq \rho \cdot \|\mathbf{Q}^x - \mathbf{Q}^y\|_\delta$, where $0 \leq \rho < 1$. Expanding the δ-norm, this implies $\sum_{k=1}^m (a_k \|Q_k^{x+} - Q_k^{y+}\|_\infty) \leq \rho \cdot \sum_{k=1}^m (a_k \|Q_k^x - Q_k^y\|_\infty)$.

Each of the m DERs consists of three reactive power injections $Q_k = [Q_k^{ab}, Q_k^{bc}, Q_k^{ca}]^\intercal$, so there are 3^m ways of choosing injections across the m DERs. Let $\phi^i \in \{1, 2, 3\}^m$ represent the i-th choice of the 3^m arrangements. Then the contraction requirement is equivalent to ensuring,

$$\sum_{k=1}^{m} \Big(a_k \, |\{Q_k^{x+} - Q_k^{y+}\}_{\phi_k^i}| \Big) \leq \rho_i \cdot \sum_{k=1}^{m} \Big(a_k \, \|Q_k^x - Q_k^y\|_\infty \Big), \tag{6.3.15}$$

for every $i = 1, \cdots, 3^m$, with $\phi_k^i \in \{1, 2, 3\}$ being the k-th element of ϕ^i, and $\rho = \max(\rho_i) < 1$. For every arrangement i, we can write,

$$\begin{aligned}
&\sum_{k=1}^{m} \Big(a_k \, |\{Q_k^{x+} - Q_k^{y+}\}_{\phi_k^i}| \Big) \\
&\quad = \sum_{k=1}^{m} \Big(a_k \, \Big| (\mathbf{Q}^x)^\intercal [\alpha_{k\phi_k^i}] \mathbf{Q}^x - (\mathbf{Q}^y)^\intercal [\alpha_{k\phi_k^i}] \mathbf{Q}^y + \beta_{k\phi_k^i}^\intercal (\mathbf{Q}^x - \mathbf{Q}^y) \Big| \Big) \\
&\quad = \sum_{k=1}^{m} \Big(a_k \, \Big| \Big((\mathbf{Q}^x - \mathbf{Q}^0) + (\mathbf{Q}^y - \mathbf{Q}^0) + 2\mathbf{Q}^0 \Big)^\intercal [\alpha_{k\phi_k^i}] (\mathbf{Q}^x - \mathbf{Q}^y) + \beta_{k\phi_k^i}^\intercal (\mathbf{Q}^x - \mathbf{Q}^y) \Big| \Big) \\
&\quad = \sum_{k=1}^{m} \Big(a_k \, \Big| \Big((\mathbf{Q}^x - \mathbf{Q}^0) + (\mathbf{Q}^y - \mathbf{Q}^0) \Big)^\intercal [\alpha_{k\phi_k^i}] (\mathbf{Q}^x - \mathbf{Q}^y) + \Big(\beta_{k\phi_k^i}^\intercal + 2(\mathbf{Q}^0)^\intercal [\alpha_{k\phi_k^i}] \Big) (\mathbf{Q}^x - \mathbf{Q}^y) \Big| \Big) \\
&\quad \leq \sum_{k=1}^{m} \Big(a_k \Big(\|(\mathbf{Q}^x - \mathbf{Q}^0) + (\mathbf{Q}^y - \mathbf{Q}^0)\|_\infty \cdot \|[\alpha_{k\phi_k^i}]\|_1 \cdot \|\mathbf{Q}^x - \mathbf{Q}^y\|_1 \\
&\qquad + \sum_{l=1}^{m} \|\Big(\beta_{k\phi_k^i}^\intercal + 2(\mathbf{Q}^0)^\intercal [\alpha_{k\phi_k^i}] \Big)_{[l]} \|_1 \cdot \|Q_l^x - Q_l^y\|_\infty \Big) \Big)
\end{aligned}$$

$$
\begin{aligned}
&\leq \sum_{k=1}^{m}\Big(a_k\Big(2\hat{r}\cdot\|[\alpha_{k\phi_k^i}]\|_1\cdot\Big(\sum_{l=1}^{m}\|Q_l^x-Q_l^y\|_1\Big)+\sum_{l=1}^{m}\|\Big(\beta_{k\phi_k^i}^{\intercal}+2(\mathbf{Q}^0)^{\intercal}[\alpha_{k\phi_k^i}]\Big)_{[l]}\|_1\cdot\|Q_l^x-Q_l^y\|_\infty\Big)\Big)\\
&\leq \sum_{k=1}^{m}\Big(a_k\Big(6\hat{r}\cdot\|[\alpha_{k\phi_k^i}]\|_1\cdot\Big(\sum_{l=1}^{m}\|Q_l^x-Q_l^y\|_\infty\Big)+\sum_{l=1}^{m}\|\Big(\beta_{k\phi_k^i}^{\intercal}+2(\mathbf{Q}^0)^{\intercal}[\alpha_{k\phi_k^i}]\Big)_{[l]}\|_1\cdot\|Q_l^x-Q_l^y\|_\infty\Big)\Big)\\
&\leq \sum_{l=1}^{m}\Big(\Big(6\hat{r}\cdot\Big(\sum_{k=1}^{m}(a_k\|[\alpha_{k\phi_k^i}]\|_1)\Big)+\sum_{k=1}^{m}a_k\|\Big(\beta_{k\phi_k^i}^{\intercal}+2(\mathbf{Q}^0)^{\intercal}[\alpha_{k\phi_k^i}]\Big)_{[l]}\|_1\Big)\cdot\|Q_l^x-Q_l^y\|_\infty\Big)\\
&:= \sum_{l=1}^{m}\Big(\delta_l^i\cdot\|Q_l^x-Q_l^y\|_\infty\Big),
\end{aligned}
\tag{6.3.16}
$$

where $\hat{r}=\max(r_1,\cdots,r_m)$. Therefore, we require $\delta_l^i/a_l<1$, $\forall l=1,\cdots,m$. For $i=1,\cdots,3^m$, define the sets,

$$
C_i=\Big\{[\alpha_{k\phi_k^i}]\in\mathbb{R}^{3m\times 3m},\beta_{k\phi_k^i}\in\mathbb{R}^{3m},\forall k\in\{1,\cdots,m\}\Big|\delta_l^i/a_l<1,\forall l=1,\cdots,m\Big\}. \tag{6.3.17}
$$

For any fixed r_k, a_k, where $k=1,\cdots,m$, the mapping (6.3.11) is a contraction on $\mathcal{S}(r)$ if there exist $[\alpha_{k\phi}]$ and $\beta_{k\phi}$ that are contained in the intersection $\cap_{i=1}^{3^m}C_i\neq\emptyset$.

Alternatively, for a given system with fixed parameters $[\alpha_{k\phi}]$, $\beta_{k\phi}$, $\gamma_{k\phi}$, $\forall k\in\{1,\cdots,m\}$, $\phi\in\{1,2,3\}$, define the sets,

$$
\tilde{C}_i=\Big\{r\in\mathbb{R}_+^m,a_1=1,a_k\geq 1,\forall k=2,\cdots,m\Big|\delta_l^i/a_l<1,\forall\, l=1,\cdots,m\Big\},\ \forall i=1\cdots 3^m. \tag{6.3.18}
$$

In that case, the mapping (6.3.11) is a contraction on $\mathcal{S}(r)$ for $\{r,a\}\in\cap_{i=1}^{3^m}\tilde{C}_i\neq\emptyset$.

6.3.3.3 Computation

It is anticipated that most distribution feeders will have few critical nodes that require balancing, so m will be small. Therefore verifying the 3^m intersections of equation (6.3.18) will be manageable. Moreover, the computation required for checking each condition is negligible.

If, however, m is large, a heuristic can be exploited to reduce the dimensionality. The proposed heuristic is motivated by the observation that if two critical nodes are on different branches, then the reactive power injections of one controller have little impact on the other controller. Therefore, when analyzing the interactions between such Steinmetz controllers, those controllers can be (approximately) decoupled. Based on this intuition, controllers can be categorized into multiple groups, where interactions within groups are relatively tight but interactions between groups are weak. When analyzing the convergence of the controllers from one group, the injections from the other groups can be neglected. By doing so, the total number of intersections required to be checked reduces

to $3^{m_1} + 3^{m_2} + \cdots + 3^{m_n}$, where n is the number of groups, m_i is the number of Steinmetz controllers within the i-th group, and $m_1 + m_2 + \cdots + m_n = m$.

6.3.3.4 Interpretations

The theoretical results that have been derived may be viewed from two perspectives, operation and design. In the first setting, the network topology and system parameters, such as line impedances and loading conditions, are given. Based on that information, an injection range can be certified for the reactive power resources such that starting from within that range ensures the decentralized and distributed controllers will converge to the unique operating point. The second interpretation suggests that given the network topology and a desired injection range, system parameters that ensure convergence can be determined.

Note that the Banach fixed-point theorem is a sufficient result, so the derived conditions are conservative relative to the true convergence region. Nevertheless, they provide valuable guidance for determining convergence characteristics for realistic systems, as discussed further in Section 6.5.

The analysis in this chapter considers a general quadratic mapping which is suitable for modeling many applications. For example, the power flow equations are formulated as affinely parameterized quadratic equations in [142], where existence of power flow solutions is studied.

6.4 Time Delays in Measurement and Control Implementation

The previous analysis can be extended to incorporate time delays in the measurement process and in updating reactive power injections. In generic cases, different controllers could have different time delays. For a specific control injection Q_k, the measurement delay τ_k^m and the control implementation delay τ_k^c can be combined as $\tau_k := \tau_k^m + \tau_k^c$. Such time-delay effects can be incorporated in the mapping model by,

$$\mathbf{Q}(t+1) = [(Q_1(t+1))^\intercal, \cdots, (Q_m(t+1))^\intercal]^\intercal, \tag{6.4.1}$$

where for $k = 1, \cdots, m$,

$$Q_k(t+1) = [Q_{k1}(t+1), Q_{k2}(t+1), Q_{k3}(t+1)]^\intercal$$

$$
\begin{aligned}
&= \begin{bmatrix} (\mathbf{Q}(t-\tau_k))^\intercal [\alpha_{k1}]\mathbf{Q}(t-\tau_k) + \beta_{k1}^\intercal \mathbf{Q}(t-\tau_k) + \gamma_{k1} \\ (\mathbf{Q}(t-\tau_k))^\intercal [\alpha_{k2}]\mathbf{Q}(t-\tau_k) + \beta_{k2}^\intercal \mathbf{Q}(t-\tau_k) + \gamma_{k2} \\ (\mathbf{Q}(t-\tau_k))^\intercal [\alpha_{k3}]\mathbf{Q}(t-\tau_k) + \beta_{k3}^\intercal \mathbf{Q}(t-\tau_k) + \gamma_{k3} \end{bmatrix} \\
&:= f_k\Big(\mathbf{Q}(t-\tau_k)\Big). \qquad (6.4.2)
\end{aligned}
$$

It can be observed from equation (6.4.1) that the injections from all distributed controllers Q_k where $k = 1, \cdots, m$, from time t up until time $t - \hat{\tau}$ where $\hat{\tau} = \max(\tau_1, \cdots, \tau_m) + 1$ are coupled together to determine the control injection at time $t + 1$, i.e., $\mathbf{Q}(t + 1)$. To analyze the convergence property of the time-delayed system (6.4.1), we need to enlarge the state $\mathbf{Q}$ by defining an augmented state $\hat{\mathbf{Q}}$, where

$$
\hat{\mathbf{Q}}^+ = [\mathbf{Q}(t + \hat{\tau}), \cdots, \mathbf{Q}(t + 1)]^\intercal, \qquad (6.4.3)
$$

$$
\hat{\mathbf{Q}}^- = [\mathbf{Q}(t), \cdots, \mathbf{Q}(t - \hat{\tau} + 1)]^\intercal, \qquad (6.4.4)
$$

where $\hat{\tau} = \max(\tau_1, \cdots, \tau_m) + 1$. For $\tilde{\tau} = 1, \cdots, \hat{\tau}$,

$$
\mathbf{Q}(t + \tilde{\tau}) = [(Q_1(t + \tilde{\tau}))^\intercal, \cdots, (Q_m(t + \tilde{\tau}))^\intercal]^\intercal, \qquad (6.4.5)
$$

in which for $k = 1, \cdots, m$,

$$
\begin{aligned}
Q_k(t + \tilde{\tau}) &= [Q_{k1}(t + \tilde{\tau}), Q_{k2}(t + \tilde{\tau}), Q_{k3}(t + \tilde{\tau})]^\intercal \\
&= \begin{bmatrix} \mathbf{Q}(t+\tilde{\tau}-\tau_k-1)^\intercal [\alpha_{k1}]\mathbf{Q}(t+\tilde{\tau}-\tau_k-1) + \beta_{k1}^\intercal \mathbf{Q}(t+\tilde{\tau}-\tau_k-1) + \gamma_{k1} \\ \mathbf{Q}(t+\tilde{\tau}-\tau_k-1)^\intercal [\alpha_{k2}]\mathbf{Q}(t+\tilde{\tau}-\tau_k-1) + \beta_{k2}^\intercal \mathbf{Q}(t+\tilde{\tau}-\tau_k-1) + \gamma_{k2} \\ \mathbf{Q}(t+\tilde{\tau}-\tau_k-1)^\intercal [\alpha_{k3}]\mathbf{Q}(t+\tilde{\tau}-\tau_k-1) + \beta_{k3}^\intercal \mathbf{Q}(t+\tilde{\tau}-\tau_k-1) + \gamma_{k3} \end{bmatrix}. \qquad (6.4.6)
\end{aligned}
$$

Now, the enlarged system with state $\hat{\mathbf{Q}}$ can be written into a new quadratic mapping form,

$$
\hat{\mathbf{Q}}^+ = \hat{\mathcal{F}}(\hat{\mathbf{Q}}^-). \qquad (6.4.7)
$$

The same contraction analysis as shown in Section 6.3 can be applied to equation (6.4.7). As a result, the convergence property of the time-delayed system (6.4.1) can be established.

6.5 Case Studies

This section presents a number of case studies that demonstrate the balancing results of the decentralized and distributed Steinmetz controllers and test the convergence results.

Table 6.1: Constant-Power Loads of the 5-Bus System.

Index	S_{ab}	S_{bc}	S_{ca}
node 5	50 kVA p.f.=0.85 lag.	30 kVA p.f.=0.90 lag.	100 kVA p.f.=0.95 lag.
node 4	40 kVA p.f.=0.95 lag.	20 kVA p.f.=0.80 lag.	70 kVA p.f.=0.85 lag.
node 3	50 kVA p.f.=0.85 lag.	30 kVA p.f.=0.90 lag.	100 kVA p.f.=0.95 lag.
node 2	40 kVA p.f.=0.95 lag.	20 kVA p.f.=0.80 lag.	70 kVA p.f.=0.85 lag.

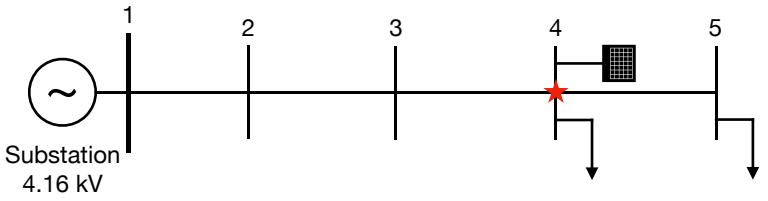

Figure 6.4: One-line diagram for the 5-bus network of Case 1.

Various control schemes and distributed resource deployment options are investigated. The cases consider a 5-bus distribution network, the IEEE standard 13-bus test feeder and the IEEE standard 34-bus test feeder.

The one-line diagram for the 5-bus network is shown in Fig. 6.2 and Figs. 6.4–6.6. This network is considered in cases 1 to 4. In each of these cases, a black arrow indicates a constant-power load, the value of which is specified in Table 6.1. The voltage at node 1 is balanced 4.16 kV line-to-line.

Case 1. We first test the balancing and convergence properties of a single Steinmetz controller. Consider node 4 in Fig. 6.4 to be the critical node that is to be balanced, and assume that a three-phase PV inverter and Steinmetz controller are deployed there. For the given system parameters, the certified operating region for PV reactive power injection at node 4 is $\mathcal{S} = \left\{Q_4 \in \mathbb{R}^3 \middle| \|Q_4 - Q_4^0\|_\infty \leq 43.5 \text{ p.u.}\right\}$, where[5] $Q_4 = [Q_4^{ab}, Q_4^{bc}, Q_4^{ca}]^\intercal$. Since the certified region is large, it was not necessary to estimate the fixed point. Therefore Q_4^0 was chosen as the zero vector. Although the convergence condition provided in the chapter is a sufficient condition, it is clear that in this single Steinmetz controller case the certified region of 43.5 p.u. is much larger than the normal operating range of inverters. Hence, this individual Steinmetz controller is robust to disturbances.

The VUF at the critical node 4 is reduced from 1.35% to 0.0089%. In fact, the VUF is also

[5]For clarity of presentation we use node number throughout this section, i.e., the subscript refers to the 4-th node in the system.

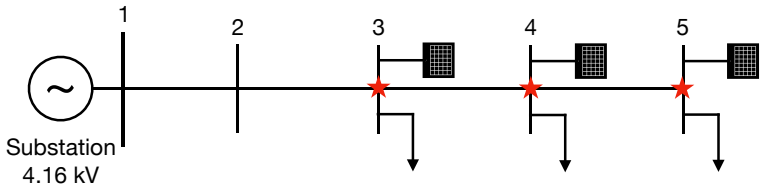

Figure 6.5: One-line diagram for the 5-bus network of Case 3.

reduced at the other three nodes, from 0.44% to 0.0029% (node 2), from 0.89% to 0.0059% (node 3), and from 1.66% to 0.32% (node 5). The converged reactive power compensation injected at node 4 is $Q_4 = [-0.5920, 0.6165, -0.0245]^\intercal$.

Case 2. This case provides an initial analysis of interactions between two Steinmetz controllers. Referring to Fig. 6.2, both nodes 4 and 5 are critical nodes that are to be balanced, and three-phase PV inverters and Steinmetz controllers are placed at these two nodes. Based on the estimate provided by the linear program $\mathcal{P}1$, Q_4^0 is chosen as $[-0.1681, 0.2118, -0.0197]^\intercal$, and Q_5^0 is $[-0.4234, 0.4046, 0.0096]^\intercal$. The certified convergence regions for the two PV inverters are $\mathcal{S}_4 = \left\{Q_4 \in \mathbb{R}^3 \middle| \|Q_4 - Q_4^0\|_\infty \leq 3.5 \text{ p.u.}\right\}$, and $\mathcal{S}_5 = \left\{Q_5 \in \mathbb{R}^3 \middle| \|Q_5 - Q_5^0\|_\infty \leq 1.65 \text{ p.u.}\right\}$, where $Q_4 = [Q_4^{ab}, Q_4^{bc}, Q_4^{ca}]^\intercal$, and $Q_5 = [Q_5^{ab}, Q_5^{bc}, Q_5^{ca}]^\intercal$. The coefficients a_k of the norm $\|\cdot\|_\delta$ in Subsection 6.3.3.2 are $a_4 = 1$ and $a_5 = 2.6$. Note that when determining the certified convergence regions, there is flexibility to choose from a range of feasible combinations of radii r_k and norm scale parameters a_k. We report the largest achievable radius.

In this test example, the VUF at nodes 4 and 5 reduced from 1.35% to 0% and from 1.66% to 0%, respectively. The VUF at both nodes 2 and 3 also reduced to 0%. At convergence, the reactive power compensation at nodes 4 and 5 was $Q_4 = [-0.1714, 0.2086, -0.0372]^\intercal$ and $Q_5 = [-0.4203, 0.4077, 0.0127]^\intercal$, respectively. Note that these fixed points are very close to the estimates provided by the linear program.

Case 3. To further explore the interactions between multiple decentralized Steinmetz controllers, we now consider three controllers. Assume that nodes 3, 4 and 5 are critical nodes, each equipped with a three-phase PV inverter and a Steinmetz controller. The corresponding system diagram is shown in Fig. 6.5.

The estimated fixed points provided by the linear program $\mathcal{P}1$ are $Q_3^0 = [-0.3486, 0.4742, 0.0826]^\intercal$, $Q_4^0 = [-0.1971, 0.1831, -0.0628]^\intercal$ and $Q_5^0 = [-0.4623, 0.3661, -0.0290]^\intercal$. The certified convergence regions for the three PV inverters are $\mathcal{S}_3 = \left\{Q_3 \in \mathbb{R}^3 \middle| \|Q_3 - Q_3^0\|_\infty \leq 0.9 \text{ p.u.}\right\}$, $\mathcal{S}_4 = \left\{Q_4 \in \mathbb{R}^3 \middle| \|Q_4 - Q_4^0\|_\infty \leq 0.35 \text{ p.u.}\right\}$ and $\mathcal{S}_5 = \left\{Q_5 \in \mathbb{R}^3 \middle| \|Q_5 - Q_5^0\|_\infty \leq 0.2 \text{ p.u.}\right\}$, where as usual Q_3, Q_4 and Q_5 denote line-to-line reactive power compensation injected at the corresponding nodes. Across a large range of feasible solutions, we chose the solution that achieved the largest region for the furthest downstream node. The corresponding

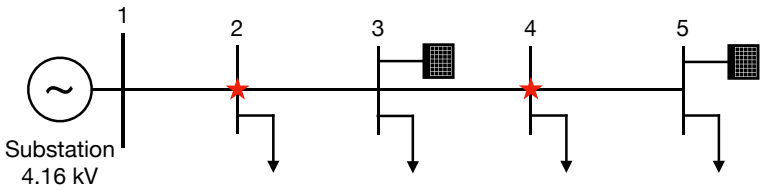

Figure 6.6: One-line diagram for the 5-bus network of Case 4.

norm scale parameters were $a_3 = 1$, $a_4 = 2.1$, $a_5 = 5$. In this example, the VUF at nodes 3, 4 and 5 reduced from 1.53%, 2.01% and 2.34%, respectively, to 0% in all cases. The VUF at node 2 also reduced from 0.75% to 0%. The converged reactive power compensation at nodes 3, 4 and 5 was $Q_3 = [-0.4206, 0.4078, 0.0127]^\intercal$, $Q_4 = [-0.1715, 0.2087, -0.0372]^\intercal$ and $Q_5 = [-0.4205, 0.4078, 0.0127]^\intercal$, respectively.

We are now in a position to provide an interpretation of the construction of the norm which is used to show contraction when multiple controllers interact. Given the radial structure of the distribution network, it is clear that the power injection at a downstream node has a direct effect on the power seen at an upstream node. However, the power injection at an upstream node only influences the power of a downstream node through changing the voltage profile, which affects the losses between the two nodes. This observation is also reflected in the relative magnitudes of the coefficient matrices $[\alpha_{k\phi}]$, $\beta_{k\phi}$, $\gamma_{k\phi}$, $\forall k \in \{1, \cdots, m\}$, $\phi \in \{1, 2, 3\}$. When there are multiple controllers, the injections of the other controllers behave as disturbances. It follows from the strong/weak coupling relationship that the injection at a downstream node can be viewed as a significant disturbance to the upstream node and therefore should be penalized by placing higher weight in the contraction norm. Doing so effectively distorts the state space to enforce contraction.

In cases 1, 2 and 3, it was assumed that three-phase DERs with Steinmetz controllers were available at the critical nodes. This led to a totally decentralized scheme where individual controllers did not communicate with each other, nor was a central energy management system required. Only local measurements of line-to-neutral voltages and line currents were needed. The resulting control system is cheap to implement, while the convergence guarantees ensure robustness to disturbances. However, DERs are not always available at critical nodes. In particular, three-phase PV inverters are rare in actual distribution networks. To address this issue, the distributed control scheme discussed in Subsection 6.2.3 can be employed. By taking advantage of the radial structure of distribution feeders, the network is first subdivided into partitions based on the critical nodes that must be balanced. The DERs within each partition are deployed for balancing the associated critical node. Only limited communication is required within each partition.

Case 4. The balancing and convergence properties of the distributed control scheme

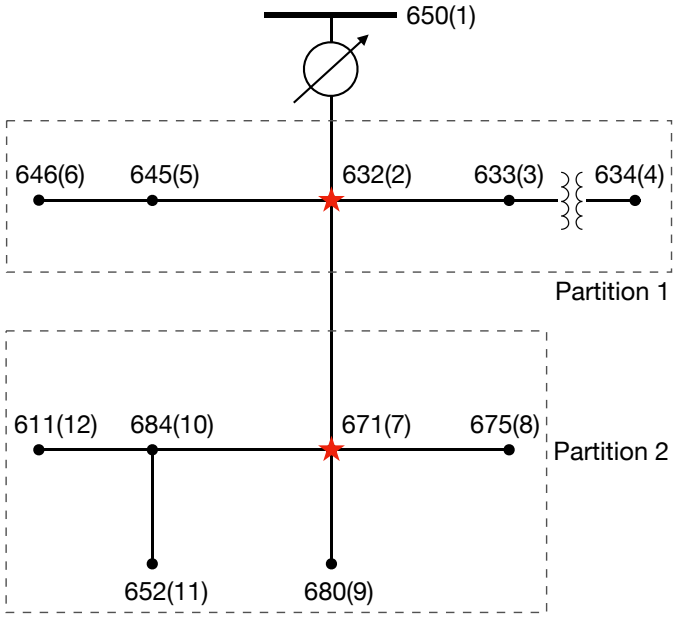

Figure 6.7: IEEE 13-bus test feeder.

were further tested using the 5-bus system. As shown in Fig. 6.6, nodes 2 and 4 are critical nodes, while two three-phase PV inverters and Steinmetz controllers are sited at nodes 3 and 5. In this test case, the only communication required is to send the measurements of voltage and current at nodes 2 and 4 to nodes 3 and 5, respectively. The certified convergence regions at nodes 3 and 5 are $\mathcal{S}_3 = \left\{Q_3 \in \mathbb{R}^3 \middle| \|Q_3 - Q_3^0\|_\infty \leq 7.8\,\text{p.u.}\right\}$, and $\mathcal{S}_5 = \left\{Q_5 \in \mathbb{R}^3 \middle| \|Q_5 - Q_5^0\|_\infty \leq 4.2\,\text{p.u.}\right\}$, where Q_3 and Q_5 refer to the line-to-line reactive power compensation, and Q_3^0 and Q_5^0 were chosen to be zero vectors. Here we report the solution that gave the largest contraction region for the downstream node, i.e., node 5. The coefficients a_k in the contraction norm were $a_3 = 1$ and $a_5 = 2.5$. The VUF at nodes 2 and 4 reduced from 0.90% to 0%, and from 2.17% to 0.14%, respectively. The VUF at nodes 3 and 5 also reduced, from 1.68% to 0.14% and from 2.50% to 0.29%, respectively. The converged reactive power compensation at nodes 3 and 5 was $Q_3 = [-0.5911, 0.6108, -0.0197]^\intercal$ and $Q_5 = [-0.5922, 0.6122, -0.0199]^\intercal$, respectively.

We further tested the distributed Steinmetz controller and the convergence results on a modified IEEE 13-bus system shown in Fig. 6.7. The system configuration is documented in [143]. We considered delta-connected constant-power spot loads in this example. The in-line voltage regulator was fixed at its default value, having identical taps on all three phases. The impedance of line 650–632 was balanced. The lines 684–611 and 684–652 were changed to configuration 604.

Case 5. In this example, node 2 (632) is the critical node that must be balanced. Three single-phase PV inverters are connected to nodes 7 (671), 6 (646) and 12 (611), on phases

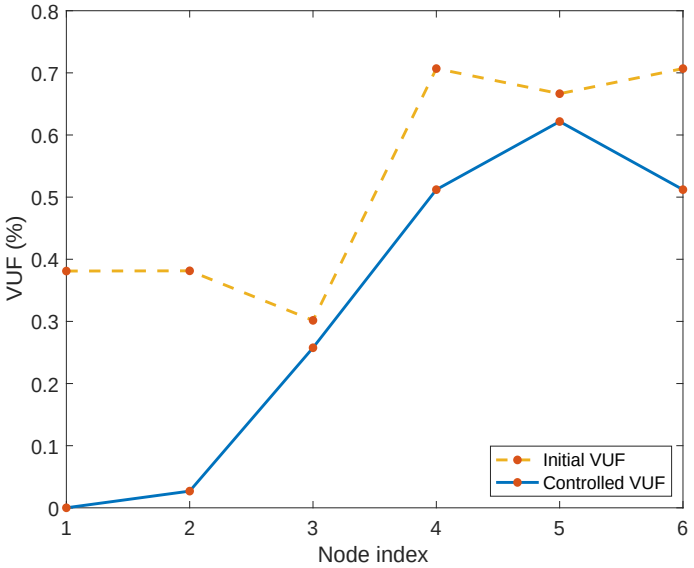

Figure 6.8: Initial and controlled VUF at three-phase buses, for Case 5.

ab, bc and ca, respectively. In this case the only communication required was to send the voltage and current measurements at node 632 to the three nodes which were equipped with PV inverters. Coordinating three single-phase inverters to balance the critical node was effectively equivalent to using a three-phase inverter.

We were able to certify a contraction region $\mathcal{S} = \left\{Q \in \mathbb{R}^3 \middle| \|Q - Q^0\|_\infty \leq 102.9 \text{ p.u.}\right\}$, where $Q = [Q_7^{ab}, Q_6^{bc}, Q_{12}^{ca}]^\intercal$, and Q^0 was chosen as the zero vector. The result demonstrates that this distributed control scheme, which utilizes three highly-dispersed single-phase PV inverters, is very robust to disturbances. Starting from any reactive power injection within the certified contraction region, the system is guaranteed to converge to the unique fixed point, assuming system parameters are constant. The VUF at the critical node 2 was reduced from 0.38% to 0%. The initial and controlled VUF of all three-phase nodes in the network are shown in Fig. 6.8. The converged reactive power injections were $Q_7^{ab} = 1.6307$, $Q_6^{bc} = -0.6853$, $Q_{12}^{ca} = -0.9455$.

Case 6. Interactions between multiple distributed single-phase Steinmetz controllers were investigated using the modified IEEE 13-bus system. Referring to Fig. 6.7, consider both nodes 2 (632) and 7 (671) to be critical nodes. The network was subdivided into two partitions based on these two critical nodes, as shown by the two dashed rectangles in Fig. 6.7. The DERs within each partition were available to assist in balancing the associated critical node. For this example, there are three single-phase PV inverters within the first partition, connected to phases ab and ca at node 3 (633) and to phase bc at node 6 (646). Similarly, within the second partition there are three single-phase PV inverters, connected to nodes 8 (675), 9 (680) and 12 (611), on phases ab, bc and ca, respectively.

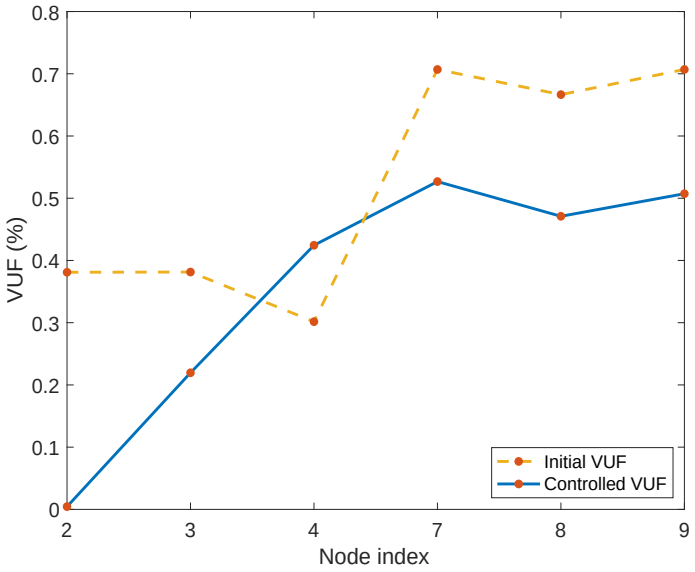

Figure 6.9: Initial and controlled VUF at three-phase buses, for Case 6.

Note that only local communication within each partition is required. These single-phase inverters effectively form two full Steinmetz controllers. The interactions between distributed controllers were analyzed and a convergence guarantee was achieved. We certified a contraction region of $\mathcal{S}_{p1} = \left\{Q_{p1} \in \mathbb{R}^3 \middle| \|Q_{p1} - Q_{p1}^0\|_\infty \leq 20 \text{ p.u.}\right\}$ and $\mathcal{S}_{p2} = \left\{Q_{p2} \in \mathbb{R}^3 \middle| \|Q_{p2} - Q_{p2}^0\|_\infty \leq 9 \text{ p.u.}\right\}$ for controllers in the first and second partitions, where $Q_{p1} = [Q_3^{ab}, Q_6^{bc}, Q_3^{ca}]^\intercal$, $Q_{p2} = [Q_8^{ab}, Q_9^{bc}, Q_{12}^{ca}]^\intercal$. The certified contraction region was relatively large compared to the normal operating range of inverters. The linear program $\mathcal{P}1$ provided the estimates $Q_{p1}^0 = [4.0392, 0.1747, -0.8055]^\intercal$ and $Q_{p2}^0 = [-1.5752, 0.8831, 0.0001]^\intercal$. The contraction norm coefficients were $a_{p1} = 1$, and $a_{p2} = 3$.

The VUF at critical nodes 2 and 7 was reduced from 0.38% to 0.0044% and from 0.71% to 0.53%, respectively. Fig. 6.9 shows the initial and controlled VUF at all three-phase nodes in the system. Note that the IEEE 13-bus network has a very unbalanced structure, with unbalanced line configurations and missing phases. Steinmetz-based control, however, aims to balance the load, i.e., make the equivalent local plus downstream load appear balanced. Nevertheless, it still attenuated VUF at the critical nodes in this example. Fig. 6.10 shows the convergence of the reactive power injections at the six distributed controllers. Convergence was achieved in two iterations, with the converged reactive power injections being $Q_3^{ab} = 3.0434$, $Q_6^{bc} = -1.8804$, $Q_3^{ca} = -1.1630$, $Q_8^{ab} = -1.3447$, $Q_9^{bc} = 1.1145$, $Q_{12}^{ca} = 0.2302$.

Finally the performance of the distributed Steinmetz controller was evaluated using a modified IEEE 34-bus system shown in Fig. 6.11. This network is long and lightly loaded, with full details provided in [144]. We fixed the two in-line voltage regulators at their

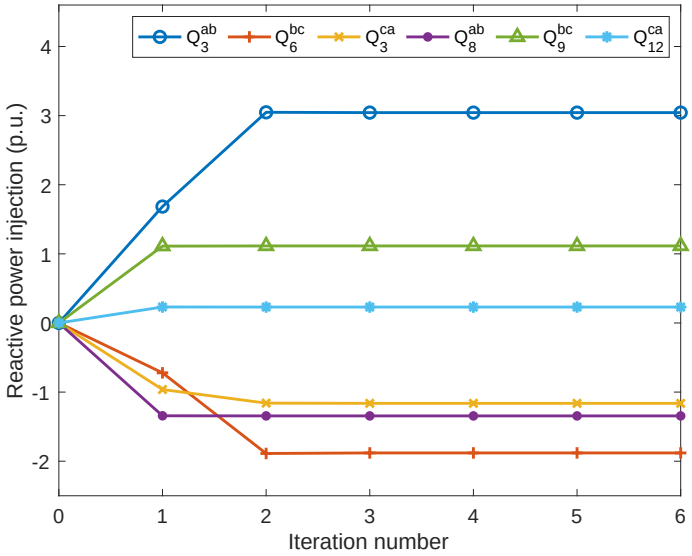

Figure 6.10: Convergence of the Steinmetz controllers, for Case 6.

default values. Similarly to prior work [145, 146], we translated all constant-impedance and constant-current loads into constant-power loads. We also included balanced wye-connected constant-power loads in this example. Distributed load was aggregated at the adjacent node farthest from the substation. The load profile is given in Table 6.2.

Table 6.2: Constant-Power Loads of the IEEE 34-Bus System.

Index	Connection	Constant power load
node 27	wye	$[135 + j105,\ 135 + j105,\ 135 + j105]$
node 30	wye	$[20 + j16,\ 20 + j16,\ 20 + j16]$
node 32	wye	$[9 + j7,\ 9 + j7,\ 9 + j7]$
node 13	delta	$[0 + j0,\ 5 + j2,\ 0 + j0]$
node 16	delta	$[10 + j5,\ 10 + j5,\ 25 + j10]$
node 22	delta	$[150 + j75,\ 150 + j75,\ 150 + j75]$
node 23	delta	$[7 + j3,\ 2 + j1,\ 6 + j3]$
node 25	delta	$[4 + j2,\ 15 + j8,\ 13 + j7]$
node 29	delta	$[20 + j16,\ 20 + j16,\ 20 + j16]$
node 30	delta	$[16 + j8,\ 20 + j10,\ 110 + j55]$
node 31	delta	$[30 + j15,\ 10 + j6,\ 42 + j22]$
node 32	delta	$[18 + j9,\ 22 + j11,\ 0 + j0]$

Case 7. Interactions between multiple distributed single-phase Steinmetz controllers were again considered, this time using the modified IEEE 34-bus network. Referring to Fig. 6.11, both nodes 4 (808) and 23 (858) are critical nodes, and the network is subdivided into the two corresponding partitions shown by the dashed frames. There are three single-phase PV inverters within the first partition, connected to phases ab at node 7 (814), bc at

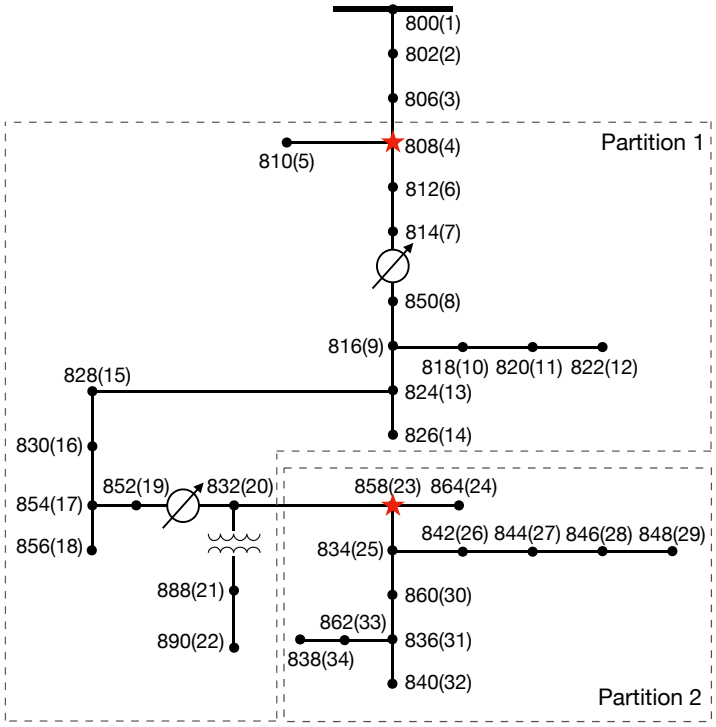

Figure 6.11: IEEE 34-bus test feeder.

node 9 (816), and ca at node 17 (854). Similarly, there are three single-phase PV inverters within the second partition, connected to nodes 26 (842), 32 (840) and 33 (862), on phases ab, bc and ca, respectively. These single-phase inverters effectively form two full Steinmetz controllers. As in the previous cases, we analyzed the interactions between distributed controllers and certified contraction regions of $\mathcal{S}_{p1} = \left\{Q_{p1} \in \mathbb{R}^3 \middle| \|Q_{p1} - Q_{p1}^0\|_\infty \leq 2.6 \text{ p.u.}\right\}$ and $\mathcal{S}_{p2} = \left\{Q_{p2} \in \mathbb{R}^3 \middle| \|Q_{p2} - Q_{p2}^0\|_\infty \leq 1.2 \text{ p.u.}\right\}$ for the controllers in the first and second partitions, where $Q_{p1} = [Q_7^{ab}, Q_9^{bc}, Q_{17}^{ca}]^\intercal$, $Q_{p2} = [Q_{26}^{ab}, Q_{32}^{bc}, Q_{33}^{ca}]^\intercal$. The linear program $\mathcal{P}1$ provided the estimates $Q_{p1}^0 = [0.0, 0.0, 0.0]^\intercal$ and $Q_{p2}^0 = [-0.1904, 0.6642, 0.0]^\intercal$. The contraction norm coefficients were $a_{p1} = 1$ and $a_{p2} = 4.3$.

The VUF at critical nodes 4 and 23 was reduced from 0.3769% and 2.3659% to 0.1546% and 0.8817%, respectively. Fig. 6.12 shows the initial and controlled VUF at all three-phase nodes in the network. Note that the distributed Steinmetz controller attenuated VUF at all the three-phase nodes in this example, including the critical nodes. The largest VUF of 3.4450%, at node 22, was reduced to 1.7646% after applying the Steinmetz controllers.

Fig. 6.13 shows the reactive power injections at the six distributed controllers converged in a few iterations. The converged reactive power injections in per unit were $Q_7^{ab} = -0.0266$, $Q_9^{bc} = 0.0598$, $Q_{17}^{ca} = -0.0331$, $Q_{26}^{ab} = -0.3484$, $Q_{32}^{bc} = 0.5061$, $Q_{33}^{ca} = -0.1577$. Note that the estimates provided by the linear program $\mathcal{P}1$ are close to the final converged reactive

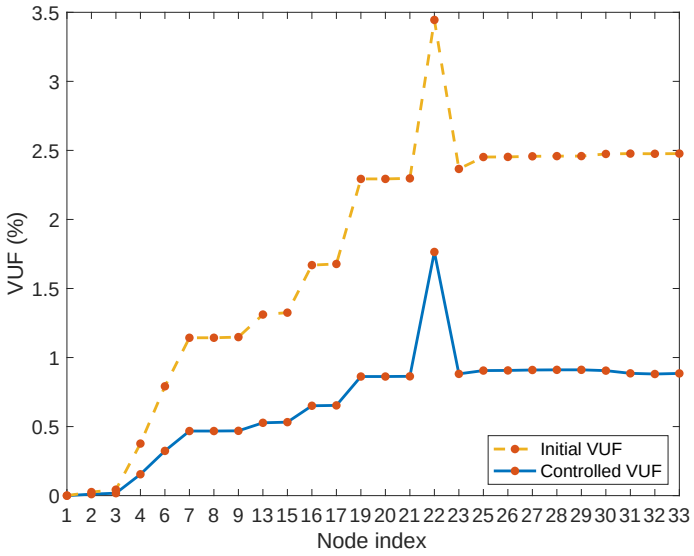

Figure 6.12: Initial and controlled VUF at three-phase buses, for Case 7.

power injections.

Case 8. To test the performance of the controllers in an extremely unbalanced case, the loads at nodes 13, 16 and 23 were increased to ten times their values given in Table 6.2. Everything else remained the same as in Case 7. The interactions between distributed controllers were analyzed and contraction regions of $\mathcal{S}_{p1} = \left\{Q_{p1} \in \mathbb{R}^3 \middle| \|Q_{p1} - Q_{p1}^0\|_\infty \leq 2.1 \text{ p.u.}\right\}$ and $\mathcal{S}_{p2} = \left\{Q_{p2} \in \mathbb{R}^3 \middle| \|Q_{p2} - Q_{p2}^0\|_\infty \leq 0.8 \text{ p.u.}\right\}$ were certified, where again $Q_{p1} = [Q_7^{ab}, Q_9^{bc}, Q_{17}^{ca}]^\intercal$, $Q_{p2} = [Q_{26}^{ab}, Q_{32}^{bc}, Q_{33}^{ca}]^\intercal$. The contraction norm coefficients were $a_{p1} = 1$ and $a_{p2} = 3.8$.

The VUF at critical nodes 4 and 23 was reduced from 0.7829% and 4.8148% to 0.2205% and 1.3357%, respectively. Fig. 6.14 shows the initial and controlled VUF at all three-phase nodes in the network. Note that the initial VUF in Case 8 was around twice that of Case 7. Distributed Steinmetz controllers attenuated VUF at all the three-phase nodes including the critical nodes. The VUF at node 22 was reduced from 6.6876% to 2.58%. Fig. 6.15 shows the reactive power injections at the six distributed controllers again converged in just a few iterations. The converged values for reactive power injections in per unit were $Q_7^{ab} = -0.2816$, $Q_9^{bc} = 0.6129$, $Q_{17}^{ca} = -0.3313$, $Q_{26}^{ab} = -0.5989$, $Q_{32}^{bc} = 0.6530$, $Q_{33}^{ca} = -0.0541$. These reactive power injections were generally more extreme than case 7. Nevertheless, they were all within the certified contraction region.

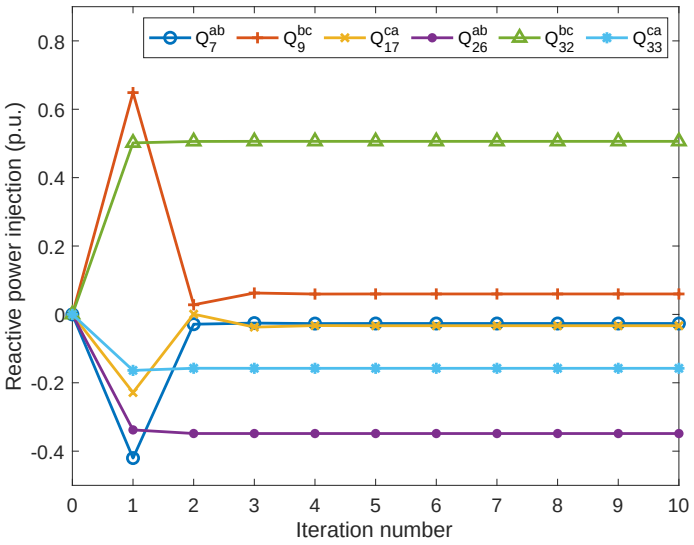

Figure 6.13: Convergence of the Steinmetz controllers, for Case 7.

6.6 Chapter Conclusion

The chapter derives convergence guarantees for decentralized and distributed Steinmetz-based controllers for mitigating voltage unbalance in distribution networks. The proposed control strategies balance voltages by utilizing the reactive power availability of distributed energy resources (DERs) such as solar photovoltaic (PV). Analysis of interactions between multiple Steinmetz-based controllers is undertaken and convergence conditions are established.

The analysis adopts a linear multi-phase power flow model derived from a fixed-point form of the power flow equations. An optimization formulation was developed to compute a sufficiently accurate approximation for the final converged point, resulting in a high-fidelity linear power flow model. This power flow model allowed the Steinmetz-based control schemes to be written explicitly as a quadratic mapping of the reactive power injections from one iteration to the next. Banach fixed-point theory was used to prove convergence of the control scheme. The analysis can be extended to incorporate time delays in the measurement process and in implementing updated reactive power injections.

Convergence conditions were tested using one small network and two IEEE standard distribution test feeders. Results illustrate the convergence analysis, and highlight the effectiveness and robustness of the proposed decentralized and distributed Steinmetz-based controllers.

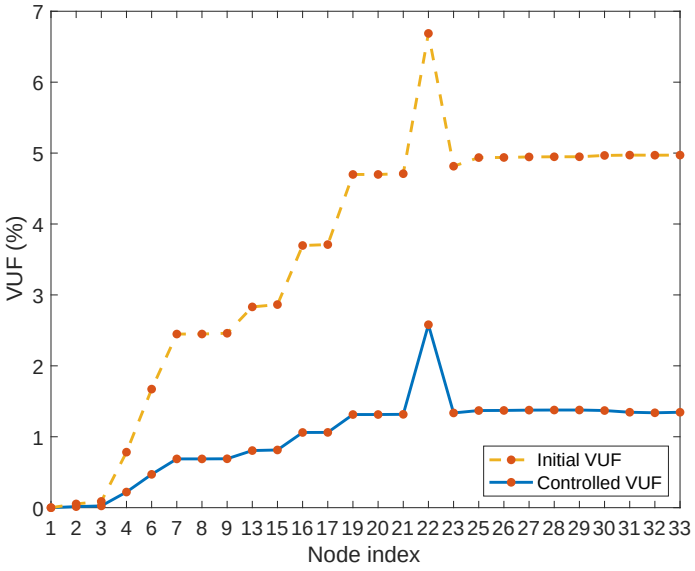

Figure 6.14: Initial and controlled VUF at three-phase buses, for Case 8.

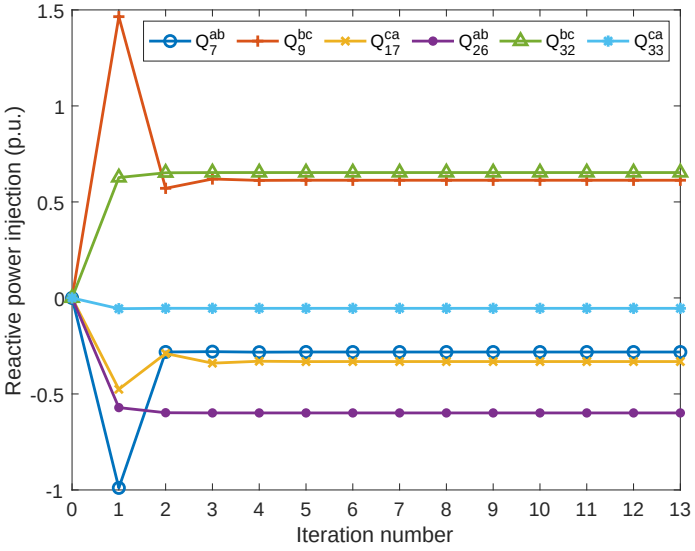

Figure 6.15: Convergence of the Steinmetz controllers, for Case 8.

CHAPTER 7

Chance-Constrained Optimal Capacity Design for a Renewable-Only Islanded Microgrid

7.1 Chapter Introduction

Microgrids are defined as small-scale power systems that group a variety of distributed energy resources (DERs), such as renewable resources, storage systems and loads, to provide high reliability. A microgrid can operate in either grid-connected mode or islanded mode. This chapter considers islanded microgrids supplied solely by renewable resources, where backup power supply from the main power grid is not available. Sufficient capacity must be available within the microgrid to safely supply loads, while excessive capacity should be avoided to minimize the overall cost. This implies that in rare cases where renewable generation is extremely limited, for example cloudy breezeless days, loads with low priority are subject to load shedding, as a last resort. Optimal design of the capacity of DERs within islanded microgrids must therefore consider the trade-off between energy sufficiency and economics.

Numerous aspects of optimal microgrid capacity design have been considered previously. Optimal sizing of a microgrid with a wind turbine, solar photovoltaic (PV) and fuel cell is studied in [147] using an evolutionary computation technique. Sizing a variety of DERs in a microgrid is considered in [148] where the focus is on satisfying regulatory constraints imposed by government. Much work has been done on incorporating multiple objectives into the design of microgrids. A multi-objective optimization problem is formulated in [149] to consider both cost and power availability. A genetic algorithm is applied to solve the optimization problem, however a trade-off is required between the multiple feasible solutions. Simultaneous minimization of levelized cost of energy and CO_2 emissions is considered in [150] through application of a strength pareto evolutionary algorithm. Design criteria considered in [151] include minimum cost, CO_2 emissions

and maximum reliability. Markov models for wind generation, solar PV and loads are generated in [152] and [153].

Most literature handles stochastic variables using Monte Carlo simulation and heuristic algorithms, which cannot provide probability guarantees in a tractable way. Recently there has been substantial interest though in chance-constrained (CC) formulations. CC problems are generally difficult to solve analytically, except for rare cases where the uncertain variables are uniformly or normally distributed [41]. However, under certain light assumptions, randomized optimization methods [42] can solve CC problems and provide solutions with *a priori* probability guarantees and appealing tractability properties. A CC formulation for the optimal power flow (OPF) problem was first proposed in [154] using a solution methodology that does not scale well, while the scenario approach [42] was applied in [155] to solve the CC OPF problem.

In this chapter, we explicitly pose microgrid capacity design as a stochastic optimization problem with chance constraints, and solve it using a randomized optimization method. The scenario approach [42] may require a large number of scenarios, depending on the number of decision variables. Considering the high dimension of our problem with respect to the decision variables, we have instead adopted a related randomized optimization technique, the probabilistically robust method [156], in which the required number of scenarios depends on the number of uncertain variables. This approach [156] initially constructs a CC problem to establish a robust set for the uncertain variables, then a robust counterpart of the original problem is solved with uncertain variables confined to the computed robust set.

To apply [156], we need to choose the shape of the robust set that encloses the randomly selected scenarios. We have found that a hyper-rectangular robust set, as proposed in [156], can be overly conservative. This chapter therefore introduces two methods for reshaping the robust set to reduce conservativeness. Firstly, a cutting-based reshaping method is proposed which takes into account the physical characteristics of wind and solar generation and load. This method is efficient and does not incur many extra scenarios for maintaining the desired probability guarantee. Secondly, a reshaping method that exploits principal component analysis (PCA) [157] is proposed. PCA identifies the principal directions that capture the most variation in data and thereby provides a way to reduce data dimensionality. Its applications in power systems are largely related to wind speed forecasting [158] and data compression [159]. In this chapter, we use PCA to remove unnecessary parts in the robust set and hence improve the solution for the original CC problem.

To facilitate the use of randomized methods we need a formulation where certain

decision variables are defined as a function, i.e., a "control policy", of the uncertain variables. In our microgrid design problem, an affine control policy [160] is proposed to dispatch battery power under uncertain renewable generation and load. In contrast, a nonlinear control policy is designed for load shedding control. These control policies are integrated into the stochastic CC problem, the solution to which provides the optimal policy parameters, DER capacities, the upper bound on the load shedding ratio, and a forecast dispatch for the battery power. Note that both the affine policy for battery dispatch and the nonlinear policy for load shedding are purely to aid the design process and should not be interpreted as determining the actual operating strategy.[1] In an operational setting, the battery in a renewable-only islanded microgrid has to continually compensate for power shortages due to insufficient renewable generation, while load shedding is rather an emergency action scheme.

The chapter is organized as follows: Section 7.2 describes the microgrid structure and presents the problem description. Control policies for battery power dispatch and load shedding are proposed in Section 7.3, and the stochastic CC optimization problem is formulated in Section 7.4. Section 7.5 introduces the robust reformulation as well as the two methods for refining the robust set. Robust reformulation of the original CC problem is provided in Section 7.6. Shrinking horizon implementation of the control policy is proposed in Section 7.7. Numerical results and validation tests are provided in Section 7.8 and conclusions are given in Section 7.9.

7.2 Microgrid Structure and Problem Description

7.2.1 Microgrid Structure

The chapter considers an islanded microgrid system that is built around a central electrical bus. Various DERs, including a wind turbine, solar PV and energy storage, together with load are connected to the central bus. Fuel-based power plants are excluded on the basis of their environmental impact, and grid connection is not considered due to the high cost of rural area electrification. We assume a load shedding scheme is available to cope with rare weather conditions when renewable generation is extremely limited.

The stochasticity of renewable resources and load must be carefully considered. The uncertainty and intermittency of renewable generation make reliable power supply challenging especially in our setting where backup from conventional power generation or the

[1] Though a shrinking horizon implementation of the battery control policy is developed for on-line operation.

grid is not available. Battery energy storage is vital in managing this issue, charging when there is excess generation from renewable resources and discharging when generation is insufficient. Such battery management will be taken into account in the microgrid design process.

7.2.2 Problem Description

The problem of interest is the optimal capacity design for DERs and load shedding in an isolated microgrid. Specifically, our objective is to determine the power rating $\overline{p}_{\mathrm{w}}$ of wind turbines, the power rating $\overline{p}_{\mathrm{pv}}$ of solar PV, the power rating $\overline{p}_{\mathrm{b}}$ and energy capacity $\overline{e}_{\mathrm{b}}$ of battery energy storage, and the maximum allowable proportion of load that may be shed, which we refer to as the load shedding ratio limit $\overline{r}_{\mathrm{sh}}$. We consider a time horizon of $T = 24$ hours with one-hour resolution, indexed by $t = 0, \ldots, T-1$.

The uncertain variables consist of the normalized (unit capacity) wind power $\tilde{\mathbf{p}}^0_{\mathrm{w}} \in \mathbb{R}^T_+$, normalized solar PV power $\tilde{\mathbf{p}}^0_{\mathrm{pv}} \in \mathbb{R}^T_+$, and actual load $\tilde{\mathbf{p}}_{\mathrm{d}} \in \mathbb{R}^T_+$. We use tilde to denote random variables and the superscript "0" to denote normalized variables throughout the chapter.

Define $\tilde{\mathbf{p}}_{\mathrm{w}} \in \mathbb{R}^T_+$ and $\tilde{\mathbf{p}}_{\mathrm{pv}} \in \mathbb{R}^T_+$ as the random variables for the actual power outputs of the wind turbine and solar PV system, respectively,

$$\tilde{\mathbf{p}}_{\mathrm{w}} = \overline{p}_{\mathrm{w}} \cdot \tilde{\mathbf{p}}^0_{\mathrm{w}}, \qquad \tilde{\mathbf{p}}_{\mathrm{pv}} = \overline{p}_{\mathrm{pv}} \cdot \tilde{\mathbf{p}}^0_{\mathrm{pv}}.$$

For each type of random variable, we assume there is a single forecast trajectory, which is deterministic and obtained based on exogenous information. The forecasts for normalized wind power, normalized solar PV power, and actual load are denoted by $\mathbf{p}^{0\mathrm{f}}_{\mathrm{w}} \in \mathbb{R}^T_+$, $\mathbf{p}^{0\mathrm{f}}_{\mathrm{pv}} \in \mathbb{R}^T_+$, and $\mathbf{p}^{\mathrm{f}}_{\mathrm{d}} \in \mathbb{R}^T_+$, respectively. Similarly, define the forecasts for actual wind and solar power output as $\mathbf{p}^{\mathrm{f}}_{\mathrm{w}} \in \mathbb{R}^T_+$, $\mathbf{p}^{\mathrm{f}}_{\mathrm{pv}} \in \mathbb{R}^T_+$ with,

$$\mathbf{p}^{\mathrm{f}}_{\mathrm{w}} = \overline{p}_{\mathrm{w}} \cdot \mathbf{p}^{0\mathrm{f}}_{\mathrm{w}}, \qquad \mathbf{p}^{\mathrm{f}}_{\mathrm{pv}} = \overline{p}_{\mathrm{pv}} \cdot \mathbf{p}^{0\mathrm{f}}_{\mathrm{pv}}.$$

The optimal design problem can be formulated as a CC optimization problem of the form,

$$\begin{aligned} \min_{x \in \mathbb{R}^{n_x}} \quad & J(x) \\ \text{subject to} \quad & \Pr\Big(\delta \in \Delta | \max_{j=1,\ldots,m} g_j(x,\delta) \le 0\Big) \ge 1 - \epsilon, \end{aligned} \tag{7.2.1}$$

where $\delta \in \Delta \subseteq \mathbb{R}^{n_\delta}$ are the random variables, $x \in \mathbb{R}^{n_x}$ are the decision variables, $\Pr(B|A)$

denotes the probability of A conditioned on B, and ϵ is a pre-defined maximal probability of violation. Instead of enforcing hard constraints, we only require the constraints to be satisfied with high probability so as to render a less conservative design.

7.3 Control Policies

To handle the stochasticity introduced by renewable resources and load, control policies are designed to generate trajectories for battery charging/discharging and load shedding under arbitrary generation and load conditions.

7.3.1 Affine Policy for Battery Dispatch

In this subsection, we develop an affine policy for battery power dispatch $\tilde{\mathbf{p}}_{\mathrm{b}}(t)$, $t = 0, \ldots, T-1$. The policy must ensure that the battery state of charge (SoC) at the end-of-horizon, $t = T$, is equal to the SoC at the beginning of the horizon, $t = 0$, with both being equal to a target value. Furthermore, there should be a mechanism for encouraging extra charging (discouraging discharging) when net generation exceeds its forecast value and vice versa when net generation is less than forecast.

Let the net generation/load mismatch from forecast at each time-step $t = 0, ..., T-1$ be given by,

$$\begin{aligned}\tilde{\mathbf{p}}_{\mathrm{mis}}(t) &= \tilde{\mathbf{p}}_{\mathrm{w}}(t) + \tilde{\mathbf{p}}_{\mathrm{pv}}(t) - \tilde{\mathbf{p}}_{\mathrm{d}}(t) - \left(\mathbf{p}^{\mathrm{f}}_{\mathrm{w}}(t) + \mathbf{p}^{\mathrm{f}}_{\mathrm{pv}}(t) - \mathbf{p}^{\mathrm{f}}_{\mathrm{d}}(t)\right) \\ &= \overline{p}_{\mathrm{w}}\left(\tilde{\mathbf{p}}^{0}_{\mathrm{w}}(t) - \mathbf{p}^{0\mathrm{f}}_{\mathrm{w}}(t)\right) + \overline{p}_{\mathrm{pv}}\left(\tilde{\mathbf{p}}^{0}_{\mathrm{pv}}(t) - \mathbf{p}^{0\mathrm{f}}_{\mathrm{pv}}(t)\right) - \left(\tilde{\mathbf{p}}_{\mathrm{d}}(t) - \mathbf{p}^{\mathrm{f}}_{\mathrm{d}}(t)\right) \\ &= \overline{p}_{\mathrm{w}} \cdot \Delta\tilde{\mathbf{p}}^{0}_{\mathrm{w}}(t) + \overline{p}_{\mathrm{pv}} \cdot \Delta\tilde{\mathbf{p}}^{0}_{\mathrm{pv}}(t) - \Delta\tilde{\mathbf{p}}_{\mathrm{d}}(t), \end{aligned} \tag{7.3.1}$$

where the new uncertain variables $\Delta\tilde{\mathbf{p}}^{0}_{\mathrm{w}}(t)$, $\Delta\tilde{\mathbf{p}}^{0}_{\mathrm{pv}}(t)$, $\Delta\tilde{\mathbf{p}}_{\mathrm{d}}$ are defined as,

$$\begin{aligned}\Delta\tilde{\mathbf{p}}^{0}_{\mathrm{w}}(t) &\triangleq \tilde{\mathbf{p}}^{0}_{\mathrm{w}}(t) - \mathbf{p}^{0\mathrm{f}}_{\mathrm{w}}(t), \\ \Delta\tilde{\mathbf{p}}^{0}_{\mathrm{pv}}(t) &\triangleq \tilde{\mathbf{p}}^{0}_{\mathrm{pv}}(t) - \mathbf{p}^{0\mathrm{f}}_{\mathrm{pv}}(t), \\ \Delta\tilde{\mathbf{p}}_{\mathrm{d}}(t) &\triangleq \tilde{\mathbf{p}}_{\mathrm{d}}(t) - \mathbf{p}^{\mathrm{f}}_{\mathrm{d}}(t).\end{aligned}$$

Assuming perfect efficiency, the battery SoC for both the forecast and the uncertain trajectory are given by,

$$\mathbf{e}^{\mathrm{f}}_{\mathrm{b}}(t+1) = \mathbf{e}^{\mathrm{f}}_{\mathrm{b}}(t) + \mathbf{p}^{\mathrm{f}}_{\mathrm{b}}(t), \tag{7.3.2}$$

$$\tilde{\mathbf{e}}_{\mathrm{b}}(t+1) = \tilde{\mathbf{e}}_{\mathrm{b}}(t) + \tilde{\mathbf{p}}_{\mathrm{b}}(t), \tag{7.3.3}$$

for $t = 0, ..., T-1$, where $\mathbf{p}_{\mathrm{b}}^{\mathrm{f}}(t)$ is the forecast battery power dispatch and $\tilde{\mathbf{p}}_{\mathrm{b}}(t)$ is the (stochastic) battery power dispatch, with positive values acting as load on the microgrid. Consider the battery dispatch policy,

$$\tilde{\mathbf{p}}_{\mathrm{b}}(t) = \mathbf{p}_{\mathrm{b}}^{\mathrm{f}}(t) + \mathbf{d}(t) \cdot \tilde{\mathbf{p}}_{\mathrm{mis}}(t) - \mathbf{d}_2(t) \sum_{i=0}^{T-1} \mathbf{d}(i) \cdot \tilde{\mathbf{p}}_{\mathrm{mis}}(i), \tag{7.3.4}$$

where the weights $\mathbf{d}(t), \mathbf{d}_2(t) \in \mathbb{R}^T$ are decision variables. If the policy satisfies $\sum_{t=0}^{T-1} \mathbf{d}_2(t) = 1$ then equation (7.3.4) ensures that $\tilde{\mathbf{e}}_{\mathrm{b}}(T) = \mathbf{e}_{\mathrm{b}}^{\mathrm{f}}(T)$.

Note however that policy (7.3.4) involves multiplication of the decision variables $\mathbf{d}(t)$ and $\mathbf{d}_2(t)$, causing the optimization problem underpinning the design process to be nonlinear and difficult to handle. This can be addressed by replacing the bilinear terms $\mathbf{d}(\cdot)\mathbf{d}_2(\cdot)$ in equation (7.3.4) with a matrix design variable $D \in \mathbb{R}^{T \times T}$ to give,

$$\begin{aligned}
\tilde{\mathbf{p}}_{\mathrm{b}}(t) &= \mathbf{p}_{\mathrm{b}}^{\mathrm{f}}(t) + \mathbf{d}(t) \cdot \tilde{\mathbf{p}}_{\mathrm{mis}}(t) - \sum_{i=0}^{T-1} D(t,i) \cdot \tilde{\mathbf{p}}_{\mathrm{mis}}(i) \\
&= \mathbf{p}_{\mathrm{b}}^{\mathrm{f}}(t) + \mathbf{d}(t)\overline{p}_{\mathrm{w}}\Delta\tilde{\mathbf{p}}_{\mathrm{w}}^{0}(t) + \mathbf{d}(t)\overline{p}_{\mathrm{pv}}\Delta\tilde{\mathbf{p}}_{\mathrm{pv}}^{0}(t) - \mathbf{d}(t)\Delta\tilde{\mathbf{p}}_{\mathrm{d}}(t) \\
&\quad - \sum_{i=0}^{T-1} D(t,i)\Big(\overline{p}_{\mathrm{w}} \cdot \Delta\tilde{\mathbf{p}}_{\mathrm{w}}^{0}(i) + \overline{p}_{\mathrm{pv}} \cdot \Delta\tilde{\mathbf{p}}_{\mathrm{pv}}^{0}(i) - \Delta\tilde{\mathbf{p}}_{\mathrm{d}}(i)\Big),
\end{aligned} \tag{7.3.5}$$

where it is required that $\sum_{i=0}^{T-1} D(i,t) = \mathbf{d}(t),\ \forall t = 0, ..., T-1$, to guarantee that $\tilde{\mathbf{e}}_{\mathrm{b}}(T) = \mathbf{e}_{\mathrm{b}}^{\mathrm{f}}(T)$.

It should be further noted that the mismatch $\tilde{\mathbf{p}}_{\mathrm{mis}}$ involves design variables $\overline{p}_{\mathrm{w}}$ and $\overline{p}_{\mathrm{pv}}$, so the optimization problem is still nonlinear. This motivates a further transformation of the control policy,

$$\begin{aligned}
\tilde{\mathbf{p}}_{\mathrm{b}}(t) &= \mathbf{p}_{\mathrm{b}}^{\mathrm{f}}(t) + \mathbf{d}_{\mathrm{w}}(t)\Delta\tilde{\mathbf{p}}_{\mathrm{w}}^{0}(t) + \mathbf{d}_{\mathrm{pv}}(t)\Delta\tilde{\mathbf{p}}_{\mathrm{pv}}^{0}(t) - \mathbf{d}(t)\Delta\tilde{\mathbf{p}}_{\mathrm{d}}(t) \\
&\quad - \sum_{i=0}^{T-1} \Big(D_{\mathrm{w}}(t,i)\Delta\tilde{\mathbf{p}}_{\mathrm{w}}^{0}(i) + D_{\mathrm{pv}}(t,i)\Delta\tilde{\mathbf{p}}_{\mathrm{pv}}^{0}(i) - D(t,i)\Delta\tilde{\mathbf{p}}_{\mathrm{d}}(i)\Big),
\end{aligned} \tag{7.3.6}$$

where we require

$$\sum\nolimits_{i=0}^{T-1} D_{\mathrm{w}}(i,t) = \mathbf{d}_{\mathrm{w}}(t), \tag{7.3.7a}$$

$$\sum\nolimits_{i=0}^{T-1} D_{\mathrm{pv}}(i,t) = \mathbf{d}_{\mathrm{pv}}(t), \tag{7.3.7b}$$

$$\sum\nolimits_{i=0}^{T-1} D(i,t) = \mathbf{d}(t), \tag{7.3.7c}$$

in order to guarantee that $\tilde{\mathbf{e}}_{\mathrm{b}}(T) = \mathbf{e}_{\mathrm{b}}^{\mathrm{f}}(T)$. The resulting policy is affine in the decision

variables and will be used to dispatch the battery in the optimization problem.

Affine policy (7.3.6), (7.3.7) will be integrated into the stochastic optimization problem ($\mathcal{P}1$) in Subsection 7.4.4. The solution to ($\mathcal{P}1$) will provide the optimal values for the policy parameters $\mathbf{d}_{\mathrm{w}}, \mathbf{d}_{\mathrm{pv}}, \mathbf{d} \in \mathbb{R}^T$, $D_{\mathrm{w}}, D_{\mathrm{pv}}, D \in \mathbb{R}^{T\times T}$, the optimal capacities for the wind turbine, solar PV, battery energy storage system, the maximum allowable load shedding ratio, as well as the nominal forecast trajectory $\mathbf{p}_{\mathrm{b}}^{\mathrm{f}}(t)$ of the battery power.

7.3.2 Policy for Load Shedding

The proportion of load that must be shed at any time $t = 0, \ldots, T-1$ is described by the load shedding ratio $\mathbf{r}_{\mathrm{sh}}(t)$, with the policy governing load shedding given by,

$$\mathbf{r}_{\mathrm{sh}}(t) = \begin{cases} 1 - \tilde{\mathbf{p}}_{\mathrm{g}}(t)/\tilde{\mathbf{p}}_{\mathrm{d}}(t), & \text{if } \tilde{\mathbf{p}}_{\mathrm{g}}(t) \leq \tilde{\mathbf{p}}_{\mathrm{d}}(t) \\ 0, & \text{if } \tilde{\mathbf{p}}_{\mathrm{g}}(t) \geq \tilde{\mathbf{p}}_{\mathrm{d}}(t), \end{cases} \tag{7.3.8}$$

where $\tilde{\mathbf{p}}_{\mathrm{g}}(t) = \tilde{\mathbf{p}}_{\mathrm{w}}(t) + \tilde{\mathbf{p}}_{\mathrm{pv}}(t) - \tilde{\mathbf{p}}_{\mathrm{b}}(t)$. Note that when $\tilde{\mathbf{p}}_{\mathrm{g}}(t) \geq \tilde{\mathbf{p}}_{\mathrm{d}}(t)$, it is implied that the excess renewable generation can be curtailed without penalty.

This load shedding policy is not explicitly included in the optimization formulation, but rather enters implicitly through power sufficiency requirements. Consequently, only one design variable is required, the upper limit $\bar{r}_{\mathrm{sh}}$ on the load shedding ratio. This variable appears in both the stochastic and deterministic power sufficiency constraints (7.4.2), (7.4.3), as well as in the non-negativity constraints (7.4.7) and the objective function (7.4.1). A high penalty is applied to the limit $\bar{r}_{\mathrm{sh}}$ since we hope to satisfy load for the majority of the time, only invoking load shedding as a last resort to deal with rare periods of low generation.

7.4 Chance-Constrained Problem Formulation

The overall objective is to design the capacities for DERs and load shedding ratio limit in a microgrid to guarantee energy sufficiency with *a priori* probability guarantee while minimizing the net present cost (NPC) of the microgrid system.

7.4.1 Objective Function

The objective is to minimize the overall NPC of the microgrid, which is composed of the NPC for each component as follows:

$$\overline{p}_{\mathrm{w}} \cdot \mathrm{NPC}_{\mathrm{w}} + \overline{p}_{\mathrm{pv}} \cdot \mathrm{NPC}_{\mathrm{pv}} + \overline{p}_{\mathrm{b}} \cdot \mathrm{NPC}_{\mathrm{b}} + \overline{e}_{\mathrm{b}} \cdot \mathrm{NPC}_{\mathrm{b}} + c_{\mathrm{sh}}(\overline{r}_{\mathrm{sh}}), \tag{7.4.1}$$

where $c_{\mathrm{sh}}(\cdot)$ denotes a two-piece linear penalty function for the upper limit $\overline{r}_{\mathrm{sh}}$ of the load shedding ratio. For low values of $\overline{r}_{\mathrm{sh}}$ the slope of $c_{\mathrm{sh}}(\cdot)$ is relatively gentle whereas for high values, beyond the break-point, the slope is steep in order to penalize undesirably high load shedding. NPC is computed as the difference between the present value of cash outflows and cash inflows over the microgrid lifetime. The cash flows in the future are discounted to present value through a discount rate. For each type of component, NPC consists of capital cost, replacement cost, operation and maintenance (O&M) cost, and salvage value over the system lifetime [161, 162]. Typical parameters for the economic model for each type of DER are provided in Section 7.8.

7.4.2 Stochastic Constraints

To manage the stochasticity from renewable resources and load, we formulate a stochastic chance constraint. Rather than requiring the constraints to hold for all time, we only require them to be satisfied with a pre-defined probability,

$$\begin{aligned} \Pr\Big(& \tilde{\mathbf{p}}_{\mathrm{w}}(t) + \tilde{\mathbf{p}}_{\mathrm{pv}}(t) - \tilde{\mathbf{p}}_{\mathrm{b}}(t) \geq \tilde{\mathbf{p}}_{\mathrm{d}}(t)(1 - \overline{r}_{\mathrm{sh}}), \\ & -\overline{p}_{\mathrm{b}} \leq \tilde{\mathbf{p}}_{\mathrm{b}}(t) \leq \overline{p}_{\mathrm{b}}, \\ & \underline{\mathrm{SoC}}\, \overline{e}_{\mathrm{b}} \leq \tilde{\mathbf{e}}_{\mathrm{b}}(t) \leq \overline{\mathrm{SoC}}\, \overline{e}_{\mathrm{b}}, \\ & t = 0, \ldots, T-1 \Big) \geq 1 - \epsilon, \end{aligned} \tag{7.4.2}$$

where ϵ is a pre-defined maximal probability of violation. We assume a minimum SoC ($\underline{\mathrm{SoC}}$) of 30% and a maximum SoC ($\overline{\mathrm{SoC}}$) of 90%, in order to prolong the battery life. The first inequality in (7.4.2) captures the power sufficiency requirement, under the assumption that excess renewable generation can be curtailed. The second and third inequalities are the power and energy capacity constraints for the battery, where $\tilde{\mathbf{p}}_{\mathrm{b}}(t)$ and $\tilde{\mathbf{e}}_{\mathrm{b}}(t)$ are governed by equations (7.3.6), (7.3.7) and (7.3.3) in Subsection 7.3.1.

7.4.3 Deterministic Constraints

The forecast trajectory must satisfy the deterministic power sufficiency requirement,

$$\overline{p}_{\mathrm{w}} \cdot \mathbf{p}_{\mathrm{w}}^{0\mathrm{f}}(t) + \overline{p}_{\mathrm{pv}} \cdot \mathbf{p}_{\mathrm{pv}}^{0\mathrm{f}}(t) - \mathbf{p}_{\mathrm{b}}^{\mathrm{f}}(t) \geq \mathbf{p}_{\mathrm{d}}^{\mathrm{f}}(t)(1 - \overline{r}_{\mathrm{sh}}), \tag{7.4.3}$$

for $t = 0, ..., T-1$. Additional constraints for the battery include:

$$-\overline{p}_{\mathrm{b}} \leq \mathbf{p}_{\mathrm{b}}^{\mathrm{f}}(t) \leq \overline{p}_{\mathrm{b}}, \tag{7.4.4}$$

$$\underline{\mathrm{SoC}}\ \overline{e}_{\mathrm{b}} \leq \mathbf{e}_{\mathrm{b}}^{\mathrm{f}}(t) \leq \overline{\mathrm{SoC}}\ \overline{e}_{\mathrm{b}}, \tag{7.4.5}$$

for $t = 0, ..., T-1$. Also, we assume that the battery SoC at the end of each day is equal to that at the beginning of the day, with both set at 60% of the battery capacity,

$$\mathbf{e}_{\mathrm{b}}(0) = \mathbf{e}_{\mathrm{b}}^{\mathrm{f}}(0) = 60\% \cdot \overline{e}_{\mathrm{b}} = \mathbf{e}_{\mathrm{b}}^{\mathrm{f}}(T). \tag{7.4.6}$$

Non-negativity constraints need to be enforced for the power and energy capacities of the DERs, and for the load shedding limit,

$$\overline{p}_{\mathrm{w}} \geq 0, \quad \overline{p}_{\mathrm{pv}} \geq 0, \quad \overline{p}_{\mathrm{b}} \geq 0, \quad \overline{e}_{\mathrm{b}} \geq 0, \quad 1 - \overline{r}_{\mathrm{sh}} \geq 0, \quad \overline{r}_{\mathrm{sh}} \geq 0. \tag{7.4.7}$$

7.4.4 Chance-Constrained Problem Formulation

The stochastic CC optimization problem described in Subsections 7.4.1-7.4.3 is summarized in the following compact form,

$$\begin{aligned}
(\mathcal{P}1) \quad \min \quad & (7.4.1) \\
\text{subject to} \quad & \text{Chance constraint } (7.3.3),\ (7.3.6),\ (7.4.2), \\
& \text{Affine policy constraints } (7.3.7), \\
& \text{Deterministic constraints } (7.3.2),\ (7.4.3) - (7.4.6), \\
& \text{Non-negativity constraints } (7.4.7).
\end{aligned}$$

7.5 Robust Set Formulation

A standard scenario-based approach [42] can be used to solve the CC problem ($\mathcal{P}1$) for a given probability guarantee. However, a large number of scenarios are required to achieve a sufficiently high confidence level. This results in a heavy computational burden.

Furthermore, it may be challenging to obtain a sufficiently large data-set. Instead, we resort to a robust reformulation approach proposed in [156], which firstly constructs a CC problem ($\mathcal{P}2$) to search for a hyper-rectangular robust set for the uncertain variables,

$$
\begin{aligned}
(\mathcal{P}2)\quad & \min\ \|\overline{\lambda}_{\mathrm{w}} - \underline{\lambda}_{\mathrm{w}}\|_1 + \|\overline{\lambda}_{\mathrm{pv}} - \underline{\lambda}_{\mathrm{pv}}\|_1 + \|\overline{\lambda}_{\mathrm{d}} - \underline{\lambda}_{\mathrm{d}}\|_1 \\
& \text{subject to}\quad \Pr\Big((\Delta\tilde{\mathbf{p}}^0_{\mathrm{w}}, \Delta\tilde{\mathbf{p}}^0_{\mathrm{pv}}, \Delta\tilde{\mathbf{p}}_{\mathrm{d}}) \in \Delta \subseteq \mathbb{R}^{3T} \Big| \\
& \qquad \Delta\tilde{\mathbf{p}}^0_{\mathrm{w}} \in [\underline{\lambda}_{\mathrm{w}}, \overline{\lambda}_{\mathrm{w}}], \Delta\tilde{\mathbf{p}}^0_{\mathrm{pv}} \in [\underline{\lambda}_{\mathrm{pv}}, \overline{\lambda}_{\mathrm{pv}}], \Delta\tilde{\mathbf{p}}_{\mathrm{d}} \in [\underline{\lambda}_{\mathrm{d}}, \overline{\lambda}_{\mathrm{d}}]\Big) \geq 1 - \epsilon,
\end{aligned}
$$

where vector inclusion should be interpreted as element-wise.

This first step is solved using a standard scenario-based approach, by replacing the chance constraint with a set of scenarios, each of which is a realization of the random variables. The required number of scenarios N_t is given by [156] as,

$$
N_t \geq \lceil \frac{1}{\epsilon} \frac{e}{e-1} (n_x - 1 + \ln \frac{1}{\beta}) \rceil, \tag{7.5.1}
$$

where $n_x = 2n_\delta$ is the number of design variables and $n_\delta = 3T$ is the number of uncertain variables, ϵ is the specified maximal probability of violation, and $1 - \beta$ is the confidence level. After solving ($\mathcal{P}2$), we obtain a robust set

$$
B^* = [\underline{\lambda}^*_{\mathrm{w}}, \overline{\lambda}^*_{\mathrm{w}}] \times [\underline{\lambda}^*_{\mathrm{pv}}, \overline{\lambda}^*_{\mathrm{pv}}] \times [\underline{\lambda}^*_{\mathrm{d}}, \overline{\lambda}^*_{\mathrm{d}}]. \tag{7.5.2}
$$

Next a robust counterpart of the original problem ($\mathcal{P}1$) is solved with uncertain variables constrained to the robust set B^*. This hyper-rectangular robust set can be very conservative when it comes to high-dimensional random vectors or random variables with large variance, both of which can occur in microgrid design. The following two subsections therefore present methods to reduce conservativeness of the robust set formulation.

7.5.1 Cutting-Based Approach

The box-shaped robust set is conservative because it cannot account for temporal relationships in stochastic renewable generation and load. This can result in the robust set incorporating the unlikely situation where wind and solar are at minimum availability over the entire horizon.[2] We therefore propose an approach to reshape the hyper-rectangular robust set, so as to better capture temporal relationships and reduce conservativeness.

[2]This situation arises when one scenario is at minimum availability at the first time-step, another is at minimum for the second time-step, and so on.

The portion of the hyper-rectangular robust set that induces high design cost is the part where renewable generation is minimal over the entire time horizon while load is maximal. Such realizations are unlikely to occur in reality but are included in the robust set as a consequence of the hyper-rectangular shape. We therefore introduce a hyperplane to cut off this unrealistic portion. Referring to Fig. 7.1(a), which represents a three-dimensional case for illustration, this hyperplane is defined by the following steps:

1 Compute the original hyper-rectangular robust set.

2 Compute the diagonal direction of this hyper-rectangle, starting from the corner of minimum wind and solar generation and maximum load.

3 Project all the scenario points onto the diagonal direction and locate the closest scenario to the starting corner of step 2.

4 Define the hyperplane such that it contains this closest scenario and is orthogonal to the diagonal direction. This hyperplane defines a halfspace opposite to the diagonal direction.

5 Reshape the original robust set by cutting off its intersection with the halfspace.

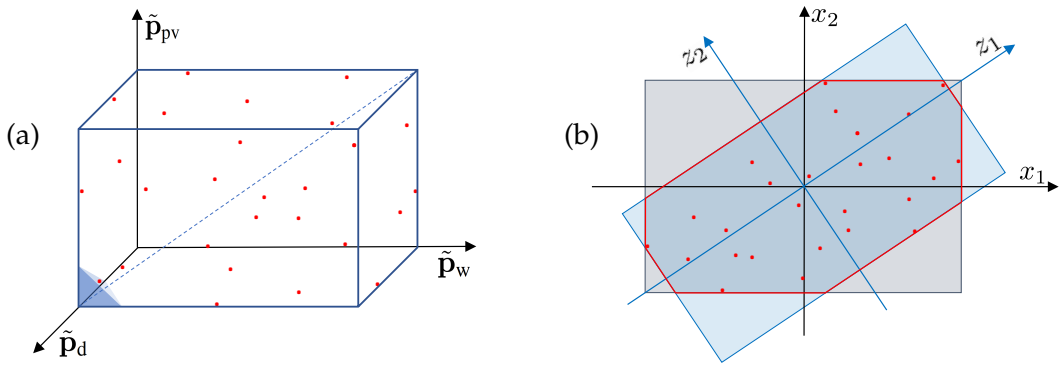

Figure 7.1: Reshape the box robust set by: (a) cutting-based method; (b) PCA-based method.

By introducing this hyperplane, we only introduce one extra design variable in ($\mathcal{P}2$), namely the distance of the hyperplane to the corner. Thus only a small number of extra scenarios are required. If the corresponding number of extra scenarios are included, solutions with the same probability guarantee can be achieved. We can similarly introduce more hyperplanes to cut off different corners of the hyper-rectangular robust set. However,

the first hyperplane is the most helpful, since it corresponds to the case of minimal wind and solar generation with maximal load.

7.5.2 PCA-Based Approach

To further refine the robust set, we exploit principal component analysis (PCA) [157]. PCA searches for a linear coordinate transformation of the original random variables, and converts the data into a new set of coordinates, i.e., the principal components (PCs). These PCs are uncorrelated and arranged such that the first few PCs capture most of the variations in the data whereas the last few PCs describe near constant relationships in the data. Usually, PCA is used for data reduction and reconstruction, by neglecting most of the small PCs. However, in this chapter we use PCA to extract the directions of the PCs and use this information to guide the reshaping of the robust set.

In data analysis, we consider normalized random variables $\tilde{\mathbf{p}}_{\mathrm{w}}^0$, $\tilde{\mathbf{p}}_{\mathrm{pv}}^0$, and $\tilde{\mathbf{p}}_{\mathrm{d}}^0$, where the uncertain load $\tilde{\mathbf{p}}_{\mathrm{d}}$ is scaled by its maximum value to obtain $\tilde{\mathbf{p}}_{\mathrm{d}}^0$. Define the normalized random vector $\tilde{\mathbf{x}} = [(\tilde{\mathbf{p}}_{\mathrm{w}}^0)^\top \ (\tilde{\mathbf{p}}_{\mathrm{pv}}^0)^\top \ (\tilde{\mathbf{p}}_{\mathrm{d}}^0)^\top]^\top \in \mathbb{R}_+^{3T}$. Assume we have obtained the required number of scenarios $\mathbf{x}_1, \mathbf{x}_2, \ldots, \mathbf{x}_N$, each of which is a realization of the random vector, i.e., the observations. Stack these observations together to obtain the data matrix $\mathbf{X} = [\mathbf{x}_1 \ \mathbf{x}_2 \ \ldots \ \mathbf{x}_N]^\top \in \mathbb{R}_+^{N\times 3T}$, and center the data matrix by subtracting the mean of each column from the entries of that column. Formally, we define the mean vector as $\mathbf{x}_0 = \frac{1}{N}\sum_{i=1}^N \mathbf{x}_i$, then the centred data matrix can be expressed as $\mathbf{X}_c = \mathbf{X} - \mathbf{1}_N \cdot \mathbf{x}_0^\top$, where $\mathbf{1}_N$ is the N-length vector of 1s. Construct the sample covariance matrix $\mathbf{S} \in \mathbb{R}^{3T\times 3T}$ as,

$$\mathbf{S} = \frac{1}{N-1}\mathbf{X}_c^\top \mathbf{X}_c. \tag{7.5.3}$$

Singular value decomposition (SVD) provides an efficient way of computing PCs. Apply SVD to the data matrix $\mathbf{X}_c$, which gives $\mathbf{X}_c = \mathbf{U}\mathbf{L}\mathbf{A}^\top$. The diagonal matrix $\mathbf{L} \in \mathbb{R}^{3T\times 3T}$ collects $\sqrt{l_k}$, $k = 1, \ldots, 3T$ as its diagonal entries in descending order, where $\frac{l_k}{N-1}$ are the eigenvalues of the covariance matrix $\mathbf{S}$. Matrices $\mathbf{A} \in \mathbb{R}^{3T\times 3T}$ and $\mathbf{U} \in \mathbb{R}^{N\times 3T}$ have orthonormal columns, with the columns $\mathbf{a}_k$ of $\mathbf{A}$ being the eigenvectors of $\mathbf{S}$. The k-th PC is denoted by $\mathbf{z}_k = \mathbf{a}_k^\top \cdot \tilde{\mathbf{x}}$. Since $\mathbf{A}$ is orthogonal, we have $\mathbf{Z} := \mathbf{X}_c\mathbf{A} = \mathbf{U}\mathbf{L}$, and now the data points are converted to a $3T$-dimension space with coordinates $\mathbf{z}_k$, $k = 1, \ldots, 3T$ in the orthogonal coordinate system given by the columns of $\mathbf{A}$.

To refine the robust set, we introduce two hyperplanes for each PC. These two hyperplanes are normal to the PC direction and their offsets to the origin are determined by the

two outermost data points in this PC direction.[3] As illustrated by Fig. 7.1(b), the intersection of the halfspaces defined by these four hyperplanes give rise to a hyper-rectangle (the light blue rectangle) in the PC space. Intersecting this set with the original robust set (the gray rectangle) gives a smaller robust set, i.e., the polytope with red boundary. The refined robust set still encompasses all the data points yet is less conservative. Furthermore, as an implication of PCA, the last few PC directions contain the least variance in the data, which suggests they give very efficient cuts. Finally, the polytopic shape of the refined robust set makes it computationally tractable for optimization problem reformulation as shown in Section 7.6.

Note that the probability guarantee can again be achieved if the appropriate number of extra scenarios are added. For each hyperplane that we introduce, one extra design variable is added that describes the offset in the PC direction. We can in total introduce $2 \times 3T$ hyperplanes for all the PCs.

7.6 Robust Reformulation

With the refined robust set computed from Section 7.5, we now reformulate the original CC problem ($\mathcal{P}1$) into its robust counterpart. The stochastic constraints in (7.4.2) can be reformulated using affine policy (7.3.6), (7.3.7). The expression for $\tilde{\mathbf{p}}_\mathrm{b}$ over the entire time horizon in vector form is given by,

$$\tilde{\mathbf{p}}_\mathrm{b} = \mathbf{p}_\mathrm{b}^\mathrm{f} + A_\mathrm{w}\Delta\tilde{\mathbf{p}}_\mathrm{w}^0 + A_\mathrm{pv}\Delta\tilde{\mathbf{p}}_\mathrm{pv}^0 - A_\mathrm{d}\Delta\tilde{\mathbf{p}}_\mathrm{d}, \tag{7.6.1}$$

where $A_\mathrm{w} \triangleq \mathrm{diag}(\mathbf{d}_\mathrm{w}) - D_\mathrm{w}$, $A_\mathrm{pv} \triangleq \mathrm{diag}(\mathbf{d}_\mathrm{pv}) - D_\mathrm{pv}$, and $A_\mathrm{d} \triangleq \mathrm{diag}(\mathbf{d}) - D$. The notation $\mathrm{diag}(\cdot)$ expands a vector into a matrix with the vector lying on its diagonal.

Based on battery energy dynamics (7.3.3), $\tilde{\mathbf{e}}_\mathrm{b}$ can be expressed in vector form as,

$$\tilde{\mathbf{e}}_\mathrm{b} = T_r \cdot \tilde{\mathbf{p}}_\mathrm{b} + \mathbf{1}_T \cdot \tilde{\mathbf{e}}_\mathrm{b}(0), \tag{7.6.2}$$

where T_r denotes the lower triangular matrix with ones, and $\mathbf{1}_T$ denotes the T-length vector of ones. Substituting equation (7.6.1) into equation (7.6.2) gives,

$$\tilde{\mathbf{e}}_\mathrm{b} = T_r\mathbf{p}_\mathrm{b}^\mathrm{f} + T_rA_\mathrm{w}\Delta\tilde{\mathbf{p}}_\mathrm{w}^0 + T_rA_\mathrm{pv}\Delta\tilde{\mathbf{p}}_\mathrm{pv}^0 - T_rA_\mathrm{d}\Delta\tilde{\mathbf{p}}_\mathrm{d} + \mathbf{1}_T\mathbf{e}_\mathrm{b}(0). \tag{7.6.3}$$

[3] Alternatively, we can take advantage of statistical results to further shrink the robust set. For example, we could exclude the data points outside the 3-σ range when determining the offsets of the cutting hyperplanes.

The power sufficiency constraint can be written as,

$$\mathrm{diag}(\overline{p}_{\mathrm{w}})\tilde{\mathbf{p}}^{0}_{\mathrm{w}} + \mathrm{diag}(\overline{p}_{\mathrm{pv}})\tilde{\mathbf{p}}^{0}_{\mathrm{pv}} - \tilde{\mathbf{p}}_{\mathrm{b}} \geq \mathrm{diag}(1-\overline{r}_{\mathrm{sh}})\tilde{\mathbf{p}}_{\mathrm{d}}. \tag{7.6.4}$$

Substituting equation (7.6.1) into equation (7.6.4) gives,

$$\mathbf{p}^{\mathrm{f}}_{\mathrm{b}} + A'_{\mathrm{w}}\Delta\tilde{\mathbf{p}}^{0}_{\mathrm{w}} + A'_{\mathrm{pv}}\Delta\tilde{\mathbf{p}}^{0}_{\mathrm{pv}} - A'_{\mathrm{d}}\Delta\tilde{\mathbf{p}}_{\mathrm{d}} \leq B_{\mathrm{f}}, \tag{7.6.5}$$

where

$$\begin{aligned}
A'_{\mathrm{w}} &\triangleq \mathrm{diag}(\mathbf{d}_{\mathrm{w}}) - D_{\mathrm{w}} - \mathrm{diag}(\overline{p}_{\mathrm{w}}) = A_{\mathrm{w}} - \mathrm{diag}(\overline{p}_{\mathrm{w}}),\\
A'_{\mathrm{pv}} &\triangleq \mathrm{diag}(\mathbf{d}_{\mathrm{pv}}) - D_{\mathrm{pv}} - \mathrm{diag}(\overline{p}_{\mathrm{pv}}) = A_{\mathrm{pv}} - \mathrm{diag}(\overline{p}_{\mathrm{pv}}),\\
A'_{\mathrm{d}} &\triangleq \mathrm{diag}(\mathbf{d}) - D - \mathrm{diag}(1-\overline{r}_{\mathrm{sh}}) = A_{\mathrm{d}} - \mathrm{diag}(1-\overline{r}_{\mathrm{sh}}),\\
B_{\mathrm{f}} &\triangleq \mathrm{diag}(\overline{p}_{\mathrm{w}})\mathbf{p}^{0\mathrm{f}}_{\mathrm{w}} + \mathrm{diag}(\overline{p}_{\mathrm{pv}})\mathbf{p}^{0\mathrm{f}}_{\mathrm{pv}} - \mathbf{p}^{\mathrm{f}}_{\mathrm{d}}.
\end{aligned}$$

Substituting expressions (7.6.5), (7.6.1) and (7.6.3) into (7.4.2), the chance constraint can be written as a function of design variables and uncertain variables directly. The robust reformulation of ($\mathcal{P}1$) can therefore be expressed as the robust linear program (LP):

$$\begin{aligned}
(\mathcal{P}3)\quad \min\quad & (7.4.1)\\
\text{subject to}\quad & \mathbf{p}^{\mathrm{f}}_{\mathrm{b}} + A'_{\mathrm{w}}\Delta\tilde{\mathbf{p}}^{0}_{\mathrm{w}} + A'_{\mathrm{pv}}\Delta\tilde{\mathbf{p}}^{0}_{\mathrm{pv}} - A'_{\mathrm{d}}\Delta\tilde{\mathbf{p}}_{\mathrm{d}} \leq B_{\mathrm{f}},\\
& \mathbf{p}^{\mathrm{f}}_{\mathrm{b}} + A_{\mathrm{w}}\Delta\tilde{\mathbf{p}}^{0}_{\mathrm{w}} + A_{\mathrm{pv}}\Delta\tilde{\mathbf{p}}^{0}_{\mathrm{pv}} - A_{\mathrm{d}}\Delta\tilde{\mathbf{p}}_{\mathrm{d}} \leq \mathbf{1}_T\overline{p}_{\mathrm{b}},\\
& \mathbf{p}^{\mathrm{f}}_{\mathrm{b}} + A_{\mathrm{w}}\Delta\tilde{\mathbf{p}}^{0}_{\mathrm{w}} + A_{\mathrm{pv}}\Delta\tilde{\mathbf{p}}^{0}_{\mathrm{pv}} - A_{\mathrm{d}}\Delta\tilde{\mathbf{p}}_{\mathrm{d}} \geq -\mathbf{1}_T\overline{p}_{\mathrm{b}},\\
& T_r\cdot(\mathbf{p}^{\mathrm{f}}_{\mathrm{b}} + A_{\mathrm{w}}\Delta\tilde{\mathbf{p}}^{0}_{\mathrm{w}} + A_{\mathrm{pv}}\Delta\tilde{\mathbf{p}}^{0}_{\mathrm{pv}} - A_{\mathrm{d}}\Delta\tilde{\mathbf{p}}_{\mathrm{d}}) + \mathbf{1}_T\mathbf{e}_{\mathrm{b}}(0) \leq \mathbf{1}_T(\overline{\mathrm{SoC}}\,\bar{e}_{\mathrm{b}}),\\
& T_r\cdot(\mathbf{p}^{\mathrm{f}}_{\mathrm{b}} + A_{\mathrm{w}}\Delta\tilde{\mathbf{p}}^{0}_{\mathrm{w}} + A_{\mathrm{pv}}\Delta\tilde{\mathbf{p}}^{0}_{\mathrm{pv}} - A_{\mathrm{d}}\Delta\tilde{\mathbf{p}}_{\mathrm{d}}) + \mathbf{1}_T\mathbf{e}_{\mathrm{b}}(0) \geq \mathbf{1}_T(\underline{\mathrm{SoC}}\,\bar{e}_{\mathrm{b}}),\\
& \qquad\qquad \forall\,[\Delta\tilde{\mathbf{p}}^{0}_{\mathrm{w}}, \Delta\tilde{\mathbf{p}}^{0}_{\mathrm{pv}}, \Delta\tilde{\mathbf{p}}_{\mathrm{d}}] \in B^*,\\
& \text{Affine policy constraints}\ \ (7.3.7),\\
& \text{Deterministic constraints}\ \ (7.3.2),\ (7.4.3) - (7.4.6),\\
& \text{Non-negativity constraints}\ \ (7.4.7),
\end{aligned}$$

where B^* is determined in Section 7.5.

From Proposition 1 in [156], any feasible solution of ($\mathcal{P}3$) is an ϵ-level feasible solution of the original CC problem ($\mathcal{P}1$), with probability at least $1-\beta$. Problem ($\mathcal{P}3$) is a robust LP with polytopic uncertainty set, which can be converted into a tractable regular LP by transforming to its dual problem [41].

7.7 Shrinking Horizon Implementation

At the off-line microgrid design phase, we obtain optimal capacity design for DERs and load shedding, a forecast battery trajectory $\mathbf{p}_{\mathrm{b}}^{\mathrm{f}}$, and control policy parameters for dispatching battery power $\mathbf{p}_{\mathrm{b}}$, over the horizon $t = 0, \ldots, T-1$. In this section we discuss on-line implementation of the designed battery control policy, where the microgrid has been constructed according to the optimal capacity design.

Direct on-line implementation of the proposed policy uses day-ahead weather forecasts and generates a schedule for battery power $\mathbf{p}_{\mathrm{b}}$ over the complete horizon. This is an open-loop scheme. On the other hand, the proposed policy can be implemented using a shrinking horizon formulation. The motivation is that updated weather forecasts for the remaining time horizon can become available. We thereby modify the affine policy (7.3.6), (7.3.7) to take into account the varying horizon, and update battery power dispatch for the remaining period according to updated forecast information. This then provides a closed-loop implementation.

Consider closed-loop implementation at time-step k, i.e., we are interested in the horizon $t = k, ..., T-1$. The modified affine policy over the reduced horizon has the form,

$$\begin{aligned}\mathbf{p}_{\mathrm{b}}(t) = \mathbf{p}_{\mathrm{b}}^{\mathrm{f}}(t) + \mathbf{a}(t)\Big(\mathbf{e}_{\mathrm{b}}^{\mathrm{f}}(k) - \mathbf{e}_{\mathrm{b}}(k)\Big) + \mathbf{d}_{\mathrm{w}}(t)\Delta\tilde{\mathbf{p}}_{\mathrm{w}}^{0}(t) + \mathbf{d}_{\mathrm{pv}}(t)\Delta\tilde{\mathbf{p}}_{\mathrm{pv}}^{0}(t) - \mathbf{d}(t)\Delta\tilde{\mathbf{p}}_{\mathrm{d}}^{0}(t) \\ - \sum_{i=k}^{T-1} \mathbf{b}_{\mathrm{w}}(i) \cdot D_{\mathrm{w}}(t,i)\Delta\tilde{\mathbf{p}}_{\mathrm{w}}^{0}(i) - \sum_{i=k}^{T-1} \mathbf{b}_{\mathrm{pv}}(i) \cdot D_{\mathrm{pv}}(t,i)\Delta\tilde{\mathbf{p}}_{\mathrm{pv}}^{0}(i) \\ + \sum_{i=k} \mathbf{b}_{\mathrm{d}}(i) \cdot D(t,i)\Delta\tilde{\mathbf{p}}_{\mathrm{d}}(i). \end{aligned} \tag{7.7.1}$$

where $\mathbf{a}(t) \triangleq \frac{\sum_{i=k}^{T-1}\left(D_{\mathrm{w}}(t,i)+D_{\mathrm{pv}}(t,i)+D(t,i)\right)}{\sum_{i=k}^{T-1}\sum_{j=k}^{T-1}\left(D_{\mathrm{w}}(i,j)+D_{\mathrm{pv}}(i,j)+D(i,j)\right)}$, $\mathbf{b}_{\mathrm{w}}(i) \triangleq \frac{\mathbf{d}_{\mathrm{w}}(i)}{\sum_{j=k}^{T-1} D_{\mathrm{w}}(j,i)}$, $\mathbf{b}_{\mathrm{pv}}(i) \triangleq \frac{\mathbf{d}_{\mathrm{pv}}(i)}{\sum_{j=k}^{T-1} D_{\mathrm{pv}}(j,i)}$, $\mathbf{b}_{\mathrm{d}}(i) \triangleq \frac{\mathbf{d}(i)}{\sum_{j=k}^{T-1} D(j,i)}$.

7.8 Results and Analysis

7.8.1 Data Resources and Model Parameters

7.8.1.1 Renewable Generation and Load Data

Wind and solar are the two renewable resources under consideration. Aggregated wind generation data with five-minute resolution are drawn from Bonneville Power Administration (BPA)'s website [163], and averaged within each hour to give hourly resolution

data. Due to the pure renewable microgrid setting under consideration, we target regions with adequate wind resource. Thus, we make the assumption that the minimum hourly wind power is no less than 1% of its rating, and that wind goes above 10% of its rating at least once during the day. Five-minute resolution solar power data are collected from NREL's Solar Power Data for Integration Studies data base [164], and averaged within each hour to give hourly resolution data. Both the wind and solar power data are scaled to give normalized data. Load data are collected from the same BPA data-set. We consider the microgrid to be on the scale of 100 kW peak demand. The original load data are thus scaled to match that microgrid peak.

7.8.1.2 Economic Model Parameters

The overall life time of the microgrid is assumed to be 20 years and the interest rate is assumed to be 12% in our analysis [149]. The piece-wise linear penalty function for load shedding bound is set to be,

$$c_{\text{sh}}(\bar{r}_{\text{sh}}) := \max\left(10^7 \bar{r}_{\text{sh}} \ , \ 10^8(\bar{r}_{\text{sh}} - 0.7) + 0.7 \times 10^7\right). \tag{7.8.1}$$

Economic parameters for each component in the microgrid are selected based on relevant literature and are summarized in Table 7.1, representing unit capacity (kW) costs. The battery parameters apply to both power rating and energy capacity. NPC for all components is computed as described in [161, 162], and are given in Table 7.1.

Table 7.1: Economic Parameters for DERs in the Microgrid.

Type of DER	Wind Turbine	Solar PV	Battery
Life Time	20 years [165]	25 years [165]	5 years [149]
Capital	\$2776 [153]	\$3800 [166]	\$274 [153]
Replacement	\$2776	\$3800	\$274
O&M (/kW/yr)	\$32.15 [167]	\$32.64 [167]	\$10 [148]
NPC (\$)	\$3180	\$4210	\$913

7.8.2 Results and Discussion

Numerical test cases are presented in this subsection to explore the proposed formulations. The performance of the two robust-set reshaping processes, i.e. cutting-based and PCA-based approaches, are compared. Combining the two approaches is also considered. Monte Carlo tests are undertaken to validate results. The Matlab-based CVX toolbox with the Gurobi solver is used to solve the optimization problem ($\mathcal{P}3$). The number of scenarios

required to solve for the robust set is given by equation (7.5.1). We set the violation level at $\epsilon = 0.1$, with a confidence level of $1 - \beta = 0.999$. The number of design variables n_x depends on the number of hyperplanes that are added to refine the robust set.

The optimal design results are summarized in Table 7.2. The base case using the original box robust set is computed first, where $n_x = 2n_\delta = 6T$ and the required number of scenarios is $N_t = 2372$. Based on the data and parameters presented earlier, the optimal design ratings for microgrid components are given in the column labeled "Box" in Table 7.2. The cost refers to the optimal value of the objective function (7.4.1), including the penalty term for load shedding. The shedding rate refers to the ratio of scenarios that require load shedding among the total scenarios that are used to form the robust set.

Table 7.2: Optimal Design Results for the Microgrid.

Type	Box	Cut	PCA	Cut + PCA
$\overline{p}_{\text{w}}$(kW)	2684	1907	2681	1857
$\overline{p}_{\text{pv}}$(kW)	0	59	0	63
$\overline{p}_{\text{b}}$(kW)	6	120	6	97
$\overline{e}_{\text{b}}$ (kWh)	62	1866	64	1426
$\overline{r}_{\text{sh}}$(%)	70	70	70	70
Cost (Million)	\$15.59	\$15.12	\$15.58	\$14.55
Shedding rate	0.1771	0.1838	0.1771	0.1400

Next the cutting-based robust set reshaping approach described in Subsection 7.5.1 is tested, where $n_x = 2n_\delta + 1 = 6T + 1$ and the required number of scenarios is $N_t = 2388$ for one extra hyperplane. The capacity design results are given in the column "Cut" of Table 7.2. The PCA-based robust set reshaping method of Subsection 7.5.2 is also tested, where we include the 3-σ limits and all $3T$ PC directions. Although $n_x = 2n_\delta + 2n_\delta = 12T$, we still implement 2388 scenarios for comparison. The capacity design results are given in the "PCA" column of Table 7.2.

In the robust optimization formulation under consideration, using the cutting approach to eliminate the small corner of the robust set effectively reduces conservatism and leads to cost reduction. In contrast, the PCA method eliminates more volume from the robust set. In fact, since the last few PCs have near zero variances, we can even reduce the dimension of the robust set by identifying these near constant relationships. The resulting robust set becomes a "slice" of the original robust set. Note that such dimensional reduction may not directly affect the performance of the LP. However, performance improvement is often attained because the smaller robust set allows more freedom for optimizing the battery-dispatch affine policy.

These results demonstrate the effectiveness of the cutting- and PCA-based robust set

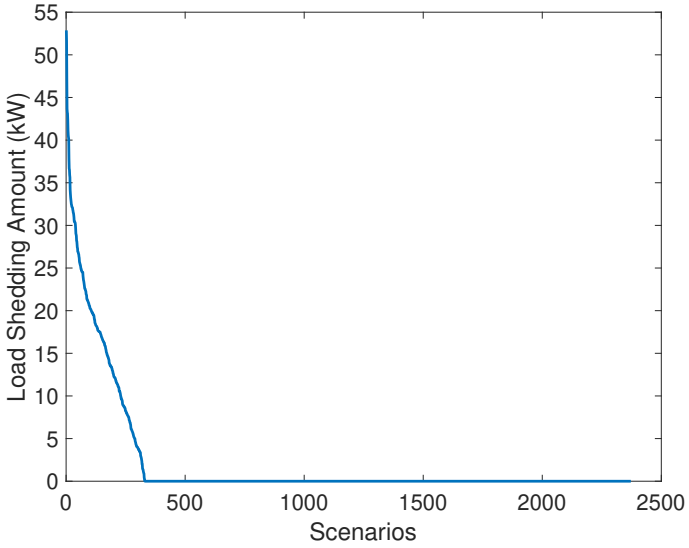

Figure 7.2: Profile of maximum load shedding for scenarios in the data-set.

reshaping concepts. Combining these two reshaping methods gives the capacity design results in the last column of Table 7.2. The cost is the lowest among all the cases, and the cost reduction is larger than the sum of the reductions achieved by the individual reshaping methods. Moreover, the load shedding rate is also the lowest among all the cases. This synergistic improvement is a consequence of the smaller robust set for this combined method, which allows a less restrictive, and hence more effective, battery dispatch policy. As a result, by combining these two robust-set reshaping methods we achieve both lower design cost and reduced probability of load shedding.

The upper limit $\bar{r}_{\text{sh}}$ for the load shedding ratio is 70% for all cases. This corresponds to the break point of the piece-wise linear cost function (7.8.1) governing the load shedding limit. This may seem large, however the percentage of scenarios in the data-set that actually invoke load shedding is small. Due to the robust nature of our approach, scenarios that actually require load shedding are rare, and the amount of load shedding is small for most of them. For the combined design approach, among the entire 2388 scenarios, only 14% require some load shedding. Fig. 7.2 shows the profile for the maximum load shedding for each of the 2388 scenarios, ordered from the highest load shedding amount to the lowest. The curve drops quickly and is zero for most scenarios.

To demonstrate the affine control policy for battery dispatch, we plot the SoC dynamics for various cases in Fig. 7.3. The nominal forecast trajectory is shown as a purple line, and four random scenarios are plotted as dashed lines. It is clear that the SoC at the end of the horizon is always driven back to its initial value, and all trajectories satisfy the upper and lower SoC constraints. The plot also shows, as dash-dot blue lines, two boundary cases

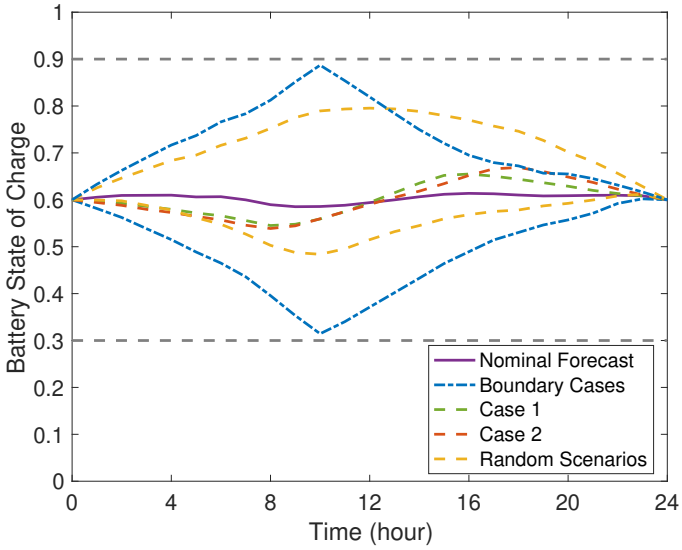

Figure 7.3: Battery SoC dynamics under affine policy.

that approach the upper and lower SoC limits. Fig. 7.4 shows the renewable generation, the negative of battery power dispatch ($-\tilde{\mathbf{p}}_b$), load and net power for the boundary case that (almost) touches the lower SoC limit. Here, the net power is defined as the total generation minus the total load, without taking into account load shedding. As can be seen, there is very limited wind over the initial six hours of this day and no sunshine over the initial nine hours, so the battery has to discharge to supply the load. Then, in the second half of the day, the wind generation is exceptionally high, allowing the battery to charge at high power based on the policy. Such cases highlight the need for high battery capacity in purely-renewable microgrids.

Fig. 7.3 shows two randomly selected scenarios, labeled Case 1 and Case 2. The renewable generation, the negative of battery power dispatch, load and net power for Case 1 are plotted in Fig. 7.5. It is clear that the net power is positive for the entire time horizon, so all the load can be supplied by the microgrid. There are rare occasions when the load cannot be met entirely, with load shedding required in such situations. An illustration is provided in Fig. 7.6, which corresponds to Case 2. In this case, renewable generation is insufficient overnight to meet the load requirement. The battery discharges at high power to compensate for the generation deficiency. However, load shedding is required, with the control policy (7.3.8) addressing the deficiency. The maximum load shedding is 27.3 kW. Case 2 also illustrates the necessity for high wind power rating in the design of the purely-renewable microgrid. In this case, wind generation is low over most of the day, and solar generation is only available during the daytime. As a result, the wind turbine rating needs to be sufficiently high to meet the demand.

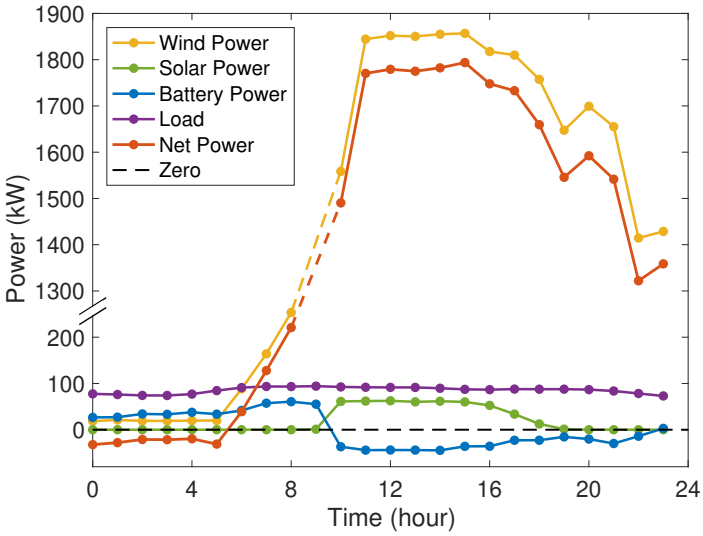

Figure 7.4: Generation and load: a boundary case.

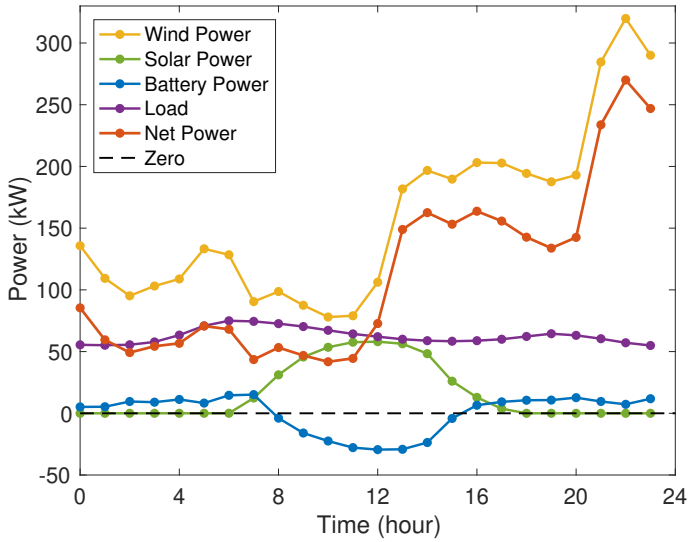

Figure 7.5: Generation and load: a randomly selected case in the data-set.

7.9 Chapter Conclusion

This chapter considers the optimal capacity design for DERs in a renewable-only islanded microgrid. This is a challenging problem due to the stochasticity of renewable resources and load. To address the stochasticity explicitly, we formulate the problem as a stochastic chance-constrained (CC) optimization problem. An affine policy for dispatching battery power is proposed and integrated into the optimization formulation. A probabilistically robust method is adopted to solve this CC problem by first computing a robust set for uncertain variables and then solving a robust counterpart of the original optimization

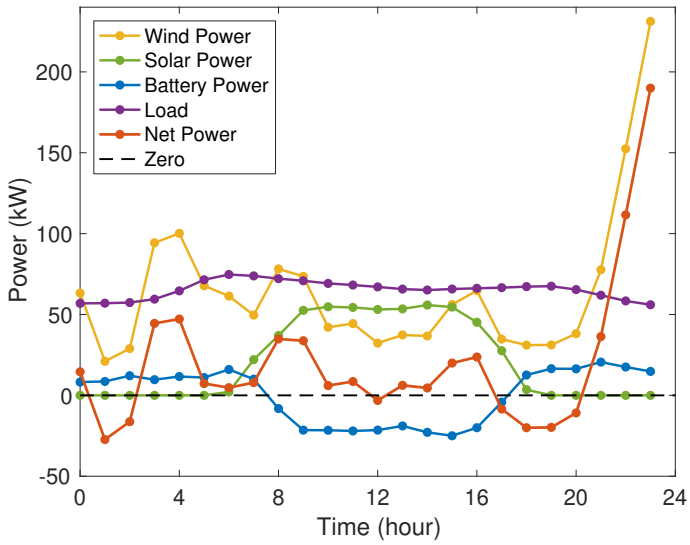

Figure 7.6: Generation and load: a case requiring load shedding and large wind turbine capacity.

problem.

Two methods are proposed for reducing the conservativeness of the robust formulation. The first cutting-based approach is motivated by the physical characteristics of the random variables and the geometry of the robust set. The second approach makes use of principal component analysis (PCA) to identify the principal directions in the data, which guides the reshaping of the robust set. These two methods can be combined to considerably reduce the original hyper-rectangular robust set, resulting in less conservative designs for microgrid capacity.

A probability guarantee can be provided with this technique. The optimal solution gives design capacities for the wind turbine, solar PV, battery system and load shedding. A forecast trajectory for battery power is obtained, as well as an affine policy that governs battery dispatch for different realizations of the stochastic generation and load. For on-line implementation, the proposed policy can be modified to a shrinking horizon scheme to take into account updated forecast information at each time-step. Numerical results show that the proposed methods balance design cost and reliability.

CHAPTER 8

Interconnecting Multiple Energy Carriers: Optimal Design and Operation of Energy Hubs

8.1 Chapter Introduction

Distributed energy resources (DERs), including renewable generation and storage, are experiencing substantial technology improvements and cost reductions, with off-grid energy systems becoming technically and economically viable. As such systems evolve, it is likely that they will incorporate multiple energy carriers, typically electricity, heat, gas (natural gas or liquefied petroleum gas) and hydrogen (H_2), along with the respective energy conversion processes. These *energy hubs* [168–170] offer the potential for highly versatile operating strategies, depending on hub composition and component sizing. Designing energy hubs to achieve a balanced trade-off between equipment cost and operational flexibility is becoming increasingly important.

In this chapter, we consider energy hubs that incorporate electricity, heat, gas and hydrogen. Figure 8.1 provides a schematic diagram showing typical energy flow paths, storage and conversion processes, though the methodology developed in the chapter is applicable for generic energy hub configurations [171]. Energy hubs of interest have no electrical connection to the distribution grid; rather, they are self-powered by solar and wind resources. However, guaranteeing energy sufficiency under all possible weather conditions would require excessively large component sizes, resulting in very high cost. Instead, purchase of gas (either from a network or by delivery) as a backup energy source is allowed, but only under rare weather conditions.

Two forms of energy storage are considered, namely batteries and hydrogen, with the latter requiring electrolysis and fuel-cell conversion. These two forms of storage offer complementary characteristics, with batteries better for shorter-term storage, and hydrogen having longer-term benefits [172]. Furthermore, hydrogen offers a number of

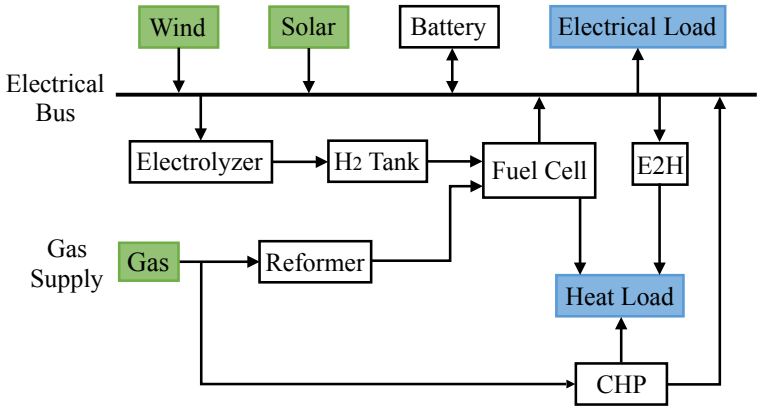

Figure 8.1: Schematic diagram of an isolated energy hub.

advantages which may see it play a greater role in future energy hubs. Firstly, it eliminates end-of-life environmental challenges associated with batteries, and secondly, it offers another energy transfer mechanism, potentially enabling energy delivery via hydrogen to neighboring hubs and/or fuel-cell vehicles. We have not, however, considered such hydrogen-based energy transfer in this chapter.

This chapter begins by considering the capacity design of isolated energy hubs. The design problem takes into account uncertainty in solar and wind resources and electrical load, and seeks a minimum cost design while ensuring that the electrical and heat loads can be satisfied with high probability. We have chosen to formulate capacity design as a chance-constrained optimization problem that explicitly accounts for stochasticity and enforces probabilistic constraints. Doing so allows a more prescriptive specification of the likelihood that a design will incur abnormal operation, in particular, excessive load shedding.

Chance-constrained problems are in general computationally challenging [173]. Considering the high dimension of our capacity design problem, we do not solve the chance-constrained problem directly, but derive and solve a robust reformulation. This robust reformulation conveniently allows the battery charging/discharging complementarity to be expressed via an equivalent linear representation, under an affine battery dispatch policy. The resulting problem can be solved as a linear program, which is computationally attractive. However, a consequence of the robust reformulation, and restriction to an affine policy, is that the design may be conservative. Accordingly, we propose a novel algorithm which iterates between the robust design problem and a validation problem, dynamically adjusting the level of conservativeness. The proposed algorithm is computationally tractable, and effectively reduces the design conservativeness. Furthermore, a novel cluster-based multi-policy strategy is proposed, which enables a more flexible

control structure. The clustering is based on principal component analysis (PCA) [157].

The design problem considered in this chapter assumes a fixed energy hub structure and determines the optimal sizes for hub components. Related work includes [174] which studied the optimal sizing of a combined heat and power (CHP) plant for a residential customer, where a storage tank and back-up boiler are considered. Reference [175] adopted a linearized model for energy hubs and optimized component type and size, with a focus on reliability constraints. These previous references did not consider the integration of renewable resources. The design of a wind-integrated energy hub is considered in [176]. Unlike the current chapter which formulates energy hub design as a chance-constrained optimization problem, [176] considered reliability indices such as "loss-of-load expectation" and "expected energy not supplied". However, such a formulation does not provide a formal probabilistic guarantee on operational reliability, which can be provided by chance-constrained methods. Reference [177] considered the sizing of DERs within a multi-source energy plant, focusing on the effect of different climatic scenarios. Structural design of energy hubs has also been investigated. For instance, in [178, 179], energy hub structure is characterized by a coupling matrix, the elements of which are treated as design variables. In [180], configuration planning is formulated as a mixed-integer linear program based on the modeling of branch energy flows within an energy hub.

Reliable and efficient operation of energy hubs can be achieved through a two-level control strategy. Higher level day-ahead scheduling uses weather and load forecast information in a multi-period optimization to establish reference trajectories for battery state of charge (SoC) and hydrogen tank storage level, as well as for the dispatch of the reformer and the CHP plant. Lower level on-line control uses the most up-to-date forecast information in a model predictive control (MPC) scheme [181] to track the reference trajectories established by the higher-level optimization, and compensate for errors in the day-ahead forecasts for renewable generation and load. MPC is an optimization-based control method which achieves feedback through repeated optimization over a moving horizon. MPC is well suited for achieving (near) optimal operation of energy hub systems. It can continually adapt to updated forecast information, while the feedback inherent in MPC can reject noise and suppress the effects of unmodeled dynamics. The shorter time horizon of the lower-level MPC ensures the computational demand is consistent with on-line implementation.

This two-level control strategy is motivated by the use of unit commitment and economic dispatch in power systems. Optimal power flow of energy hub systems has been studied in [168, 182]. References [183] and [184] considered unit commitment and economic dispatch of energy hub systems, respectively. Case studies were undertaken in [185]

to explore potential benefits of networked operation of energy hubs for achieving cost and greenhouse gas emission reduction. In [186], two-level MPC was applied to multi-carrier energy systems, taking into account heat storage in conjunction with CHP. An extension [187] further considered the intermittency of renewable resources and investigated the value of battery and heat storage. Reference [188] used economic MPC in a two-layer architecture for applications including microgrids.

The stochasticity introduced by renewable generation and load has drawn particular attention recently. An energy hub approach to building energy management was considered in [189], where exogenous uncertain in-feeds were modeled as stochastic processes. This resulted in a multi-stage stochastic optimization formulation. In follow-up work [190], a robust approach was adopted by constructing a family of distributions for the exogenous disturbance.

Beyond small-scale energy hub systems, a variety of studies have considered large-scale energy networks that involve electricity and gas infrastructures [191–193]. An optimization framework for large-scale energy hub networks was developed in [171] and used in [194], [195] to investigate mitigation of cascading outages. Joint expansion planning of coupled natural gas and power systems is studied in [196], where tractable convex relaxations are proposed.

This chapter makes the following contributions:

1 Energy hub capacity design is formulated as a chance-constrained optimization problem, allowing the stochasticity of renewable generation and load to be explicitly taken into account. This is an extension of Chapter 7 on microgrid capacity design to an energy hub setting with multiple energy carriers.

2 An affine policy is proposed for battery dispatch. This enables the chance-constrained optimal design problem to be reformulated as a robust counterpart problem. Consequently, the complementarity arising from battery charging/discharging can be manipulated such that the resulting optimization problem is a straightforward linear program. This builds on the formulation in Chapter 7 by allowing imperfect battery charging/discharging efficiency.

3 To resolve the conservativeness of the robust design problem, we develop an iterative framework to adjust the reliability level of the design based on the results of a validation problem. We provide two algorithms, based on the bisection method and the stochastic gradient method, to achieve this adjustment. This framework effectively addresses conservativeness yet is computationally tractable.

4 A cluster-based multi-policy strategy is proposed to achieve more flexible battery dispatch control, thereby improving the design outcomes.

5 A two-level operating strategy, incorporating day-ahead scheduling and on-line reference-tracking MPC, is used for operating isolated and networked energy hub systems. The benefits of energy sharing provided by networked operation are showcased.

The chapter proceeds as follows. Section 8.2 provides an overview of the energy hub design and operational issues that are addressed by the chapter. Section 8.3 develops the mathematical models for hybrid energy hubs. The capacity design problem is formulated and addressed in Section 8.4, while Section 8.5 focuses on energy hub operation. Section 8.6 presents a case study that illustrates optimal design and operation of an isolated energy hub. The extension to networked operation of multiple energy hubs is considered in Section 8.7, and a three-hub networked example is presented in Section 8.8. Conclusions are provided in Section 8.9.

8.2 Problem Statement

8.2.1 System Models

We consider autonomous (isolated) energy hubs that accommodate emerging distributed energy technologies, such as wind turbines, solar photovoltaic (PV) panels, battery storage, fuel cells, hydrogen production from both steam reforming and electrolysis, hydrogen storage and CHP. The aim is to reliably supply electrical and heat loads at minimum cost. An example of an energy hub is shown in Fig. 8.1. There is no grid connection, therefore backup electric power from the grid is not available.

Renewable resources, primarily wind and solar, form the main source of electrical energy. Energy storage plays a vital role in mitigating the stochasticity and intermittency of the renewable resources. Battery storage reacts quickly to provide short-term power balance, by discharging when renewable generation is deficient and charging when there is excess generation. Compared to batteries, fuel cells have relatively slower dynamics. Fuel cells can be deployed together with an electrolyzer and hydrogen tank to provide bulk energy storage. The electrolyzer decomposes water to generate hydrogen which is stored in the hydrogen tank. The fuel cell uses the hydrogen as a feedstock to supply the load. A steam reforming process can also produce hydrogen from gas to feed the fuel

cell. However, our overall aim is to minimize the use of fossil fuel by exploiting clean and cheap renewable resources whenever available.

Also note that the fuel cell generates heat as a by-product. This can be captured and used to supply heat load. Our energy hub model also incorporates CHP which can produce electricity and heat simultaneously by consuming gas. In addition, an electricity-to-heat path is modeled. It can be realized through various technologies, the most common of which is water heating.

An electrical load-shedding scheme is available to cope with rare weather conditions where renewable generation is limited throughout the entire day. Such a scheme helps ensure energy hub designs are not overly conservative.

8.2.2 Optimal Capacity Design

The capacity design problem for isolated energy hubs seeks to determine the optimal capacity of DERs as well as the optimal electrical load-shedding limit, such that the loads can be reliably supplied while plant costs are minimized. The uncertainty inherent in renewable resources requires careful treatment. To explicitly take into account such stochasticity, the optimal capacity design problem is formulated as a chance-constrained optimization problem of the form,

$$\begin{aligned} (\mathcal{P}0) \quad & \min_{x \in \mathcal{X} \subseteq \mathbb{R}^{n_x}} \; J(x) \\ \text{subject to} \quad & \Pr\Big(\max_{j=1,\dots,m} g_j(x,\delta) \leq 0 | \delta \in \Delta \Big) \geq 1 - \epsilon, \end{aligned} \tag{8.2.1}$$

where $x \in \mathcal{X} \subseteq \mathbb{R}^{n_x}$ are the decision variables, with the set $\mathcal{X}$ denoting deterministic constraints, $J(x)$ is the objective function, $\delta \in \Delta \subseteq \mathbb{R}^{n_\delta}$ is the random vector, and the notation $\Pr(A|B)$ denotes the probability of A conditioned on B. Constraint (8.2.1) is a chance constraint, where instead of enforcing a hard constraint, we only require the inner constraint to be satisfied with high probability. Parameter ϵ is a pre-specified maximal probability of violation. We use β to denote the confidence parameter, which characterizes the bound on the probability of failure, where (8.2.1) is not satisfied, associated with a solution to $\mathcal{P}0$ provided by a scenario approach [42].

8.2.3 Optimal Operation

With the capacity of the energy hub components determined by the design process, the operation problem considers the design of an optimal dispatch policy for operating the

energy hub system. Unlike the design problem where a range of possible scenarios must be considered, in the operational setting the controller responds to the actual system condition and the current forecast, effectively a single scenario. We require a controller that achieves optimal operation with respect to specified objectives. The operation of isolated energy hubs will initially be investigated. We then consider the operation of several energy hubs that are connected via electrical and/or gas networks

8.3 Energy Hub Models

The mathematical models for each component in the hybrid energy hub are described in this section. The models are developed in the context of a time horizon of $T = 24$ time-steps, each of one hour duration.

8.3.1 Uncertain Renewable Resources and Load

Energy hub design and operation must take into account the uncertain nature of renewable generation and load. We capture this uncertainty in wind generation, solar PV generation and load through the random vector variables $\tilde{\mathbf{p}}_{\mathrm{w}}, \tilde{\mathbf{p}}_{\mathrm{pv}}, \tilde{\mathbf{p}}_{\mathrm{d}} \in \mathbb{R}_{+}^{T}$, respectively. Their collection is defined as the random trajectory $\tilde{\mathbf{p}} \triangleq [(\tilde{\mathbf{p}}_{\mathrm{w}})^{\intercal}, (\tilde{\mathbf{p}}_{\mathrm{pv}})^{\intercal}, (\tilde{\mathbf{p}}_{\mathrm{d}})^{\intercal}]^{\intercal} \in \mathbb{R}_{+}^{3T}$.

For the capacity design problem, we further define the normalized random trajectory $\tilde{\mathbf{p}}^{0} \triangleq [(\tilde{\mathbf{p}}_{\mathrm{w}}^{0})^{\intercal}, (\tilde{\mathbf{p}}_{\mathrm{pv}}^{0})^{\intercal}, (\tilde{\mathbf{p}}_{\mathrm{d}})^{\intercal}]^{\intercal} \in \mathbb{R}_{+}^{3T}$, where $\tilde{\mathbf{p}}_{\mathrm{w}}^{0}$ and $\tilde{\mathbf{p}}_{\mathrm{pv}}^{0}$ denote normalized (unit capacity) wind power and solar PV power. The load $\tilde{\mathbf{p}}_{\mathrm{d}}$ takes actual values.

8.3.2 Power Balance/Sufficiency Constraints

This work assumes that excess renewable generation can be curtailed. The design problem therefore enforces the electrical power sufficiency constraint,

$$\begin{aligned} &\overline{p}_{\mathrm{w}} \tilde{\mathbf{p}}_{\mathrm{w}}^{0}(t) + \overline{p}_{\mathrm{pv}} \tilde{\mathbf{p}}_{\mathrm{pv}}^{0}(t) + \mathbf{p}_{\mathrm{fc}}(t) + \mathbf{p}_{\mathrm{rfm}}(t)\, \eta_{\mathrm{rfm}}\, \eta_{\mathrm{fc}} + \mathbf{p}_{\mathrm{chp}}(t)\, \eta_{\mathrm{chp}}^{\mathrm{e}} \\ &\quad \geq \tilde{\mathbf{p}}_{\mathrm{d}}(t)(1 - \hat{r}_{\mathrm{sh}}^{\mathrm{e}}) + f(\mathbf{p}_{\mathrm{b}}(t))\mathbf{p}_{\mathrm{b}}(t) + \mathbf{p}_{\mathrm{elz}}(t) + \mathbf{p}_{\mathrm{e2h}}(t), \end{aligned} \tag{8.3.1}$$

where $\mathbf{p}_{\mathrm{b}}(t) \geq 0$ implies battery charging with efficiency $f(\mathbf{p}_{\mathrm{b}}(t)) = 1/\eta_{\mathrm{c}}$, and $\mathbf{p}_{\mathrm{b}}(t) < 0$ when the battery is discharging with efficiency $f(\mathbf{p}_{\mathrm{b}}(t)) = \eta_{\mathrm{d}}$. The design variables $\overline{p}_{\mathrm{w}}$ and $\overline{p}_{\mathrm{pv}}$ refer to the power capacities of the wind turbine and solar PV units, respectively. The bold letter $\mathbf{p}$ refers to the power trajectory for each of the corresponding DERs, as indicated by the subscripts. The reformer produces hydrogen from gas with efficiency

η_{rfm}, with the hydrogen converted to electricity by the fuel cell with efficiency η_{fc}. Also, the proportion of the CHP that is utilized for electricity production is given by $\eta^{\text{e}}_{\text{chp}}$. Note that the electrical load-shedding limit $0 \leq \hat{r}^{\text{e}}_{\text{sh}} \leq 1$ is a parameter (not a decision variable) in the capacity design problem.

Due to the presence of random variables $\tilde{\mathbf{p}}^0_{\text{w}}$, $\tilde{\mathbf{p}}^0_{\text{pv}}$ and $\tilde{\mathbf{p}}_{\text{d}}$, constraint (8.3.1) will be formulated as a stochastic constraint in the chance-constrained design problem of Subsection 8.4.1.

The heat load $\mathbf{p}_{\text{heat}}(t)$ is assumed to be an exogenous deterministic input. A sufficiency constraint needs to be enforced for heat power,

$$\Big(\frac{\mathbf{p}_{\text{fc}}(t)}{\eta_{\text{fc}}} + \mathbf{p}_{\text{rfm}}(t)\eta_{\text{rfm}}\Big)(1-\eta_{\text{fc}})\eta_{\text{h}} + \mathbf{p}_{\text{e2h}}(t) + \mathbf{p}_{\text{chp}}(t)\eta^{\text{h}}_{\text{chp}} \geq \mathbf{p}_{\text{heat}}(t), \tag{8.3.2}$$

where $\Big(\frac{\mathbf{p}_{\text{fc}}(t)}{\eta_{\text{fc}}} + \mathbf{p}_{\text{rfm}}(t)\eta_{\text{rfm}}\Big)(1-\eta_{\text{fc}})$ gives the portion of the total fuel cell power that is not converted to electricity (the losses), while η_{h} specifies the proportion of those losses that are recovered for usable heat. The proportion of the CHP that is utilized for heat production is given by $\eta^{\text{h}}_{\text{chp}}$.

In the validation sub-problem of the design process of Section 8.4, and in the operation problem, a specific realization of the random variables is considered. This results in (8.3.1) becoming a deterministic power balance constraint, with the realization replacing the random variables. A renewable curtailment term $\mathbf{p}^{\text{e}}_{\text{curt}}(t) \geq 0$ is introduced to enforce electrical power balance,

$$\begin{aligned}&\mathbf{p}_{\text{w}}(t) + \mathbf{p}_{\text{pv}}(t) + \mathbf{p}_{\text{fc}}(t) + \mathbf{p}_{\text{rfm}}(t)\eta_{\text{rfm}}\eta_{\text{fc}} + \mathbf{p}_{\text{chp}}(t)\eta^{\text{e}}_{\text{chp}} \\ &\quad = \mathbf{p}_{\text{d}}(t)(1-\mathbf{r}^{\text{e}}_{\text{sh}}(t)) + f(\mathbf{p}_{\text{b}}(t))\mathbf{p}_{\text{b}}(t) + \mathbf{p}_{\text{elz}}(t) + \mathbf{p}_{\text{e2h}}(t) + \mathbf{p}^{\text{e}}_{\text{curt}}(t).\end{aligned} \tag{8.3.3}$$

Similarly, a heat balance constraint needs to be enforced during validation and operation, with (8.3.2) becoming,

$$\Big(\frac{\mathbf{p}_{\text{fc}}(t)}{\eta_{\text{fc}}} + \mathbf{p}_{\text{rfm}}(t)\eta_{\text{rfm}}\Big)(1-\eta_{\text{fc}})\eta_{\text{h}} + \mathbf{p}_{\text{e2h}}(t) + \mathbf{p}_{\text{chp}}(t)\eta^{\text{h}}_{\text{chp}} = \mathbf{p}_{\text{heat}}(t) + \mathbf{p}^{\text{h}}_{\text{curt}}(t), \tag{8.3.4}$$

where the curtailment term $\mathbf{p}^{\text{h}}_{\text{curt}}(t) \geq 0$ has been introduced to enforce heat balance.

8.3.3 Battery Energy Storage

From (8.3.1), the battery power exchanged with the grid is given by $f(\mathbf{p}_{\text{b}}(t))\mathbf{p}_{\text{b}}(t)$, which takes into account efficiency loss. Hence, the battery state of charge (SoC) evolves accord-

ing to,

$$\mathbf{e}_{\mathrm{b}}(t+1) = \mathbf{e}_{\mathrm{b}}(t) + \mathbf{p}_{\mathrm{b}}(t), \tag{8.3.5}$$

$$\mathbf{e}_{\mathrm{b}}(0) = \omega_{\mathrm{b}} \bar{e}_{\mathrm{b}}, \tag{8.3.6}$$

where ω_{b} specifies the initial SoC as a proportion of the battery energy capacity $\bar{e}_{\mathrm{b}}$. To ensure equitable use of battery storage over consecutive days, its SoC should return to a level that is no less than its value at the start of the 24-hour period,

$$\mathbf{e}_{\mathrm{b}}(T) \geq \mathbf{e}_{\mathrm{b}}(0). \tag{8.3.7}$$

We recognize that repetition of this requirement over successive days might result in a build up of stored energy. However, the gist of this constraint is that energy storage should be accounted for fairly over the period of interest.

A control policy for battery dispatch is desirable in the chance-constrained capacity design problem of Subsection 8.4.1 to ensure appropriate charging/discharging in response to realizations of random renewable generation and load. Such a policy could be quite general. However, to ensure a tractable chance-constrained formulation, we assume it has an affine structure,

$$\mathbf{p}_{\mathrm{b}} \triangleq \mathbf{p}_{\mathrm{b}}^{\mathrm{n}} + A\delta, \tag{8.3.8}$$

where $\delta \triangleq \tilde{\mathbf{p}}^0 - \mathbf{p}^{0\mathrm{n}}$, the affine policy matrix A is a design variable and,

- $\mathbf{p}^{0\mathrm{n}} \triangleq [(\mathbf{p}_{\mathrm{w}}^{0\mathrm{n}})^\intercal, (\mathbf{p}_{\mathrm{pv}}^{0\mathrm{n}})^\intercal, (\mathbf{p}_{\mathrm{d}}^{\mathrm{n}})^\intercal]^\intercal \in \mathbb{R}_+^{3T}$ describes a deterministic nominal trajectory for the normalized random variables, which is provided as exogenous information[1],
- $\mathbf{p}_{\mathrm{b}}^{\mathrm{n}}$ is a nominal dispatch trajectory for the battery, which is determined by the optimization problem.

Based on battery energy dynamics (8.3.5), (8.3.6), $\mathbf{e}_{\mathrm{b}}$ and $\mathbf{e}_{\mathrm{b}}^{\mathrm{n}}$ can be expressed in vector form as,

$$\mathbf{e}_{\mathrm{b}} = T_r\, \mathbf{p}_{\mathrm{b}} + \mathbf{e}_{\mathrm{b}}(0)\mathbf{1}_{T+1}, \tag{8.3.9}$$

$$\mathbf{e}_{\mathrm{b}}^{\mathrm{n}} = T_r\, \mathbf{p}_{\mathrm{b}}^{\mathrm{n}} + \mathbf{e}_{\mathrm{b}}^{\mathrm{n}}(0)\mathbf{1}_{T+1}, \tag{8.3.10}$$

where $T_r \in \mathbb{R}^{(T+1)\times T}$ denotes a concatenated matrix consisting of a zero row vector as its first row and a lower triangular matrix with entries of ones, and $\mathbf{1}_{T+1}$ denotes the

[1]This nominal trajectory may be generated, for example, by averaging over a collection of scenarios.

vector of dimension $T+1$ with all ones as its entries. Substituting equation (8.3.8) into equation (8.3.9), using equation (8.3.10) and noting that $\mathbf{e}_{\mathrm{b}}(0) = \mathbf{e}_{\mathrm{b}}^{\mathrm{n}}(0)$ gives,

$$\begin{aligned}\mathbf{e}_{\mathrm{b}} &= T_r\,(\mathbf{p}_{\mathrm{b}}^{\mathrm{n}} + A\,\delta) + \mathbf{e}_{\mathrm{b}}(0)\mathbf{1}_{T+1} \\ &= \mathbf{e}_{\mathrm{b}}^{\mathrm{n}} + T_r A\,\delta. \end{aligned} \tag{8.3.11}$$

If the condition,

$$\sum_{i=1}^{T} A(i,j) = 0,\ \forall j = 1,\ldots 3T, \tag{8.3.12}$$

is satisfied then $\mathbf{e}_{\mathrm{b}}(T) = \mathbf{e}_{\mathrm{b}}^{\mathrm{n}}(T)$.

Further discussion of affine battery-dispatch policies is provided in Chapter 7. We remark that response policies could be introduced for other DERs. We are only considering a policy for the battery because it is the most complex due to the charging/discharging complementarity arising from imperfect efficiency, and the requirement that the battery SoC returns at least to its initial value. Similar techniques can be used for designing affine policies for other devices.

8.3.4 Hydrogen Storage

The variation in the mass of hydrogen in the hydrogen tank is given by,

$$\mathbf{m}_{\mathrm{h_2}}(t+1) = \mathbf{m}_{\mathrm{h_2}}(t) + \Big(\frac{\mathbf{p}_{\mathrm{elz}}(t)\eta_{\mathrm{elz}}}{C_{\mathrm{elz}}} - \frac{\mathbf{p}_{\mathrm{fc}}(t)}{C_{\mathrm{fc}}\eta_{\mathrm{fc}}}\Big), \tag{8.3.13}$$

where $\mathbf{p}_{\mathrm{elz}}$ and $\mathbf{p}_{\mathrm{fc}}$ are the "charging" power of the electrolyzer and the "discharging" power of the fuel cell, with efficiencies η_{elz} and η_{fc}, respectively. It is assumed that the electrolyzer consumes C_{elz} kWh of electrical energy from the energy hub for electrolyzing water to produce 1 kg of hydrogen, and that the fuel cell produces C_{fc} kWh of energy by consuming 1 kg of hydrogen from the hydrogen tank [162].

Similar to battery storage, an additional constraint,

$$\mathbf{m}_{\mathrm{h_2}}(T) \geq \omega_{\mathrm{h_2}}\overline{m}_{\mathrm{h_2}} = \mathbf{m}_{\mathrm{h_2}}(0), \tag{8.3.14}$$

is imposed to ensure that the storage level of the hydrogen tank is at least as high as it was at the beginning of the day. In (8.3.14), $\omega_{\mathrm{h_2}}$ specifies the initial storage level as a proportion of the hydrogen tank mass capacity $\overline{m}_{\mathrm{h_2}}$.

8.3.5 Non-Negativity Constraints

In the energy hub design problem, the capacity values for energy hub components are decision variables. Non-negativity constraints ensure realistic designs:

$$\begin{aligned} &\overline{p}_{\mathrm{w}} \geq 0, \quad \overline{p}_{\mathrm{pv}} \geq 0, \quad \overline{p}_{\mathrm{b}} \geq 0, \quad \overline{e}_{\mathrm{b}} \geq 0, \quad \overline{p}_{\mathrm{elz}} \geq 0, \\ &\overline{m}_{\mathrm{h_2}} \geq 0, \quad \overline{p}_{\mathrm{fc}} \geq 0, \quad \overline{p}_{\mathrm{e2h}} \geq 0, \quad \overline{p}_{\mathrm{rfm}} \geq 0, \quad \overline{p}_{\mathrm{chp}} \geq 0. \end{aligned} \tag{8.3.15}$$

Upper limits on the capacity variables are not explicitly shown, but reasonability limits are enforced.

8.3.6 Capacity Constraints

Trajectories for energy hub components must satisfy capacity limits:

$$-\overline{p}_{\mathrm{b}} \leq \mathbf{p}_{\mathrm{b}}(t) \leq \overline{p}_{\mathrm{b}}, \tag{8.3.16}$$

$$\omega_{\mathrm{l}} \overline{e}_{\mathrm{b}} \leq \mathbf{e}_{\mathrm{b}}(t) \leq \omega_{\mathrm{u}} \overline{e}_{\mathrm{b}}, \tag{8.3.17}$$

$$0 \leq \mathbf{p}_{\mathrm{elz}}(t) \leq \overline{p}_{\mathrm{elz}}, \tag{8.3.18}$$

$$0 \leq \mathbf{m}_{\mathrm{h_2}}(t) \leq \overline{m}_{\mathrm{h_2}}, \tag{8.3.19}$$

$$0 \leq \mathbf{p}_{\mathrm{fc}}(t) + \mathbf{p}_{\mathrm{rfm}}(t)\, \eta_{\mathrm{rfm}}\, \eta_{\mathrm{fc}} \leq \overline{p}_{\mathrm{fc}}. \tag{8.3.20}$$

$$0 \leq \mathbf{p}_{\mathrm{e2h}}(t) \leq \overline{p}_{\mathrm{e2h}}, \tag{8.3.21}$$

$$0 \leq \mathbf{p}_{\mathrm{rfm}}(t) \leq \overline{p}_{\mathrm{rfm}}, \tag{8.3.22}$$

$$0 \leq \mathbf{p}_{\mathrm{chp}}(t) \leq \overline{p}_{\mathrm{chp}}, \tag{8.3.23}$$

$$0 \leq \mathbf{r}^{\mathrm{e}}_{\mathrm{sh}}(t) \leq \overline{r}^{\mathrm{e}}_{\mathrm{sh}}, \tag{8.3.24}$$

where ω_{l} and ω_{u} denote the lower and upper energy level specifications for the battery. The electrical load-shedding limit $\overline{r}^{\mathrm{e}}_{\mathrm{sh}}$ is enforced in the validation sub-problem and in operation. It is a parameter specifying the proportion of the total load that is controllable, and is not a design variable.

8.4 Capacity Design

The capacity design problem for an isolated energy hub is challenging because of the intrinsic stochasticity in the renewable resources and load, and the fact that the capacity design needs to take into account a wide range of possible scenarios. This section presents the complete formulation of an iterative algorithm for determining the optimal capacity

design for such energy hubs. This design process computes the optimal capacities for the DERs (including storage devices), for a specified load-shedding limit, such that the electrical and heat loads are satisfied with sufficiently high probability while the overall net present cost (NPC) of the energy hub is minimized.

The capacity design algorithm consists of two phases. A chance-constrained optimization problem determines optimal component capacities for a given value of a virtual load-shedding parameter $\hat{r}^{\mathrm{e}}_{\mathrm{sh}}$. The resulting design is then validated by checking a set of deterministic multi-period feasibility problems that use the true load-shedding limit $\bar{r}^{\mathrm{e}}_{\mathrm{sh}}$. The outcome of this feasibility test guides the selection of a new value for the virtual load-shedding limit $\hat{r}^{\mathrm{e}}_{\mathrm{sh}}$ and the process repeats. The proposed iterative framework effectively achieves a trade-off between reliability and cost. The remainder of this section provides full details of each phase of this algorithm.

8.4.1 Chance-Constrained Optimization Formulation

The chance-constrained optimization problem consists of an objective function together with stochastic and deterministic constraints. This subsection describes these various components of the problem together with the complete formulation.

8.4.1.1 Objective Function

The objective function to be minimized is composed of the NPCs of all the devices that form the energy hub, with the capacities of less desirable (gas utilizing) units, namely the reformer and CHP, being penalized:

$$\begin{aligned} J_{\mathrm{design}} = {} & \overline{p}_{\mathrm{w}} \cdot \mathrm{NPC}_{\mathrm{w}} + \overline{p}_{\mathrm{pv}} \cdot \mathrm{NPC}_{\mathrm{pv}} + \overline{p}_{\mathrm{b}} \cdot \mathrm{NPC}_{\mathrm{b}} + \overline{e}_{\mathrm{b}} \cdot \mathrm{NPC}_{\mathrm{b}} \\ & + \overline{p}_{\mathrm{elz}} \cdot \mathrm{NPC}_{\mathrm{elz}} + \overline{m}_{\mathrm{h_2}} \cdot \mathrm{NPC}_{\mathrm{h_2}} + \overline{p}_{\mathrm{fc}} \cdot \mathrm{NPC}_{\mathrm{fc}} \\ & + \overline{p}_{\mathrm{e2h}} \cdot \mathrm{NPC}_{\mathrm{e2h}} + c_{\mathrm{rfm}}(\overline{p}_{\mathrm{rfm}}) + c_{\mathrm{chp}}(\overline{p}_{\mathrm{chp}}), \end{aligned} \tag{8.4.1}$$

where $c_{\mathrm{rfm}}(\cdot)$ and $c_{\mathrm{chp}}(\cdot)$ denote two-piece linear penalty functions for the capacities of the reformer and CHP, respectively. The case study of Subsection 8.6.1 provides examples of these penalty functions.

8.4.1.2 Stochastic Constraints

Chance constraints are formulated to explicitly deal with the random variables in the model. Compared with the usual hard constraints that require a condition to hold at all

time, chance constraints only require constraint satisfaction with a pre-specified probability. The chance constraint for the capacity design problem can be written,

$$\Pr\Big((8.3.1), (8.3.7), (8.3.16), (8.3.17) \text{ are satisfied, } t = 0, ..., T-1\Big) \geq 1 - \epsilon, \tag{8.4.2}$$

where ϵ is a specified tolerance on the probability of violation. The chance constraint (8.4.2) gathers the constraints that involve random variables, namely the electrical power sufficiency constraint (8.3.1), and the battery power (8.3.16) and energy (8.3.7), (8.3.17) capacity constraints. The term $\mathbf{p}_{\mathrm{b}}$ that appears in (8.3.1), (8.3.16) is dispatched according to the policy (8.3.8). This dispatch policy also determines $\mathbf{e}_{\mathrm{b}}$ in (8.3.7), (8.3.17) through (8.3.11).

8.4.1.3 Deterministic Constraints

The nominal battery dispatch trajectory $\mathbf{p}_{\mathrm{b}}^{\mathrm{n}}$ used by the affine policy (8.3.8) must satisfy the deterministic version of the electrical power sufficiency constraint,

$$\begin{aligned} &\overline{p}_{\mathrm{w}}\mathbf{p}_{\mathrm{w}}^{0\mathrm{n}}(t) + \overline{p}_{\mathrm{pv}}\mathbf{p}_{\mathrm{pv}}^{0\mathrm{n}}(t) + \mathbf{p}_{\mathrm{fc}}(t) + \mathbf{p}_{\mathrm{rfm}}(t)\,\eta_{\mathrm{rfm}}\,\eta_{\mathrm{fc}} + \mathbf{p}_{\mathrm{chp}}(t)\,\eta_{\mathrm{chp}}^{\mathrm{e}} \\ &\quad \geq \mathbf{p}_{\mathrm{d}}^{\mathrm{n}}(t)(1 - \hat{r}_{\mathrm{sh}}^{\mathrm{e}}) + f(\mathbf{p}_{\mathrm{b}}^{\mathrm{n}}(t))\mathbf{p}_{\mathrm{b}}^{\mathrm{n}}(t) + \mathbf{p}_{\mathrm{elz}}(t) + \mathbf{p}_{\mathrm{e2h}}(t), \end{aligned} \tag{8.4.3}$$

where $\mathbf{p}^{0\mathrm{n}} \triangleq [(\mathbf{p}_{\mathrm{w}}^{0\mathrm{n}})^\intercal, (\mathbf{p}_{\mathrm{pv}}^{0\mathrm{n}})^\intercal, (\mathbf{p}_{\mathrm{d}}^{\mathrm{n}})^\intercal]^\intercal$ is the (exogenous) normalized nominal trajectory for the random variables.

8.4.1.4 Complete Formulation

The decision variables for the chance-constrained optimization problem consist of the capacities $P_{\mathrm{cap}} = [\overline{p}_{\mathrm{w}}, \overline{p}_{\mathrm{pv}}, \overline{p}_{\mathrm{b}}, \overline{e}_{\mathrm{b}}, \overline{p}_{\mathrm{elz}}, \overline{m}_{\mathrm{h_2}}, \overline{p}_{\mathrm{fc}}, \overline{p}_{\mathrm{rfm}}, \overline{p}_{\mathrm{chp}}, \overline{p}_{\mathrm{e2h}}]$, the policy variables $\mathbf{p}_{\mathrm{b}}^{\mathrm{n}}$, A, and the dispatch trajectories $\mathbf{p}_{\mathrm{dis}} = [(\mathbf{p}_{\mathrm{elz}})^\intercal, (\mathbf{m}_{\mathrm{h_2}})^\intercal, (\mathbf{p}_{\mathrm{fc}})^\intercal, (\mathbf{p}_{\mathrm{rfm}})^\intercal, (\mathbf{p}_{\mathrm{chp}})^\intercal, (\mathbf{p}_{\mathrm{e2h}})^\intercal]^\intercal$. The optimization problem can be expressed as,

$$\begin{aligned} (\mathcal{P}1) \quad \min \quad & (8.4.1) \\ \text{subject to} \quad & \text{Chance constraint (8.4.2) with equation (8.3.5) used implicitly,} \\ & \text{Non-negativity constraints (8.3.15),} \\ & \text{Deterministic constraints} \\ & (8.3.2), (8.3.6), (8.3.12)\text{-}(8.3.14), (8.3.18)\text{-}(8.3.23), (8.4.3), \text{ and} \\ & (8.3.5)\text{-}(8.3.7), (8.3.16), (8.3.17) \text{ applied to } \mathbf{p}_{\mathrm{b}}^{\mathrm{n}} \text{ and } \mathbf{e}_{\mathrm{b}}^{\mathrm{n}}. \end{aligned}$$

Chance-constrained optimization problems are strongly NP hard [173] and are in general computationally challenging [197]. However, if the problem is convex, i.e., the objective function is convex and the constraints are convex in the decision variables, a scenario approach [42] can be used to solve the chance-constrained problem. Theoretical results certify the number of scenarios required to provide an *a priori* probability guarantee for the solution. Unfortunately, the capacity design problem $\mathcal{P}1$ is nonconvex due to the binary variables describing battery charging/discharging. *A priori* performance bounds on a scenario approach for mixed-integer problems are provided in [198], though they are quite conservative. A more recent development [199] establishes results for a generalization of the scenario approach for nonconvex optimization and decision making problems. It uses an important concept of support subsample, and provides an *a posteriori* level of violation for the obtained solution. This result is very general in the sense that the probabilistic guarantee holds for a solution that can be obtained based on an arbitrary scenario decision rule, in fact not even necessarily from an optimization problem.

Our problem has a large number of decision variables, so satisfying the scenario requirements of [198] is infeasible due to both data limitations and computational requirements. Therefore, Subsection 8.4.4 introduces a robust reformulation of the chance-constrained problem $\mathcal{P}1$. By exploiting the affine structure of the battery dispatch policy (8.3.8), $\mathcal{P}1$ can be transformed into a robust linear program (LP). Furthermore, by considering the dual problem of the robust LP, we can transform the problem into a regular LP, which is computationally attractive.

However, the robust reformulation and the restriction to an affine policy may result in conservative designs. We therefore propose an algorithm that iterates between the robust reformulation of $\mathcal{P}1$ and a validation problem that is described in Subsection 8.4.2. The iterative procedure is presented in Subsection 8.4.3. After a solution is obtained, an *a posteriori* probability guarantee can be provided using a result from [200].

8.4.2 Validation

Validation of the capacity design provided by the robust optimization program uses N_s scenarios that are randomly selected from the data-set of N scenarios. Each of the N_s scenarios is checked to determine whether, for the latest capacity design and the true load-shedding limit $\overline{r}^{\mathrm{e}}_{\mathrm{sh}}$, there exist feasible trajectories such that conditions (8.3.3), (8.3.4), (8.3.5)-(8.3.7), (8.3.13), (8.3.14), and (8.3.16)-(8.3.24) are satisfied. If such dispatches exist for all N_s scenarios then the current design is assumed to be feasible. Otherwise, if a feasible dispatch policy cannot be computed for any one of the selected scenarios then the current

design is infeasible. This feasibility problem can be reformulated through McCormick relaxation (exact in the case of binary variables) [201], which leads to a multi-period mixed-integer linear feasibility problem.

In order to establish a meaningful value for N_s, we consider the situation where a small number αN of the data-set scenarios are infeasible. We wish to ensure that by checking N_s randomly selected scenarios, infeasibility will be identified with probability $1 - \vartheta$. For this setting, the relationship between α, ϑ and N_s is given by,

$$\vartheta = \binom{(1-\alpha)N}{N_s} \Big/ \binom{N}{N_s}. \tag{8.4.4}$$

In the design example of Section 8.6, the data-set consists of $N = 1000$ scenarios and we have chosen to check feasibility of $N_s = 100$ scenarios. For these values of N and N_s, if at least 5% of the scenarios are infeasible then equation (8.4.4) gives $\vartheta \leq 0.0045$. In other words, we will identify infeasibility with probability at least $1 - 0.0045 = 0.9955$.

8.4.3 Iterative Design Method

To address the conservativeness that arises in reformulating the chance-constrained problem as a tractable problem, we propose an iterative design method to determine the optimal capacities for energy hub components. The proposed method consists of iterating between the chance-constrained design problem and the validation problem. We utilize the maximum allowable load shedding $\hat{r}^{e}_{sh}$ as a scalar auxiliary parameter to bridge the two problems. Variation of this parameter, which we refer to as the virtual load-shedding limit, allows a trade-off between reliability and economics of the design. The design process is expressed diagrammatically in Fig. 8.2.

The chance-constrained design problem solves a robust optimization program, where a robust set is constructed using the available data-set describing random renewable generation and load. A capacity design result is produced by this robust design problem and supplied to the validation problem. The validation problem randomly selects a set of scenarios from the data-set. Note that the validation problem solves a multi-period optimization to determine whether there exist feasible dispatch policies for the selected scenarios, given the capacities designed by the chance-constrained design problem. Accordingly, battery dispatch is no longer restricted to the affine policy, but rather reflects the fact that actual operation of the energy hub could utilize a more flexible control strategy. This allows more realistic behavior, alleviating some of the conservativeness inherent in the chance-constrained design problem.

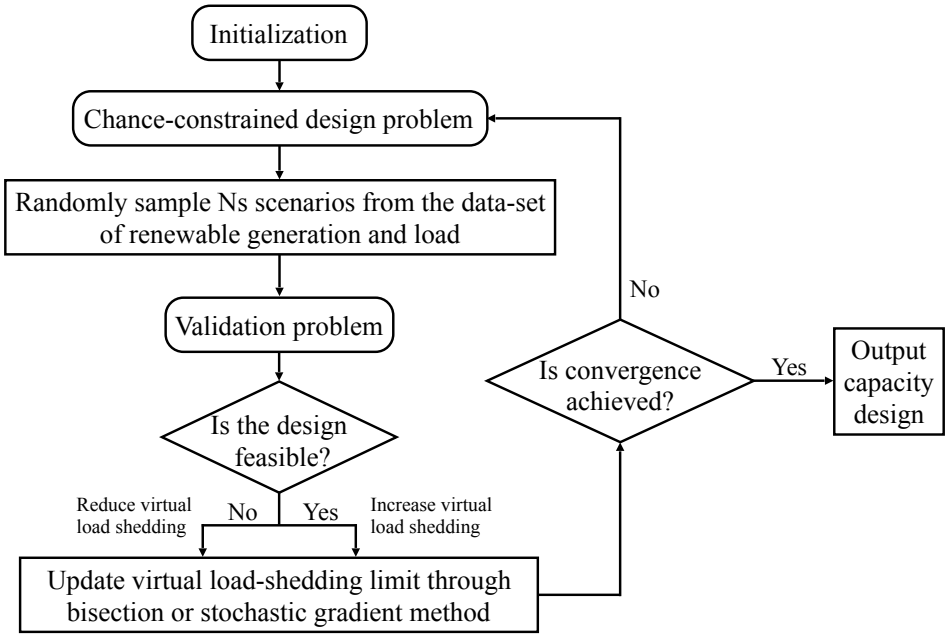

Figure 8.2: Block diagram of the iterative design method.

As previously mentioned, the virtual load-shedding term is in place to bridge between the two sub-problems. In the chance-constrained design problem, the virtual load-shedding parameter appears in the electrical power sufficiency constraints (8.3.1) and (8.4.3). Decreasing the value of $\hat{r}^{e}_{sh}$ tightens the sufficiency constraint and therefore increases the conservativeness of the design. Conversely, increasing $\hat{r}^{e}_{sh}$ relaxes the constraint, admitting a less conservative design but potentially resulting in an unacceptably high level of load shedding.

In contrast, the multi-period validation assessment enforces the actual value of the load-shedding limit, which is chosen to meet the desired level of reliability. Given that true load-shedding limit, the validation problem assesses whether the current design is viable for all the randomly selected scenarios. If the design is not viable, then the value of the virtual load-shedding limit $\hat{r}^{e}_{sh}$ is increased, otherwise it is decreased. A variety of methods can be used to achieve the appropriate change in $\hat{r}^{e}_{sh}$. Two algorithms, based on the bisection method and the stochastic gradient method, are presented in Subsection 8.4.5.

Conceptually, the multi-period optimization could be embedded into the chance-constrained capacity design problem, yielding a bi-level optimization formulation. However, the inner multi-period optimization would need to be solved for every sampled scenario, yielding a computationally intractable problem. In contrast, the proposed design procedure iterates between a standard LP and a mixed-integer linear feasibility problem, so computations are straightforward and convergence is fast.

8.4.4 Robust Reformulation

The chance-constrained problem $\mathcal{P}1$ can be solved through a robust reformulation. Reference [156] introduces such a robust reformulation approach for problems where the constraints are convex in the random variables. In such cases an *a priori* probability guarantee can be provided for any feasible solution of the reformulated problem. This approach firstly formulates a new chance-constrained problem,

$$\begin{aligned}&(\widehat{\mathcal{P}}2) \quad \min \ \|\overline{\xi} - \underline{\xi}\|_1 \\ &\text{subject to } \Pr\left(\delta \in [\underline{\xi}, \overline{\xi}] \middle| \delta \in \Delta \subseteq \mathbb{R}^{3T}\right) \geq 1 - \epsilon,\end{aligned}$$

to construct a hyper-rectangular robust set $B^* = [\underline{\xi}^*, \overline{\xi}^*]$ for the random vector. Then a robust counterpart of the original problem $\mathcal{P}1$, which we will refer to as $\mathcal{P}2$, is solved with the random vector confined to the computed robust set.

8.4.4.1 Robust Set Reshaping Methods

The hyper-rectangular robust set proposed in [156] can lead to very conservative results, especially when the dimension of the random vector is high or the random variables have large variance. Two methods are proposed in Chapter 7 to address this conservativeness by reshaping the robust set. Full details are provided in [202] and we only summarize the main ideas here.

The box-shaped robust set includes an unnecessary portion corresponding to minimal renewable generation and maximal load occurring over the entire horizon. Such conditions are rarely encountered in reality. Motivated by this observation, a cutting-based approach is proposed that trims off this troublesome portion of the robust set by introducing a single new hyperplane. Only one extra design variable is added, that being the offset of the hyperplane from the corner of the original box-shaped robust set. The resulting robust set is still polytopic, so by adding the appropriate number of scenarios, the same probability guarantee can be achieved.

Furthermore, the box-shaped robust set is conservative because it completely ignores the auto-correlation inherent in the trajectories of random scenarios. Therefore, a PCA method is exploited to further refine the robust set. The PCA method transforms the data into new coordinates given by the principle components (PCs). These PCs are arranged in descending order such that the first few PCs capture the largest variance in the data, whereas the last few PCs describe near constant relationships in the data. Two hyperplanes can be introduced for each PC direction. The hyperplanes lie normal to the PC direction,

with their offsets from the origin determined by the two outermost data points along the PC direction.

8.4.4.2 Reformulation for Battery Dispatch

This subsection considers reformulation of the robust counterpart problem $\mathcal{P}2$ to resolve the complementarity introduced by battery charging and discharging. Recall that $\mathbf{p}_{\mathrm{b}}$ is the power received/released by the battery terminals, with positive $\mathbf{p}_{\mathrm{b}}$ acting as a load on the energy hub. The charging and discharging efficiencies are denoted by η_{c} and η_{d}, respectively, with the usual assumption that $0 \leq \eta_{\mathrm{c}}, \eta_{\mathrm{d}} \leq 1$. Referring to the affine policy (8.3.8), we have at each time t,

$$\mathbf{p}_{\mathrm{b}}(t) = \mathbf{p}_{\mathrm{b}}^{\mathrm{n}}(t) + a_t \delta, \tag{8.4.5}$$

where a_t is the t-th row of matrix A. If $\mathbf{p}_{\mathrm{b}}(t) = \mathbf{p}_{\mathrm{b}}^{\mathrm{n}}(t) + a_t\delta \geq 0$, then the battery is charging at time t with efficiency η_{c}. If $\mathbf{p}_{\mathrm{b}}(t) = \mathbf{p}_{\mathrm{b}}^{\mathrm{n}}(t) + a_t\delta < 0$, then the battery is discharging at time t with efficiency η_{d}. Substituting equation (8.4.5) into the electrical power sufficiency constraint (8.3.1) and reorganizing gives,

$$f(\mathbf{p}_{\mathrm{b}}^{\mathrm{n}}(t) + a_t\delta)(\mathbf{p}_{\mathrm{b}}^{\mathrm{n}}(t) + a_t\delta) - c_t\delta \leq B^{\mathrm{n}}(t), \tag{8.4.6}$$

where c_t is the t-th row of the matrix,

$$C \triangleq [\overline{p}_{\mathrm{w}} I_T,\ \overline{p}_{\mathrm{pv}} I_T,\ -(1 - \hat{r}_{\mathrm{sh}}^{\mathrm{e}}) I_T],$$

with I_T referring to the identity matrix of dimension T, and $B^{\mathrm{n}}(t)$ is the t-th entry of the vector,

$$B^{\mathrm{n}} \triangleq C\mathbf{p}^{0\mathrm{n}} - \mathbf{p}_{\mathrm{elz}} + \mathbf{p}_{\mathrm{fc}} - \mathbf{p}_{\mathrm{e2h}} + \mathbf{p}_{\mathrm{rfm}}\, \eta_{\mathrm{rfm}}\, \eta_{\mathrm{fc}} + \mathbf{p}_{\mathrm{chp}} \eta_{\mathrm{chp}}^{\mathrm{e}}.$$

We assume that a polytopic robust set has been constructed, based on the techniques described in Subsection 8.4.4.1. This robust set can be described by $D\delta \leq d$. In the robust counterpart problem, constraint (8.4.6) can be written as,

$$\max_{D\delta \leq d} \{f(\mathbf{p}_{\mathrm{b}}^{\mathrm{n}}(t) + a_t\delta)(\mathbf{p}_{\mathrm{b}}^{\mathrm{n}}(t) + a_t\delta) - c_t\delta\} \leq B^{\mathrm{n}}(t). \tag{8.4.7}$$

Claim 1. *Constraint (8.4.7) is equivalent to,*

$$\max_{\substack{D\delta \leq d \\ \gamma_t \in \{0,1\}}} \left\{ \left(\gamma_t \frac{1}{\eta_c} + (1 - \gamma_t)\eta_d\right)(\mathbf{p}_b^n(t) + a_t\delta) - c_t\delta \right\} \leq B^n(t). \tag{8.4.8}$$

Proof. Given any $\hat{\delta} \in \{D\delta \leq d\}$, we have,

$$\max_{\gamma_t \in \{0,1\}} \left\{ \left(\gamma_t \frac{1}{\eta_c} + (1-\gamma_t)\eta_d \right) \left(\mathbf{p}_b^n(t) + a_t \hat{\delta} \right) \right\} \geq f(\mathbf{p}_b^n(t) + a_t\hat{\delta})(\mathbf{p}_b^n(t) + a_t\hat{\delta}).$$

Hence, (8.4.8) $\Rightarrow$ (8.4.7).

Let (δ^*, γ_t^*) be the optimal solution of the left hand side of equation (8.4.8). Due to maximization, it can be seen that $\gamma_t^* = 0$ if $\mathbf{p}_b^n(t) + a_t\delta^* < 0$, and $\gamma_t^* = 1$ if $\mathbf{p}_b^n(t) + a_t\delta^* \geq 0$. By definition of the function f, we have $f(\mathbf{p}_b^n(t) + a_t\delta^*) = \gamma_t^* \frac{1}{\eta_c} + (1-\gamma_t^*)\eta_d$. Hence (8.4.7) $\Rightarrow$ (8.4.8). □

It is then straightforward to show that (8.4.8) is equivalent to the condition,

$$\max_{D\delta \leq d} \left\{ \max \left\{ \frac{1}{\eta_c}(\mathbf{p}_b^n(t) + a_t\delta) - c_t\delta, \eta_d(\mathbf{p}_b^n(t) + a_t\delta) - c_t\delta \right\} \right\} \leq B^n(t). \tag{8.4.9}$$

There are two sub-problems in condition (8.4.9),

$$\max_{D\delta \leq d} \{ \frac{1}{\eta_c}(\mathbf{p}_b^n(t) + a_t\delta) - c_t\delta \} \leq B^n(t), \tag{8.4.10}$$

$$\max_{D\delta \leq d} \{ \eta_d(\mathbf{p}_b^n(t) + a_t\delta) - c_t\delta \} \leq B^n(t). \tag{8.4.11}$$

At this point, the robust counterpart problem $\mathcal{P}2$ has been reformulated into a robust LP, with polytopic uncertainty set. It can be converted to a regular LP by taking the dual. For example, taking the dual of (8.4.10) and (8.4.11) gives,

$$\min_{\substack{\frac{1}{\eta_c}a_t - c_t = (\lambda_t^c)^\intercal D \\ \lambda_t^c \geq 0}} \left\{ d^\intercal \lambda_t^c - (B^n(t) - \frac{1}{\eta_c}\mathbf{p}_b^n(t)) \right\} \leq 0, \tag{8.4.12}$$

$$\min_{\substack{\eta_d a_t - c_t = (\lambda_t^d)^\intercal D \\ \lambda_t^d \geq 0}} \left\{ d^\intercal \lambda_t^d - (B^n(t) - \eta_d\mathbf{p}_b^n(t)) \right\} \leq 0, \tag{8.4.13}$$

where λ_t^c and λ_t^d are the t-th columns of the dual variable matrices λ^c, $\lambda^d \in \mathbb{R}^{L\times T}$, with L denoting the number of constraints used to define the robust set.

Recombining constraints (8.4.12) and (8.4.13) gives,

$$d^\intercal \lambda_t^c - (B^n(t) - \frac{1}{\eta_c}\mathbf{p}_b^n(t)) \leq 0, \tag{8.4.14}$$

$$d^\intercal \lambda_t^d - (B^n(t) - \eta_d\mathbf{p}_b^n(t)) \leq 0, \tag{8.4.15}$$

$$\frac{1}{\eta_c}a_t - c_t = (\lambda_t^c)^\intercal D, \tag{8.4.16}$$

$$\eta_{\mathrm{d}} a_t - c_t = (\lambda_t^{\mathrm{d}})^\intercal D, \tag{8.4.17}$$

$$\lambda_t^{\mathrm{c}} \geq 0, \tag{8.4.18}$$

$$\lambda_t^{\mathrm{d}} \geq 0. \tag{8.4.19}$$

8.4.5 Numerical Algorithms

Two algorithms have been considered for updating the virtual load-shedding parameter $\hat{r}^{\mathrm{e}}_{\mathrm{sh}}$ during the iterations between the robust optimization and the validation problem, namely the bisection method [203] and the stochastic gradient (SG) method [204]. The bisection algorithm is straightforward to implement while the stochastic gradient method can compensate for the randomness in scenario selection and guarantee convergence in a probabilistic sense. In both cases, the iterative update is applied to the scalar $\hat{r}^{\mathrm{e}}_{\mathrm{sh}}$. Therefore the required gradient information at each iteration is reduced to a scalar indicator variable, namely a flag indicating whether or not the validation problem is feasible.

The bisection and stochastic gradient methods are presented in Algorithms 1 and 2, respectively. Note that for both algorithms, when the virtual load-shedding limit $\hat{r}^{\mathrm{e}}_{\mathrm{sh}} \in [0, \bar{r}^{\mathrm{e}}_{\mathrm{sh}}]$, the validation problem is guaranteed to be feasible due to the robust formulation of the design problem.

8.4.6 Cluster-Based Multi-Policy Design

One of the main reasons for the conservativeness of the robust counterpart reformulation is that the affine control policy for battery dispatch does not have sufficient flexibility to cope with the wide range of possible realizations of the random variables. In this subsection we propose a novel multi-policy design approach based on clustering the random trajectories to reformulate the chance-constrained problem $\mathcal{P}0$, and hence the capacity design problem $\mathcal{P}1$.

We first subdivide the total probability space into k disjoint clusters, and design for each cluster a different nominal battery dispatch trajectory $\mathbf{p}_{\mathrm{b}}^{\mathrm{n}}$ and parameterization A of the affine control policy. The problem $\mathcal{P}0$ is transformed into,

$$\begin{aligned}
(\mathcal{P}3) \min_{x \in \mathcal{X} \subseteq \mathbb{R}^{n_x}} \quad & J(x) \\
\text{subject to} \quad & \Pr\Big(\max_{j=1,\dots,m_1} g_j^1(x,\delta) \leq 0 \mid \delta \in \Delta_1 \Big) \geq 1-\epsilon, && (8.4.20) \\
& \Pr\Big(\max_{j=1,\dots,m_2} g_j^2(x,\delta) \leq 0 \mid \delta \in \Delta_2 \Big) \geq 1-\epsilon, && (8.4.21) \\
& \quad \dots \\
& \Pr\Big(\max_{j=1,\dots,m_k} g_j^k(x,\delta) \leq 0 \mid \delta \in \Delta_k \Big) \geq 1-\epsilon. && (8.4.22)
\end{aligned}$$

Algorithm 1 Bisection algorithm for iterative design

Input: Data-set Ω of renewable generation and load, sample size $N_s > 0$, actual load-shedding limit $\overline{r}^e_{sh} \in [0, 1]$, and convergence tolerance $tol > 0$.
Output: Capacity design P_{cap} and corresponding virtual load-shedding limit $\hat{r}^e_{sh}$.
Initialization: $\underline{\mu} \leftarrow 0, \overline{\mu} \leftarrow 1, \mu \leftarrow 0$.
while $\overline{\mu} - \underline{\mu} \geq tol$ **do**
    Solve the robust design problem of Subsection 8.4.4 with $\hat{r}^e_{sh} = \mu$ to obtain a capacity design $P_{cap}(\mu)$.
    Randomly sample N_s scenarios from Ω.
    Solve the validation problem of Subsection 8.4.2 with the designed $P_{cap}(\mu)$, the actual load-shedding limit $\overline{r}^e_{sh}$, and the N_s sampled scenarios to check the feasibility of the design.
    if feasible **then**
        $\underline{\mu} \leftarrow \mu$
    else
        $\overline{\mu} \leftarrow \mu$
    end if
    $\mu \leftarrow (\underline{\mu} + \overline{\mu})/2$
end while
$P_{cap} \leftarrow P_{cap}(\underline{\mu})$ and $\hat{r}^e_{sh} \leftarrow \underline{\mu}$

Note that the design variables P_{cap} (component capacities) for problem $\mathcal{P}3$ are the same across all the clusters. Therefore, the objective functions of $\mathcal{P}3$ and $\mathcal{P}0$ are the same, since the cost is only a function of P_{cap}. However, the nominal dispatch trajectory and the affine policy will generally be different for each different cluster, leading to different functions g^i_j for the different chance constraints, $i = 1, \cdots, k$.

We enforce the requirement that every specific scenario (realization of the random trajectory) belongs to exactly one cluster,

$$\Pr(\delta \in \Delta_1) + \Pr(\delta \in \Delta_2) + \cdots + \Pr(\delta \in \Delta_k) = 1. \tag{8.4.23}$$

Thus, the total probability of constraint satisfaction is given by,

$$\sum_{i=1}^{k} \Pr\Big(\max_{j=1,\ldots,m_i} g^i_j(x, \delta) \leq 0 \mid \delta \in \Delta_i \Big) \cdot \Pr(\delta \in \Delta_i) \geq 1 - \epsilon, \tag{8.4.24}$$

where the $1 - \epsilon$ lower bound is a direct consequence of the structure of the chance-constraints in $\mathcal{P}3$, taking into account equation (8.4.23). Thus, by formulating the chance-constrained problem as $\mathcal{P}3$, we achieve the desired bound on the violation probability ϵ.

Algorithm 2 Stochastic gradient algorithm for iterative design

Input: Data-set Ω of renewable generation and load, sample size $N_s > 0$, actual load-shedding limit $\overline{r}^e_{sh} \in [0,1]$, initial step size $\eta_{ini} \in [0,1]$, and convergence tolerance $tol > 0$.
Output: Capacity design P_{cap} and corresponding virtual load-shedding limit $\hat{r}^e_{sh}$.
Initialization: iteration index $k \leftarrow 0$, step size $\eta^0 \leftarrow \eta_{ini}$, virtual load-shedding limit $\mu^0 \leftarrow 0$, phase flag $\upsilon \leftarrow 1$.
while $\eta^k \geq tol$ **do**
    Solve the robust design problem of Subsection 8.4.4 with $\hat{r}^e_{sh} = \mu^k$ to obtain a capacity design $P_{cap}(\mu^k)$.
    Randomly sample N_s scenarios from Ω.
    Solve the validation problem of Subsection 8.4.2 with the designed $P_{cap}(\mu^k)$, the actual load-shedding limit $\overline{r}^e_{sh}$, and the N_s sampled scenarios to check the feasibility of the design.
    if $\upsilon = 1$ and feasible **then**
        $\eta^{k+1} \leftarrow \eta^k$, $\mu^{k+1} \leftarrow \mu^k + \eta^{k+1}$
    else if $\upsilon = 2$ and feasible **then**
        $\eta^{k+1} \leftarrow \eta^k/2$, $\mu^{k+1} \leftarrow \mu^k + \eta^{k+1}$
    else
        $\upsilon \leftarrow 2$, $\eta^{k+1} \leftarrow \eta^k$, $\mu^{k+1} \leftarrow \mu^k - \eta^{k+1}$
    end if
    $k \leftarrow k + 1$
end while
$P_{cap} \leftarrow P_{cap}(\mu^{k-1})$ and $\hat{r}^e_{sh} \leftarrow \mu^{k-1}$

We can proceed as in Subsection 8.4.4 to compute robust sets for each cluster. The aforementioned cutting- and PCA-based robust set reshaping approaches can be applied to each cluster. We set the confidence parameters to be $\beta_1, \cdots, \beta_k$ for the k chance constraints in $\mathcal{P}3$. Recall that $1 - \beta_k$ denotes the confidence bound for the validity of each chance constraint. Then by subadditivity of probability measure [205], the overall confidence level is at least $1 - \hat{\beta}$, with $\hat{\beta} = \sum_{i=1}^{k} \beta_i$.

The process of clustering results in a more flexible control structure, which leads to less conservative capacity design. Furthermore, the clustering approach can be used to discard unwanted data, though at the cost of reducing the violation probability guarantee. Assume that the last cluster Δ_k gathers scenarios that correspond to bad cases (random renewable generation and load trajectory realizations) with low probabilities. Let $\rho \triangleq \Pr(\delta \in \Delta_k)$. Then $\sum_{i=1}^{k-1} \Pr(\delta \in \Delta_i) = 1 - \rho$. We delete the last chance constraint (8.4.22) in $\mathcal{P}3$. Then the

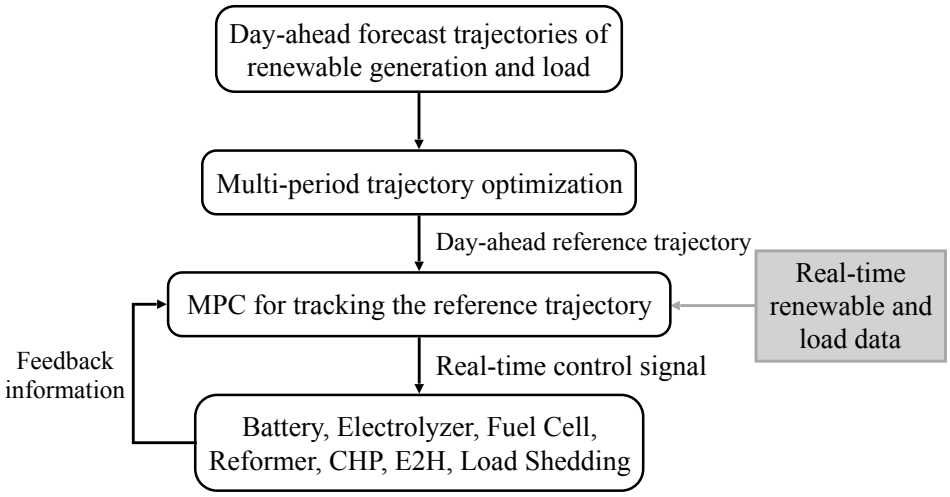

Figure 8.3: Block diagram of the two-level operating framework.

total probability of constraint satisfaction is,

$$\sum_{i=1}^{k-1} \Pr\Big(\max_{j=1,\dots,m_i} g_j^i(x,\delta) \le 0 \mid \delta \in \Delta_i \Big) \cdot \Pr(\delta \in \Delta_i) \ge (1-\epsilon)(1-\rho), \tag{8.4.25}$$

with overall confidence level of at least $1 - \sum_{i=1}^{k-1} \beta_i$. The probability ρ of the event $\delta \in \Delta_k$ can be estimated using the available data.

8.5 Operation

Operation of an isolated energy hub involves dispatching the DERs and regulating storage devices to reliably and economically satisfy demand. In the operational setting the capacities of energy-hub components are fixed at the values determined by the design process of Section 8.4. We consider a two-level operating scheme that incorporates day-ahead optimal scheduling together with real-time MPC. A schematic diagram of this operating strategy is provided in Fig. 8.3.

8.5.1 Higher-Level Day-Ahead Scheduling

At the higher-level, a multi-period optimization problem is solved using the day-ahead forecast of the renewable generation and load. The higher-level optimization problem minimizes the fuel cost, i.e., the cost of gas being purchased from external sources, as well as penalizes electrical load shedding, over the entire time horizon of $T = 24$ hours. The

higher-level problem encourages charging of the storage devices, namely the battery and hydrogen tank, whenever possible, and guarantees that the SoC of each storage device at the end of the day is no less than its starting energy level. The scheduled dispatch trajectories provided by the higher-level problem are taken as reference trajectories for the lower-level real-time MPC scheme, which has a shorter prediction horizon but finer resolution.

For simplicity of notation, all the control variables for the isolated energy hub are collected into the control vector, $\mathbf{u} = [(\mathbf{p}_{\mathrm{b}})^{\intercal}, (\mathbf{p}_{\mathrm{elz}})^{\intercal}, (\mathbf{p}_{\mathrm{fc}})^{\intercal}, (\mathbf{p}_{\mathrm{rfm}})^{\intercal}, (\mathbf{p}_{\mathrm{chp}})^{\intercal}, (\mathbf{p}_{\mathrm{e2h}})^{\intercal}, (\mathbf{r}^{\mathrm{e}}_{\mathrm{sh}})^{\intercal}]^{\intercal}$, and $\mathbf{p}_{\mathrm{g}} = \mathbf{p}_{\mathrm{rfm}} + \mathbf{p}_{\mathrm{chp}}$ denotes the amount of gas purchased from an external gas supply. The multi-period day-ahead scheduling problem is summarized as,

$$
\begin{aligned}
(\mathcal{P}4) \quad \min \quad & J_{\mathrm{sch}} = \sum_{t=0}^{T-1} \Big(c_{\mathrm{g}} \mathbf{p}_{\mathrm{g}}(t) + c^{\mathrm{e}}_{\mathrm{sh}} \mathbf{r}^{\mathrm{e}}_{\mathrm{sh}}(t) - c_{\mathrm{h}_2} \mathbf{m}_{\mathrm{h}_2}(t) - c_{\mathrm{b}} \mathbf{e}_{\mathrm{b}}(t) \Big), \\
\text{subject to} \quad & \text{Power balance constraints (8.3.3), (8.3.4),} \\
& \text{Battery storage dynamics (8.3.5)-(8.3.7),} \\
& \text{Hydrogen storage dynamics (8.3.13), (8.3.14),} \\
& \text{Capacity constraints (8.3.16)-(8.3.24),}
\end{aligned}
$$

where c_{g}, $c^{\mathrm{e}}_{\mathrm{sh}}$, c_{h_2} and c_{b} are weighting parameters for the corresponding components. The last two terms in the objective function J_{sch} encourage higher energy level in the storage devices. The optimal dispatch trajectories, given by $\widehat{\mathbf{e}}_{\mathrm{b}}$, $\widehat{\mathbf{m}}_{\mathrm{h}_2}$, $\widehat{\mathbf{p}}_{\mathrm{rfm}}$, and $\widehat{\mathbf{p}}_{\mathrm{chp}}$, are passed to the lower-level MPC and serve as the reference trajectories for the SoC of the battery and hydrogen tank, and as the dispatch goals for the reformer and CHP.

Similar to the validation problem, the multi-period day-ahead scheduling problem for an isolated energy hub is reformulated into a mixed-integer LP through McCormick relaxation, enabling efficient solution.

8.5.2 Lower-Level On-Line Operation Using MPC

During on-line operation the energy hub faces real-time realizations of renewable generation and load which differ from the day-ahead forecast. To manage these deviations the lower-level MPC seeks to track the reference trajectories provided by the higher-level day-ahead schedule while minimizing load shedding. The tracking errors for the various quantities are weighted by parameters $\sigma_1, ..., \sigma_5$. A four-hour prediction horizon is used, with a fifteen-minute time-step. The desired tracking control is achieved via the

optimization formulation,

$$
\begin{aligned}
(\mathcal{P}5)\quad \min_{U(t)}\ J_{\mathrm{MPC}}(t) = \sum_{k=0}^{N_c-1} \Big(& \sigma_1 \Big(\mathbf{e}_{\mathrm{b}}(k|t) - \widehat{\mathbf{e}}_{\mathrm{b}}(k+t)\Big)^2 + \sigma_2 \Big(\mathbf{m}_{\mathrm{h}_2}(k|t) - \widehat{\mathbf{m}}_{\mathrm{h}_2}(k+t)\Big)^2 \\
& + \sigma_3 \Big(\mathbf{p}_{\mathrm{rfm}}(k|t) - \widehat{\mathbf{p}}_{\mathrm{rfm}}(k+t)\Big)^2 + \sigma_4 \Big(\mathbf{p}_{\mathrm{chp}}(k|t) - \widehat{\mathbf{p}}_{\mathrm{chp}}(k+t)\Big)^2 \\
& + \sigma_5 \mathbf{r}^{\mathrm{e}}_{\mathrm{sh}}(k|t)\Big),
\end{aligned}
$$

subject to Power balance constraints (8.3.3), (8.3.4),
Battery storage dynamics (8.3.5), (8.3.6),
Hydrogen storage dynamics (8.3.13), (8.3.14),
Capacity constraints (8.3.16)-(8.3.24),
$\forall k = 0, \cdots, N_c - 1,$

where t is the discrete time index and N_c is the horizon length. Standard notation $x(k|t)$ is adopted, which stands for the predicted value of x at time $t+k$, based on the information available at time t. The decision variables in $\mathcal{P}5$ are $U(t) = \Big(\mathbf{u}(0|t), \cdots, \mathbf{u}(N_c-1|t)\Big)$.

8.6 Design and Operational Results for an Isolated Energy Hub

8.6.1 Capacity Design Results

8.6.1.1 Renewable Generation and Load Data

To demonstrate the proposed methodology, we used real renewable generation data and electrical load data from online databases. Five-minute resolution aggregated wind generation data were collected from Bonneville Power Administration (BPA)'s website [163], and averaged within each hour to give hourly resolution data. Since the chapter focuses on cases where it is reasonable to assume reliance on renewable energy resources, we only considered regions with adequate renewable generation. Accordingly, we made the assumption that the minimum hourly wind power should be no less than 10% of its rating. Electrical load data were obtained from the same BPA database. Solar generation data with five-minute resolution were obtained from NREL's Solar Power Data for Integration Studies database [164]. The five-minute resolution data were averaged within each hour to give hourly resolution data.

Table 8.1: Economic Parameters for DERs in the Energy Hub.

DERs	Life (yrs)	Capital/Replace	O&M	NPC ($/kW)
WT	20 [165]	$2776 [153]	$32.15 [167]	$3180
PV	25 [165]	$3800 [166]	$32.64 [167]	$4210
Battery	5 [149]	$274 [153]	$10 [148]	$913.32
Elz	25 [206]	$2000 [206]	$25 [206]	$2310
H_2 tank	15 [206]	$1300 [206]	$15 [206]	$2110
FC	10 [206]	$3000 [206]	$175 [206]	$7020

Table 8.2: Efficiency Parameters for DERs in the Energy Hub.

η_c	η_d	η_{elz}	η_{fc}	η_{rfm}	η^e_{chp}	η^h_{chp}	η_h
0.9	0.9	0.9	0.75	0.8	0.3	0.4	1

The wind and solar generation data were scaled by their maximum values to give normalized data. We considered the isolated energy hub to be on the scale of 100 kW peak electricity demand, and the load data were scaled accordingly. The heat load was assumed to be deterministic.

8.6.1.2 Model Parameters

The energy hub was assumed to have a life of 20 years, and we used an interest rate of 12% [149]. The piece-wise linear penalty functions for reformer capacity and CHP capacity were set as,

$$c_{rfm}(\overline{p}_{rfm}) = \max\left(10^4\overline{p}_{rfm}, 10^6(\overline{p}_{rfm} - 15) + 15 \times 10^4\right),$$
$$c_{chp}(\overline{p}_{chp}) = \max\left(10^4\overline{p}_{chp}, 10^6(\overline{p}_{chp} - 15) + 15 \times 10^4\right).$$

The NPC for each component in the energy hub was computed based on the descriptions in [161, 162], and the resulting values are given in Table 8.1. The electricity-to-heat path can be fulfilled by various approaches, and the NPC was estimated to be $500/kW. Other economic parameters for the energy hub components were chosen based on relevant literature and are provided in Table 8.1. The costs are for unit capacity, and the NPC for battery systems applies to both power and energy capacity. The efficiency parameters are given in Table 8.2. The remaining parameters for the capacity design problem are collected together in Table 8.3.

Table 8.3: Parameters for DERs in the Energy Hub.

ω_b	ω_{h_2}	ω_l	ω_u	C_{elz}	C_{fc}
0.6	0.5	0.3	0.9	41.97	37.8

8.6.1.3 Results and Discussion

Algorithms 1 and 2 as described in Subsection 8.4.5 were tested and compared. In the robust design problem, the data-set describing the renewable generation and load was clustered into four clusters, based on two of the PC directions computed using PCA analysis. Within each cluster, the PCA-based method was again used to reshape the robust set. For comparison, the original single-cluster box-shaped robust set was also tested. The robust problem $\mathcal{P}2$ was transformed to a regular LP as described in Subsection 8.4.4.2, which was solved using the Matlab-based CVX toolbox in conjunction with the Gurobi solver. For the validation problem, the true load-shedding limit was set at $\bar{r}^e_{sh} = 0.25$, and $N_s = 100$ scenarios were randomly selected from the data-set at each iteration. Note that the set of test scenario differed from one iteration to the next. However, for comparison, at each iteration the same set of scenarios was used by both the bisection algorithm and the stochastic gradient algorithm. Each scenario in the test set was validated individually. Once a scenario was identified as infeasible, the corresponding value of the virtual load-shedding limit was flagged as unacceptable and the remainder of the scenarios in the test set were not considered. We remark that the validation problem for each scenario is a mixed-integer linear feasibility problem.

The optimal capacity design results are presented in Table 8.4. Note that we report the converged virtual load-shedding limit in the row labeled $\hat{r}^e_{sh}$. (This is not to be confused with the true load-shedding limit, which remained fixed at $\bar{r}^e_{sh} = 0.25$.)

It can be observed that for both the bisection algorithm and the stochastic gradient algorithm, the four-cluster design always gave a lower design cost compared to the one-cluster design, although their corresponding converged virtual load-shedding limits are the same. Interestingly, the four-cluster design results in the participation of solar PV, as well as more significant deployment of the battery.

The iterations of the algorithms for the four cases of Table 8.4 are illustrated in Figs. 8.4 and 8.5. Variation of the virtual load-shedding limit during algorithm convergence is shown in Fig. 8.4, while Fig. 8.5 shows the corresponding variation of the design cost. The bisection algorithm increased the virtual load-shedding limit aggressively at the beginning but reduced back to a safe design. In this test case, the bisection algorithm approached the converged point from the unsafe side (corresponding to larger virtual

Table 8.4: Optimal Design Results for the Energy Hub.

Type	Bisection		Stochastic Gradient	
	1-Cluster	4-Cluster	1-Cluster	4-Cluster
$\overline{p}_{\mathrm{w}}$(kW)	354.44	291.31	367.61	302.15
$\overline{p}_{\mathrm{pv}}$(kW)	0.00	2.56	0.00	2.68
$\overline{p}_{\mathrm{b}}$(kW)	5.86	10.42	5.89	10.85
$\overline{e}_{\mathrm{b}}$ (kWh)	23.11	62.47	23.30	65.20
$\overline{p}_{\mathrm{elz}}$(kW)	6.03	9.38	6.15	9.61
$\overline{m}_{\mathrm{h_2}}$(kg)	1.55	2.92	1.58	3.00
$\overline{p}_{\mathrm{fc}}$(kW)	11.43	12.06	11.48	12.14
$\overline{p}_{\mathrm{rfm}}$(kW)	15.00	15.00	15.00	15.00
$\overline{p}_{\mathrm{chp}}$(kW)	15.00	15.00	15.00	15.00
$\overline{p}_{\mathrm{e2h}}$(kW)	8.19	7.98	8.17	7.95
$\hat{r}^{\mathrm{e}}_{\mathrm{sh}}$(kW)	0.5005	0.5005	0.4859	0.4859
Cost (Million)	\$1.54	\$1.39	\$1.59	\$1.43

load-shedding limit), while the stochastic gradient algorithm converged from the safe side (corresponding to smaller virtual load-shedding limit). The optimal design cost shown in Fig. 8.5 demonstrates that for the same value of the virtual load-shedding limit, the four-cluster design always gave a lower design cost than the one-cluster design.

Recall from Algorithms 1 and 2 that the robust capacity design is parameterized by the virtual load-shedding limit, which can be expressed as $P_{\mathrm{cap}}(\hat{r}^{\mathrm{e}}_{\mathrm{sh}})$. Figure 8.6 plots this dependence of P_{cap} over the range $0 \leq \hat{r}^{\mathrm{e}}_{\mathrm{sh}} \leq 1$. The four-cluster case was considered. This provides insights into the role of the virtual load-shedding limit in the iterative design process. As expected, the design capacity for most of the components in the energy hub decreased as the virtual load-shedding limit was increased. One exception is the capacity of electricity-to-heat, which slightly increased. This indicates that as more and more electrical load can be shed, the extra available electrical power generation can be used to supply the heat load.

The previous results of this subsection used a true load-shedding limit of $\bar{r}^{\mathrm{e}}_{\mathrm{sh}} = 0.25$ in the validation problem. Recall that this actual load-shedding limit represents an engineering requirement and should not be confused with the virtual load-shedding limit, which is simply an auxiliary variable. We can test the sensitivity of the design with respect to the true load-shedding limit to explore the impact of that design choice. In particular, cases with true load-shedding limit of 0.15 and 0.35 have been further tested, using the stochastic gradient algorithm and the four-cluster robust set. Figure 8.7 shows the convergence of the virtual load-shedding limit for the cases with $\bar{r}^{\mathrm{e}}_{\mathrm{sh}} = 0.15, 0.25, 0.35$. The corresponding design cost is shown in Fig. 8.8. As can be observed, the cases with

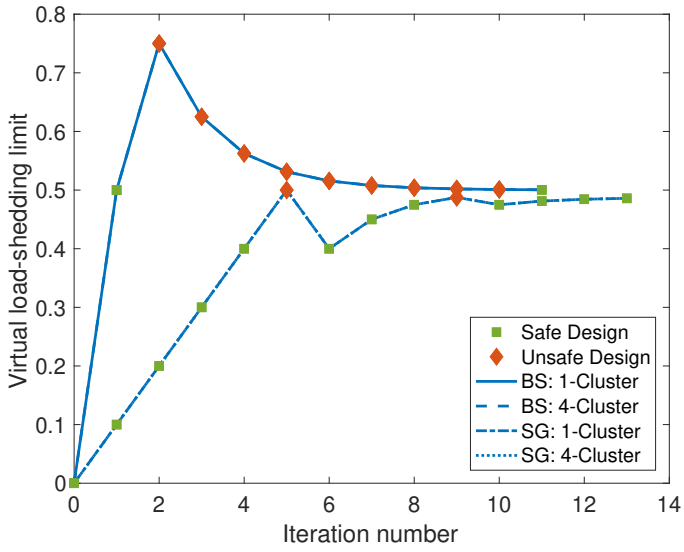

Figure 8.4: Virtual load-shedding limit variation during algorithm convergence.

true load-shedding limit of 0.25 and 0.35 gave almost the same converged virtual load-shedding limit and optimal design cost. Therefore, by choosing the level of 0.25, we effectively gained 10 kW (10% of the peak demand) of safety for almost no extra cost. In contrast, the true load-shedding level of 0.15 led to a large increase in the design cost.

The load-shedding limit of 0.25 implies that in the extreme case 25% of total electrical load can be shed. Even though this seems large, the percentage of scenarios that actually require load shedding is quite small. Figure 8.9 shows the maximum load-shedding ratio for every scenario in the data-set, ordered from the highest to the lowest. The curve drops quickly with no load shedding required for 90% of the scenarios.

An *a posteriori* probability guarantee for the design can be obtained using a result from [200],

$$\bar{\epsilon} = \max_{\zeta \in [0,1]} \left\{ \zeta : \sum_{z=0}^{N_v} \binom{N}{z} \zeta^z (1-\zeta)^{(N-z)} \right) \geq \beta \Big\}, \tag{8.6.1}$$

where $1-\beta$ is the required confidence level, and $\bar{\epsilon}$ is a corresponding upper bound on the violation probability ϵ. For our example, $N = 1000$ is the number of scenarios that were used in the evaluation, and $N_v = 7$ is the number of scenarios that had constraint violations, i.e., those that required more load shedding than permitted. For a specified confidence parameter $\beta = 0.1\%$, the upper bound on the violation probability given by equation (8.6.1) is $\bar{\epsilon} = 1.95\%$. Therefore, the design will be safe for a specified violation probability of $\epsilon = 2\%$.

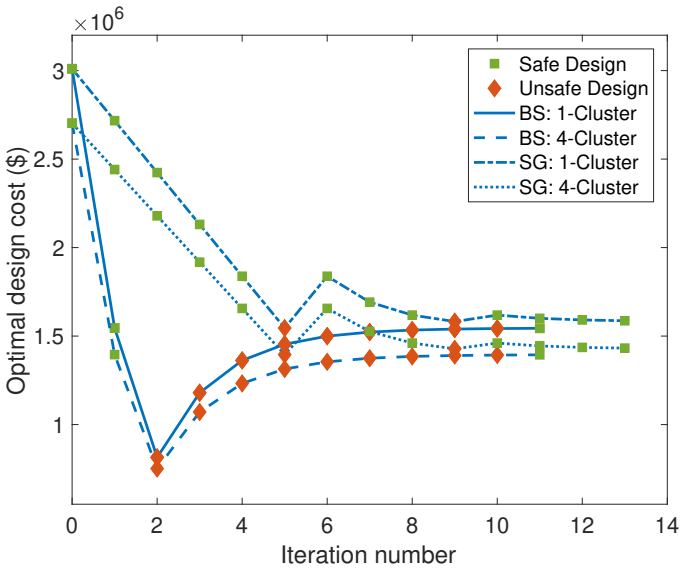

Figure 8.5: Design cost variation during algorithm convergence.

8.6.2 Operational Results for an Isolated Energy Hub

The operational characteristics of the optimally designed isolated energy hub are demonstrated in this subsection. Operation is based on the proposed two-level control scheme, consisting of higher-level day-ahead scheduling and lower-level on-line MPC.

8.6.2.1 Day-Ahead Scheduling

To illustrate day-ahead scheduling of an isolated energy hub, we considered a specific realization of renewable generation and load. The profiles for wind and solar PV generation, and for electrical and heat loads, are shown in Fig. 8.10. These curves represent the day-ahead forecast information used by the day-ahead scheduling problem.

The multi-period day-ahead scheduling problem $\mathcal{P}4$ for an isolated energy hub was reformulated into a mixed-integer LP, which we solved using the CVX toolbox with the Gurobi solver. The weighting parameters in the cost function of $\mathcal{P}4$ were chosen as $c_{\mathrm{g}} = 10^5$, $c_{\mathrm{sh}}^{\mathrm{e}} = 10^{11}$, $c_{\mathrm{h}_2} = 10^{-4}$, and $c_{\mathrm{b}} = 10^{-5}$, taking into consideration the relative importance of the four quantities. Figure 8.11 shows the schedules for the electrolyzer, fuel cell, electricity-to-heat and electrical load shedding, over the entire day. In this specific scenario, a large amount of load shedding was invoked. This was because of the drop in wind generation at hour 7, whereas the electrical load peaked at that same time. Moreover, the heat load was increasing around that time. As shown in Fig. 8.11, the electricity-to-heat power was non-zero even when the electrical load shedding was invoked. Between hours 5 and 10, the fuel cell was scheduled to produce electrical power. It can be observed that although

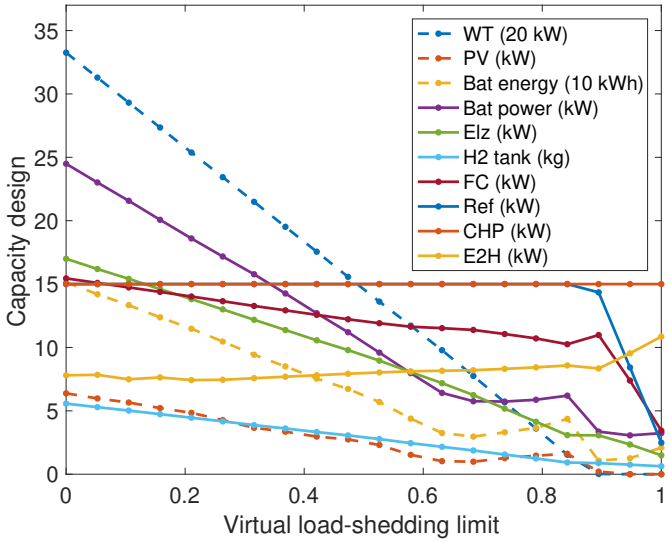

Figure 8.6: Dependence of robust capacity design P_{cap} on the virtual load-shedding limit $\hat{r}^{\text{e}}_{\text{sh}}$.

load shedding was invoked, the fuel cell did not operate at rated power to minimize instantaneous load shedding. This was due to the limited hydrogen storage. If the fuel cell had reached maximum power at an earlier time, the stored hydrogen would have been quickly depleted, and greater load shedding would have been required at a later time. This illustrates the predictive capability of multi-period scheduling.

The scheduled trajectories for the other energy hub components, namely the battery energy level, hydrogen tank storage level, reformer and CHP power, are tracked in the MPC problem, the performance of which is demonstrated next.

8.6.2.2 On-Line MPC Operation

On-line MPC operation of the optimally designed isolated energy hub must account for deviations from the forecast used in the day-ahead scheduling. To explore MPC behavior, it was assumed that updated forecast information was progressively revealed for on-line MPC use. To simulate forecast deviations, Gaussian noise was added to the forecast trajectories.

The day-ahead scheduling problem established reference trajectories for on-line MPC. In particular, the reference trajectories for battery energy levels, hydrogen tank storage levels, reformer power and CHP power were interpolated to obtain finer resolution tracking data. A step-size of 15 minutes and a control horizon of 4 hours were chosen as a balance between computational burden and control performance. The weighting param-

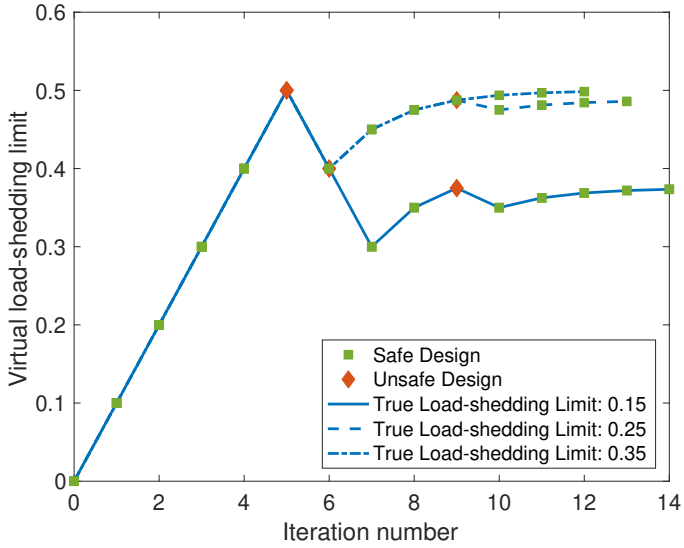

Figure 8.7: Sensitivity of convergence of the virtual load-shedding limit with respect to the true load-shedding limit.

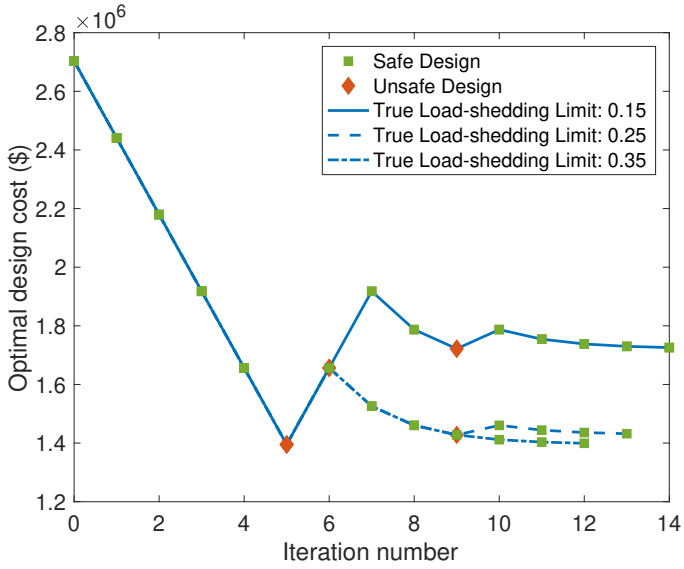

Figure 8.8: Sensitivity of convergence of the design cost with respect to the true load-shedding limit.

eters in the cost function of the MPC optimization $\mathcal{P}5$ were chosen as $\sigma_1 = 1$, $\sigma_2 = 3 \times 10^4$, $\sigma_3 = 10^2$, $\sigma_4 = 10^2$, and $\sigma_5 = 1/3 \times 10^4$, taking into account the relative magnitudes of the related quantities.

The reference storage levels of the battery and hydrogen tank are shown in Fig. 8.12, along with the MPC tracking trajectories. It is clear that MPC accurately tracked the reference trajectory for hydrogen mass. At the two critical points around hours 5 and 16,

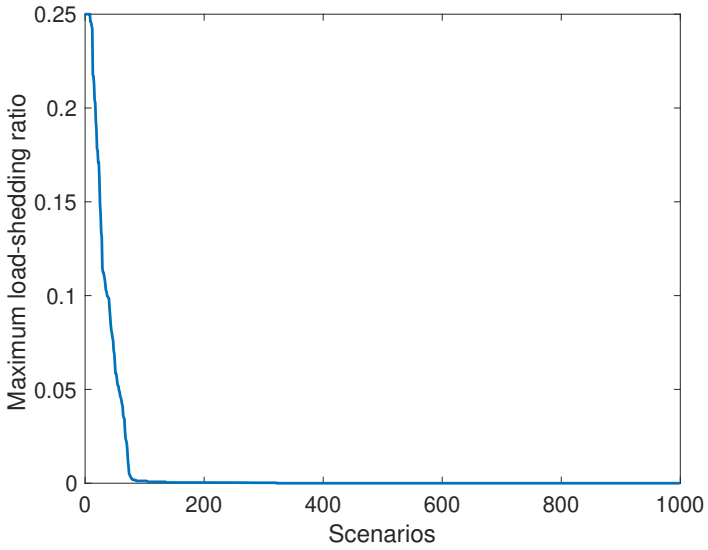

Figure 8.9: Maximum load-shedding ratio for all scenarios in the data-set.

MPC predicted a future shortage and guided the battery to respond accordingly. During the hours between 6 and 10, the two storage devices made up for insufficient generation, since in this specific scenario the electrical load peaked at hour 7, whereas the wind generation dipped at around that same time, as can be seen in Fig. 8.10. Both devices ended the day with storage levels that were at least as high as their staring values, as required by the problem formulation.

The tracking performance of the reformer and CHP is shown in Fig. 8.13. Again, MPC tracking is admirable for both devices. Moreover, the predictive capability of MPC is apparent at hour 13, where instead of completely shutting down the reformer and CHP units, the tracking trajectories remained relatively constant and smoothly increased back to high power output when the heat load started to increase at hour 17.

8.7 Networked Operation

Even though energy hubs may be designed for autonomous operation, opportunities may arise for interconnection of adjacent energy hubs. Such interconnection can potentially offer economic and reliability benefits. We therefore consider this possibility by introducing electrical and gas networks between several energy hubs. Examples of electrical and gas network structures are shown in Fig. 8.14. Other forms of energy networks, such as heat (hot water) and hydrogen [207], are also possible but will not be considered.

Such networked operation allows extra flexibility. For example, excess renewable

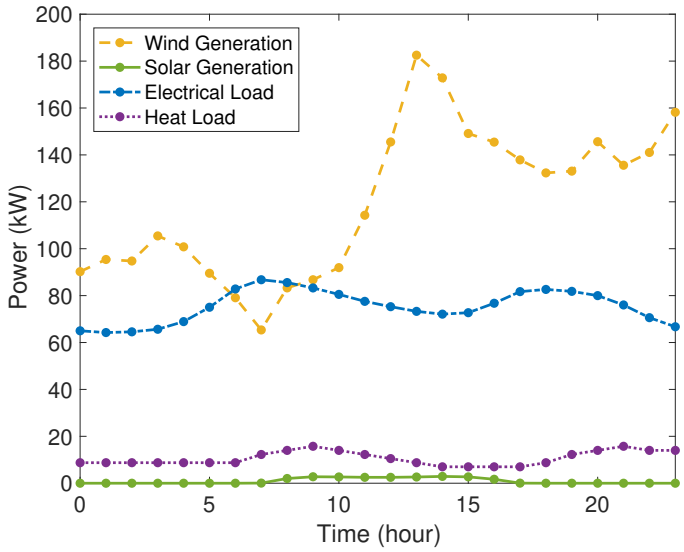

Figure 8.10: Renewable generation and load profiles for an isolated energy hub.

generation from an energy hub can be exported to adjacent energy hubs where generation may be temporarily deficient. The two-level operating scheme described in Section 8.5 can be adapted to operate networked energy hub systems to achieve this desired flexibility.

An energy network can be viewed as a graph with additional innate physical laws. The electrical network must satisfy electrical circuit laws, whereas the gas network must comply with gas laws that govern the relationship between pressure, volume, temperature and quantity of gas.

8.7.1 Energy Network Models

From an abstract perspective, an energy network can be viewed as a graph, with a set of nodes (buses) $\mathcal{B} = \{1, 2, \ldots, N_b\}$ and a set of arcs (branches) $\mathcal{A} = \{1, 2, \ldots, N_a\}$. Flow balance needs to be satisfied at every node in the network and additional physical constraints are enforced depending on the specific type of network. The most common energy networks, electricity and gas, are introduced in the following subsections.

8.7.1.1 Electrical Network

Generator and load buses of an electrical network are interconnected through distribution lines and transformers. Power flow equations describe the mathematical relationship between the complex power injected at buses and the complex voltages at those buses. These equations are nonlinear and non-convex, posing challenges for optimal power flow

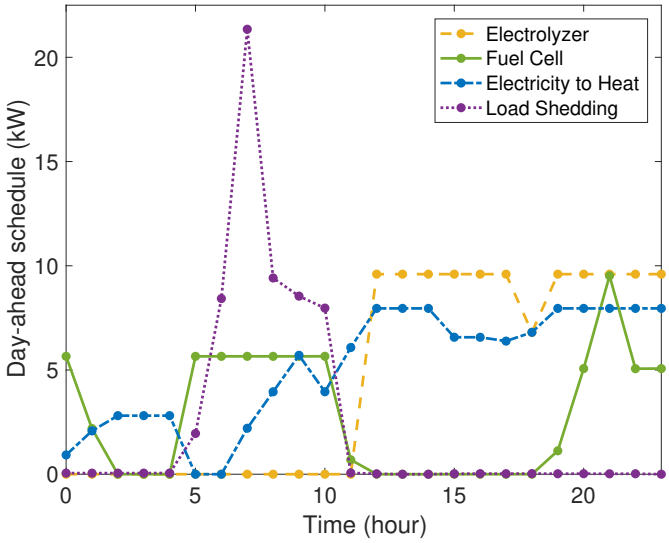

Figure 8.11: Electrolyzer, fuel cell, electricity-to-heat, and electrical load-shedding power profiles in an isolated energy hub.

problems. Various power flow approximations exist, among which the so-called DC power flow is the simplest and most widely used linear approximate model [208]. For the purpose of illustrating interactions between multiple energy hubs through an energy network, we will use the DC power flow to model the electrical network. This model is based on the approximation,

$$P_i(\theta) \approx \sum_{k=1}^{N_b^e} B_{ik}(\theta_i - \theta_k), \tag{8.7.1}$$

where P_i is the net active power injection at bus i. The DC power flow equations are in per unit, so $P_i = \mathbf{p}^{\mathrm{e}}_{\mathrm{net}}/S_{\mathrm{base}}$, where S_{base} is the power base for the system. The power balance constraint (8.3.3) within an energy hub is modified to incorporate the electrical power network interface term $\mathbf{p}^{\mathrm{e}}_{\mathrm{net}}$,

$$\begin{aligned}&\mathbf{p}_{\mathrm{w}}(t) + \mathbf{p}_{\mathrm{pv}}(t) + \mathbf{p}_{\mathrm{fc}}(t) + \mathbf{p}_{\mathrm{rfm}}(t)\eta_{\mathrm{rfm}}\eta_{\mathrm{fc}} + \mathbf{p}_{\mathrm{chp}}(t)\eta^{\mathrm{e}}_{\mathrm{chp}} \\ &\quad = \mathbf{p}_{\mathrm{d}}(t)(1 - \mathbf{r}^{\mathrm{e}}_{\mathrm{sh}}(t)) + f(\mathbf{p}_{\mathrm{b}}(t))\mathbf{p}_{\mathrm{b}}(t) + \mathbf{p}_{\mathrm{elz}}(t) + \mathbf{p}_{\mathrm{e2h}}(t) + \mathbf{p}^{\mathrm{e}}_{\mathrm{curt}}(t) + \mathbf{p}^{\mathrm{e}}_{\mathrm{net}}(t).\end{aligned} \tag{8.7.2}$$

8.7.1.2 Gas Network

Gas pipelines can be modeled in different levels of details. An accurate treatment takes into account space and time dependent hydrodynamic properties described by partial

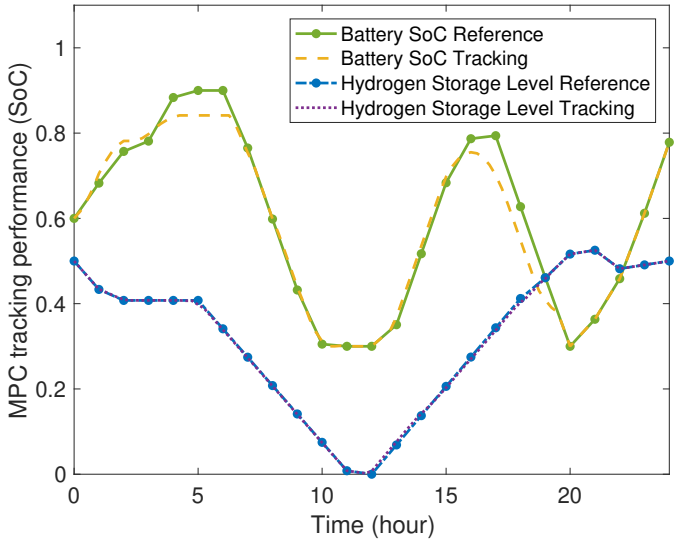

Figure 8.12: MPC performance, tracking the reference trajectories of the battery energy level and hydrogen storage level in an isolated energy hub. (SoC=1 implies the hydrogen tank is at capacity.)

differential equations [209]. Typical assumptions that allow model simplification include slow dynamic effects and isothermal flow. The constraints of a simplified gas network model can be piecewise linear or convexified [196].

Compressor units are a key component of gas networks. They increase the pressure of gas in the pipeline and deliver gas to consumers at specified conditions. The power consumption of a compressor can be modeled in various ways [210]. In this chapter, since we are modeling a small-scale gas network between energy hubs, we adopt a relatively precise model [168] that considers the dependence of power consumption on the pressure increase and gas volume flow rate. The model of a gas pipeline with compressor is shown in Fig. 8.15.

The nodal balance for a gas network is written,

$$Q_i = \sum_{k \in \mathcal{N}_i} Q_{ik}, \tag{8.7.3}$$

where Q_{ik} is the gas flow from node i to its neighboring node $k \in \mathcal{N}_i$, and Q_i is the nodal net volume flow injected at node i.

Figure 8.15 represents the model for a gas pipeline together with a compressor unit. The gas flow Q_{ik} is determined by,

$$Q_{ik} = k_{ik} s_{ik} \sqrt{s_{ik}(p_i^2 - p_k^2)}, \tag{8.7.4}$$

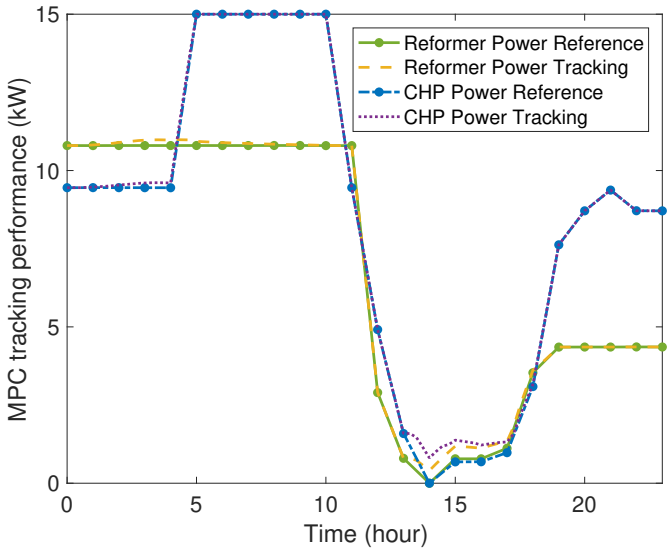

Figure 8.13: MPC performance, tracking the reference trajectories of the reformer and CHP output in an isolated energy hub.

where p_i and p_k are the pressures at nodes i and k, respectively. The term k_{ik} is a constant describing the properties of the pipe and the fluid [211]. The term s_{ik} represents the flow direction and is given by,

$$s_{ik} = \begin{cases} +1, & \text{if } p_i \geq p_k, \\ -1, & \text{if } p_i < p_k. \end{cases}$$

As mentioned earlier, the additional flow absorbed by the compressor unit can be modeled as,

$$Q_{\text{com}} = k_{\text{com}} Q_{ik}(p_i - p_r), \tag{8.7.5}$$

where p_i and p_r are the pressures after and before compression, and k_{com} is a constant describing the properties of the compressor unit.

The relationship between volume flow rate Q_{ik} and the effective power flow P_{ik} is given by,

$$P_{ik} = \text{GHV} \cdot Q_{ik}, \tag{8.7.6}$$

where the parameter GHV is the gross heating value of the gas mass.

In view of the networked energy hub system, the nodal net volume flow injection in equation (8.7.3) is given by,

$$Q_i = G_i - Q_{\text{com}} - \mathbf{p}^{\text{g}}_{\text{net}}/(\text{GHV} \cdot S_{\text{base}}), \tag{8.7.7}$$

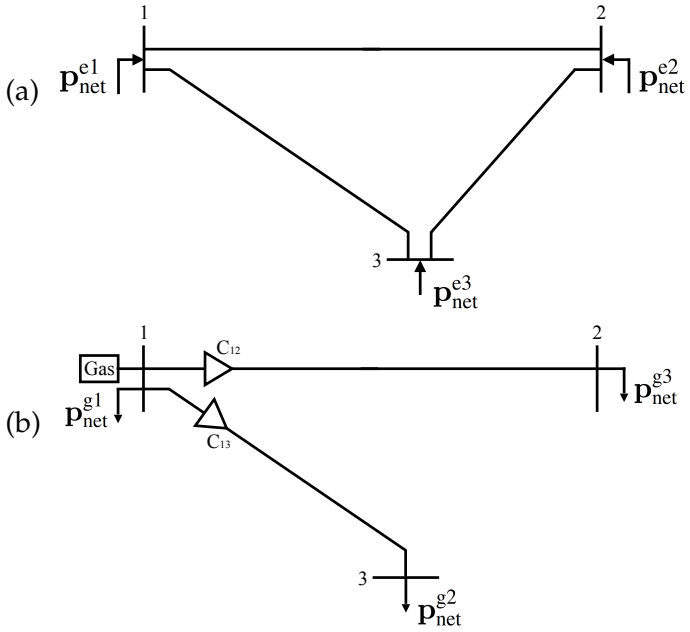

Figure 8.14: (a) Electrical network example; (b) Gas network example, C_{12} and C_{13} are compressors.

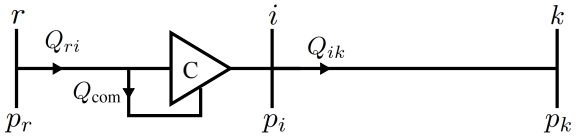

Figure 8.15: Model of gas pipeline with compressor.

where G_i is the amount of gas being purchased from an external gas supply resource. The interface $\mathbf{p}^{g}_{net}$ between the gas network and the energy hub is given by,

$$\mathbf{p}^{g}_{net} = \mathbf{p}_{rfm} + \mathbf{p}_{chp}. \tag{8.7.8}$$

8.7.2 Two-Level Operation

Two-level operation, as described in Section 8.5, can be modified to include multiple energy hubs and the energy network model. The control variables for the l-th energy hub are collected into the control vector, $\mathbf{u}^l = [(\mathbf{p}^l_b)^\intercal, (\mathbf{p}^l_{elz})^\intercal, (\mathbf{p}^l_{fc})^\intercal, (\mathbf{p}^l_{rfm})^\intercal, (\mathbf{p}^l_{chp})^\intercal, (\mathbf{p}^l_{e2h})^\intercal, (\mathbf{r}^{e,l}_{sh})^\intercal]^\intercal$, for all $l = 1, \cdots, h$. Collecting $\mathbf{u}^l$ together for all energy hubs gives $\mathbf{u} = [(\mathbf{u}^1)^\intercal, \cdots, (\mathbf{u}^h)^\intercal]^\intercal$.

The multi-period day-ahead scheduling problem $\mathcal{P}4$ is modified to give,

$$(\mathcal{P}6) \quad \min \quad J_{\text{sch-net}} = \sum_{l=1}^{h} \sum_{t=0}^{T-1} \Big(c_g \mathbf{p}^{g,l}_{net}(t) + c^e_{sh} \mathbf{r}^{e,l}_{sh}(t) - c_{h_2} \mathbf{m}^l_{h_2}(t) - c_b \mathbf{e}^l_b(t) \Big),$$

subject to Power balance constraints (8.3.4), (8.7.2),
Battery storage dynamics (8.3.5)-(8.3.7),
Hydrogen storage dynamics (8.3.13), (8.3.14),
Capacity constraints (8.3.16)-(8.3.24),
Electricity network equations (8.7.1),
Gas network equations (8.7.3)-(8.7.8),

where c_{g}, $c_{\mathrm{sh}}^{\mathrm{e}}$, c_{h_2} and c_{b} are weighting parameters.

As in the operation of isolated energy hubs, the optimal dispatch trajectories $\widehat{\mathbf{e}}_{\mathrm{b}}^{l}$, $\widehat{\mathbf{m}}_{\mathrm{h}_2}^{l}$, $\widehat{\mathbf{p}}_{\mathrm{rfm}}^{l}$, and $\widehat{\mathbf{p}}_{\mathrm{chp}}^{l}$ are passed to the lower-level MPC and serve as the reference trajectories for the l-th energy hub.

The MPC optimization formulation for a networked energy hub system is given by,

$$
\begin{aligned}
(\mathcal{P}7)\quad \min_{U(t)}\ J_{\text{MPC-net}}(t) = \sum_{l=1}^{h}\sum_{k=0}^{N_c-1} \Big(&\sigma_1\Big(\mathbf{e}_{\mathrm{b}}^{l}(k|t) - \widehat{\mathbf{e}}_{\mathrm{b}}^{l}(k+t)\Big)^2 + \sigma_2\Big(\mathbf{m}_{\mathrm{h}_2}^{l}(k|t) - \widehat{\mathbf{m}}_{\mathrm{h}_2}^{l}(k+t)\Big)^2 \\
&+ \sigma_3\Big(\mathbf{p}_{\mathrm{rfm}}^{l}(k|t) - \widehat{\mathbf{p}}_{\mathrm{rfm}}^{l}(k+t)\Big)^2 + \sigma_4\Big(\mathbf{p}_{\mathrm{chp}}^{l}(k|t) - \widehat{\mathbf{p}}_{\mathrm{chp}}^{l}(k+t)\Big)^2 \\
&+ \sigma_5\, \mathbf{r}_{\mathrm{sh}}^{\mathrm{e},l}(k|t)\Big),
\end{aligned}
$$

subject to Power balance constraints (8.3.4), (8.7.2),
Battery storage dynamics (8.3.5), (8.3.6),
Hydrogen storage dynamics (8.3.13), (8.3.14),
Capacity constraints (8.3.16)-(8.3.24),
Electricity network equations (8.7.1),
Gas network equations (8.7.3)–(8.7.8),
$\forall k = 0, \cdots, N_c - 1,$

with respect to the decision variables $U(t) = (\mathbf{u}(0|t), \cdots, \mathbf{u}(N_c - 1|t))$. Again, the tracking errors for the various quantities are weighted by parameters $\sigma_1, ..., \sigma_5$. Note that the formulation $\mathcal{P}7$ corresponds to a centralized control architecture where a central controller schedules the real-time dispatch of energy hubs connected to the network. Alternatively, a distributed implementation is possible, following approaches such as [212, 213].

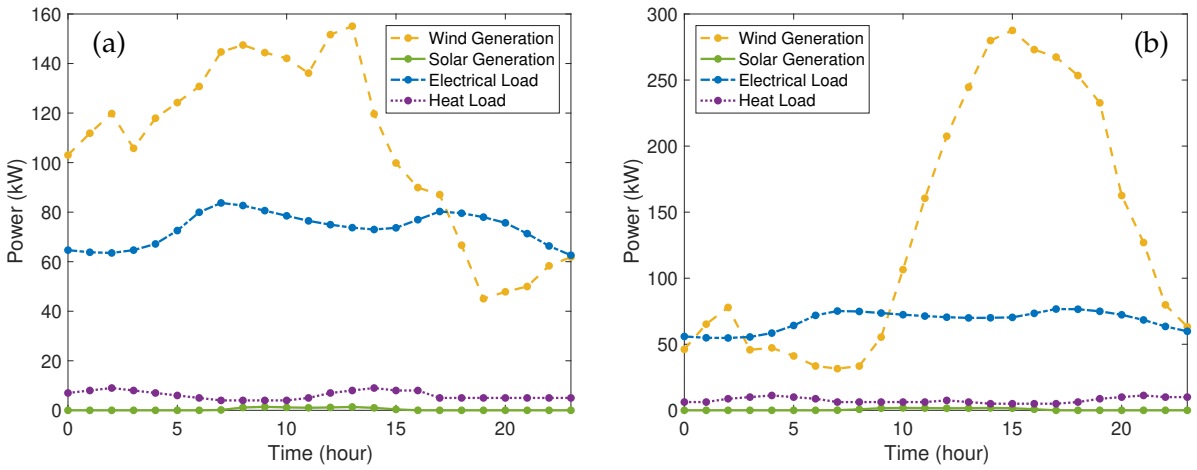

Figure 8.16: (a) Scenario profiles for EH2; (b) Scenario profiles for EH3.

8.8 Operational Results for a Networked Energy Hub System

Three energy hubs were interconnected through electrical and gas networks that have the structures shown in Fig. 8.14. All three energy hubs share the same design, which is also the same as the isolated energy hub of Section 8.6. Operational characteristics of the isolated and networked energy hub systems are compared to show the energy sharing capability provided by networked operation.

Due to spatial diversity, different renewable generation and load profiles are specified for the three energy hubs. The first energy hub EH1 is assumed to experience the same scenario as in the isolated case shown in Fig. 8.10. The scenarios for the other two energy hubs, EH2 and EH3, are shown in Fig. 8.16.

The multi-period day-ahead scheduling problem $\mathcal{P}6$ was solved first. The weighting parameters in the cost function of $\mathcal{P}6$ were chosen as $c_{\mathrm{g}} = 5 \times 10^2$, $c_{\mathrm{sh}}^{\mathrm{e}} = 10^5$, $c_{\mathrm{h_2}} = 10^{-1}$, and $c_{\mathrm{b}} = 10^{-3}$. Due to the nonlinearity of the gas network equations, the problem is a mixed-integer nonconvex program, so no global optimality guarantee can be provided. The problem was solved using the Matlab-based Yalmip toolbox with the branch and bound solver BMIBNB. This solver requires upper and lower solvers, with IPOPT and Gurobi chosen, respectively.

For the MPC optimization problem $\mathcal{P}7$, a step-size of 15 minutes and a control horizon of 4 hours were chosen. The weighting parameters in the cost function of $\mathcal{P}7$ were chosen as $\sigma_1 = 1$, $\sigma_2 = 3 \times 10^4$, $\sigma_3 = 10^2$, $\sigma_4 = 10^2$ and $\sigma_5 = 10^4$.

The reference and tracking trajectories for the battery SoCs are shown in Fig. 8.17.

Good tracking performance was achieved for all three energy hubs, especially during the second half of the day when renewable generation was abundant. The batteries in all three energy hubs were able to be charged back to their upper limits since EH3 provided plenty of wind generation during the later half of the day.

The reference and tracking trajectories of the hydrogen tank storage levels are shown in Fig. 8.18. The tracking performance of all three energy hubs was very good. Compared to Fig. 8.12, the energy sharing capability of the networked energy hubs allowed the hydrogen storage of EH1 to always remain at least half full, rather than being fully depleted and then requiring significant recharging.

The tracking performance of the reformer and CHP is shown in Figs. 8.19 and 8.20. In both plots, it can be seen that EH2 and EH3 provided perfect tracking. The tracking trajectory of the reformer in EH1, as shown by the green dashed line in Fig. 8.19, had a maximum power of 0.63 kW and a total energy consumption of 2.93 kWh. This compares with the yellow dashed line in Fig. 8.13 which shows that with the same local renewable generation and load profiles, the reformer unit required a maximum power of 11 kW and a total energy of 161.22 kWh to supply the isolated energy hub. The green lines in Fig. 8.20 show the reference and tracking trajectories of the CHP in EH1. The peak power of the CHP was 9.38 kW and it consumed total energy of 57.51 kWh. Referring to the purple dotted line in Fig. 8.13, for the isolated energy hub, the peak CHP power and the total energy consumption were 15 kW and 204.56 kWh, respectively. The reduction in gas-related energy consumption for networked operation compared to that of the isolated energy hub was 98% for the reformer and 72% for the CHP. Furthermore, the electrical load shedding was zero for all three networked energy hubs, whereas the isolated energy hub incurred peak electrical load shedding of 21.35 kW, as indicated by the purple dotted curve in Fig. 8.11.

8.9 Chapter Conclusion

This chapter considers the optimal capacity design and operation of energy hubs, which incorporate multiple energy carriers including electricity, gas, hydrogen and heat. The stochasticity of renewable generation and load is explicitly taken into account in the design of autonomous (isolated) energy hubs through a chance-constrained optimization formulation. An affine policy has been considered for battery dispatch, based on which a robust reformulation of the chance-constrained problem is derived with battery charging/discharging complementarity being expressed via an equivalent linear representation. The reformulated robust problem is a tractable linear program, having a significantly lower

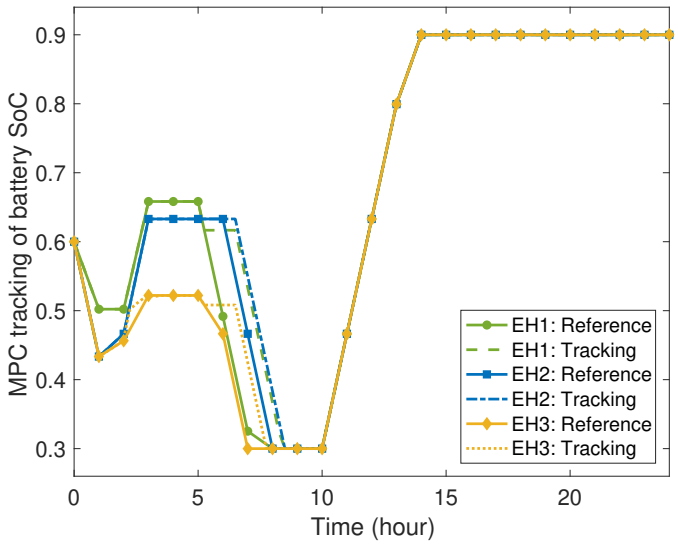

Figure 8.17: MPC performance, tracking the reference trajectories of battery energy level in a networked energy hub system.

computational complexity compared to other solution strategies, such as the scenario approach.

Although the reformulated robust design problem offers significant computational benefits, it may result in designs that are conservative. Accordingly, we propose a novel design framework which consists of iteration between a robust design problem and a validation problem. The two problems interact via a scalar auxiliary variable which acts as a virtual load-shedding term in the robust problem. It is adjusted dynamically using a bisection or stochastic gradient algorithm. This process addresses conservativeness while maintaining computational efficiency.

To further reduce design conservativeness, a novel cluster-based multi-policy formulation has been proposed and tested using publicly available data-sets for renewable generation and load. The simulation results demonstrate that the multi-cluster approach achieves less costly designs.

A strategy for achieving reliable and economic operation of energy hubs has also been considered. A two-level control structure which consists of higher-level day-ahead scheduling and lower-level on-line model predictive control has been proposed. This two-level operating strategy has been tested on isolated energy hubs as well as on networked energy hub systems. In the latter case, the energy sharing capability provided by the electrical and gas networks considerably reduces both the amount of gas purchased and the requirement for electrical load shedding.

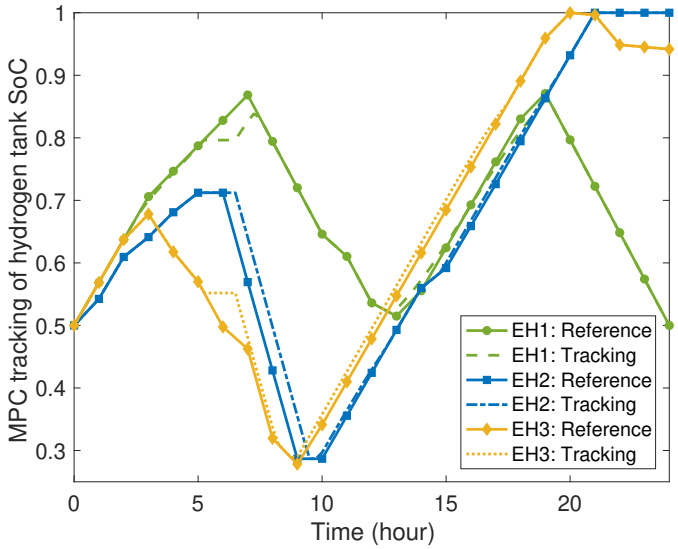

Figure 8.18: MPC performance, tracking the reference trajectories of hydrogen storage level in a networked energy hub system. (SoC=1 implies the hydrogen tank is at capacity.)

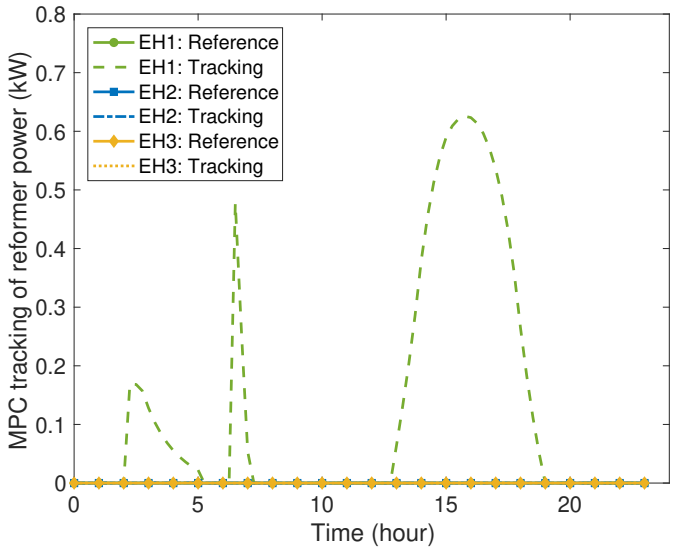

Figure 8.19: MPC performance, tracking the reference trajectories of reformer output in a networked energy hub system.

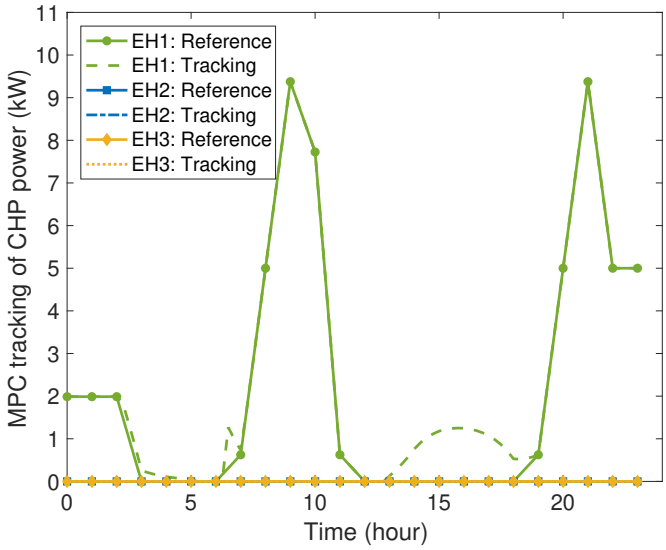

Figure 8.20: MPC performance, tracking the reference trajectories of CHP output in a networked energy hub system.

CHAPTER 9

Conclusions and Perspectives

In this dissertation, the technical challenges and opportunities faced by power systems, when shifting from centralized fossil-fuel-based generation to renewable resources and distributed energy resources (DERs) are investigated comprehensively. This dissertation addresses the critical issues of safety and stability of power systems that integrate substantial renewable DERs. Furthermore, this dissertation establishes a design process for next-generation off-grid energy systems, such as renewable-only microgrids and community-based energy hub systems. This chapter summarizes the key contributions of this dissertation and provides a discussion of future research directions.

9.1 Summary of Key Contributions and Findings

The first part of this dissertation (Chapters 2 to 5) concerns the safety and stability of power systems with the integration of variable renewable DERs. We summarize the contributions from control- and system-theoretic perspectives.

Chapters 2 and 3 analyze and quantify the impacts of uncertainties on system dynamics which enables efficient safety verification algorithms.

Chapter 2 establishes the theoretical development of the second-order trajectory sensitivity for general hybrid systems. For such complex systems, trajectory sensitivity analysis is a powerful tool for describing the perturbations of system trajectory in response to small variations in initial conditions and uncertain parameters. In this chapter, we establish the jump conditions describing the step change of second-order sensitivities at discrete (switching and state resetting) events and provide a pictorial interpretation of the mechanism. We also formulate the differential-algebraic equation (DAE) that governs second-order sensitivities over continuous pieces. These results together fully characterize second-order sensitivities for general hybrid systems, which recovers parts of the neglected information in the first-order analysis and hence improves the accuracy of

trajectory approximation.

Chapter 3 proposes an efficient method to compute numerical error bounds for the first-order trajectory approximation, based on the second-order trajectory sensitivities developed in Chapter 2. A theorem that quantifies the excursion of trajectories induced by uncertain initial conditions and external disturbances is improved and extended to DAE systems, using the mathematical tool of the logarithmic norm. This result provides a guaranteed over-approximation of the reach-set of nonlinear DAE systems. By combining this result with the efficient bound obtained from trajectory sensitivities, We provide a much less conservative reach-set estimate for DAE systems under uncertain initial conditions, uncertain parameters, and external disturbances.

Chapters 2 and 3 contribute to the fields of hybrid system analysis and nonlinear system analysis by forming the theoretical foundations for trajectory-based analysis. Various applications can be pursued, including uncertainty quantification, safety verification, and trajectory optimization. In particular, Chapter 2 considers the modeling and analysis of general hybrid systems, which is useful to capture a range of practical phenomena in power systems, including protection actions, control limits, and physical limits. The analysis reveals the behaviors of system trajectory when encountering discrete events and shows the improvements by incorporating higher-order information. Chapter 3 brings new perspectives to reach-set computation for nonlinear systems, by demonstrating the value of exploiting trajectory approximation in improving the efficiency and accuracy of reach-set computation.

Chapters 4 and 5 analyze the dynamics and stability of inverter-based power systems and propose two novel inverter control schemes.

Chapter 4 discusses how inverter-based resources should interact with other devices and the main grid in a distributed and autonomous manner. A novel inverter control scheme that can regulate the terminal bus voltage magnitude and the active power generation is proposed. This inverter control scheme can achieve autonomous switch between grid-connected operation and islanded operation, which is a desirable feature for microgrids. A detailed dynamic model for the inverter-based network is constructed, which captures the fast line dynamics and output filter dynamics, and lower-level cascaded voltage and current controllers. The steady-state behavior at both grid-connected and islanded modes is analyzed. Small-signal stability of the system is studied and the key contributing factors are characterized using a microgrid example.

Chapter 5 designs distributed and decentralized control laws for inverters in microgrids, which can explicitly certify safety constraints. A method based on barrier functions is extended to a distributed scheme. Distributed control laws are then computed for the

active and reactive power setpoints of inverters to certify the satisfaction of voltage limits during transients. Algorithmic construction of these control laws is proposed using sum-of-squares optimization. Numerical simulations are provided to illustrate the proposed method using a microgrid example. It is demonstrated that communication to neighboring subsystems in the distributed control scheme leads to lower minimum control efforts than the decentralized control scheme where only local states are used in the feedback law.

Chapters 4 and 5 contribute to the field of modeling and control of inverter-based power systems, which is of significant importance to transforming to future smart grids. Chapter 4 focuses on the detailed modeling of inverter-based systems and designs a novel inverter control scheme. This controller builds a basis for achieving future energy systems in the form of interconnected microgrids, which have the capability of autonomous islanding and re-connecting yet maintaining the safety and stability of the overall system. Chapter 5 identifies the importance of explicitly treating safety constraints for power systems with the increasing penetration of inverter-based resources. This work also recognizes the need of designing distributed and decentralized controllers for inverters due to the consideration that the current centralized control scheme is unable to handle hundreds of millions of control points in the future.

With the critical issues of safety and stability handled, the second part of this dissertation (Chapters 6 to 8) explores opportunities offered by renewable DERs. Chapter 6 exploits the collective reactive power capability of multiple DERs such as solar photovoltaics to balance the voltage at critical nodes across the distribution network. Distributed and decentralized Steinmetz-based controllers are presented. It is important to note that the control actions arising from one controller will interact with all the other controllers in the network. Such interactions could potentially be destabilizing. Therefore, the key contribution is in undertaking rigorous analysis to establish convergence guarantees for the proposed control schemes based on Banach fixed-point theory. Providing such convergence results ensures system robustness under realistic settings where parameter uncertainties and disturbances exist, and control and measurement delays remain. This work demonstrates the potential of exploiting DERs for providing grid services in future power systems.

Chapters 7 and 8 provide methods for design and operation of next-generation off-grid energy systems, including microgrids and energy hub systems.

Chapter 7 addresses the optimal capacity design problem for an islanded microgrid supplied purely by a wind turbine, solar panel, and battery system. The stochasticity of renewable generation is explicitly addressed by formulating the problem into a chance-

constrained optimization, which is then solved using a probabilistically robust method. The key contribution is the development of two approaches to reshaping the robust set, i.e., the cutting-based technique and the principal component analysis-based technique, which enable less conservative designs.

Chapter 8 takes an integrated view of optimized capacity design and operation of islanded energy hubs, which incorporate emerging DERs as well as energy storage devices to fully support the electricity and heat demand of a neighborhood. Both battery and hydrogen storage are incorporated. The problem is first expressed as a chance-constrained optimization and then reformulated as a robust counterpart problem, where the battery responds to stochastic renewable generation through a control policy. We propose an original algorithm, which iterates between the design problem and a validation process, by dynamically adjusting a scalar auxiliary variable indicating the reliability level. It is shown that the resulting design achieves a balanced trade-off between robustness and cost-efficiency. Finally, we demonstrate the potential for increasing the reliability of energy hub systems while decreasing operational costs by sharing energy between multiple energy hubs through electric and natural gas networks.

Chapters 7 and 8 are motivated by the vision that off-grid energy systems will play a greater role in the future. The world is experiencing fast advancement in smart grid technologies. However, a significant portion of households is still experiencing "energy poverty". These households have difficulty accessing modern forms of energy for cooking and heating and are often vulnerable to energy tariffs. This means that much greater effort is needed to reduce the cost of electricity so that access to convenient energy is available to all. Promoting renewable resources in energy systems will help achieve this, and the work in Chapters 7 and 8 demonstrate the potential for bringing electricity to rural areas and undeveloped countries - where it may be expensive or unfeasible to build traditional power system infrastructures - in a cost-efficient way.

9.2 Future Work

Several immediate extensions can be pursued based on the developments in this dissertation:

- Identify further applications of the theoretical results developed in Chapter 2 on the second-order trajectory sensitivities for general hybrid systems. One potential application scenario is to consider the physical and control limits that are appearing in inverter-based power systems.

- Extend the reach-set computation methods developed in Chapter 3 to hybrid systems where discrete events interact with the continuous dynamics. The difficulty lies in bounding the approximation error around the discrete events. The method could also be extended to incorporate probability distribution information.

- Incorporate the formulation of frequency-dependent reactances in the model developed in Chapter 4 for inverter-based power systems. Compare the modeling error with the case when frequency deviation is ignored.

- Replace the droop-based grid-forming model for inverters in Chapter 5 with more advanced inverter controllers. In particular, the controller developed in Chapter 4 can be considered.

- Generalize the proof given in Chapter 6 to a decoupled scheme, in order to reduce the number of conditions to be verified for a large number of controllers.

- Devise more general control policies for battery and hydrogen storage in the formulation of the chance-constrained optimization in Chapter 7 and Chapter 8.

With the aim of facilitating a successful transformation of power systems into future inverter-based smart grids, several future directions can be pursued based on the results in this dissertation.

- Much more effort is needed in understanding the fundamental dynamic properties of inverter-based power systems. System stability should be analyzed in both small-signal and large-signal senses.

- Efficient and scalable approaches that can certify the safety of networked microgrid systems need to be designed. Various types of safety constraints could be considered. Moreover, networked microgrid systems should have the capability to handle the discrete events of autonomous islanding and reconnection of multiple microgrids yet maintain the safety of the overall system.

BIBLIOGRAPHY

BIBLIOGRAPHY

[1] U.S. solar market insight 2020 year in review. Technical report, SEIA/Wood Mackenzie Power & Renewables, 2021.

[2] Erik Ela, Victor Diakov, Eduardo Ibanez, and Michael Heaney. Impacts of variability and uncertainty in solar photovoltaic generation at multiple timescales. Technical report, National Renewable Energy Lab.(NREL), Golden, CO (United States), 2013.

[3] Xiaojie Shi, Tom Key, and Aminul Huque. Can photovoltaic plants cause voltage flicker?–field measurement and screening. In *2019 IEEE 46th Photovoltaic Specialists Conference (PVSC)*, pages 1549–1555. IEEE, 2019.

[4] Frede Blaabjerg, Yongheng Yang, Dongsheng Yang, and Xiongfei Wang. Distributed power-generation systems and protection. *Proceedings of the IEEE*, 105(7):1311–1331, 2017.

[5] *Overview Map of the Danish Power Infrastructure in 1985 and 2015*. Accessed March 3rd, 2021. [Online]. Available: https://ens.dk/sites/ens.dk/files/Statistik/foer_efter_uk.pdf.

[6] Frede Blaabjerg, Remus Teodorescu, Marco Liserre, and Adrian V Timbus. Overview of control and grid synchronization for distributed power generation systems. *IEEE Transactions on Industrial Electronics*, 53(5):1398–1409, 2006.

[7] Federico Milano, Florian Dörfler, Gabriela Hug, David J Hill, and Gregor Verbič. Foundations and challenges of low-inertia systems. In *2018 Power Systems Computation Conference*, pages 1–25. IEEE, 2018.

[8] Petter Nilsson, Omar Hussien, Ayca Balkan, Yuxiao Chen, Aaron D Ames, Jessy W Grizzle, Necmiye Ozay, Huei Peng, and Paulo Tabuada. Correct-by-construction adaptive cruise control: Two approaches. *IEEE Transactions on Control Systems Technology*, 24(4):1294–1307, 2015.

[9] Aaron D Ames, Xiangru Xu, Jessy W Grizzle, and Paulo Tabuada. Control barrier function based quadratic programs for safety critical systems. *IEEE Transactions on Automatic Control*, 62(8):3861–3876, 2016.

[10] Yuxiao Chen, James Anderson, Karanjit Kalsi, Aaron D Ames, and Steven H Low. Safety-critical control synthesis for network systems with control barrier functions

and assume-guarantee contracts. *IEEE Transactions on Control of Network Systems*, 8(1):487–499, 2020.

[11] Sijia Geng and Ian A Hiskens. Reach-set estimation for DAE systems under uncertainty and disturbances using trajectory sensitivity and logarithmic norm. *IFAC-PapersOnLine*, 53(2):1955–1961, 2020.

[12] Xin Chen, Erika Abraham, and Sriram Sankaranarayanan. Taylor model flowpipe construction for non-linear hybrid systems. In *Proceedings of the 33rd IEEE Real-Time Systems Symposium*, pages 183–192, San Juan, PR, USA, December 2012.

[13] Thomas A Henzinger, Pei-Hsin Ho, and Howard Wong-Toi. Algorithmic analysis of nonlinear hybrid systems. *IEEE Transactions on Automatic Control*, 43(4):540–554, April 1998.

[14] Ian M Mitchell, Alexandre M Bayen, and Claire J Tomlin. A time-dependent Hamilton-Jacobi formulation of reachable sets for continuous dynamic games. *IEEE Transactions on Automatic Control*, 50(7):947–957, July 2005.

[15] Joseph K Scott and Paul I Barton. Bounds on the reachable sets of nonlinear control systems. *Automatica*, 49(1):93–100, January 2013.

[16] Matthias Althoff and Bruce H Krogh. Reachability analysis of nonlinear differential-algebraic systems. *IEEE Transactions on Automatic Control*, 59(2):371–383, February 2014.

[17] Neal Balu, Timothy Bertram, Anjan Bose, Vladimir Brandwajn, Gerry Cauley, David Curtice, Aziz Fouad, Lester Fink, Mark G Lauby, Bruce F Wollenberg, et al. On-line power system security analysis. *Proceedings of the IEEE*, 80(2):262–282, 1992.

[18] Michele Di Santo, Alfredo Vaccaro, Domenico Villacci, and Eugenio Zimeo. A distributed architecture for online power systems security analysis. *IEEE Transactions on Industrial Electronics*, 51(6):1238–1248, 2004.

[19] Ian A Hiskens and Jassim Alseddiqui. Sensitivity, approximation, and uncertainty in power system dynamic simulation. *IEEE Transactions on Power Systems*, 21(4):1808–1820, November 2006.

[20] Franco Blanchini. Set invariance in control. *Automatica*, 35(11):1747–1767, 1999.

[21] Stephen Prajna. Barrier certificates for nonlinear model validation. *Automatica*, 42(1):117–126, 2006.

[22] Peter Wieland and Frank Allgöwer. Constructive safety using control barrier functions. *IFAC Proceedings Volumes*, 40(12):462–467, 2007.

[23] Prabha Kundur, John Paserba, Venkat Ajjarapu, Göran Andersson, Anjan Bose, Claudio Canizares, Nikos Hatziargyriou, David Hill, Alex Stankovic, Carson Taylor, et al. Definition and classification of power system stability ieee/cigre joint task force

on stability terms and definitions. *IEEE Transactions on Power Systems*, 19(3):1387–1401, 2004.

[24] Prabha Kundur. *Power System Stability and Control*. McGraw-Hill, New York, NY, USA, 1994.

[25] Nikos Hatziargyriou, Jovica Milanovic, Claudia Rahmann, Venkataramana Ajjarapu, Claudio Canizares, Istvan Erlich, David Hill, Ian A Hiskens, Innocent Kamwa, Bikash Pal, et al. Definition and classification of power system stability revisited & extended. *IEEE Transactions on Power Systems*, 36(4):3271–3281, 2020.

[26] Amirnaser Yazdani and Reza Iravani. *Voltage-Sourced Converters in Power Systems: Modeling, Control, and Applications*. John Wiley & Sons, Hoboken, NJ, USA, 2010.

[27] Mohammad N Marwali and Ali Keyhani. Control of distributed generation systems-Part I: Voltages and currents control. *IEEE Transactions on power electronics*, 19(6):1541–1550, 2004.

[28] Md Rasheduzzaman, Jacob A Mueller, and Jonathan W Kimball. Reduced-order small-signal model of microgrid systems. *IEEE Transactions on Sustainable Energy*, 6(4):1292–1305, 2015.

[29] Nagaraju Pogaku, Milan Prodanovic, and Timothy C Green. Modeling, analysis and testing of autonomous operation of an inverter-based microgrid. *IEEE Transactions on power electronics*, 22(2):613–625, March 2007.

[30] Matthew Surprenant, Ian A Hiskens, and Giri Venkataramanan. Phase locked loop control of inverters in a microgrid. In *2011 IEEE Energy Conversion Congress and Exposition*, pages 667–672. IEEE, 2011.

[31] Usman Bashir Tayab, Mohd Azrik Bin Roslan, Leong Jenn Hwai, and Muhammad Kashif. A review of droop control techniques for microgrid. *Renewable and Sustainable Energy Reviews*, 76:717–727, 2017.

[32] Pertti Järventausta, Sami Repo, Antti Rautiainen, and Jarmo Partanen. Smart grid power system control in distributed generation environment. *Annual Reviews in Control*, 34(2):277–286, 2010.

[33] Sunetra Chowdhury, Shyama P Chowdhury, and Peter Crossley. *Microgrids and Active Distribution Networks*. The Institution of Engineering and Technology, London, United Kingdom, 2009.

[34] Pragasen Pillay and Marubini Manyage. Definitions of voltage unbalance. *IEEE Power Engineering Review*, 21(5):50–51, May 2001.

[35] William H Kersting and W Howard Phillips. Phase frame analysis of the effects of voltage unbalance on induction machines. *IEEE Transactions on Industry Applications*, 33(2):415–420, March/April 1997.

[36] San-Yi Lee and Chi-Jui Wu. On-line reactive power compensation schemes for unbalanced three phase four wire distribution feeders. *IEEE Transactions on Power Delivery*, 8(4):1958–1965, October 1993.

[37] Mukwanga W Siti, Dan Valentin Nicolae, Adisa A Jimoh, and Abhisek Ukil. Reconfiguration and load balancing in the LV and MV distribution networks for optimal performance. *IEEE Transactions on Power Delivery*, 22(4):2534–2540, October 2007.

[38] Félix Quintela, Jesusa Arévalo, Roberto Redondo, and Norberto Melchor. Four-wire three-phase load balancing with static VAr compensators. *International Journal of Electrical Power & Energy Systems*, 33(3):562–568, March 2011.

[39] Leandro R Araujo, Débora Penido, Sandoval Carneiro, and José Luiz Pereira. A three-phase optimal power-flow algorithm to mitigate voltage unbalance. *IEEE Transactions on Power Delivery*, 28(4):2394–2402, October 2013.

[40] Sijia Geng, Maria Vrakopoulou, and Ian A Hiskens. Optimal capacity design and operation of energy hub systems. *Proceedings of the IEEE*, 108(9):1475–1495, September 2020.

[41] Stephen Boyd and Lieven Vandenberghe. *Convex Optimization*. Cambridge University Press, Cambridge, U.K., 2004.

[42] Giuseppe C Calafiore and Marco C Campi. The scenario approach to robust control design. *IEEE Transactions on Automatic Control*, 51(5):742–753, May 2006.

[43] Hui Ye, Anthony N Michel, and Ling Hou. Stability theory for hybrid dynamical systems. *IEEE Transactions on Automatic Control*, 43(4):461–474, April 1998.

[44] Ian A Hiskens. Analysis tools for power systems-contending with nonlinearities. *Proceedings of the IEEE*, 83(11):1573–1587, November 1995.

[45] Roger W Brockett. Hybrid models for motion control systems. In *Essays on Control: Perspectives in the Theory and its Applications*, pages 29–53. Birkhäuser, 1993.

[46] Arjan J van der Schaft and Johannes Maria Schumacher. *An Introduction to Hybrid Dynamical Systems*. Springer, London, U.K., 2000.

[47] Christine Chevallereau, Gabriel Abba, Yannick Aoustin, Franck Plestan, Eric Westervelt, Carlos Canudas De Wit, and Jessy Grizzle. Rabbit: A testbed for advanced control theory. *IEEE Control Systems Magazine*, 23(5):57–79, October 2003.

[48] MA Pai. *Energy Function Analysis for Power System Stability*. Kluwer, Norwell, MA, USA, 1989.

[49] Stefan Pettersson. *Analysis and design of hybrid systems*. PhD thesis, Chalmers University of Technology, Gothenburg, Sweden, 1999.

[50] Stefan Kowalewski. Introduction to the analysis and verification of hybrid systems. In *Modelling, Analysis, and Design of Hybrid Systems*, pages 153–171. Springer, 2002.

[51] Ian A Hiskens and MA Pai. Trajectory sensitivity analysis of hybrid systems. *IEEE Transactions on Circuits and Systems I: Fundamental Theory and Applications*, 47(2):204–220, February 2000.

[52] Paul M Frank. *Introduction to System Sensitivity Theory*. Academic, New York, NY, USA, 1978.

[53] PV Kokotovic and RS Rutman. Sensitivity of automatic control systems (survey). *Automation and Remote Control*, 26:727–749, April 1965.

[54] R Tomović and M Vukobratovic. *General Sensitivity Theory*. Elsevier, New York, NY, USA, 1972.

[55] Hassan K Khalil. *Nonlinear Systems*. Prentice-Hall, Upper Saddle River, NJ, USA, 3rd ed edition, 2002.

[56] Jose B Cruz Jr. *System Sensitivity Analysis*. Dowden, Hutchinson and Ross, Stroudsburg, PA, USA, 1973.

[57] Ian A Hiskens. Trajectory approximation near the stability boundary. In *Proceedings of IEEE International Symposium on Circuits and Systems*, pages 533–536, Paris, France, May/Jun 2010.

[58] Hong Zhang, Shrirang Abhyankar, Emil Constantinescu, and Mihai Anitescu. Discrete adjoint sensitivity analysis of hybrid dynamical systems with switching. *IEEE Transactions on Circuits and Systems I: Regular Papers*, 64(5):1247–1259, May 2017.

[59] Lei Tang and James McCalley. Trajectory sensitivities: Applications in power systems and estimation accuracy refinement. In *Proceedings of IEEE Power & Energy Society General Meeting*, pages 1–5, Vancouver, BC, Canada, July 2013.

[60] Hyungjin Choi, Peter J Seiler, and Sairaj V Dhople. Propagating uncertainty in power-system DAE models with semidefinite programming. *IEEE Transactions on Power Systems*, 32(4):3146–3156, July 2017.

[61] Hyungjin Choi, Peter J Seiler, and Sairaj V Dhople. Propagating uncertainty in power flow with the alternating direction method of multipliers. *IEEE Transactions on Power Systems*, 33(4):4124–4133, July 2018.

[62] Sijia Geng and Ian A Hiskens. Jump conditions for second-order trajectory sensitivities at events. In *Proceedings of IEEE International Symposium on Circuits and Systems*, pages 1–5, Florence, Italy, May 2018.

[63] Alexandre Donzé and Oded Maler. Systematic simulation using sensitivity analysis. In *Proceedings of International Workshop on Hybrid Systems: Computation and Control*, pages 174–189, 2007.

[64] Ian A Hiskens and Bo Gong. Voltage stability enhancement via model predictive control of load. *Intelligent Automation & Soft Computing*, 12(1):117–124, 2006.

[65] Marek Zima and Göran Andersson. Model predictive control employing trajectory sensitivities for power systems applications. In *Proceedings of the 44th IEEE Conference on Decision and Control*, pages 4452–4456, Seville, Spain, December 2005.

[66] Lei Tang and James McCalley. Two-stage load control for severe under-frequency conditions. *IEEE Transactions on Power Systems*, 31(3):1943–1953, May 2015.

[67] Alessandro Saccon, Nathan van de Wouw, and Henk Nijmeijer. Sensitivity analysis of hybrid systems with state jumps with application to trajectory tracking. In *Proceedings of the 53rd IEEE Conference on Decision and Control*, pages 3065–3070, Los Angeles, CA, USA, 2014.

[68] Katja Daniela Mombaur. *Stability optimization of open-loop controlled walking robots*. PhD thesis, Heidelberg University, Heidelberg, Germany, 2001.

[69] A Zamora-Cárdenas and Claudio R Fuerte-Esquivel. Multi-parameter trajectory sensitivity approach for location of series-connected controllers to enhance power system transient stability. *Electric Power Systems Research*, 80(9):1096–1103, September 2010.

[70] Amin Nasri, Robert Eriksson, and Mehrdad Ghandhari. Using trajectory sensitivity analysis to find suitable locations of series compensators for improving rotor angle stability. *Electric Power Systems Research*, 111:1–8, June 2014.

[71] Mark J Laufenberg and MA Pai. A new approach to dynamic security assessment using trajectory sensitivities. In *Proceedings of the 20th International Conference on Power Industry Computer Applications*, pages 272–277, Columbus, OH, USA, May/June 1997.

[72] T.B. Nguyen, M.A. Pai, and Ian A Hiskens. Sensitivity approaches for direct computation of critical parameters in a power system. *International Journal of Electrical Power & Energy Systems*, 24(5):337–343, 2002.

[73] Mevludin Glavic and Thierry Van Cutsem. Wide-area detection of voltage instability from synchronized phasor measurements. Part I: Principle. *IEEE Transactions on Power Systems*, 24(3):1408–1416, August 2009.

[74] Guanji Hou and Vijay Vittal. Trajectory sensitivity based preventive control of voltage instability considering load uncertainties. *IEEE Transactions on Power Systems*, 27(4):2280–2288, November 2012.

[75] Lei Tang and Wei Sun. An automated transient stability constrained optimal power flow based on trajectory sensitivity analysis. *IEEE Transactions on Power Systems*, 32(1):590–599, January 2016.

[76] Marek Zima and Göran Andersson. Stability assessment and emergency control method using trajectory sensitivities. In *Proceedings of IEEE PowerTech Conference*, volume 2, page 7, Bologna, Italy, June 2003.

[77] KN Shubhanga and AM Kulkarni. Determination of effectiveness of transient stability controls using reduced number of trajectory sensitivity computations. *IEEE Transactions on Power Systems*, 19(1):473–482, February 2004.

[78] Ian A Hiskens and MA Pai. Power system applications of trajectory sensitivities. In *Proceedings of IEEE Power Engineering Society Winter Meeting*, volume 2, pages 1200–1205, New York, NY, USA, January 2002.

[79] Ian A Hiskens. Nonlinear dynamic model evaluation from disturbance measurements. *IEEE Transactions on Power Systems*, 16(4):702–710, November 2001.

[80] Max D Gunzburger. *Perspectives in Flow Control and Optimization*. SIAM, Philadelphia, PA, USA, 2002.

[81] Wendell Fleming. *Functions of Several Variables*. Springer-Verlag, New York, NY, USA, 1977.

[82] Alessandro Abate, Alessandro D'Innocenzo, Maria Domenica Di Benedetto, and Shankar Sastry. Understanding deadlock and livelock behaviors in hybrid control systems. *Nonlinear Analysis: Hybrid Systems*, 3(2):150–162, May 2009.

[83] Michael S Branicky, Vivek S Borkar, and Sanjoy K Mitter. A unified framework for hybrid control: Model and optimal control theory. *IEEE Transactions on Automatic Control*, 43(1):31–45, January 1998.

[84] Soumya Kundu, Sijia Geng, Sai Pushpak Nandanoori, Karan Kalsi, and Ian A Hiskens. Distributed barrier certificates for safe operation of inverter-based microgrids. In *Proceedings of IEEE American Control Conference*, pages 1042–1047, Philadelphia, PA, USA, July 2019.

[85] Sijia Geng and Ian A Hiskens. Second-order trajectory sensitivity analysis of hybrid systems. *IEEE Transactions on Circuits and Systems I: Regular Papers*, 66(5):1922–1934, May 2019.

[86] Bai Xue, Martin Fränzle, and Peter Nazier Mosaad. Just scratching the surface: Partial exploration of initial values in reach-set computation. In *Proceedings of the 56th IEEE Conference on Decision and Control*, pages 1769–1775, Melbourne, Australia, December 2017.

[87] Pierre-Jean Meyer, Samuel Coogan, and Murat Arcak. Sampled-data reachability analysis using sensitivity and mixed-monotonicity. *IEEE Control Systems Letters*, 2(4):761–766, October 2018.

[88] Germund Dahlquist. *Stability and error bounds in the numerical integration of ordinary differential equations*. PhD thesis, Stockholm University, Stockholm, Sweden, 1958.

[89] Eduardo D Sontag. Contractive systems with inputs. In *Perspectives in Mathematical System Theory, Control, and Signal Processing*, pages 217–228. Springer, 2010.

[90] John Maidens and Murat Arcak. Reachability analysis of nonlinear systems using matrix measures. *IEEE Transactions on Automatic Control*, 60(1):265–270, January 2015.

[91] Valerii Nikolaevich Afanasiev, V Kolmanovskii, and VR Nosov. *Mathematical Theory of Control Systems Design*, volume 341. Springer, Dordrecht, Netherlands, 2013.

[92] Gustaf Söderlind. The logarithmic norm. history and modern theory. *BIT Numerical Mathematics*, 46(3):631–652, 2006.

[93] Uros Kerin, Chris Heyde, Rainer Krebs, and Edwin Lerch. Real-time dynamic security assessment of power grids. *The European Physical Journal Special Topics*, 223(12):2503–2516, September 2014.

[94] Gerald B Folland. Higher-order derivatives and Taylor's formula in several variables. *Preprint*, pages 1–4, 2005.

[95] John M Lee. *Introduction to Smooth Manifolds*. Springer, New York, NY, USA, 2012.

[96] Shuyou Yu, Christoph Maier, Hong Chen, and Frank Allgöwer. Tube MPC scheme based on robust control invariant set with application to Lipschitz nonlinear systems. *Systems & Control Letters*, 62(2):194–200, February 2013.

[97] Nan Li, Ilya V Kolmanovsky, and Anouck Girard. A reference governor for nonlinear systems with disturbance inputs based on logarithmic norms and quadratic programming. *IEEE Transactions on Automatic Control*, 65(7):3207–3214, July 2020.

[98] Steven G Krantz and Harold R Parks. *The Implicit Function Theorem: History, Theory, and Applications*. Birkhäuser, Boston, MA, USA, 2003.

[99] Werner C Rheinboldt. Local mapping relations and global implicit function theorems. *Transactions American Mathematical Society*, 138:183–198, April 1969.

[100] James A Hansen and Cecile Penland. Efficient approximate techniques for integrating stochastic differential equations. *Monthly Weather Review*, 134(10):3006–3014, October 2006.

[101] Johannes Schiffer, Daniele Zonetti, Romeo Ortega, Aleksandar M Stanković, Tevfik Sezi, and Jörg Raisch. A survey on modeling of microgrids—from fundamental physics to phasors and voltage sources. *Automatica*, 74:135–150, 2016.

[102] M Ganjian-Aboukheili, Majid Shahabi, Qobad Shafiee, and Josep M Guerrero. Seamless transition of microgrids operation from grid-connected to islanded mode. *IEEE Transactions on Smart Grid*, 11(3):2106–2114, May 2020.

[103] Yasser Abdel-Rady I Mohamed and Amr A Radwan. Hierarchical control system for robust microgrid operation and seamless mode transfer in active distribution systems. *IEEE Transactions on Smart Grid*, 2(2):352–362, 2011.

[104] Seyed Mahdi Ashabani and Yasser Abdel-Rady I Mohamed. A flexible control strategy for grid-connected and islanded microgrids with enhanced stability using nonlinear microgrid stabilizer. *IEEE Transactions on Smart Grid*, 3(3):1291–1301, 2012.

[105] Tine L Vandoorn, Bart Meersman, Jeroen DM De Kooning, and Lieven Vandevelde. Transition from islanded to grid-connected mode of microgrids with voltage-based droop control. *IEEE Transactions on Power Systems*, 28(3):2545–2553, 2013.

[106] Ian A Hiskens and Eric M Fleming. Control of inverter-connected sources in autonomous microgrids. In *Proceedings of American Control Conference*, pages 586–590, Seattle, WA, USA, June 2008.

[107] Milan Prodanović and Timothy C Green. Control and filter design of three-phase inverters for high power quality grid connection. *IEEE Transactions on Power Electronics*, 18(1):373–380, 2003.

[108] Magdi S Mahmoud, S Azher Hussain, and Mohammad Ali Abido. Modeling and control of microgrid: An overview. *Journal of the Franklin Institute*, 351(5):2822–2859, May 2014.

[109] John W Simpson-Porco, Florian Dörfler, and Francesco Bullo. Synchronization and power sharing for droop-controlled inverters in islanded microgrids. *Automatica*, 49(9):2603–2611, September 2013.

[110] Johannes Schiffer, Romeo Ortega, Alessandro Astolfi, Jörg Raisch, and Tevfik Sezi. Conditions for stability of droop-controlled inverter-based microgrids. *Automatica*, 50(10):2457–2469, October 2014.

[111] E Barklund, Nagaraju Pogaku, Milan Prodanovic, C Hernandez-Aramburo, and Tim C Green. Energy management in autonomous microgrid using stability-constrained droop control of inverters. *IEEE Transactions on Power Electronics*, 23(5):2346–2352, September 2008.

[112] Juan C Vasquez, Josep M Guerrero, Mehdi Savaghebi, Joaquin Eloy-Garcia, and Remus Teodorescu. Modeling, analysis, and design of stationary-reference-frame droop-controlled parallel three-phase voltage source inverters. *IEEE Transactions on Industrial Electronics*, 60(4):1271–1280, April 2013.

[113] Alexander Kusko and Marc T Thompson. *Power Quality in Electrical Systems*. McGraw-Hill, New York, NY, USA, 2007.

[114] Y. Xu, C. Liu, K. P. Schneider, F. K. Tuffner, and D. T. Ton. Microgrids for service restoration to critical load in a resilient distribution system. *IEEE Transactions on Smart Grid*, 9(1):426–437, January 2018.

[115] Eduardo D Sontag. A "universal" construction of Artstein's theorem on nonlinear stabilization. *Systems & Control Letters*, 13(2):117–123, August 1989.

[116] Stephen Prajna, Ali Jadbabaie, and George J Pappas. A framework for worst-case and stochastic safety verification using barrier certificates. *IEEE Transactions on Automatic Control*, 52(8):1415–1428, August 2007.

[117] Xiangru Xu, Jessy W Grizzle, Paulo Tabuada, and Aaron D Ames. Correctness guarantees for the composition of lane keeping and adaptive cruise control. *IEEE Transactions on Automation Science and Engineering*, 15(3):1216–1229, July 2018.

[118] Thomas Gurriet, Andrew Singletary, Jacob Reher, Laurent Ciarletta, Eric Feron, and Aaron Ames. Towards a framework for realizable safety critical control through active set invariance. In *Proceedings of the 9th ACM/IEEE International Conference on Cyber-Physical Systems*, pages 98–106, Porto, Portugal, April 2018.

[119] Aaron D Ames, Xiangru Xu, Jessy W Grizzle, and Paulo Tabuada. Control barrier function based quadratic programs for safety critical systems. *IEEE Transactions on Automatic Control*, 62(8):3861–3876, August 2017.

[120] Li Wang, Dongkun Han, and Magnus Egerstedt. Permissive barrier certificates for safe stabilization using sum-of-squares. In *Proceedings of American Control Conference*, pages 585–590, Milwaukee, WI, USA, June 2018.

[121] Aleksandr Mikhailovich Lyapunov. The general problem of the stability of motion. *International Journal of Control*, 55(3):531–534, November 1992.

[122] Roberto Genesio, Michele Tartaglia, and Antonio Vicino. On the estimation of asymptotic stability regions: State of the art and new proposals. *IEEE Transactions on Automatic Control*, 30(8):747–755, August 1985.

[123] Marian Anghel, Milano Milano, and Antonis Papachristodoulou. Algorithmic construction of Lyapunov functions for power system stability analysis. *IEEE Transactions on Circuits and Systems I: Regular Papers*, 60(9):2533–2546, September 2013.

[124] Zachary William Jarvis-Wloszek. *Lyapunov based analysis and controller synthesis for polynomial systems using sum-of-squares optimization*. PhD thesis, University of California, Berkeley, CA, USA, 2003.

[125] Pablo A Parrilo. *Structured Semidefinite Programs and Semialgebraic Geometry Methods in Robustness and Optimization*. PhD thesis, Caltech, Pasadena, CA, USA, 2000.

[126] Weehong Tan. *Nonlinear control analysis and synthesis using sum-of-squares programming*. PhD thesis, University of California, Berkeley, CA, USA, 2006.

[127] Antonis Papachristodoulou, James Anderson, Giorgio Valmorbida, Stephen Prajna, Pete Seiler, and Pablo Parrilo. *SOSTOOLS: Sum of squares optimization toolbox for MATLAB*, 2013.

[128] Jos F Sturm. Using SeDuMi 1.02, a MATLAB toolbox for optimization over symmetric cones. *Optimization Methods and Software*, 11-12:625–653, Dec. 1999. Software available at http://fewcal.kub.nl/sturm/software/sedumi.html.

[129] Mihai Putinar. Positive polynomials on compact semi-algebraic sets. *Indiana University Mathematics Journal*, 42(3):969–984, 1993.

[130] Jean Bernard Lasserre. *Moments, Positive Polynomials and Their Applications*. Imperial College Press, London, U.K., 2009.

[131] Ernane AA Coelho, Porfirio C Cortizo, and Pedro FD Garcia. Small-signal stability for parallel-connected inverters in stand-alone AC supply systems. *IEEE Transactions on Industry Applications*, 38(2):533–542, March/April 2002.

[132] Tulga Ersal, Changsun Ahn, Ian A Hiskens, Huei Peng, and Jeffrey L Stein. Impact of controlled plug-in EVs on microgrids: A military microgrid example. In *Proceedings of Power & Energy Society General Meeting*, pages 1–7, Detroit, MI, USA, July 2011.

[133] Guido Cavraro, Saverio Bolognani, Ruggero Carli, and Sandro Zampieri. The value of communication in the voltage regulation problem. In *Proceedings of the 55th IEEE Conference on Decision and Control*, pages 5781–5786, Las Vegas, NV, USA, December 2016.

[134] M Tavakoli Bina and A Kashefi. Three-phase unbalance of distribution systems: Complementary analysis and experimental case study. *International Journal of Electrical Power & Energy Systems*, 33(4):817–826, May 2011.

[135] Annette Von Jouanne and Basudeb Banerjee. Assessment of voltage unbalance. *IEEE Transactions on Power Delivery*, 16(4):782–790, October 2001.

[136] O Jordi, L Sainz, and M Chindris. Steinmetz system design under unbalanced conditions. *European Transactions on Electrical Power*, 12(4):283–290, July/August 2002.

[137] Mengqi Yao, Ian A Hiskens, and Johanna L Mathieu. Mitigating voltage unbalance using distributed solar photovoltaic inverters. *IEEE Transactions on Power Systems*, 36(3):2642–2651, May 2021.

[138] Charles H. Edwards. *Advanced Calculus of Several Variables*. Academic Press, New York, NY, USA, 1973.

[139] Andrey Bernstein, Cong Wang, Emiliano Dall'Anese, Jean-Yves Le Boudec, and Changhong Zhao. Load flow in multiphase distribution networks: Existence, uniqueness, non-singularity and linear models. *IEEE Transactions on Power Systems*, 33(6):5832–5843, November 2018.

[140] Kshitij Girigoudar, Daniel K Molzahn, and Line A Roald. On the relationships among different voltage unbalance definitions. In *Proceedings of North American Power Symposium*, Wichita, KS, USA, October 2019.

[141] J Duncan Glover, Mulukutla S Sarma, and Thomas Overbye. *Power System Analysis and Design*. Cengage Learning, Boston, MA, USA, 2012.

[142] Krishnamurthy Dvijotham, Hung Nguyen, and Konstantin Turitsyn. Solvability regions of affinely parameterized quadratic equations. *IEEE Control Systems Letters*, 2(1):25–30, January 2018.

[143] William H Kersting. Radial distribution test feeders. *IEEE Transactions on Power Systems*, 6(3):975–985, August 1991.

[144] *IEEE PES Distribution Systems Analysis Subcommittee Test Feeders*. Accessed October 3rd, 2020. [Online]. Available: https://site.ieee.org/pes-testfeeders/resources/.

[145] Cong Wang, Andrey Bernstein, Jean-Yves Le Boudec, and Mario Paolone. Explicit conditions on existence and uniqueness of load-flow solutions in distribution networks. *IEEE Transactions on Smart Grid*, 9(2):953–962, March 2016.

[146] Emiliano Dall'Anese and Andrea Simonetto. Optimal power flow pursuit. *IEEE Transactions on Smart Grid*, 9(2):942–952, March 2018.

[147] Víctor Sánchez, Juan M Ramirez, and Gerardo Arriaga. Optimal sizing of a hybrid renewable system. In *Proceedings of IEEE International Conference on Industrial Technology*, pages 949–954, Valparaíso, Chile, March 2010.

[148] Chen Yuan, Mahesh S Illindala, and Amrit S Khalsa. Co-optimization scheme for distributed energy resource planning in community microgrids. *IEEE Transactions on Sustainable Energy*, 8(4):1351–1360, October 2017.

[149] Mohammad B Shadmand and Robert S Balog. Multi-objective optimization and design of photovoltaic-wind hybrid system for community smart DC microgrid. *IEEE Transactions on Smart Grid*, 5(5):2635–2643, September 2014.

[150] Rodolfo Dufo-López, José L Bernal-Agustín, José M Yusta-Loyo, José A Domínguez-Navarro, Ignacio J Ramírez-Rosado, Juan Lujano, and Ismael Aso. Multi-objective optimization minimizing cost and life cycle emissions of stand-alone PV–wind–diesel systems with batteries storage. *Applied Energy*, 88(11):4033–4041, November 2011.

[151] Masoud Sharafi and Tarek Y ElMekkawy. Multi-objective optimal design of hybrid renewable energy systems using PSO-simulation based approach. *Renewable Energy*, 68:67–79, August 2014.

[152] Yingyi Hong and Ruochen Lian. Optimal sizing of hybrid wind/PV/diesel generation in a stand-alone power system using Markov-based genetic algorithm. *IEEE Transactions on Power Delivery*, 27(2):640–647, April 2012.

[153] Li Guo, Wenjian Liu, Bingqi Jiao, Bowen Hong, and Chengshan Wang. Multi-objective stochastic optimal planning method for stand-alone microgrid system. *IET Generation, Transmission & Distribution*, 8(7):1263–1273, July 2014.

[154] Hui Zhang and Pu Li. Chance constrained programming for optimal power flow under uncertainty. *IEEE Transactions on Power Systems*, 26(4):2417–2424, November 2011.

[155] Maria Vrakopoulou, Kostas Margellos, John Lygeros, and Göran Andersson. Probabilistic guarantees for the N-1 security of systems with wind power generation. In *Reliability and Risk Evaluation of Wind Integrated Power Systems*, pages 59–73. Springer, March 2013.

[156] Kostas Margellos, Paul Goulart, and John Lygeros. On the road between robust optimization and the scenario approach for chance constrained optimization problems. *IEEE Transactions on Automatic Control*, 59(8):2258–2263, August 2014.

[157] Ian Jolliffe. *Principal Component Analysis*. Springer, Berlin, Germany, 2011.

[158] Xuejiao Ma, Yu Jin, and Qingli Dong. A generalized dynamic fuzzy neural network based on singular spectrum analysis optimized by brain storm optimization for short-term wind speed forecasting. *Applied Soft Computing*, 54:296–312, March 2017.

[159] Julio Cesar Stacchini de Souza, Tatiana Mariano Lessa Assis, and Bikash Chandra Pal. Data compression in smart distribution systems via singular value decomposition. *IEEE Transactions on Smart Grid*, 8(1):275–284, January 2017.

[160] Joseph Warrington, Paul J Goulart, Sébastien Mariéthoz, and Manfred Morari. Robust reserve operation in power systems using affine policies. In *Proceedings of the 51st IEEE Conference on Decision and Control*, pages 1111–1117, Maui, HI, USA, 2012.

[161] Gordon J Dalton, David A Lockington, and Tom E Baldock. Feasibility analysis of stand-alone renewable energy supply options for a large hotel. *Renewable Energy*, 33(7):1475–1490, July 2008.

[162] SM Hakimi and SM Moghaddas-Tafreshi. Optimal sizing of a stand-alone hybrid power system via particle swarm optimization for Kahnouj area in south-east of Iran. *Renewable Energy*, 34(7):1855–1862, July 2009.

[163] *BPA Balancing Authority Load and Total Wind Generation: 2007-2019*. Accessed September 3rd, 2019. [Online]. Available: https://transmission.bpa.gov/Business/Operations/Wind/.

[164] *Solar Power Data for Integration Studies*, 2018. [Online]. Available: https://www.nrel.gov/grid/solar-power-data.html.

[165] Rodolfo Dufo-López, José L Bernal-Agustín, and Franklin Mendoza. Design and economical analysis of hybrid PV-wind systems connected to the grid for the intermittent production of hydrogen. *Energy Policy*, 37(8):3082–3095, August 2009.

[166] Alan Goodrich, Ted James, and Michael Woodhouse. Residential, commercial, and utility-scale photovoltaic (PV) system prices in the united states: current drivers and cost-reduction opportunities. Technical Report NREL/TP-6A20-53347, National Renewable Energy Lab, Golden, CO, USA, 2012.

[167] *Transparent Cost Database*. document DOE/GO-102016-4904, 2012. [Online]. Available: http://en.openei.org/apps/ TCDB/.

[168] Martin Geidl and Göran Andersson. Optimal power flow of multiple energy carriers. *IEEE Transactions on Power Systems*, 22(1):145–155, February 2007.

[169] R Frik and P Favre-Perrod. Proposal for a multifunctional energy bus and its interlink with generation and consumption. Master's thesis, Power Systems and High Voltage Laboratories, ETH, Zürich, Switzerland, 2004.

[170] Thilo Krause, Göran Andersson, Klaus Fröhlich, and Alfredo Vaccaro. Multiple-energy carriers: modeling of production, delivery, and consumption. *Proceedings of the IEEE*, 99(1):15–27, January 2011.

[171] Mads Almassalkhi and Ian A Hiskens. Optimization framework for the analysis of large-scale networks of energy hubs. In *Proceedings of Power Systems Computation Conference*, Stockholm, Sweden, August 2011.

[172] Manuel Jesús Vasallo, José Manuel Andújar, Covadonga García, and José Javier Brey. A methodology for sizing backup fuel-cell/battery hybrid power systems. *IEEE Transactions on Industrial Electronics*, 57(6):1964–1975, June 2009.

[173] James Luedtke, Shabbir Ahmed, and George L Nemhauser. An integer programming approach for linear programs with probabilistic constraints. *Mathematical Programming*, 122(2):247–272, April 2010.

[174] Hongbo Ren, Weijun Gao, and Yingjun Ruan. Optimal sizing for residential CHP system. *Applied Thermal Engineering*, 28(5-6):514–523, April 2008.

[175] A Shahmohammadi, M Moradi-Dalvand, H Ghasemi, and MS Ghazizadeh. Optimal design of multicarrier energy systems considering reliability constraints. *IEEE Transactions on Power Delivery*, 30(2):878–886, April 2015.

[176] Amirhossein Dolatabadi, Behnam Mohammadi-Ivatloo, Mehdi Abapour, and Sajjad Tohidi. Optimal stochastic design of wind integrated energy hub. *IEEE Transactions on Industrial Informatics*, 13(5):2379–2388, October 2017.

[177] Enrico Saverio Barbieri, YJ Dai, Mirko Morini, Michele Pinelli, Pier Ruggero Spina, P Sun, and RZ Wang. Optimal sizing of a multi-source energy plant for power heat and cooling generation. *Applied Thermal Engineering*, 71(2):736–750, October 2014.

[178] Martin Geidl and Göran Andersson. Operational and structural optimization of multi-carrier energy systems. *European Transactions on Electrical Power*, 16(5):463–477, 2006.

[179] Martin Geidl and Göran Andersson. Optimal coupling of energy infrastructures. In *Proceedings of IEEE PowerTech*, pages 1398–1403, Lausanne, Switzerland, July 2007.

[180] Yi Wang, Ning Zhang, Zhenyu Zhuo, Chongqing Kang, and Daniel Kirschen. Mixed-integer linear programming-based optimal configuration planning for energy hub: Starting from scratch. *Applied Energy*, 210:1141–1150, January 2018.

[181] Eduardo F Camacho and Carlos Bordons Alba. *Model Predictive Control*. Springer-Verlag, New York, NY, USA, 2nd edition, 2004.

[182] Moein Moeini-Aghtaie, Ali Abbaspour, Mahmud Fotuhi-Firuzabad, and Ehsan Hajipour. A decomposed solution to multiple-energy carriers optimal power flow. *IEEE Transactions on Power Systems*, 29(2):707–716, March 2014.

[183] Laura M Ramirez-Elizondo and Gerardus C Paap. Unit commitment in multiple energy carrier systems. In *Proceedings of the 41st North American Power Symposium*, pages 1–6, Starkville, MS, USA, 2009.

[184] Moein Moeini-Aghtaie, Payman Dehghanian, Mahmud Fotuhi-Firuzabad, and Ali Abbaspour. Multiagent genetic algorithm: An online probabilistic view on economic dispatch of energy hubs constrained by wind availability. *IEEE Transactions on Sustainable Energy*, 5(2):699–708, April 2014.

[185] Azadeh Maroufmashat, Ali Elkamel, Michael Fowler, Sourena Sattari, Ramin Roshandel, Amir Hajimiragha, Sean Walker, and Evgueniy Entchev. Modeling and optimization of a network of energy hubs to improve economic and emission considerations. *Energy*, 93:2546–2558, December 2015.

[186] Michele Arnold, Rudy R Negenborn, Göran Andersson, and Bart De Schutter. Model-based predictive control applied to multi-carrier energy systems. In *Proceedings of IEEE Power & Energy Society General Meeting*, pages 1–8, Calgary, AB, Canada, July 2009.

[187] Michele Arnold and Göran Andersson. Model predictive control of energy storage including uncertain forecasts. In *Proceedings of Power Systems Computation Conference*, volume 2, pages 954–960, Stockholm, Sweden, 2011.

[188] Will C Clarke, Chris Manzie, and Michael J Brear. Hierarchical economic MPC for systems with storage states. *Automatica*, 94:138–150, August 2018.

[189] Georgios Darivianakis, Angelos Georghiou, Roy S Smith, and John Lygeros. A stochastic optimization approach to cooperative building energy management via an energy hub. In *Proceedings of the 54th IEEE Conference on Decision and Control*, pages 7814–7819, Osaka, Japan, December 2015.

[190] Georgios Darivianakis, Angelos Georghiou, Roy S Smith, and John Lygeros. The power of diversity: Data-driven robust predictive control for energy-efficient buildings and districts. *IEEE Transactions on Control Systems Technology*, 27(1):132–145, January 2019.

[191] Michael Chertkov, Scott Backhaus, and Vladimir Lebedev. Cascading of fluctuations in interdependent energy infrastructures: Gas-grid coupling. *Applied Energy*, 160:541–551, December 2015.

[192] Alberto Martinez-Mares and Claudio R Fuerte-Esquivel. A unified gas and power flow analysis in natural gas and electricity coupled networks. *IEEE Transactions on Power Systems*, 27(4):2156–2166, November 2012.

[193] Xiaping Zhang, Mohammad Shahidehpour, Ahmed Alabdulwahab, and Abdullah Abusorrah. Optimal expansion planning of energy hub with multiple energy infrastructures. *IEEE Transactions on Smart Grid*, 6(5):2302–2311, September 2015.

[194] Mads Almassalkhi and Ian A Hiskens. Cascade mitigation in energy hub networks. In *Proceedings of the 50th IEEE Conference on Decision and Control and European Control Conference*, pages 2181–2188, Orlando, FL, USA, December 2011.

[195] Mads Almassalkhi and Ian A Hiskens. Impact of energy storage on cascade mitigation in multi-energy systems. In *Proceedings of IEEE Power & Energy Society General Meeting*, pages 1–8, San Diego, CA, USA, July 2012.

[196] Conrado Borraz Sanchez, Russell Bent, Scott Backhaus, Seth Blumsack, Hassan Hijazi, and Pascal van Hentenryck. Convex optimization for joint expansion planning of natural gas and power systems. In *Proceedings of the 49th Hawaii International Conference on System Sciences (HICSS)*, pages 2536–2545, Koloa, HI, USA, January 2016.

[197] Xinbo Geng and Le Xie. Data-driven decision making in power systems with probabilistic guarantees: Theory and applications of chance-constrained optimization. *Annual Reviews in Control*, 47:341–363, January 2019.

[198] Peyman Mohajerin Esfahani, Tobias Sutter, and John Lygeros. Performance bounds for the scenario approach and an extension to a class of non-convex programs. *IEEE Transactions on Automatic Control*, 60(1):46–58, January 2015.

[199] Marco Claudio Campi, Simone Garatti, and Federico Alessandro Ramponi. A general scenario theory for nonconvex optimization and decision making. *IEEE Transactions on Automatic Control*, 63(12):4067–4078, December 2018.

[200] Arkadi Nemirovski and Alexander Shapiro. Convex approximations of chance constrained programs. *SIAM Journal on Optimization*, 17(4):969–996, January 2007.

[201] Garth P McCormick. Computability of global solutions to factorable nonconvex programs: Part I—Convex underestimating problems. *Mathematical Programming*, 10(1):147–175, 1976.

[202] Sijia Geng, Maria Vrakopoulou, and Ian A Hiskens. Chance-constrained optimal capacity design for a renewable-only islanded microgrid. *Electric Power Systems Research*, 189:106564, December 2020.

[203] Richard Burden and J Douglas Faires. *Numerical Analysis*. Cengage Learning, Boston, MA, USA, 2004.

[204] James C Spall. *Introduction to Stochastic Search and Optimization: Estimation, Simulation, and Control*. Wiley, Hoboken, NJ, USA, 2005.

[205] Gerald B Folland. *Real Analysis: Modern Techniques and Their Applications*. Wiley, Hoboken, NJ, USA, 1999.

[206] M Jahangir Khan and Mohammad Tariq Iqbal. Pre-feasibility study of stand-alone hybrid energy systems for applications in Newfoundland. *Renewable Energy*, 30(6):835–854, May 2005.

[207] Paul E Dodds, Iain Staffell, Adam D Hawkes, Francis Li, Philipp Grünewald, Will McDowall, and Paul Ekins. Hydrogen and fuel cell technologies for heating: A review. *International Journal of Hydrogen Energy*, 40(5):2065–2083, February 2015.

[208] Daniel K Molzahn and Ian A Hiskens. A survey of relaxations and approximations of the power flow equations. *Foundations and Trends in Electric Energy Systems*, 4(1–2):1–221, 2019.

[209] A Herrán-González, JM De La Cruz, B De Andrés-Toro, and JL Risco-Martín. Modeling and simulation of a gas distribution pipeline network. *Applied Mathematical Modelling*, 33(3):1584–1600, March 2009.

[210] Yanling Lin, Bo Chen, Jianhui Wang, and Zhaohong Bie. A combined repair crew dispatch problem for resilient electric and natural gas system considering reconfiguration and DG islanding. *IEEE Transactions on Power Systems*, 34(4):2755–2767, July 2019.

[211] E Shashi Menon. *Gas Pipeline Hydraulics*. CRC Press, Boca Raton, FL, USA, 2005.

[212] Michèle Arnold, Rudy R Negenborn, Göran Andersson, and Bart De Schutter. Distributed predictive control for energy hub coordination in coupled electricity and gas networks. In *Intelligent Infrastructures*, pages 235–273. Springer, 2010.

[213] Aswin N Venkat, Ian A Hiskens, James B Rawlings, and Stephen J Wright. Distributed MPC strategies with application to power system automatic generation control. *IEEE Transactions on Control Systems Technology*, 16(6):1192–1206, November 2008.